University of Southampton

Faculty of Engineering and the Environment

Mechanical Engineering Department

Development of a New Approach for Modelling the Tribocorrosion of Cemented Tungsten Carbide in Oil and Gas Drilling Environments

---

Stephen Herd

Thesis for the degree of Doctor of Philosophy

November 2017

UNIVERSITY OF SOUTHAMPTON

ABSTRACT

FACULTY OF ENGINEERING AND THE ENVIRONMENT
Mechanical Engineering Department

Doctor of Philosophy

DEVELOPMENT OF A NEW APPROACH FOR MODELLING THE TRIBOCORROSION OF CEMENTED TUNGSTEN CARBIDE IN OIL AND GAS DRILLING ENVIRONMENTS

by Stephen Herd

One of the primary activities involved in oil & gas recovery is the drilling operation that allows access to the reservoir rock. Cemented tungsten carbide (WC-Co) is used to protect downhole components and is subject to both abrasive wear and corrosive degradation, called a tribocorrosion system. The combined result of these degradation mechanisms produces high and sometimes unpredictable wear rates that lead to challenges in the prediction of component service life. The objective of this study is to lay the foundations for a new way of understanding of WC-Co when exposed to tribocorrosion through use of numerical modelling and experimental techniques.

A new numerical modelling technique, the combined finite-discrete element method (FDEM), is proposed as a suitable method for the study of WC-Co. FDEM software Y-Geo, originally used for geomechanical applications, is used to simulate fracture explicitly in a WC-Co microstructure. For the first time a model was able to capture the discrete steps of fracture behaviour described from experimental observations. Furthermore, the simulated final fracture path matched closely with that obtained experimentally.

Through the process of creating a fracture model a number of knowledge gaps were highlighted in the current literature. In order to move towards a greater collaboration between the modelling and experimental sides of the field a new experimental focus on the degradation of microstructure and material properties at the mesoscale is proposed. Established mechanical and electrochemical techniques are coupled in new ways in order to bring a greater understanding to the degradation of WC-Co when exposed to corrosive environments. Potentiodynamic polarisation tests in acidic solutions (sulphuric acid) indicate 'pseudo passive' behaviour, whereas alkaline solutions (sodium hydroxide) show no signs of passivation although is more prone to pitting. Nanoindentation and Palmqvist tests (used for measuring fracture toughness) are performed on the corroded surfaces and compared against uncorroded samples. There is a clear decline in the fracture properties with acidic conditions having the largest impact.

This project looks to set a new course for the study of tribocorrosion by explicitly modelling tribocorrosion through understanding the effect of corrosion on both microstructure and intrinsic material properties.

Table of Contents

Presentations

25-Oct-17
MCF General Meeting
London, UK
The Marine Corrosion Forum
Oral presentation

2-Nov-16
Engineering Science Post Graduate Conference
Southampton, UK
University of Southampton
Poster presentation and extended abstract

9-Mar-16
nCATS seminar
Southampton, UK
University of Southampton
Oral presentation

2-Dec-15
24th Mission of Tribology
London, UK
Institution of Mechanical Engineers
Oral presentation

4-Nov-15
Engineering Science Post Graduate Conference
Southampton, UK
University of Southampton
Oral presentation and extended abstract

12-Apr-15 till 16-Apr-15
20th International Conference on Wear of Materials
Toronto, Canada
Elsevier
Poster presentation

20-Mar-15
Bennet Conference
Pittsburgh, PA, USA
Carnegie Mellon University
Poster presentation

11-Jun-14
nCATS seminar
Southampton, UK
University of Southampton
Oral presentation

List of Figures

List of Tables

Abbreviations

ASKA	-	Automatic System for Kinematic Analysis
ASTM	-	American Society for Testing and Materials
BEM	-	Backscattered Electron Mode
BHA	-	Bottom Hole Assembly
CFD	-	Computational Fluid Dynamics
CMP	-	Chemical Mechanical Polishing
CMU	-	Carnegie Mellon University
CoF	-	Coefficient of Friction
DEM	-	Discrete Element Method
EBSD	-	Electron Backscatter Diffraction
EDS	-	Energy Dispersive X-Ray Spectroscopy
EDX	-	Energy Dispersive X-Ray Spectroscopy
EGS	-	Enhanced Geothermal Systems
EIS	-	Electrochemical Impedance Spectroscopy
EP	-	Equal Pressure (model)
EPSRC	-	Engineering and Physical Sciences Research Council
EW	-	Equal Wear (model)
FCC	-	Face Centre Cubic
FDEM	-	Finite-Discrete Element Method
FEM	-	Finite Element Method
FIB	-	Focused Ion Beam
FPZ	-	Fracture Process Zone
GUI	-	Graphical User Interface
HCP	-	Hexagonal Close Packed
ISE	-	Indentation Size Effect

KOP	-	Kick Off Point
LEFM	-	Linear Elastic Fracture Mechanics
LNG	-	Liquefied Natural Gas
MMC	-	Metal Matrix Composite
MLZ	-	Multiligament zone
MWD	-	Measurement While Drilling
nCATS	-	National Centre for Advanced Tribology at Southampton
NBS	-	No Binary Search
NPL	-	National Physical Laboratory
P-B	-	Pilling-Bedworth
PCD	-	Poly Crystalline Diamond
PFTL	-	Particle Flow and Tribology Lab
RE	-	Reference Electrode
RSS	-	Rotary Steerable System
SCE	-	Saturated Calomel Electrode
SEM	-	Scanning Electron Microscopy
SENB	-	Single Edge Notched Beam
SHE	-	Standard Hydrogen Electrode
SIF	-	Stress Intensity Factor
TCI	-	Tungsten Carbide Insert
TRS	-	Transverse Rupture Strength
UK	-	United Kingdom
US(A)	-	United States (of America)
VGW	-	Virtual Geoscience Workbench
XFEM	-	Extended Finite Element Method

Nomenclature

Symbols

A	-	Area	[m^3]
A_a	-	Apparent area of contact	[m^3]
A_c	-	Indenter projected area	[m^3]
A_W	-	Atomic weight	[g mol^{-1}]
a	-	Crack length	[m]
a_1	-	Fitting parameter	[dimensionless]
a_2	-	Fitting parameter	[dimensionless]
a_3	-	Fitting parameter	[dimensionless]
a_4	-	Fitting parameter	[dimensionless]
a_5	-	Fitting parameter	[dimensionless]
a_6	-	Fitting parameter	[dimensionless]
a_7	-	Fitting parameter	[dimensionless]
a_8	-	Fitting parameter	[dimensionless]
a_9	-	Fitting parameter	[dimensionless]
a_{10}	-	Fitting parameter	[dimensionless]
a_{11}	-	Fitting parameter	[dimensionless]
a_{12}	-	Fitting parameter	[dimensionless]
a_{13}	-	Fitting parameter	[dimensionless]
b	-	Specimen width	[m]
C	-	Contiguity	[dimensionless]
c_{MR}	-	Concentration mass ratio	[dimensionless]
D	-	Normalised displacement	[dimensionless]
D_d	-	Average wear debris particle diameter during	

		low-cycle micro-fatigue wear	[m]
D_m	-	Average particle diameter in the influence of degradation	[m]
d	-	Displacement	[m]
d_{WC}	-	Mean carbide grain size	[m]
d_s	-	Sliding distance	[m]
E	-	Young's / Elastic modulus	[Pa]
E_a	-	Anodic potential	[V]
E_c	-	Cathodic potential	[V]
E_{cor}	-	Corrosion potential	[V]
E_{OCP}	-	Open Circuit potential	[V]
E_P	-	Polarised potential	[V]
E_0	-	Equilibrium potential	[V]
E^*	-	Relative / Indentation modulus	[Pa]
f_c	-	Contact frequency between sliding surfaces or cyclic loading frequency	[Hz]
G_{IC}	-	Energy release rate (Mode I)	[J mol^{-1}]
g_{CFS}	-	Maximum attainable crack growth rate during the generation of a low-cycle micro-fatigue wear debris particle in corrosion fatigue conditions	[m cycle^{-1}]
g_r	-	Average crack growth rate during the generation of a low-cycle micro-fatigue wear debris particle in the reference environment	[m cycle^{-1}]
g_R	-	Resultant crack growth rate during the generation of a wear debris particle in the reference environment	[m cycle^{-1}]

g_S	-	Resultant crack growth rate during the generation of a wear debris particle in the corrosive environment under sustained stresses	[m cycle^{-1}]
H	-	Hardness	[Pa]
H_B	-	Hardness of binder	[Pa]
H_{comp}	-	Hardness of composite material	[Pa]
H_{WC}	-	Hardness of WC	[Pa]
$H_{WC\text{-}Co}$	-	Hardness of WC	[Pa]
H_V	-	Vickers Hardness	[HV]
h	-	Indentation depth	[m]
h_e	-	Element size	[m]
h_{max}	-	Indentation depth at maximum load	[m]
h_p	-	Contact depth	[m]
h_r	-	Residual displacement depth	[m]
I	-	Current	[A]
I_a	-	Anodic current	[A]
j	-	Current density	[A cm^{-2}]
j_a	-	Anodic current density	[A cm^{-2}]
j_{cor}	-	Corrosion current density	[A cm^{-2}]
j_p	-	Passive current density	[A cm^{-2}]
j_0	-	Exchange current density	[A cm^{-2}]
K_I	-	Stress intensity factor (Mode I)	[Pa m$^{0.5}$]
K_{IC}	-	Fracture toughness (Mode I)	[Pa m$^{0.5}$]
K_W	-	Wear coefficient	[dimensionless]
L	-	Length	[m]
L_{pr}	-	Length of fracture profile	[m]

l_d	-	Fracture length parameter	[m]
l_s	-	Total sliding distance	[m]
l_w	-	Length of wear track	[m]
M_m	-	Molar mass	[g mol^{-1}]
M_W	-	Molecular weight	[kg mol^{-1}]
N_{BC}	-	Average number of binder/carbide intercepts	[m^{-1}]
N_C	-	Number of critical micro-cracks on a unit area of the wear surface that are ready to propagate	[dimensionless]
N_{CC}	-	Average number of carbide/carbide intercepts	[m^{-1}]
N_{Co}	-	Number of point counts for Co	[dimensionless]
N_s	-	Solution normality	[normal]
N_{WC}	-	Number of point counts for WC	[dimensionless]
n	-	Number of electrons in a reaction	[dimensionless]
P	-	Applied load	[N]
P_n	-	Normal wear load	[N]
P_{max}	-	Maximum applied load	[N]
P_0	-	Threshold indentation load	[N]
P_ε	-	Overvoltage	[V]
P_η	-	Overpotential	[V]
PBR	-	Pilling-Bedworth ratio	[dimensionless]
p_c	-	Contact penalty	[dimensionless]
p_f	-	Fracture penalty	[dimensionless]
R_L	-	Linear Roughness	[dimensionless]
R_{KO}	-	Electron penetration depth	[m]
r	-	Radius	[m]
r_p	-	Irwin's estimated plastic zone size	[m]

s	-	Width	[m]
t	-	Time	[s]
t_s	-	Total sliding time	[s]
V_{AC}	-	Abrasion-Corrosion wear	[m^3]
V_{CHEM}	-	Wear accelerated corrosion	[m^3]
V_{MECH}	-	Corrosion accelerated wear	[m^3]
V_{PA}	-	Pure abrasive wear	[m^3]
V_{PC}	-	Pure corrosion wear	[m^3]
V_R	-	Polish rate	[]
V_S	-	Synergistic wear	[m^3]
V_{TOT}	-	Total wear due to tribocorrosion	[m^3]
V_B^f	-	Volume fraction binder	[wt.%]
V_{Co}^f	-	Volume fraction binder	[wt.%]
V_{WC}^f	-	Volume fraction WC	[wt.%]
v_l	-	Linear velocity	[m s^{-1}]
W	-	Palmqvist toughness	[N m^{-1}]
w_m	-	Mass loss	[kg]
w_v	-	Wear volume	[m^3]
X	-	Cycles, time or distance	[variable]
Y	-	Stress intensity constant	[dimensionless]
Z_a	-	Atomic number	[dimensionless]
z	-	Stress scaling function	[dimensionless]
z_e	-	Valence of metal for andic reaction during corrosion	[dimensionless]
α_d	-	Fracture angle parameter	[degrees]

β_a	-	Anodic Tafel coefficient	[V decade^{-1}]
β_b	-	Cathodic Tafel coefficient	[V decade^{-1}]
β_{BERK}	-	Berkovich indenter geometry shape factor	[dimensionless]
ΔV_A	-	Change of abrasive wear due to corrosion	[m^3]
ΔV_C	-	Change of corrosive wear due to abrasion	[m^3]
δ	-	Element displacement	[m]
δ_a	-	Allowable element penetration	[m]
δ_c	-	Critical failure displacement	[m]
δ_t	-	Critical yield displacement	[m]
ε	-	Strain	[dimensionless]
ε_c	-	Critical Strain	[dimensionless]
ζ_c	-	Critical viscous damping	[dimensionless]
θ_α	-	Half central angle	[degrees]
Λ	-	Tip geometry function	[dimensionless]
λ	-	Binder mean free path	[m]
ν	-	Poisson's ratio	[dimensionless]
ρ	-	Density	[kg cm^{-3}]
σ	-	Stress	[Pa]
σ^A	-	Standard deviation of asperity height	[m]
σ_b	-	Bonding strength	[Pa]
σ_c	-	Critical stress criteria	[Pa]
σ_y	-	Yield stress	[Pa]
σ_∞	-	Remote stress	[Pa]
τ_i	-	Reaction time for the chemical reaction controlling corrosion fatigue	[s]
τ_0	-	Characteristic passivation time	[s]

ψ	-	Apex angle	[degrees]

Units

A	-	Ampere
C	-	Coulomb
°C	-	Degree Celsius
d	-	Day
F	-	Farad
ft	-	Foot
g	-	Gram
gf	-	Gram Force, conversion of gf to N ×9.807
HV	-	Vickers Hardness, conversion of HV to GPa ×0.009807
Hz	-	Hertz
h	-	Hour
J	-	Joule
L	-	Litre
M	-	Molar
m	-	Metre
min	-	Minute
mol	-	Mole
N	-	Newton
Pa	-	Pascal
ppm	-	Parts Per Million
s	-	Second
V	-	Volt
W	-	Watt

wt.%	-	Weight Percent
Ω	-	Ohm
”	-	Inch

Physical Constants

F	-	Faraday’s constant	96,500 C mol^{-1}

Declaration of Authorship

I, Stephen Herd, declare that the thesis entitled "Tribocorrosion of cemented tungsten carbide in oil and gas drilling environments" and the work presented in the thesis are both my own, and have been generated by me as the result of my own original research. I confirm that:

- this work was done wholly or mainly by me while in candidature for a research degree at this University;
- where any part of this thesis has previously been submitted for a degree or any other qualification at this University or any other institution, this has been clearly stated;
- where I have consulted the published work of others, this is clearly attributed;
- where I have quoted from the work of others, the source is always given. With the exception of such quotations, this thesis is entirely my own work;
- I have acknowledged all main sources of help;
- where the thesis is based on work done by myself jointly with others, I have made clear
- exactly what was done by others and what I have contributed myself; and,
- parts of this work have been published as:
  i. R.J.K. Wood, S. Herd and M.R. Thakare, *A critical review of the tribocorrosion of cemented and thermal sprayed tungsten carbide*. Tribology International. [accepted 6 October 2017]
  ii. S. Herd, R.J.K. Wood, J.A. Wharton, and C.F. Higgs III, *Explicit fracture modelling of cemented tungsten carbide (WC-Co) at the mesoscale*. Materials Science and Engineering: A. [accepted 26 November 2017]
  iii. S. Herd, R.J.K. Wood, J.A. Wharton *Effect of corrosion on the microstructure of cemented tungsten carbide (WC-Co)*. To be submitted.

Signed

Stephen Herd

Date

Acknowledgements

I would like to thank my supervisors Professor Robert Wood and Dr Julian Wharton at the University of Southampton for their time and help with this project. Their academic rigour and critical analysis played an important part in the ideas underpinning this work.

A special thanks goes to Professor Fred Higgs to whom I applied to and who made the initial proposal for the project, a collaboration between Carnegie Mellon University and the University of Southampton, providing me with a great opportunity to be a visiting research student at one of the leading universities in computation science and engineering. Not only did I learn about a new way of looking at problems, I saw a different academic approach.

A special thank you to members of the nCATS department who have helped with setting up of experiments and discussions of results especially: Richard Cook, Vanesa Martinez and Behrad Mahmoodi for help on the nanoindenter; Anna Crosby and Rachael for helping with electrochemistry; Pawee Kucita for SEM; Alex Richardson for polishing; and Adam Kessler who helped with the haiku. Thanks to all the other PhD students who made my time back at university an exciting and memorable, including those at Carnegie Mellon.

I also wish to thank those that helped me in the preparation for a PhD, especially to those who wrote my references: Graeme Manson, my undergraduate tutor; Robert Howell, my undergraduate final year project supervisor; and Derek Hudson, my manager while I was working in Thailand at Foster Wheeler.

Thank you to my parents, mainly for not panicking when I told them I was leaving my well paid comfy job to do a PhD, but also for the support and instilling the importance of education. Finally, my girlfriend Madeleine. I know I was a pain, but I really did appreciate your optimism. Sorry for missing all those holidays.

Tribocorrosion

Difficult to understand

New approach was found

Chapter 1 – Introduction

1.1 Background

Energy world consumption continues to rise primarily from demand in developing economies, China and India accounting for 90% alone, where their populations continue to grow and living standards improve [1]. Although green technologies such as wind and solar have seen rapid growth over recent years, the cost of deployment and intermittency remains the primary constraints to wider uptake of renewables. These factors mean that hydrocarbons are expected to continue to dominate the energy mix for the next 30 years [2].

Oil and gas are major contributors to transportation, electricity and heating sectors, but as oil and gas field are depleted the search for new sources becomes more challenging. Fields are becoming deeper and smaller, requiring improved technology to make recovery economically viable. One of the main stages in the lifecycle of oil and gas production is drilling from the surface to the reservoir rock containing the hydrocarbons. This is an extremely harsh environment and subjects exposed downhole components to high wear. Cemented tungsten carbide is a composite material that displays excellent hardness and fracture toughness making it ideally suited to this high abrasion environment. The material is used for drill bits and inserts, designed to protect the highest wearing sections of the drill assembly. The

degradation of these components will be the focus of this study. One of the primary wear mechanisms is by the sliding of abrasive slurry particles against the material surface in a chemically active solution. This combination of mechanical and chemical degradation processes is considered a tribocorrosion system and poses significant challenges to wear prediction. It has been well documented that wear in tribocorrosion systems differ to that of their separate parts, typically detrimentally. However, the magnitude of this increased wear and mechanisms that contribute to this change in wear rate are not well understood.

1.2 Aims and Scope of Research

The aim of this study is to improve fundamental understanding of the interaction between mechanical degradation and electrochemistry in cemented tungsten carbide with cobalt binder (WC-Co). From this understanding conclusions can be drawn about how this affects abrasion and corrosion wear mechanisms which typically lead to accelerated material loss, decrease component life and reduce drilling efficiency.

The primary objectives of this project are:

- An extensive literature review will be conducted to assess the current knowledge of cemented tungsten carbide in tribocorrosion environments. Review of wear and corrosion specific literature will provide a detailed understanding of the respective mechanisms. A review of computational models will summarise approaches which are relevant to the material of interest.
- Propose and validate a suitable modelling approach which is capable of capturing the main material behaviours, as well as the wear and corrosion processes, that have been highlighted from the literature review with a view to understand tribocorrosive wear of WC-Co better and ultimately be able to predict wear.
- Established mechanical and electrochemical experimental techniques will be combined to provide an understanding of the behaviour of cemented tungsten carbide under corrosion and mechanical wear and will bridge gaps in the current literature.

To create a clear framework boundaries to the project are also set:

- Material grades will be restricted to straight compositions of cemented tungsten carbide so as to limit the number of variables. Coating and alloying additions will not be considered in this study.
- Corrosive solutions used will be simplified to acidic and alkaline solutions so as to reduce the complexity of corrosive behaviour.
- Temperature and pressure are not considered. All experiments are conducted at room temperature and atmospheric pressure.

In order to achieve these objectives a finite-discrete element model (FDEM) has been used for the first time to simulate fracture explicitly of WC-Co. This modelling approach has the potential to capture many of the critical wear mechanisms that are identified in the literature review and address the shortcomings of current wear models, principally fracture behaviour. The validation of the FDEM is performed through a series of studies which build up to a model capable of simulating fracture of WC-Co at the mesoscale. This scale is chosen in order to capture wear interactions between abrasive and phases in the bulk material, as well as microstructural effects which influence properties of the bulk material, both important factors which were highlighted in the literature.

Having presented the new modelling approach, key gaps in our understanding necessary to simulation degradation of WC-Co are highlighted. The current experimental methods for studying tribocorrosion are critiqued and conclude that many of the typical approaches are not able to inform the modelling approach used. In order to help bridge this gap between computational and experimental approaches a new focus on intrinsic material properties and interaction at the grain scale is proposed.

Appropriate electrochemical and mechanical testing methods that are able to inform that modelling and close gaps in our understanding are selected from the literature review. Electrochemical and mechanical experiments are conducted on commercially available grades of WC-Co while post analysis techniques are used to analyse and compare samples following corrosion in both acidic and alkaline solutions. Fracture tests on these sample allow comparison of corrosion on fracture properties as well as characterisation of the behaviour.

This project is a collaboration between the National Centre for Advanced Tribology at Southampton (nCATS) research group at the University of Southampton and the Particle Flow and Tribology Lab (PFTL) at Carnegie Mellon University (CMU). Experience of experimental electrochemical and mechanical testing will be combined with expertise in computational modelling from the respective research groups. This project is funded by the Engineering and Physical Sciences Research Council (EPSRC) Green Tribology grant EP/J001023/1.

1.3 Structure

The report consists of eleven chapters and is prepared as a single body of work covering both numerical modelling and experimental aspects of the project. An outline of the thesis structure is given by the flowchart in Figure 1-1. There are three main bodies of work covering the primary goals of the project: literature review, numerical modelling and experimental tests.

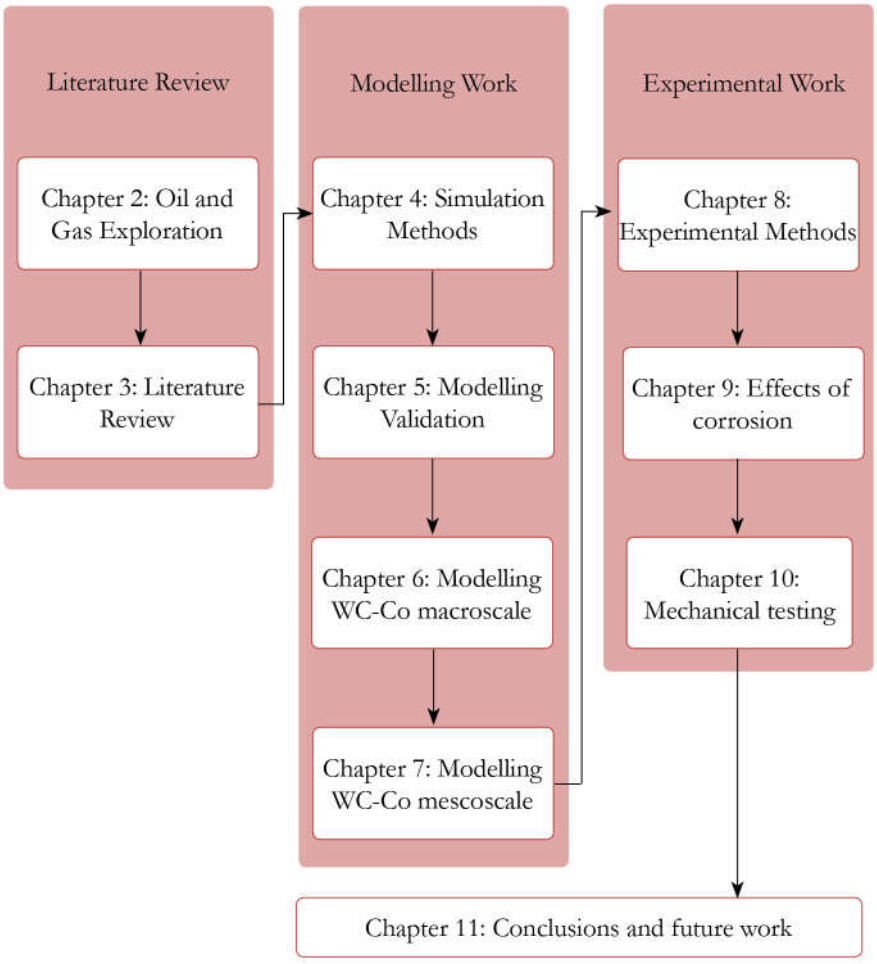

Figure 1-1: Outline of thesis structure.

To help the reader navigate the report an overview of each chapter is provided here:

Literature Review

Chapter 2 presents an introduction to oil and gas exploration and sets out the background and motivation behind the project. The engineering challenges associated with the material of interest are explained, principally the tribological system and the implications on operations for wear of these components. In this section most measurements are given in imperial units with metric equivalents as this is industry standard.

In Chapter 3 a comprehensive literature review of cemented tungsten carbide is conducted for the fields of interest. It is split up into six main sections: material properties, fracture mechanics, tribology, tribocorrosion, electrochemistry and modelling. These sections summarise the primary physics involved and current understanding of the degradation mechanisms of the material. Finally, there is a review of the main modelling studies that have been conducted to date. This understanding of state of the art, combined with knowledge of the degradation mechanisms, helps to prioritise what aspects of WC-Co tribocorrosion need to be modelled. An introduction to a new modelling approach which can address these gaps is provided.

Numerical Modelling

Having identified fracture to be a major barrier to progression of a tribocorrosion model in the literature review, Chapter 4 justifies the general modelling approach used. This is followed by a more in-depth explanation of modelling parameters and methodology used in subsequent modelling chapters.

Chapter 5 presents the simulation results that are used to validate the model. A series of modelling parameters including mesh studies and material properties are applied to simple geometries to investigate the effect on the accuracy of simulation results. These findings will then be applied to future simulations.

In Chapter 6 simulations of a Brazilian (indirect tensile) test are performed for cemented tungsten carbide. This demonstrates how properties applied to elements can be scaled up to macroscale properties. A discussion of the post-processing of simulation data carried out using Matlab shows how this can help to provide further analysis of fracture and validate simulation results.

In Chapter 7 modelling of WC-Co is done at the mesoscale. An image from a fracture experiment is used as a template to create a mesh and validate the simulated fracture path. Fracture propagation is simulated dynamically and behaviour compared to that described from experimental studies.

Experimental Tests

In Chapter 8 the most appropriate electrochemical and mechanical testing methods that can inform that modelling are selected from the literature review. The methodology used in subsequent chapters is discussed.

In Chapter 9 electrochemical experiments using a standard three-cell electrode set up are conducted in both acidic and alkaline solutions. The results and conclusions from open circuit potential, potentiodynamic polarisation and potentiostatic polarisation are presented and discussed. Analysis of the surface by scanning electron microscope (SEM) and Energy Dispersive X-Ray Spectroscopy (EDX) is used to assist with the understanding of differing corrosion behaviour.

Chapter 10 presents results from indentation and fracture tests of WC-Co samples exposed to corrosive environment from Chapter 9. Surface properties and fracture characterisation are compared against uncorroded control samples as well as different corrosive solutions.

Conclusions and Future Work

Chapter 11 provides a summary of the main findings of the thesis and discusses the overall impact and contribution of this work to the field. This chapter also suggests possible areas of future work required to continue this research as well as particular areas of knowledge gaps that have been highlighted in this project.

Chapter 2 – Oil and Gas Exploration

Chapter Highlights

A brief introduction to the drilling process in oil and gas exploration is given so that the context and the engineering challenges can be fully understood. This also demonstrates the continued importance of studying the degradation mechanisms in cemented tungsten carbide.

- Cemented tungsten carbide is used to protect part of downhole components which see the highest wear and extend their service life.
- Although cemented tungsten carbide has high abrasion resistance, it is still subject to high wear rates requiring components to be replaced.
- Drilling fluid emerses downhole components, which subjects them to electrochemical corrosion.
- Improvement in wear performance will impact operational efficiency, which reduces costs and increase safety.

2.1 Geology

Before drilling commences geologists perform seismic surveys to image rock formations and help identify potential formations where oil and gas reservoirs may

form. In conventional developments reservoir rocks have high permeability and porosity, such as sandstone and limestone. Caprocks above this formation are also required to trap the hydrocarbons in the reservoir rock, preventing it from migrating further towards the surface. Typical caprocks include shale and salt.

The Mohs scale was created by the German geologist Friedrich Mohs in 1824 to categorise the hardness of various minerals [3]. It is composed of ten minerals, one being assigned to the softest material, talc, to ten for the hardest material, diamond. The position of a mineral in the table is based on its ability to scratch another. It is generally viewed that harder rocks cause greater wear. However, these tests are conducted at high loads and therefore provide properties at the macroscale. Beste and Jacobson [4] reasoned that this was not an accurate reflection of properties at a microscale at which wear typically occurs. They therefore conducted detailed hardness measurements on a variety of rock types which had a broad range of particle hardness within one sample. Thus although the overall hardness of a rock may be soft, these harder particles would be capable of abrading WC-Co drill bits. This effect was then demonstrated when scratch tests carried out by Beste et al. [5] on various rock found that sandstone wore cemented tungsten carbide samples in dry conditions at twice the rate of materials which were much harder. The quartz content in the sandstone was found to be more critical to the wear rates observed than the hardness of the overall rock. The grain size of sandstone is these tests were in the range of 200 μm – 2000 μm.

2.2 Shale Gas and Hydraulic Fracturing

At this point it may be appropriate to include a short discussion on the recent development of shale gas and the use of hydraulic fracturing (often referred to as 'fracking') to stimulate production. Shale gas is classed as an unconventional gas, which also includes tight gas and coalbed methane, see Figure 2-1. Shale gas and tight gas are characterised by low permeability rock formations that they are found in, which prevents the migration of gas therefore requiring stimulation in order to create economic flow rates [6].

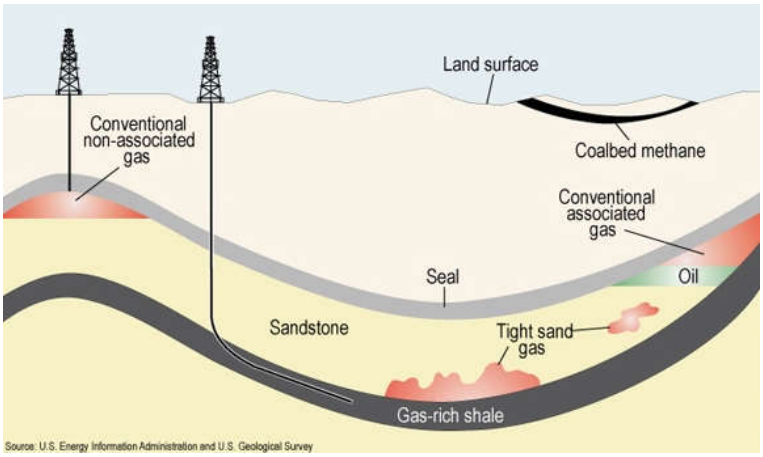

Figure 2-1: Schematic geology of natural gas resources [7].

Drilling methods are similar to that of conventional fossil fuels, however due to relatively lower fuel density in the rock shale gas recovery relies more heavily on use of directional, and more specifically horizontal drilling techniques, to maximise surface area of the well and to make production costs economical.

Although hydraulic fracturing has been used since the 1940s, and directional drilling since the 1930s, the dramatic increase in its use over the past decade in the United States (US) has led to a number of concerns from local communities and environmental groups. These concerns include possible contamination of aquifers, increased seismic activity and worries about the introduction of another fossil fuel source [8-10]. Proponents assert that shale gas is a local resource which should be utilised and provides energy security for the United Kingdom (UK), helping alleviate falling gas supplies from the North Sea and rely less heavily on imported gas from Norway and Qatar [11, 12]. In the US, shale gas has been credited with the rapid fall in energy prices and carbon dioxide emissions, primarily due to the reduction of electricity produced from coal fired power plants. There are now a number of projects which are converting existing liquefied natural gas (LNG) import to export terminals [13].

In 2011 the European Council outlined the need to explore unconventional fossil fuels, including shale gas. Environmental concerns over the risks involved with fracking have hindered development outside the US, especially in europe. As a result, the UK government has commissioned numerous studies from various stakeholders on the potential of shale gas and the possible impact of its development [14-16].

While oil and gas extraction remains the primary user of directional drilling and hydraulic fracturing technology, research has also applied similar methods to geothermal energy, named Enhanced Geothermal Systems (EGS) [17, 18]. This allows otherwise uneconomical geothermal energy to be developed by stimulation of fractures, a process called hydroshearing, in impermeable rock formations thereby increasing flow circulation of water which is pumped down the injection well, see Figure 2-2.

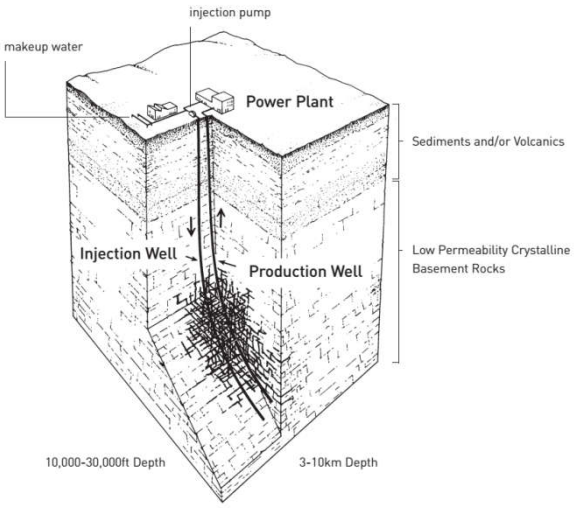

Figure 2-2: Schematic of a conceptual two-well Enhanced Geothermal System in hot rock in a low-permeability rock formation [17].

2.3 Drill Rig Components

Drill rigs come in a variety of sizes and designs. While onshore designs are somewhat standard, offshore rigs include submersibles, semisubmersibles, jack-ups and drillship designs, see Figure 2-4. However the same general components can be found in all of these rig designs.

a) **b)**

Figure 2-3: a) Onshore drilling rig located in Texas, USA and b) Offshore jack-up drilling rig located in the North Sea Forties field [19].

Above ground the most visible structure is the derrick, which provides the vertical height required to raise drillpipe into place before being lowered into the borehole. The derrick also houses the hoisting mechanism at the top of the structure to provide the vertical motion, allowing controlled descent and removal of the drill string. Rotary motion is provided through either a rotary table on the derrick floor or through a topdrive system which is integrated into the hoisting mechanism.

The drill string is primarily made up of drillpipe which comes in approximately 30 ft (9 m) sections which are screwed together to extend the reach of the drill string. As the drill descends additional lengths of drillpipe are screwed together. It transfers mechanical power, both vertical and rotational, from the rig to the drill bit. The drillpipe is hollow, allowing the circulation of drilling fluid during the drilling operation.

Located at the lower end of the drill string is the bottom hole assembly (BHA). This consists of a number of different components, both mechanical and instrumentation which can be combined depending on drilling and operator requirements. Common components which make up the assembly include drill bits, stabilisers, drill collars and measurement while drilling (MWD) instrumentation. Cemented tungsten carbide material is typically found in these BHA components, where abrasive wear mechanisms are greatest.

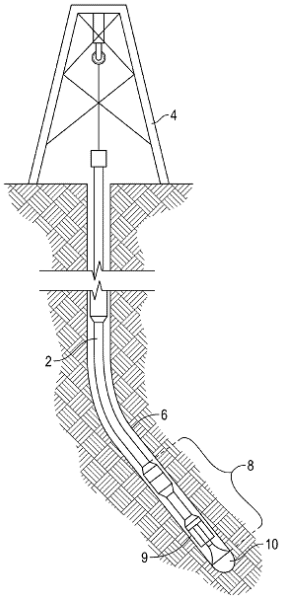

Figure 2-4: Main drill rig components 4) Derrick structure 2) Drill pipe 6) Wellbore 8) BHA 9) RSS and 10) Drill bit [20].

The two most common drill bit types used in oil and gas drilling are roller cone and fixed cutter, see Figure 2-5. Roller cone, also referred to as tricone bits, use percussive impacts to crush rock into fragments. The cones are mounted on bearings such that as the drill string rotates the cutting teeth engage the rock and the body is allowed to rotate freely. The two most common cutter bits are mill tooth bits and tungsten carbide insert (TCI) bits. Tungsten carbide inserts or buttons are used in harder rock formations where wear of the steel in the milled tooth bits is excessive and would be operationally prohibitive. The high cost of oil and gas drilling has also resulted in the use of polycrystalline diamond (PCD) covered tungsten carbide bits which provide greater wear resistance. These fixed cutter bits use a different mode of cutting, by means of shearing, and rely on the torque applied to the drill itself rather than relying on internal moving parts. Ultimately the choice of drill bit depends on a number of variables including geology, operational costs and experience.

a) b)

Figure 2-5: Example of a) tricone drill with TCI bits and b) fixed cutter with PCD drill bit [21, 22].

Several methods are used to achieve deviated wells required for horizontal drilling, the most advanced of which are Rotary Steerable Systems (RSS). These allow the drill bit to be directed in real time by surface controls which is achieved through either applying pressure against the bore walls or by flexing the drive shaft. Both systems are located in the BHA, usually just above the drill bit. One method of applying pressure to the bore wall is through hydraulically operated pads. Due to the nature of its design, they will be subject to high abrasion as pads will contact the rock. As such, TCIs are used to prolong service life of these components.

Stabilisers provide stability to the BHA during drilling by reducing buckling, vibrations and differential sticking which leads to unwanted deviation. They come in a variety of configurations depending on its application. Reamers, similar in appearance to stabilisers, are used to ensure a defined bore size is met prior to the next stage of the drilling process as well as smoothing of the bore wall. They are therefore exposed to the same conditions as those seen by the stabiliser. As these components are designed to contact against the borewall they are often prone to increased wear. On some designs tungsten carbide hard facing or TCIs are used to control this wear. Often reamers and stabilisers can provide dual functionality.

2.4 Drilling Process

A typical well is drilled in several stages, starting with a large drill bit, followed by a series of smaller bits until final depth is reached. Following drilling of each section of the well, pipe (called casing) is inserted into the borehole and cemented into place.

This is designed to stabilise the well and prevent hydrocarbons from entering the rock formation. The first casing is called conductor casing and is generally around 16-48" (400-1200 mm) diameter. The final and smallest casing is production casing which is about 4-9⅝" (100-250 mm) diameter.

Between each of the drilling operations the drillstring has to be removed from the borehold in order to install the casing, called tripping. This is a routine operation and is required when changing operation, for example between drilling and casing installation. Tripping is also required to replace worn drill bits and damaged components or drill pipe. As this is an integral part of the drilling process trip time is an important factor when considering well design and drilling method. Trip times depends primarily on the total length of the well, as a rule of thumb one hour per 100 ft (~300 m) plus 1-2 h for handling components at the surface is used [23]. Although this is a standard operating on a drill rig, contractors are keen to reduce the number of times this has to be performed as it slows progress and increases safety risk. As drilling depth increases the time to trip out pipe increases, further adding to the monetary cost.

In developments that require horizontal drilling the initial drilling process will begin in the same way as conventional wells. Vertical drilling will continue to a depth called the kick-off point (KOP) at which point directional drilling equipment is used which allows build rates of up to 15°/100 ft (15°/30 m). A higher build rate enables operators to increase the depth of the vertical part of the well prior to the KOP, thus maximising the development of the rock formation, but also places greater strain on downhole components.

Due to the high costs involved as well as the production of a high-value product, economics drive well design and operational procedure, optimising for minimum cost per foot drilled. Once drilling is complete, completion activities can begin which will allow production of the well.

The drill string is exposed to extremely harsh operating conditions, especially so in horizontal drilling as drilling components experience increased contact with the rock face resulting in increased wear. Understanding of the degradation mechanisms will help to predict in the service life of components and therefore scheduled maintenance cycles and reduce tripping pipe.

2.5 Drilling Fluid

Drilling fluid, also referred to as drilling mud, performs several essential functions during the drilling process. Mud pumps continuously circulated drilling fluid down through the drill string, out through nozzles in the drill bit, lifting rock cuttings back up the annulus of the borehole to the surface where it is filtered. The most commonly used drilling fluids are water based which are primarily composed of bentonite clay along with a number of other additives which aid the drilling process [24]. Pneumatic and oil based are the other two classification of drilling fluids, although are only used in specific situations where water based fluids are not suitable. In addition to removing cuttings the drilling fluid provides wellbore stability, cooling and lubrication of the drill bit and drill string, corrosion inhibitors and sometimes mechanical power.

Sodium hydroxide (NaOH) is added as a corrosion inhibitor by keeping drilling fluid alkaline, in a pH range between 8 and 11 [24, 25]. Corrosion is further reduced as NaOH is used to control the solubility of calcium and magnesium. It also acts as a sulphide scavenger for hydrogen sulphide (H_2S) which may be present in formations. H_2S is a highly toxic gas and can also cause severe corrosion problems for metals due to sulphide stress cracking and hydrogen embrittlement. As well as being damaging to equipment, the release of H_2S is highly dangerous for drill crews and is an immediate danger to health at concentrations around 100 ppm, fatality at 700-1000 ppm.

Immersion of components in this solution exposes them to a chemically active environment. This results in corrosion of the material in addition to the mechanical wear mechanisms from rock abrasion. The combination of these degradation mechanisms is the focus of this project.

Chapter 3 – Literature Review

Chapter Highlights

This chapter introduces cemented tungsten carbide and its mechanical and corrosion properties. A thorough understanding of all the main properties is required to identify the necessary attributes of a model and what fundamental physics needs to be encapsulated.

- Material properties of the bulk material are defined by the properties of the individual phases, the composition and the microstructure.
- Brittle failure is a primary degradation mechanism of cemented tungsten carbide.
- Corrosion behaviour of cemented tungsten carbide differs between acidic and alkaline solutions and can dramatically alter the microstruture.
- Current approaches to understand tribocorrosion (the combined action of mechanical and chemical degradation mechanisms) are unable to accurately predict wear and are subject to high error.
- Numerical methods offer a method for investigating tribocorrosion, although are currently not sufficiently developed.

3.1 Composition of Cemented Tungsten Carbide

3.1.1 An Overview

Cemented tungsten carbides are a well-established ceramic composite which dates back to the 1920s, developed from the search for an alternative hard material to expensive and restricted supply of diamond used in drawing dies [26]. Although tungsten carbide was first synthesised in the 1890s by French chemist Henri Moissan the material was too brittle to be useful [27, 28]. It was not until 20 years later when the Osram group in Berlin trialled sintering it with nickel and later cobalt that a practical engineering material was produced. Karl Schröter's patents [29, 30] submitted in 1923 are widely regarded as the first manufacturing techniques for cemented tungsten carbide and still forms the basis for manufacturing processes used today. As well as oil and gas drilling cemented tungsten carbide is used in many high wear applications including machining tools, metal forming and mining [31].

Cemented carbides are composite materials that primarily comprise of a ceramic reinforcement with a metal matrix, not typically making up more than 30% of the total weight. The hard tungsten monocarbide (WC) grains have an interpenetrating network of a softer, ductile binder metal from the iron group of metals such as nickel (Ni) or more commonly cobalt (Co). This combination of hardness and ductility creates a material that has good fracture toughness and provides excellent resistance to erosion and abrasion. Additionally, alloying elements such as Cr_3C_2 and VC, are added to the binder to improve certain characteristics such as corrosion resistance and fracture toughness or used as a grain growth inhibitor during the sintering process. Cemented tungsten carbides have also been combined with other refractory ceramic materials, such as TiC and TiN, to further enhance particular mechanical properties.

By varying the composition of the cemented carbide, properties of the bulk material can be modified allowing optimisation for a particular application. Typically hardness values vary between 1000-2000 HV and toughness between 7-25 MPa $m^{0.5}$ [32]. Increasing the binder phase content will enhance the ductility of the material thereby increasing the fracture toughness, but at the expense of reducing the hardness, see Figure 3-1. Although binder content for typical compositions can vary

between 3% and 30%, oil and gas application tend to only use grades up to 20% due to the requirement for high abrasion resistance materials [33, 34].

By convention the composition of the cemented carbides are written carbide followed by binder phase materials and content, e.g., WC-11Co indicates tungsten carbide with 11 weight percent (wt.%) cobalt binder phase.

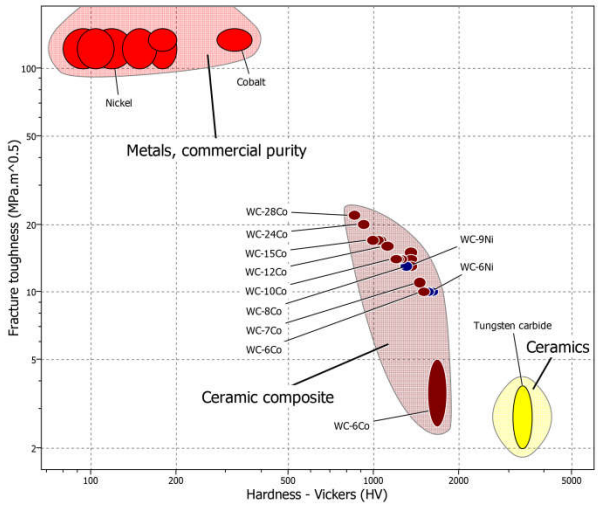

Figure 3-1: Ashby plot showing how hardness and fracture toughness varies with WC and binder ratios, (red) commercially pure Co/Ni, (yellow) pure WC, (brown) WC-Co, (blue) WC-Ni [32].

The terminology surrounding cemented tungsten carbide is highly inconsistent, and no single standard appears to have been adopted in open literature or industry. Cemented tungsten carbide and its various compositions are also sometimes referred to as hardmetals, translated from the German equivalent "Hartmetall". The term hardmetal was originally used to refer to the ceramic materials containing carbides, nitrides, borides and silicide, but is now also often used to encompass all ceramic composites [35]. Confusingly, however, it is often used to singularly identify tungsten carbide based compositions, likely due to its prevalence in industry. Other commonly used terms include 'sintered carbide', which comes from the manufacturing method used, or even simply as tungsten carbide as this is the dominant phase. Cemented tungsten carbides are sometimes referred to as a cermet or metal matrix composite (or MMC). While there are no official definitions, these terms are typically reserved for other ceramics and compositions [35, 36]. The confusion has perhaps led to the isolation of some work within the field as it is sometimes not clear initially if studies are investigating the same material.

The primary focus of this project is cemented tungsten carbide with a cobalt binder phase (WC-Co) without any additional alloying elements. While a brief summary of WC-Co this presented here, due to its long and well-established history, comprehensive information about the material properties, manufacture and its applications can be found in many textbooks [27, 37-39]. Nickel binders (WC-Ni) are the next most widely used. While these compositions theoretically provide more corrosive resistance, this is to the detriment of mechanical properties resulting in a material with poorer abrasion resistance. Such compositions are therefore only used when the environment is such that corrosion becomes a limiting factor and components are unable to meet their abrasion lifetime, in which case using a more corrosion resistant composition becomes more important.

Research continues in the development of manufacturing techniques including the development of ultrafine grained, binderless materials and alloying additions, much of which is not covered here due to its specialist nature and such materials have yet to be adopted by industry. Tungsten carbide is also associated with thermal sprayed coatings. While there are many similarities, their fundamental microstructure and phase composition makes them sufficiently different to not be considered in this work.

3.1.2 Manufacture

WC-Co is manufactured using powder metallurgy techniques, the most common method being liquid phase sintering. A powder mixture of tungsten carbide and cobalt binder are blended together in a vacuum furnace at temperatures around 1350-1500°C [40]. Packed particles will bond together when temperatures brought to around half their melting point in a process called sintering. In liquid phase sintering with mixed powders at least one of the phases is increased beyond its melting point, Co in WC-Co mixtures. Liquid phase cobalt then causes dissolution of some of the carbide particles. As the mixture cools the low solubility of the tungsten carbide causes it to precipitate out, creating a heterogeneous material with clear separation of phases, see Figure 3-2. Anisotropic growth of the tungsten carbide grains results in faceted single crystals with a hexagonal cross-section. Through close control of manufacturing variables, including particle size,

temperature, pressure and time, it is possible to obtain a structure with low porosity and homogenous distribution of carbides and binder phase.

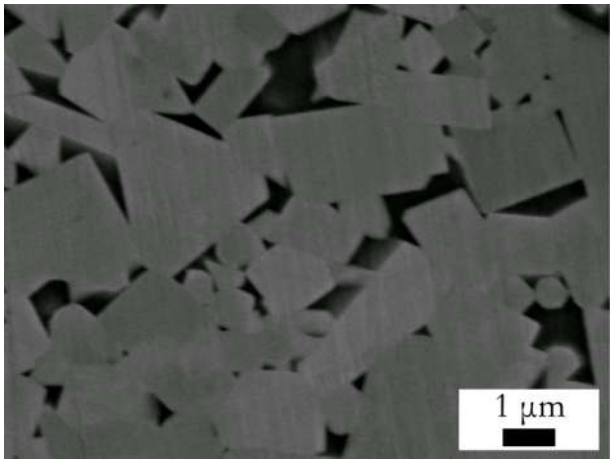

Figure 3-2: SEM image showing typical microstructure of WC-6Co sample. Lighter grain like features are ceramic tungsten carbide (WC), and darker regions are the cobalt (Co) binder phase.

3.1.3 Tungsten Carbide

Tungsten belongs to the VIa group of transition metals and can form two carbides, W_2C and WC, with the latter being used in cemented carbides. WC crystals have a hexagonal structure with lattice parameters typically a = 0.291 nm and c = 0.284 nm [41], although in WC-Co an irregular hexagon is formed producing three types of facets, one basal $\{0001\}$ and two prismatic $\{10\bar{1}0\}$, see Figure 3-3. Truncation of the crystal results in three long and three short facets. This crystal feature, along with elongation of the grain, has been attributed to the relative Co, W and C content in the binder [42-44].

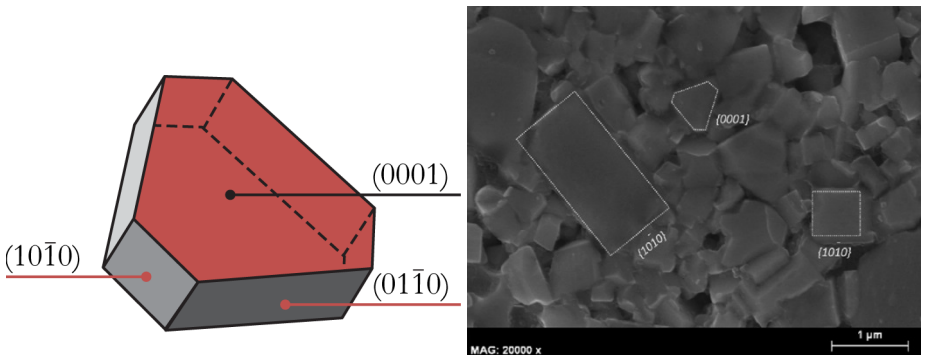

Figure 3-3: a) WC crystal with facets labelled and b) SEM image of etched WC-Co sample with crystal orientation indicated [45].

The irregular crystal structure leads WC grain to be highly anisotropic. This effect has been investigated through the use of indentation techniques by various authors to measure the hardness of the different planes [45-48]. From these experiments, two hardness measurements were obtained for the three facets. Basal facets exhibited approximately ×1.5 higher hardness compared with prismatic facets. Using nanoindentation Duszová et al. [47] and Csanádi et al. [48] obtained similar values for basal and prismatic facets of 40 GPa and 30 GPa respectively.

3.1.4 Cobalt Binder Phase

Cobalt's desirable wettability and mechanical properties make it an excellent complementary material to WC [41]. The properties of the cobalt powder however are significantly altered during the manufacture of WC-Co. During the sintering process, some of the diffused tungsten and carbon will remain in the binder phase effectively creating a Co-W-C alloy and the relative percentage of which can be controlled by adjusting the sintering conditions. Sutthiruangwong et al. [49] achieved tungsten contents of between 18 wt.% and 39 wt.%. Mapping by Hellsing [50] found that tungsten diffusion in the binder was fairly even except for a small tungsten depleted zone on the order of 50 nm near the carbide grain interface. A similar result was also obtained by Hochstrasser et al. [51].

Cobalt has two allotropes: hexagonal close packed (HCP) usually found at temperatures below 400°C and face centre cubic (FCC) which is stable at higher temperatures [52]. Studies have shown however that a large percentage of the cobalt binder retains its high-temperature FCC form in the cemented carbide after cooling although the fraction of FCC to HCP in WC-Co is still unclear [53-55]. Roebuck et al. [56] found that tungsten and carbon additions to cobalt increased the stability of the FCC phase. Although, electron backscatter diffraction techniques used by Mingard et al. [54] on WC-Co found samples to have mixed quantities of cobalt phases with no clear correlation with W content. The hardness of cobalt binder was also changed through the sintering process. Nanoindentation on WC-Co by Engqvist [57] found significantly higher hardness than for pure cobalt alone, 8 GPa in comparison to 2 GPa. This was attributed to the W and C additions, as well as residual stresses which result from the sintering process.

3.1.5 Composite Material

The exact geometry of cemented carbides has been a subject of debate. A skeleton structure was first proposed by Dawihl [58] to explain the bulk material's high hardness and low ductility. This model was later corroborated by Henjered et al. [59] who found only small amounts of cobalt, approximately one atomic layer thick, at the interface between carbide interfaces. The extremely high yield strength of these thin layers makes the bulk analogous to a skeleton structure and explains its high strength.

The properties of the composite can be predicted based on the proportions and material properties from the constituent parts. The rule of mixtures is an established approach that has been used to predict global properties of materials for a variety of heterogeneous materials. The rule provides a theoretical upper and lower bound using a weighted mean of the properties of constituent parts [60]. These upper and lower bounds were further refined by Hashin and Shtrikman [61]. When compared with experimental data from a number of studies these models hold up well, although the refined solution appears to be over constrained and does not capture all results, see Figure 3-4 [62, 63].

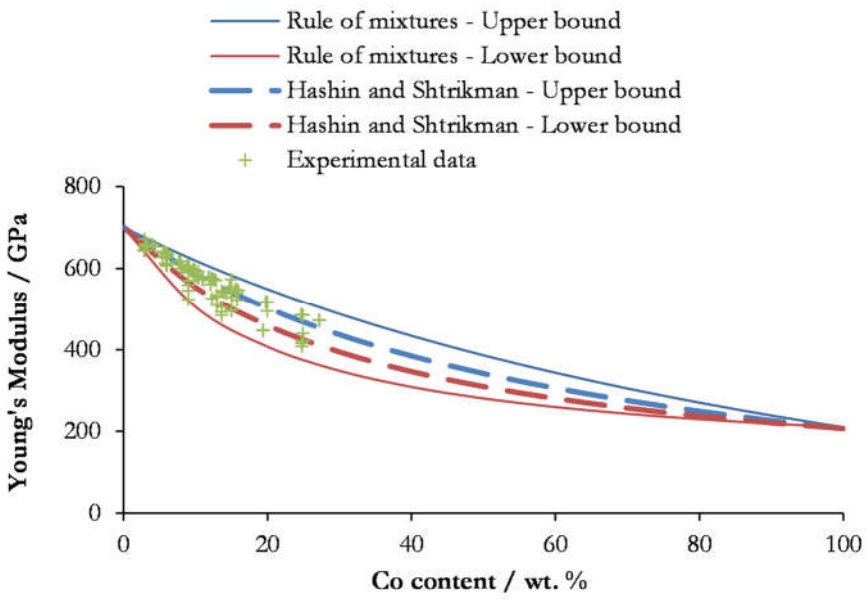

Figure 3-4: Theoretical upper and lower bounds for Young's Modulus of WC-Co composite [60-63].

During the cooling stage of the sintering process, residual stresses are created which arise from the difference in thermal expansion coefficients between the binder and ceramic phases. These stresses have been found to be a function of temperature,

binder content and carbide size. For a typical WC-10Co composition residual stresses tend to be around 2 GPa for Co (tensile) and 400 MPa for WC (compressive) [64]. Application and unloading of tensile and compressive loads on cemented tungsten carbides were found to give a hysteresis response, attributed to relaxation of the thermal residual stresses. Under cyclic loading conditions relaxation stabilises quickly after around three cycles.

3.2 Microstructural Parameters of Cemented Tungsten Carbide

3.2.1 Influence on Properties and Measurement

The mechanical properties of WC-Co which are of most commonly cited are the hardness, fracture toughness and transverse rupture strength (TRS). These properties are heavily influenced by the quantity of the constituent parts and their properties. Using this hypothesis Chermant et al. [65] proposed a relationship between the hardness of the composite based on the rule of mixtures approach:

$$\frac{1}{H_{\text{comp}}} = \frac{V_{WC}^{f}}{H_{\text{WC}}} + \frac{V_{B}^{f}}{H_{\text{B}}} \tag{3.1}$$

Where H_{comp}, is the hardness of the composite material, V_{WC}^{f} and H_{WC} is the volume fraction and hardness of WC, V_{B}^{f} and H_{B} is the volume fraction and hardness of the binder phase. Although the constituents of the material are commonly quoted in terms of weight percentage as this is the most practical given the powder manufacturing method used, it is more suitable to use the volume fraction when calculating the bulk properties. This can be converted from knowing the density of the phases, WC density is around 15.6 g cm^{-3} and the cobalt binder phase typically varies between 8.8 g cm^{-3} to 9.5 g cm^{-3}, depending on the amount of diffused C and W.

However, as with other heterogeneous materials, in addition to the properties of the individual phases and composition, the microstructure of the material also plays an important role in determining the bulk material properties. Numerous studies have looked at the relationship between microstructure and the macroscale behaviour of the material. A comparison of WC-Co properties from three studies against the relationship proposed by Chermant (assuming 2100 HV for WC and 340 HV for

Co) is shown in Figure 3-5. The size of the circles indicates the binder mean free path value which is a microstructural measure (discussed later in Section 3.2.4). While the relationship clearly displays a reasonable fitting to Equation (3.1) it is clear that the microstructural measurement also has an effect on the hardness. Smaller values of binder mean free path tend to increase the material's hardness, as indicated by the smaller diameter circles above the Chermant model, while larger values lower the hardness. It should be noted that while all these parameters have an effect on the overall properties of the material, they are all interrelated, making interpretation of the effect of a single parameter difficult to conclude.

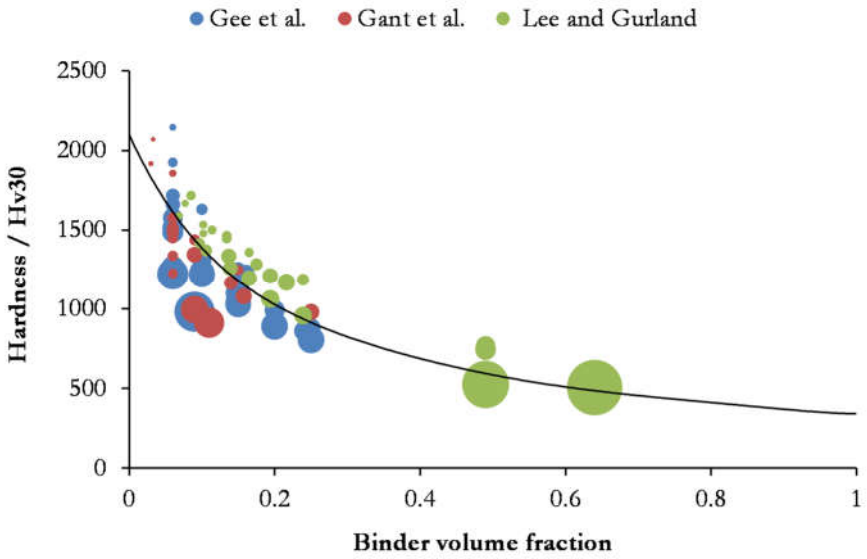

Figure 3-5: Comparison of bulk material properties from various studies to Chermant et al. hardness model. The diameter of the circle indicates binder mean linear intercept value [63, 66-68].

Microstructural properties are often measured using the linear intercept method which can be carried out using standard image analysis techniques. This is performed by drawing a test line of random orientation on an image and averaging number of point intercepts per unit length. For accurate measurements 1000 points are required for measurement. This method can also be used for calculating volume fractions. For example, the cobalt binder phase fraction can be calculated using:

$$V_{\mathrm{Co}}^{\mathrm{f}} = \frac{N_{\mathrm{Co}}}{N_{\mathrm{Co}} + N_{\mathrm{WC}}} \tag{3.2}$$

Where N_{Co} and N_{WC} are a number of random point counts for Co and WC phases respectively along the test line.

3.2.2 Tungsten Carbide Grain Size

Although the hardness of individual tungsten carbide grains is anisotropic their random orientation results in the bulk material being isotropic [45]. The hardness of a material can generally be described by the Hall-Petch relationship, which indicates that the hardness of bulk material, H, increases as WC grain size decreases:

$$H = a_1 + \frac{a_2}{\sqrt{d_{WC}}} \tag{3.3}$$

Where a_1 and a_2 are constants and d_{WC} is the mean grain size. This has led to the development of ever finer grained materials with the goal of achieving higher hardness with additions such as vanadium or chromium carbide being used as WC grain growth inhibitors [69]. Grain size for WC-Co tends to be on the micron scale, typically ranging between 0.5 μm and 10 μm. Roebuck [70] noted however that while the general Hall-Petch relationship holds true, other empirically based mathematic expressions which are non-linear appear to have improved fit for coarse and fine grains suggesting that the Hall-Petch approach is not accurate across all length scales. Furthermore, tests performed on a range of grain sizes by Okamoto et al. [71] found that the size of grain will also influence the failure mechanism. They observed that materials with large grains (20 − 30 μm) fail in a ductile manner whereas those grains in the standard size range exhibit brittle fracture. Using the linear intercept method the mean grain size can be calculated by [67]:

$$d_{WC} = \frac{2V_{WC}^{f}}{2N_{CC} + N_{BC}} \tag{3.4}$$

Where N_{CC} and N_{BC} are the average number of carbide/carbide and binder/carbide intercepts per unit line length.

3.2.3 Contiguity

Contiguity of the carbide is the ratio between the area of WC/WC interface to the total surface area of the grains, therefore ranging in value between zero and one. Zero indicates a fully dispersed carbide in a matrix and as the value tends towards

one the carbide is in a completely agglomerated structure. Contiguity is strongly related to composition and so follows similar trends in how it relates to bulk properties. Furthermore, contiguity is a measure of how connected WC particles are in the bulk material. Under loading, more connected carbide structures are superior in distributing the load and therefore bulk hardness increases as contiguity → 1. Lee and Gurland [67] related the contiguity to the hardness of the bulk material:

$$H_{\text{WC-Co}} = H_{\text{WC}} V_{\text{WC}}^{\text{f}} C + H_B \left(1 - V_{\text{WC}}^{\text{f}} C\right) \tag{3.5}$$

Where $H_{WC\text{-}Co}$ is the hardness of the composite material and C is the contiguity. Using the linear intercept method, the contiguity can be calculated by [67]:

$$C = \frac{2N_{\text{CC}}}{2N_{\text{CC}} + N_{\text{BC}}} \tag{3.6}$$

3.2.4 Binder Mean Free Path

The hardness of the binder phase has also been correlated with the binder mean free path, λ, which is a measure of the average distance of binder between carbide grains, which can also be thought of as the thickness of the cobalt layer. The definition of binder mean free path however is not well-defined, which can cause difficulty when comparing various results [31]. One of the more popular definitions is [67]:

$$\lambda = d_{\text{WC}} \frac{V_{\text{Co}}^{\text{f}}}{\left(1 - V_{\text{Co}}^{\text{f}}\right)\left(1 - C\right)} \tag{3.7}$$

As would be expected on a measure that is related to cobalt content, hardness increases as λ decreases [72].

3.3 Fracture Mechanics

3.3.1 Linear Elastic Fracture Mechanics

Fracture is an important behaviour to understand in the degradation process of brittle materials. Not only does it play a part in how small wear fragments are formed, but evidence of significant fracture into the bulk material has also been observed directly by Beste et al. [73] in worn drill bits, see Figure 3-6.

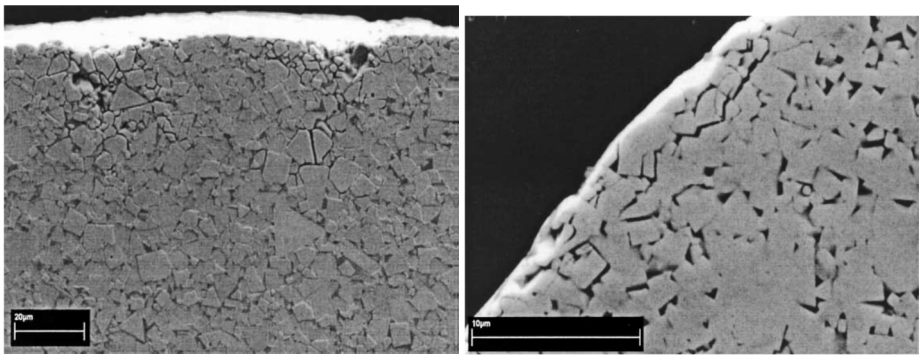

a) **b)**

Figure 3-6: Evidence of fracture observed on worn drill bits a) fractures initiating at surface and propagating down and b) lateral cracks propagating parallel to the surface [73].

While theory dictates that failure will occur when a given external force exerts a stress higher than the material's yield stress, in reality materials often fail at global stresses below their yield point, i.e. failure occurs at $\sigma_{\infty} < \sigma_{y}$. This is due to uneven stress distribution due to geometry or flaws in the material that give rise to localised stress above the material's yield stress, see Figure 3-7.

In response to notable structural failures in the 1940s and 1950s as a result of new manufacturing methods and fatigue, significant research into fracture mechanics was conducted [74]. This began in the field of linear elastic fracture mechanics (LEFM) which sought to resolve the solution for stresses in linear elastic materials. It is based on Hooke's law and is an important foundation upon which other more advanced fracture mechanics theory is based. The most important concept of this field is stress concentration due to geometrical features. The seminal work by Kirsch [75] introduced an analytical solution for stresses around a hole in an infinite plate, see Figure 3-7.

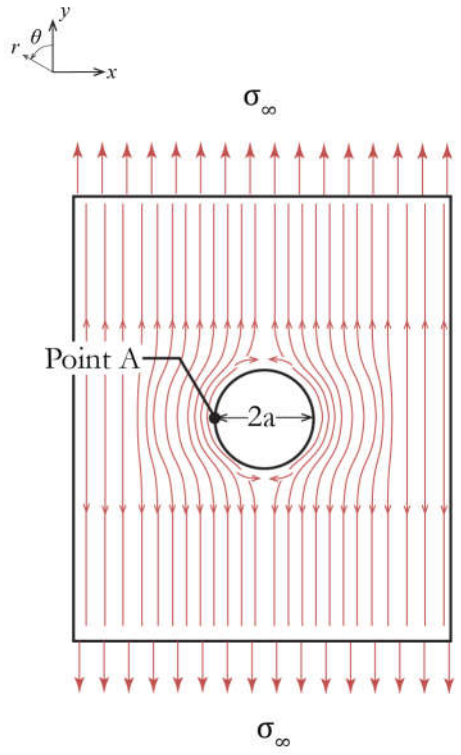

Figure 3-7: Stress distribution around hole in infinitely wide plate.

In the case of uniaxial tension, Kirsch's solution for stress in polar coordinates are described by:

$$\sigma_{\theta\theta} = \frac{\sigma_\infty}{2}\left(1+\left(\frac{a}{r}\right)^2\right) - \frac{\sigma_\infty}{2}\left(1+3\left(\frac{a}{r}\right)^4\right)\cos 2\theta \tag{3.8}$$

$$\sigma_{rr} = \frac{\sigma_\infty}{2}\left(1+\left(\frac{a}{r}\right)^2\right) + \frac{\sigma_\infty}{2}\left(1-4\left(\frac{a}{r}\right)^2+3\left(\frac{a}{r}\right)^4\right)\cos 2\theta \tag{3.9}$$

From this the maximum stress in the plate, which is located a Point A in Figure 3-7, is calculated to be three times the applied remote stress. In an ideal material, fracture initiation will therefore initiate at this location when remote stress is a third that of the tensile strength of the material.

3.3.2 Crack Tip LEFM

Irwin [74] made several significant contributions to the field of fracture mechanics. One of the most important was the development of the stress intensity factor (SIF). This factor is able to mathematically calculate the stress distribution around a crack tip in a linear elastic material. The stress along the crack plane was expressed as:

$$\sigma_{yy} = \frac{K}{\sqrt{2\pi r}} \cos\left(\frac{\theta}{2}\right)\left[1 + \sin\left(\frac{\theta}{2}\right)\sin\left(\frac{3\theta}{2}\right)\right] \tag{3.10}$$

The stress is defined in terms of polar coordinates r and θ with origin at the crack tip. Similar expressions for σ_{xx} and τ_{xy} were also developed. K is the SIF defined:

$$K = Y\sigma_{\infty}\sqrt{\pi a} \tag{3.11}$$

Where Y is a constant which depends on geometry and loading. For a through thickness crack in an infinitely wide plate (as illustrate in Figure 3-7) $Y = 1$, and for an edge crack $Y = 1.12$, which accounts for the edge boundary condition at which $\sigma_{xx} = 0$. This model has been widely adopted in the field of facture mechanics due to its simplicity in implementation.

This solution however creates a mathematical singularity where at the crack tip stresses will tend to infinity, as $r \to 0$, $\sigma_{yy} \to \infty$. To address this Irwin introduced a new criterion, so fracture is said to occur when K is equal to or larger than the critical stress intensity factor, K_{IC}. When substituted for K, Equation (3.10) can be rewritten in terms of yield stress, σ_y. K_{IC} is a measure of a material's fracture toughness which is a measure of the resistance of a material to crack propagation. The underlying formulation takes account of the test geometry making fracture toughness a material property that is geometry independent. The critical stress intensity factor indicates the mode of loading through the use of subscript I, II or III as illustrated in Figure 3-8.

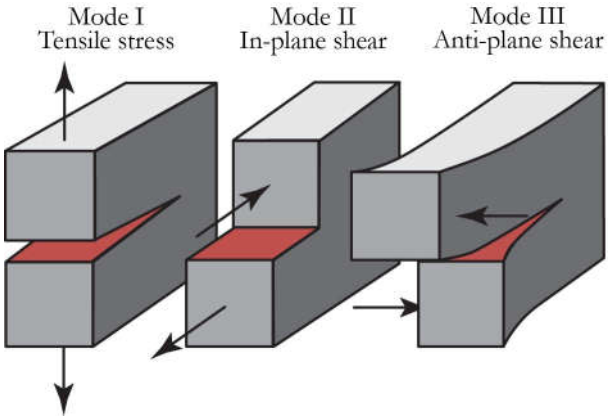

Figure 3-8: Loading and fracture modes.

LEFM however is only valid if the size of the plastic zone ahead of the crack is significantly smaller than the length of the crack or specimen in which stresses are redistributed. Irwin estimated the plastic zone size, r_p, to be:

$$r_p = \frac{1}{\pi}\frac{K_{IC}^{\ 2}}{\sigma_y^{\ 2}} \tag{3.12}$$

This indicated that the plastic zone of a material is depended on its fracture toughness and yield stress. In this region the material is unable to carry high stresses due to deformation and will exhibit non-linear behaviour. In the event of high r_p compared to the length scale of interest, LEFM no longer becomes valid.

The fracture process zone (FPZ) is the area immediately surrounding the crack tip, typically much smaller than the plastic zone. This is a small area over which micromechanical non-linear mechanisms occur and allow the fracture to propagate. The size of this region depends on the properties of the material, those with larger fracture toughness will have larger process zones that are able to distributed stresses in the form of microcracking or void formation. As the size of this zone decreases fracture behaviour of the material approaches that of LEFM.

3.3.3 Fracture Toughness Measurement Using the Three-Point Bend Test

Using a three-point bend test set up Chermant and Osterstock [68] obtained the critical stress intensity factor from specimens with V- or U-shaped notches across a range of WC-Co grades, using a geometry similar to that shown in Figure 3-9.

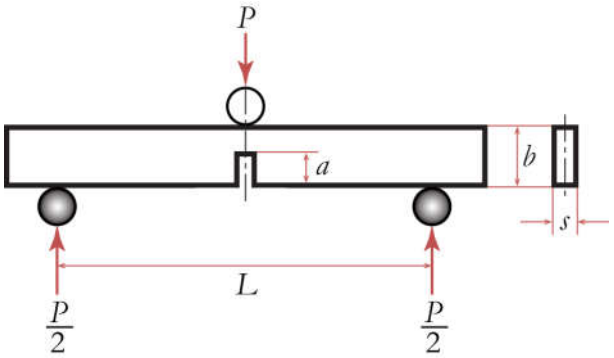

Figure 3-9: Three-point bend test set-up with notched specimen.

K_{IC} could then be calculated using the following expression which is derived from Equation (3.11):

$$K_{IC} = Y \frac{3P_{max}L}{2sb^2}\sqrt{a} \tag{3.13}$$

Where P_{max} is the maximum applied load, and geometry described by a, b, L and s as indicated in Figure 3-9. Geometric parameter for the geometry shown is defined as:

$$Y = 1.93 - 3.07\left(\frac{a}{b}\right) + 14.53\left(\frac{a}{b}\right)^2 - 25.11\left(\frac{a}{b}\right)^3 + 25.8\left(\frac{a}{b}\right)^4 \tag{3.14}$$

Using Irwin's approximation the plastic zone size was found to be a function of binder fraction. However all values were relatively low, typically on the order of 7 WC gain lengths, therefore satisfying the conditions for valid calculation of K_{IC}. Charmant and Osterstock concluded that LEFM analysis is a valid approach to the study of WC-Co. For specimens with between 3 wt.% and 25 wt.% binder content and grain sizes between 0.7 μm and 2.2 μm, K_{IC} values were in the range of 8.8 MPa $m^{0.5}$ to 20.7 MPa $m^{0.5}$. The brittle behaviour of the material produces a linear load-displacement followed by sudden failure, see Figure 3-10. The curves also exhibit strain-softening post failure as shown by the load reducing as displacement increases. Strain-softening behaviour is common to many quasi-brittle heterogeneous materials including ceramics, concrete and rocks. This effect is due to coalescence of microcracks which form areas of damage localisation. Finally, a linear relationship between K_{IC} and λ^2 / d_{WC} was established, suggesting that crack propagation in WC-Co is determined by plastic deformation of the binder phase.

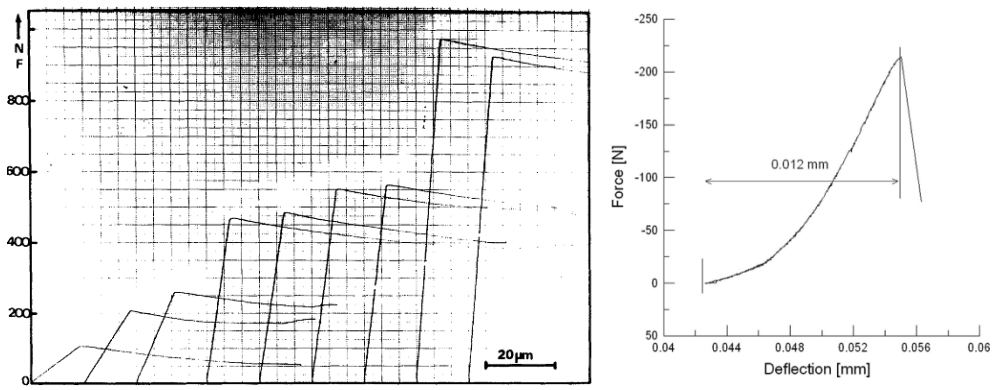

Figure 3-10: Examples of experimental load displacement-curves for WC-Co samples using three point bend test a) WC-10Co and b) WC-17Co [68, 76].

Pickens and Gurland [77] obtained similar K_{IC} values using single edge notched beam specimens (SENB) under three-point loading, see Figure 3-9. A small crack of 635 μm and root radius of 18 μm was introduced into the specimen by electron discharge machining, followed by a high voltage discharge to induce a microcrack at the root on the order of 75 μm length, to represent a natural crack. Results are presented in Figure 3-11.

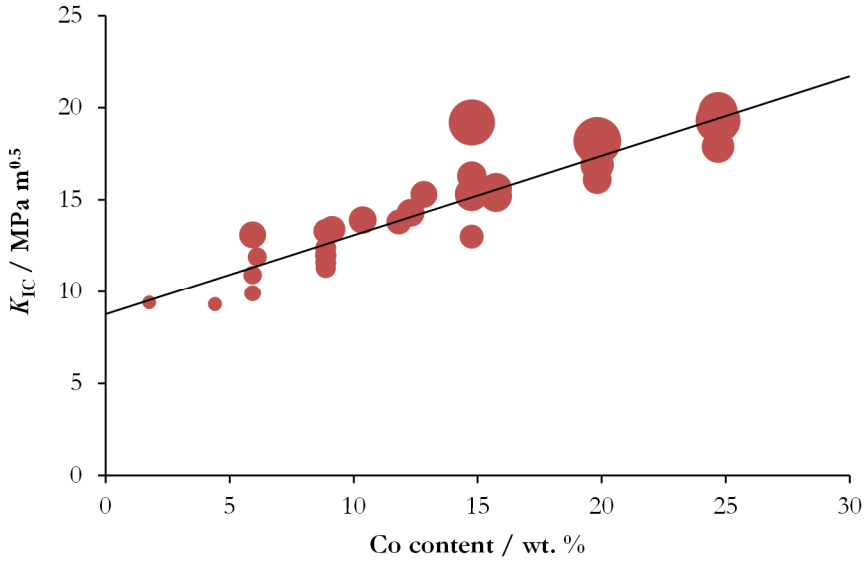

Figure 3-11: K_{IC} relation to binder content and binder mean free path (as indicated by circle diameter) [77].

A linear relationship between fracture toughness and binder content was found. As with hardness properties discussed in Section 3.2.1, the binder mean free path also appeared to have some influence on fracture toughness. For a given binder content larger circles above the average line and smaller below in Figure 3-11 indicate that larger binder mean free path results in higher K_{IC}. Given that the binder phase is introduced to provide improved fracture toughness to the material, it would therefore be logical to see this sort of effect from a binder related microstructural parameter.

3.3.4 Fracture Toughness Measurement using the Palmqvist Method

Palmqvist [78] introduced a method of fracture toughness measurement for ceramic materials using indentation techniques. This has a number of advantages over more conventional fracture toughness tests as they only require small specimens and do not need special geometries or addition of machined notches, which is one of the

primary challenges in measuring properties of brittle materials. The most common indentation method is the Vickers indentation technique, which measures the radial cracks that form at the edges of the pyramidal indent, see Figure 3-12.

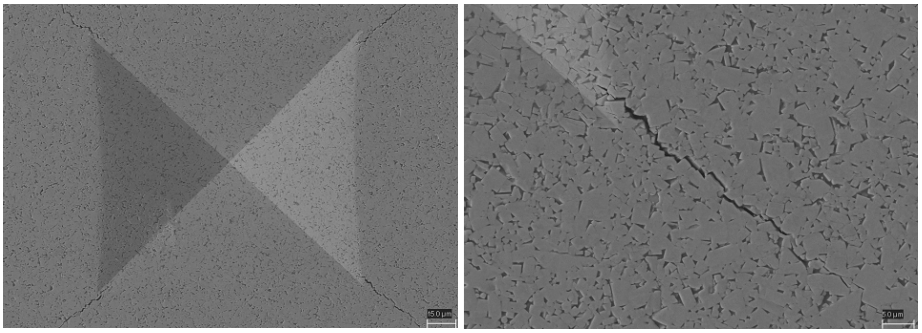

a) **b)**

Figure 3-12: a) Vickers indentation from 30 kgf load on WC-3Co sample and b) crack at edge of indent used to calculate fracture toughness [79].

Exner [80] applied the Palmqvest method to WC-Co and established a relationship between crack length and indenter applied load, P. This was later modified by Ogilvy et al. [81] and Perrott [82] to include the threshold indentation load, P_0:

$$W = \frac{\left(P - P_0\right)}{4\bar{a}} \tag{3.15}$$

Where W is the Palmqvist crack resistance (a measure of fracture toughness) and $\bar{a}$ is the mean radial crack length. Shetty et al. [83] compared two indentation crack models, the Palmqvist crack and the half-penny crack, to see which best described that in WC-Co. Palmqvist cracks are characterised by radial cracks that propagate at a shallow angle to the surface and are used to calculate $\bar{a}$ see Figure 3-13a. In the half-penny model an additional median crack is formed at the tip of the indenter and propagates along the loading axis, see Figure 3-13b.

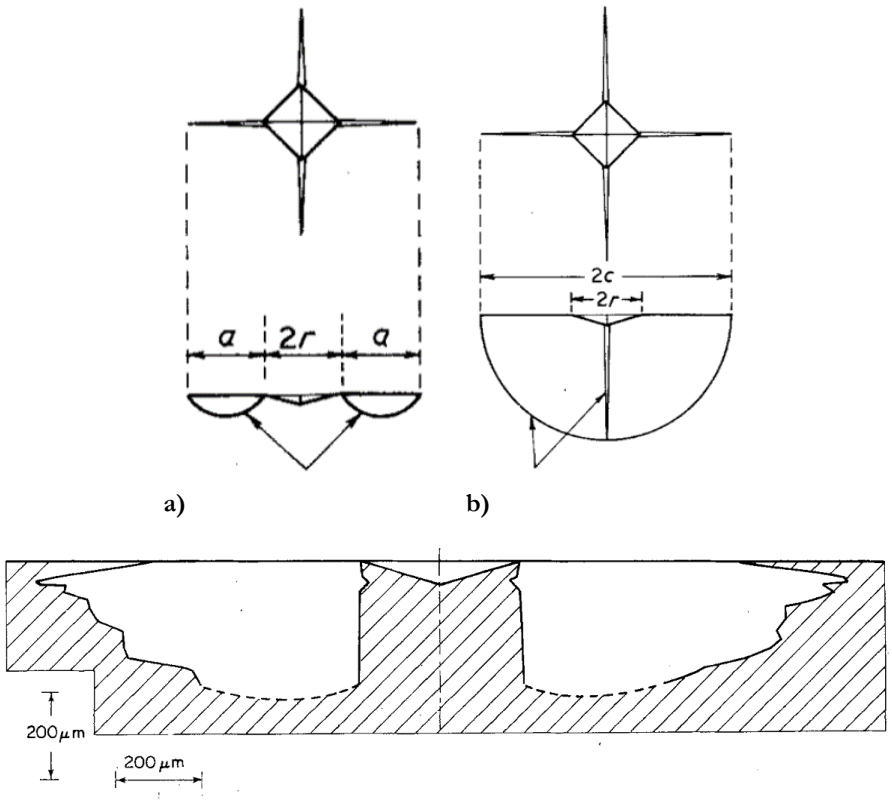

Figure 3-13: Crack geometries a) idealised Palmqvist b) idealised half-penny and c) crack shape for WC-5Co at indentation of 1200 N [83].

Sectioning of indentation in WC-Co samples found only radial cracks suggesting that the Palmqvist crack model is more appropriate for analysis, Figure 3-13c. This was supported by a more accurate fitting of the load to crack length relationship that had a linear dependency rather than a ⅔ power dependency as would be expected for a half-penny model [83, 84]. From this Shetty came up with a method that allowed fracture toughness to be approximated using the metric hardness, *H*, obtained from measuring the length of the indentation diagonals and crack resistance values obtained from Equation (3.15):

$$K_{IC} = \Lambda\left(HW\right)^{0.5} \tag{3.16}$$

Where Λ is a function of tip geometry, apex angle ψ, and Poisson's ratio of the material:

$$\Lambda = \frac{1}{3\left(1-\nu^2\right)\left(2^{0.5}\pi\tan\psi\right)^{0.33}} \tag{3.17}$$

This relationship however is only valid up to values of around 15 MPa $m^{0.5}$, above which the fracture toughness is overestimated owing to assumptions in the crack model which do not take account of plastic and elastic deformation.

While this method appears to be useful, it has been seen that results are very sensitive to surface preparation, leading to a considerable scatter of results in the literature. An extensive surface preparation regime was used by Exner [80] and Shetty [83] in order to minimise residual stresses in the surface to negligible. This could be measured by measuring the length of the indenter cracks after each step of the process. The crack lengths increased with each layer removed until values were stable.

3.3.5 Characterisation of WC-Co Fractures

Further information about the nature of fracture in WC-Co was derived from the SEM images obtained from the three point bend test. From their analysis Sigl and Exner [85] concluded that fracture progresses in discrete steps:

i. Initially, there is the formation of fracture in the WC phase ahead of the crack tip;

ii. This is followed by deformation of the Co binder which forms voids and ligaments;

iii. Finally, these voids coalesce to form the final fracture path.

Furthermore, although the binder deforms plastically, WC-Co behaviour is dictated by the dominant WC phase and acts as a brittle material. This correlated with previous findings from Chermant and Osterstock [68]. Pickens and Gurland [77] found differences between fine and coarse grained specimens. Fracture of fine grained alloys initiated through interfacial decohesion occurring along carbide/ carbide and carbide/cobalt interfaces. In coarse grained specimens fracture is primarily through transgranular fracture of carbide grains. This was followed by the plastic deformation and rupture of ligaments as described previously.

Sigl and Exner extended their analysis of the fracture paths obtained using geometrical analysis of the fractures. They used three parameters to categorise fractures: length distributions $N(l_d)$, angular distribution $N(\alpha_d)$ and linear roughness R_L as defined by:

$$R_L = \sum \frac{l_d}{L_{pr}} \tag{3.18}$$

Where L_{pr} is the profile length of the fracture. Fracture parameters and an example of a length distribution results are shown in Figure 3-14.

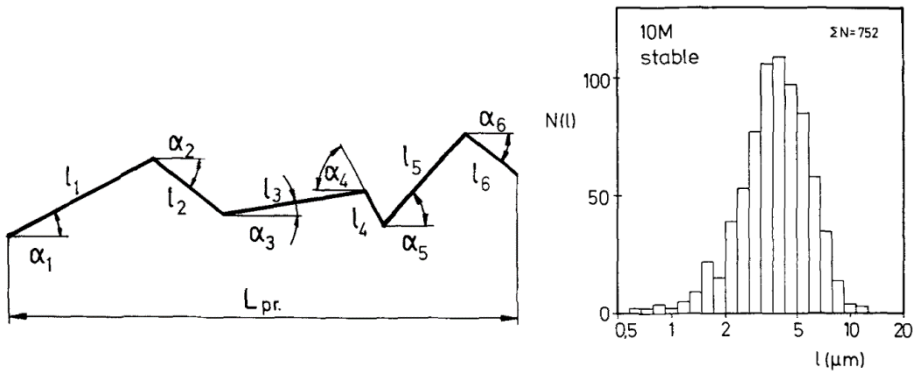

a) **b)**

Figure 3-14: a) Schematic of fracture profile with parameters indicated and b) Typical distribution for $N(l_d)$ fracture parameter for WC-10Co test [85].

It was found that there was no discernible difference in fracture parameters between stable and unstable crack propagation. This was further demonstrated when comparing fracture energies for the two types of fracture. Analysis of the fracture paths found that they were strongly influenced by the microstructure, with fractures deviating along carbide-carbide and carbide-binder interfaces. It suggested that stable cracks propagate in a start-stop manner, moving quickly over short distances before stopping after each advance. Assuming that the speed of these advances is the same as for unstable crack propagation, it would follow that fracture parameters would be equivalent and be solely a function of loading dynamics. Sigl and Exner identified four fracture types, in order of frequency:

i. Intergranular fracture along carbide/carbide interfaces,

ii. Transgranular fracture of carbides,

iii. Fracture near carbide/binder interface and

iv. Transgranular fracture of binder phase.

For the materials tested, binder content was relatively low (grades between WC-6Co and WC-15Co) so carbide phase will dominate and consequently fracture through this phase. However once accounting for this volume difference, fracture was more

prevalent in the cobalt and carbide/binder interface, see Figure 3-15. This indicates that fracture is not based on mechanical properties of the phases alone and that microstructure also influences the fracture behaviour.

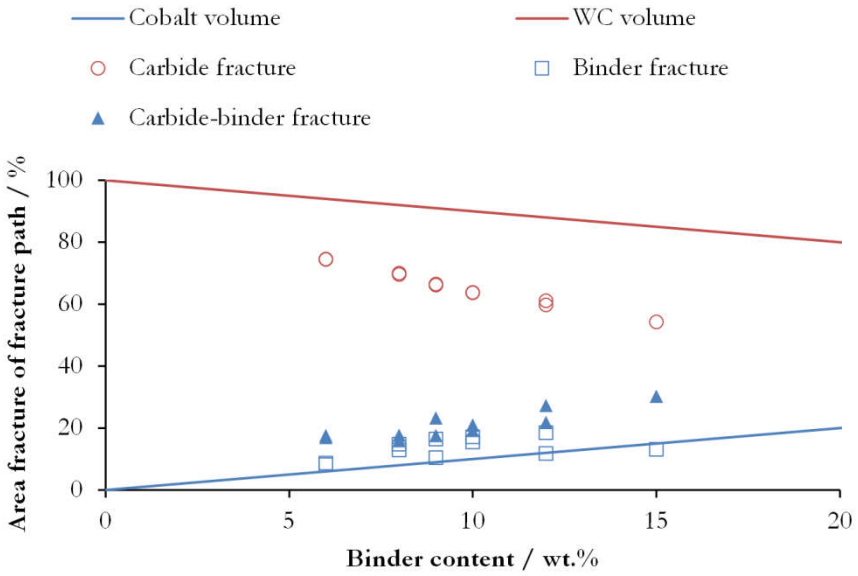

Figure 3-15: Area fractions of crack paths by phase. Adapted from Sigl and Exner [85].

Fracture was found to occur alongside carbide/binder interfaces rather than exactly on it, suggesting a stronger bond between carbide and binder compared to the bonding within the binder itself. This could therefore also be considered a mode of binder fracture, further increasing the percentage of binder fracture area.

Mingard et al. [86] built upon the Sigl and Exner by using observing crack growth in-situ combined with high resolution SEM and electron backscatter diffraction (EBSD). EBSD allowed analysis of fracture paths with respect to crystal orientation. They found that fracture tended to occur along $\{10\bar{1}0\}$ planes, while plastic deformation was greater along $\{11\bar{2}0\}$ planes.

Evidence for a multiligament FPZ was found from significant binder deformation although it was still continuous. These are created through local stresses near the crack tip which cause nucleation sites to grow and become microvoids. No microcracks or crack branching was seen in the carbide phase, suggesting that formation of ligaments is an important mechanism that provides fracture toughness to the material by shielding stresses at the crack tip. This mechanism was also

observed by Tarrago et al. [87] when studying fatigue in WC-Co, see Figure 3-16. Deformation outside of the fracture path, however, was limited suggesting a relatively small plastic zone, with an upper size limit equal to the binder mean free path. This mechanism would explain previously described findings from Charmant and Osterstock [68] and Pickens and Gurland [77] on a dependency between fracture toughness and binder mean free path. Additional the multiligament model suggests that FPZ is larger than the plastic zone. The small size of the plastic zone and the dominant WC phase for the materials of interest ensure that LEFM remains a valid approach to the study of WC-Co.

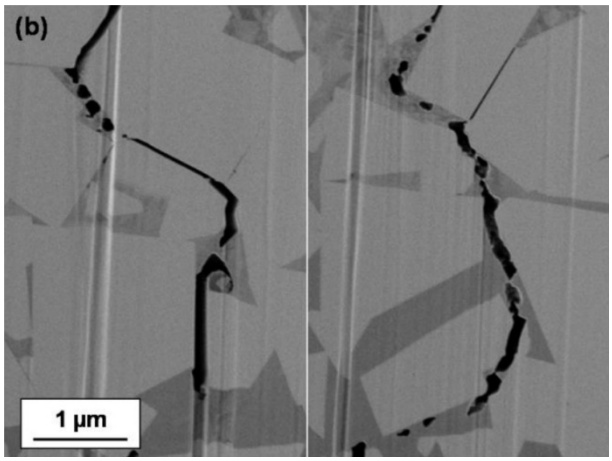

Figure 3-16: FIB-SEM image of fracture showing microvoids in binder phase [87].

A schematic of the primary fracture features and areas of WC-Co is presented in Figure 3-17 which summarise findings from multiple studies.

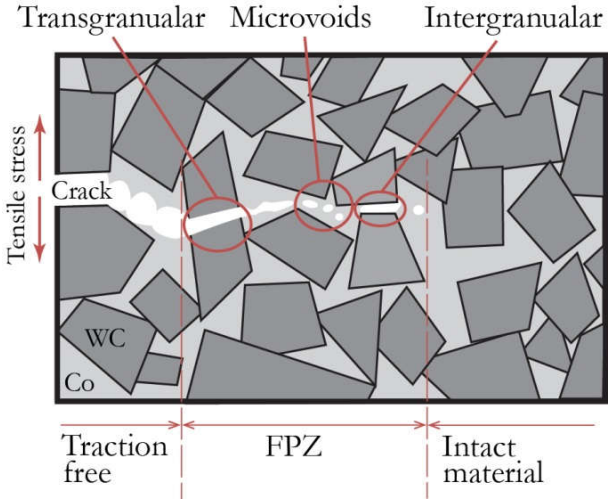

Figure 3-17: Schematic of crack propagation in WC-Co. Adapted from Ettmayer [31].

3.4 Mechanical Wear

3.4.1 Contact Mechanics

Surface roughness or discrete particles in a contact will limit contact between two bodies to only a few points, regardless of the apparent contact area. This means that for the majority of cases load between two surfaces is transferred through the contact of asperities alone. This can significantly increase stress at a given location on the surface of the material due to the effective reduction in area.

At the yield stress the material response will transfer to a plastic response. Plastic deformation occurs through the breaking of atomic bonds through movement of dislocations. Slip occurs along the most densely packed crystallographic planes, meaning that lattice structures with closely packed planes such as FCC allow more plastic deformation. The resulting slip planes group together to form slip bands, evidence of which has been observed on WC grains after applying loading to the material, see Figure 3-18. The ability of the carbide grains to undergo high plastic deformation before the onset of brittle fracture has been cited as one of the fundamental properties giving the material high abrasion resistance [53, 88]. However, as displacement is minimal it is difficult to split stress-strain behaviour between elastic and plastic behaviour. This explains why such behaviour has only become of recent interest as imaging techniques such as focused ion beam (FIB) and SEM have improved. As such, WC has been assumed to act in a purely brittle manner.

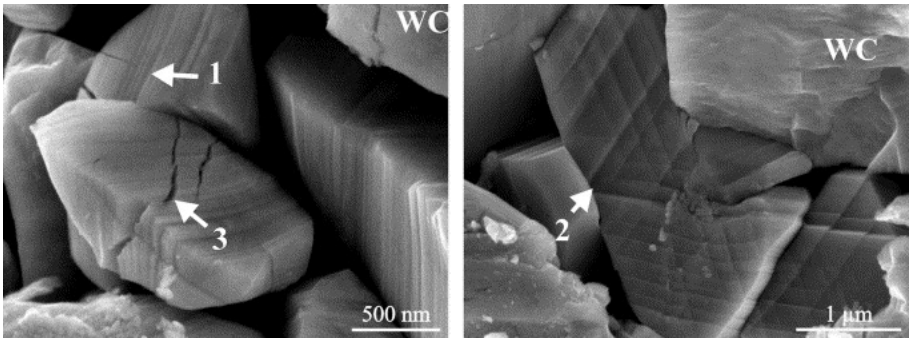

Figure 3-18: SEM micrographs following grinding of WC-10Co sample: 1 and 2 evidence of slip planes on WC grains, 3 cracking of WC grain [89].

As with bulk cobalt, the binder has been shown to undergo phase transformation under strain from FCC back to its stable HCP structure [90]. This is thought to

reduced ductility of the binder and inhibits the materials ability to restrict crack propagation [91].

3.4.2 Archard Wear Model

A commonly and well established model used in tribology to describe sliding or abrasive wear is the Archard equation [92, 93]. Archard derived the wear volume, w_v, as a function of sliding distance, d_s, hardness of the softer material, H, and dimensionless wear coefficient, K_W:

$$w_v = \frac{K_W P d_s}{H} \tag{3.19}$$

The Archard equation predicts wear volume to be directly proportional to applied load and sliding distance while inversely proportional to hardness. Jia and Fischer [94] extended the Archard model to abrasion wear of WC-Co. Following testing of grades containing between 6 wt.% and 15 wt.% Co and WC grain size of 0.07 μm to 1.2 μm, the authors found the Archard equation could also be a reasonable approximation for this type of wear after the following empirical linear relationship for K_W was applied:

$$K_W = 0.027 + 0.017 d_{WC} \tag{3.20}$$

However, this relationship was only found to hold true for sample with hardness above 1400 HV and when abraded against diamond. Sample with lower hardness, WC grain size between 1 μm and 2.5 μm and containing between 10 wt.% and 20 wt.% Co, were also dependant on d_{WC} but had a different linear relationship. This difference was attributed to abrasion events being smaller than the WC grain size in coarser grained samples but larger than WC grain size in finer grained samples. Experiments also found that hardness of the abrasive altered the damage mode of the WC-Co. Harder abrasives cause material removal by fracturing of WC grains, whereas softer abrasives removed the binder phase. This meant that no relationship between d_{WC} and K_W could be established for the ZrO_2 abrasive which has a hardness of 1400 HV. Without being able to account for changes in wear mechanism due to WC grain size or abrasive hardness this restricts the use of Equation **Error! Reference source not found.** to a fairly small range of applicable tribological WC-Co systems.

Using the Archard equation as a basis Axen and Jacobson [95] developed a wear model for multiphase materials. Two wear modes were included, equal wear (EW) and equal pressure (EP), which indicate an upper and lower band of wear resistance for the material, with systems often exhibiting a mixed mode regime. The model showed good correlation with tests conducted on a variety of fairly soft materials, hardness values of the abraded surface varying between 38 and 210 HV. The model, however, suffers from some limitations. Axen noted that for a given number of standard material properties the model is unable to predict which form of wear mode. Furthermore, the validity of the model has not been verified for high fractions of reinforcement phase as would be seen in typical WC-Co materials.

According to the Archard model, only the softer material hardness is considered when calculating wear rate therefore suggests only the softer material wears. As WC is one of the hardest materials, this would suggest that wear of WC should not occur which is not the case. A mode of failure which would explain this discrepancy was proposed by Lee and Gurland [67] who observed slip lines originated at carbide interfaces due to high local stress concentrations, see Figure 3-19. This way the contacting object is not required to apply remote stresses greater than its yield stress. This also provides a physical reason to the importance of contiguity values which gives an indication of the average amount of contact between carbide grains.

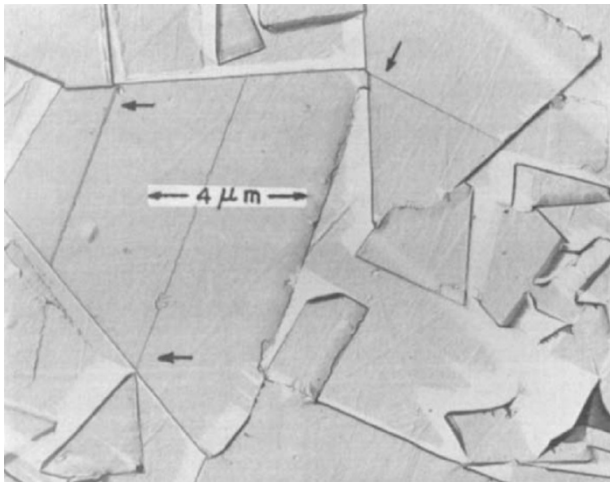

Figure 3-19: Slip lines occurring at contact points, indicated by arrows, with neighbouring carbide grains [67].

Across a range of WC-Co grades, testing by Gant and Gee [96] using an ASTM G65 rig and a water slurry mixture found specific wear rates to be in the order of 10^{-15} to

10^{-12} m^3 N^{-1} m^{-1} for binder contents between 3% and 16%. The study found that changing from silica to a harder alumina abrasive increased the volume loss by an order of magnitude. In addition to the stress concentration effects, this perhaps indicates differing mechanisms that dominate as discussed by Jia and Fischer [94] earlier. This behaviour cannot be directly calculated by the Archard model as neither the hardness of the abrading material or the wear mechanism is considered. Furthermore, microscratch tests by Gee [66] found a nonlinear relationship between wear volume and sliding distance for a constant load. This is likely due to the modification of the surface though increase of contact area and build up of degradation, highlighting another limitation of direct use of this model.

3.4.3 Abrasive Wear

Abrasion is the mode of deterioration of a surface by the act of movement of a harder material across its surface. Abrasive wear can occur by a number of mechanisms, see Figure 3-20a, and will depend on the nature of the material as well as the type of contact. Unlike the majority of engineering metals which experience material loss by plastic flow or cutting, the primary wear mechanisms for WC-Co is reported to be the preferential removal of the binder phase and microfracture [33]. Ahn et al. [97] combined the relevant abrasion modes of brittle materials with fracture behaviour discussed earlier in Section 3.3, to provide a model of the primary degradation mechanisms in brittle materials, see Figure 3-20b.

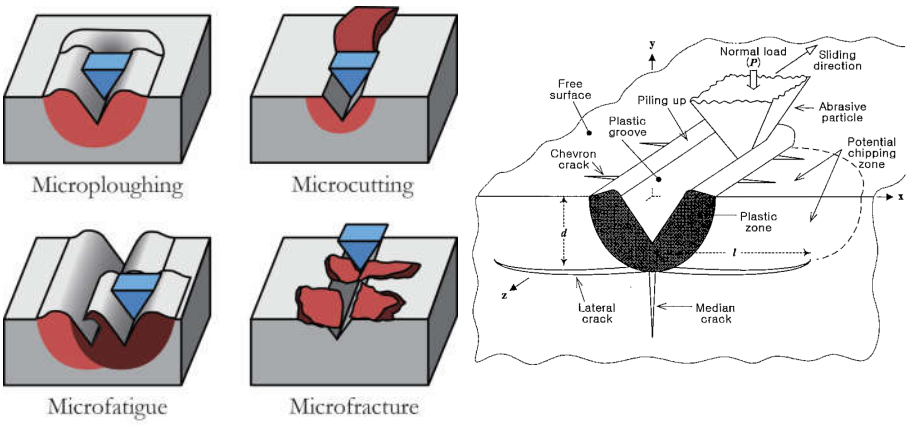

Figure 3-20: a) Comparison of abrasive wear mechanisms. Adapted from [98] and b) schematic of abrasive wear mechanisms in brittle materials [97].

Analysis of worn drill bits by Beste et al. [73] found that samples with high cobalt content were characterised by a very rough surface. Grooving of the binder had occurred with fracture of WC grains adjacent to these areas. On the other hand low cobalt samples were characterised by fracturing of WC grains. The appearance of a smoother surface suggested that WC and Co phases wear at the same rate, and would therefore likely be dictated by the more dominant WC phase. Analysis of worn drilling bits by Beste and Jacobson [99] observed plastic deformation, fracture, loosening and removal of WC grains presenting a highly roughened surface but with no sign of directionality. Due to the uniformity of the wear Beste concluded that wear was primarily by removal of individual grains or smaller.

Gant and Gee [100] compared the dry abrasive wear performance of a range of WC-Co grades against tool steels that are widely used. On average wear performance of WC-Co grades which contained 6–10% Co had almost four times better wear performance than the tool steels tested, see Figure 3-21a. They also found that grades which contained 20–25% Co had roughly the same wear performance. The differing wear performances of the WC-Co grades were attributed to a change in wear mechanism. Examination of SEM images, see Figure 3-21b and Figure 3-21c, reveal distinct differences in surface morphology as described by Beste.

Larsen-Basse et al. [101] noted that despite fracture being the primary mode of wear, WC-Co grades with higher fracture toughness had the least abrasion resistance. Further work by Blombery et al. [102] postulated that preferential removal of the binder phase was the rate controlling step in the wear of cemented tungsten carbide. Wear occurred in a two-step process whereby fine abrasives first removed the binder phase from the surface. Once this has been depleted the fracture toughness of the surface layer decreases leading to increased fracturing of the carbide skeleton and microspalling. This mode of failure is similar to other ceramic materials [103]. Blombery also noted that wear occurred at a rate an order of magnitude greater when specimens were abraded against loose quartz particles compared to a sandstone block which contains quartz particles. This suggests that understanding of the contact at the microscale is required to predict wear performance.

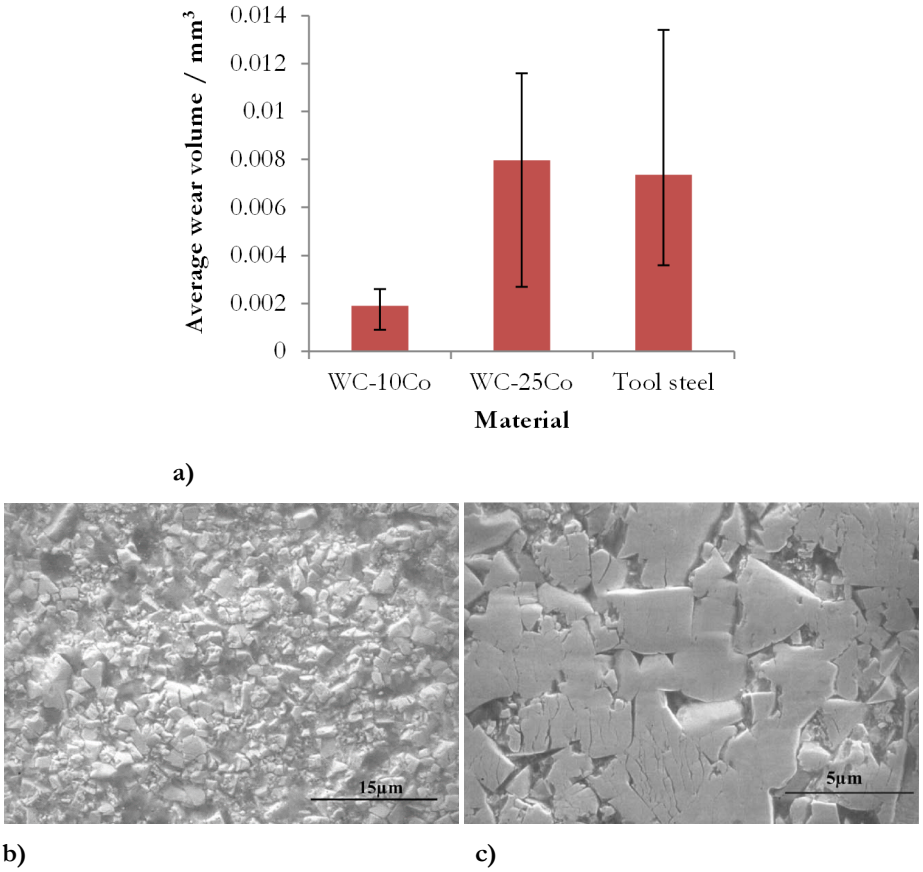

Figure 3-21: a) Average volumetric wear loss for samples across 5 test conditions. SEM comparison of wear surfaces of b) high cobalt sample (WC-20Co) and c) low cobalt sample (WC-6Co) [100].

One of the preferential binder removal mechanisms was observed in sliding wear tests by Larsen-Basse [104] where micrographs of the wear track showed evidence of cobalt smeared on top of the surface. It was therefore proposed that removal of the binder phase occurred through an extrusion action which is caused by compressive stresses being transferred from the carbide grains, see Figure 3-22. Abrasion tests conducted by Gant and Gee [100] using a modified ASTM G65 rig found that binder extrusion occurred in hardmetal grades with binder fractions of 6-9 wt.%. In contrast those with high cobalt fractions, 20-25 wt.%, grooving of the binder appeared to be more prevalent.

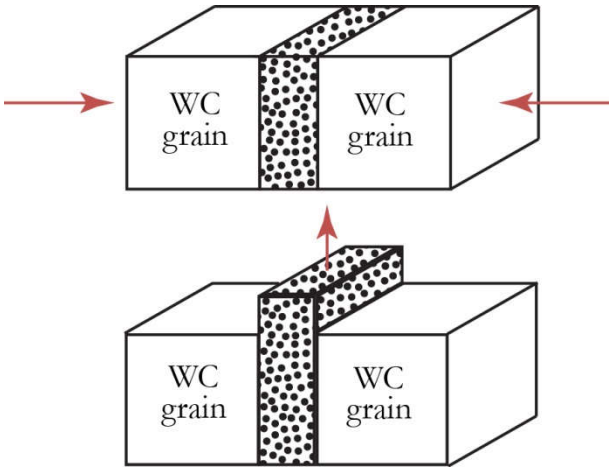

Figure 3-22: Binder extrusion mechanism proposed by Larsen-Basse [104].

Microabrasion testing has been used in a number of laboratories to assess the wear performance when abrasives on the same order of magnitude as the carbide grains are used. The test involves using a rotating ball on flat geometry while abrasive particles are fed into the contact. Shipway and Howell [105] used the microabrasion test to analyse grades with different grain sizes. They found that wear rate increased for finer grained sample contradicting the notion that higher hardness, as described by the Hall-Petch relationship, equates to higher abrasion resistance as predicted by the Archard equation. This was attributed to a modified removal mechanism of the binder phase, suggesting that finer abrasives cut into the binder phase, as opposed to the binder extrusion model, which then undermines the carbide grains leading to pullout. The larger grains are exposed to more binder phase meaning that they will take longer to be undermined. A change in wear mechanism as the binder content decreases was also observed by Shetty et al. [106] using a slurry jet impingement set up. At high binder content the primary mode of wear was through binder extrusion. Wear transitioned to transgranular degradation at compositions around 5 wt.% Co, while intergranular brittle failure dominated at very low binder compositions.

Gee [66] showed that similarity in wear mechanisms between the scratch tests and abrasion tests confirms scratch testing as a means to study abrasive wear on a fundamental level. A micro-scratch rig was then developed by the National Physics Laboratory (NPL) in the UK allowing the examination of the damage build-up on a single wear area by SEM, in a technique named stepwise wear [107]. In a number of subsequent studies conducted using this rig there was evidence to support the theory of plastic strain accumulating in the WC grains until a critical value is reached,

at which point fracture occurs [108-110]. Slip and pile up was also observed in nanoindentation experiments by Csanádi et al. [48], suggesting the property of any individual WC in a contact is dependent on which slip plane is activated.

The resistance of WC-Co to abrasive wear has been shown to be highly dependent on its mechanical and microstructural properties. However, it was noted by Ogilvy et al. [81] that whereas abrasion resistance appears very sensitive to composition and can vary by orders of magnitude, mechanical properties such as K_{IC} and H of the bulk material only differ by factors of around 1.5. This was attributed to the mode of wear which is principally through surface fracture. Using the same rig as Gee [66], Zuñega et al. [111] performed high load multi scratch testing followed by FIB-SEM of the region below scratch surface. Damage to the material was primarily through fracture of the carbide grains with plastic slip only seen at the edge of the scratch region. Fractures were primarily transgranular and seen to extend to between 5 μm - 10 μm below the surface, see Figure 3-23.

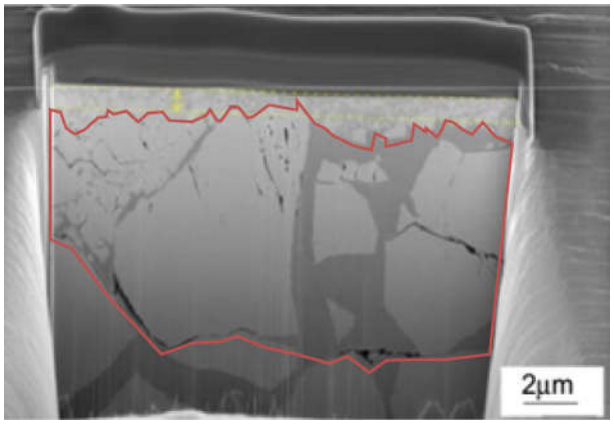

Figure 3-23: FIB-SEM image highlighting region under scratch dominated by fracture after 10 passes for WC-11Co, WC grain size 6.4 μm [111].

Analysis of worn drill bits as well as abrasion and scratch testing on cemented tungsten carbide have also shown evidence of tribolayer formation, see Figure 3-24. In laboratory experiments this is composed of crushed WC grains mixed with cobalt [96, 108, 111], while in worn drill bits it has also included a rock layer as well [99, 112, 113]. However, the effects of this film have not been examined in detail. It has been proposed that this may be beneficial to a certain degree as cobalt could act as a solid lubricant in the contact, although friction data from scratch tests do not support this hypothesis [114]. The coefficient of friction (CoF) tends to increase for the first 5-10 μm before reaching steady state conditions for the remainder of the

test. This general trend was reported for both coarse and fine grained materials, with cobalt films being reported in the latter. If cobalt did act as a lubricant it would be expected that friction would reduce as the cobalt film forms, which is not the case.

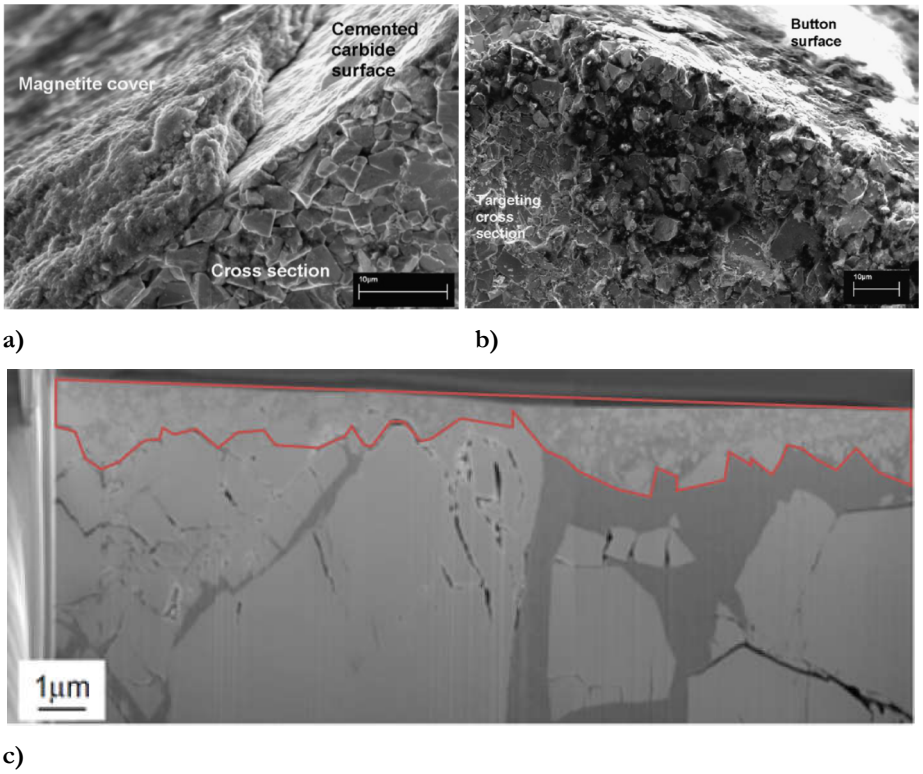

Figure 3-24: Cross section of cemented tungsten carbide surface subjected to wear a) used WC-6Co drill bit showing rock cover layer b) intermixed layer with rock and material fragments replacing binder phase and c) highlighting evidence of embedding worn material at surface [99, 111].

3.5 Tribocorrosion

3.5.1 Introduction

Tribocorrosion is the study of combined surface degradation by mechanical and chemical processes. Numerous studies have shown that the interaction between these two mechanisms produces wear rates which differ to that of their separate parts. Tribocorrosion processes are present in a number of engineering applications including drilling, mining, orthopaedic implants and chemical-mechanical polishing (CMP; a process used in the manufacture of integrated circuits). While tribocorrosion can also be in the form of erosion and fretting wear, the focus of this project will be on abrasive processes. Due to the small field this project will also

draw upon experimental and modelling techniques used for other materials and conditions such as those previously cited.

Commonly mentioned processes which affect the abrasion and corrosion conditions are formation and removal of oxide or passivation films and modification of the surface which can change corrosion kinetics and abrasion resistance [115]. Oxide layers can change the mechanical response while damage of passive films by mechanical loading can increase corrosion rate by exposing unprotected material. The complex nature of these interactions has made prediction and modelling of tribocorrosion systems challenging.

3.5.2 Tribocorrosion of Cemented Tungsten Carbide

Studies which specifically look at drill bits have found evidence that both abrasive and corrosion are both key mechanisms to their degradation. Beste and Jacobson [99] highlighted this effect on from "non-abrasive" rock types such as magnetite and calcite, where drill bits exhibited a polished appearance, see Figure 3-25. They concluded that while this is not a significant wear mechanism in itself, drill bits require regrinding so as to avoid propagation of cracks which could lead to a catastrophic fracture. The authors compared this appearance to the wear mechanism of CMP, with the final surface displaying a very smooth and polished appearance.

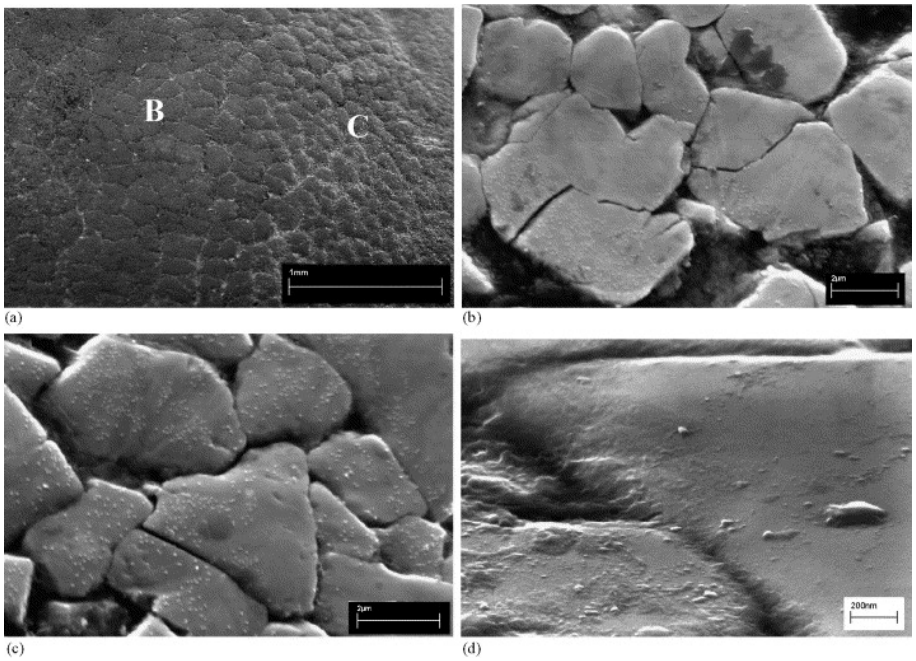

Figure 3-25: Surface of worn drill bit exhibiting polished surface [99].

When comparing cemented carbides with various binder compositions Wenzel and Allen [116] found that performance under static corrosion conditions does not always directly correspond to improved tribocorrosion resistance. Although nickel binders have better performance in corrosive environments they have a detrimental impact on the bulk material properties making it more susceptible to erosion damage. Furthermore, as discussed earlier, oxide formation which results in passivation behaviour is an important aspect of a material's static corrosion performance. However, the applicability of this phenomena in dynamic abrasive systems is not well understood. Passive films take time to form and are often mechanically weak which makes them susceptible to removal when load is applied to them. Wenzel and Allen found that passivation behaviour did not correspond to any improvement in the tribocorrosion performance of a material. This highlights the importance of studying both wear and corrosion mechanisms together.

The tribocorrosion response of WC-Co has been studied in laboratory conditions primarily through one of two methods, use of abrasion rigs or sliding contacts such as scratch testing. One of the first tribocorrosion experiments on WC-Co was carried out by Engqvist et al. [117] using pin-on-disc tests in various pH media, ranging between 1 and 14. Preferential dissolution of the binder phase was observed in acidic solution with WC grains showing little sign of corrosive attack, see Figure 3-26a. In alkaline solutions heavily corroded WC grains were found and cobalt oxides including CoO and $CoWO_4$ were detected although they were thought to provide no wear protection, see Figure 3-26b. Surprisingly, wear rate was found to increase with pH, see Figure 3-26c. Instability of the WC phase in alkaline solution was reported to be the cause of this.

Scratch experiments carried out by Gee [108, 118] in acidic media showed accelerated degradation mechanisms similar to those in dry conditions and lack of transfer film. Use of FIB revealed the extent of subsurface degradation, see Figure 3-27. Cobalt dissolution of around 5 μm under the scratch region was visible which would undermine the carbide grains. It was also noted that even under one pass slip and fracturing of the carbide grains was observed, which indicates that there is modification to the grain properties.

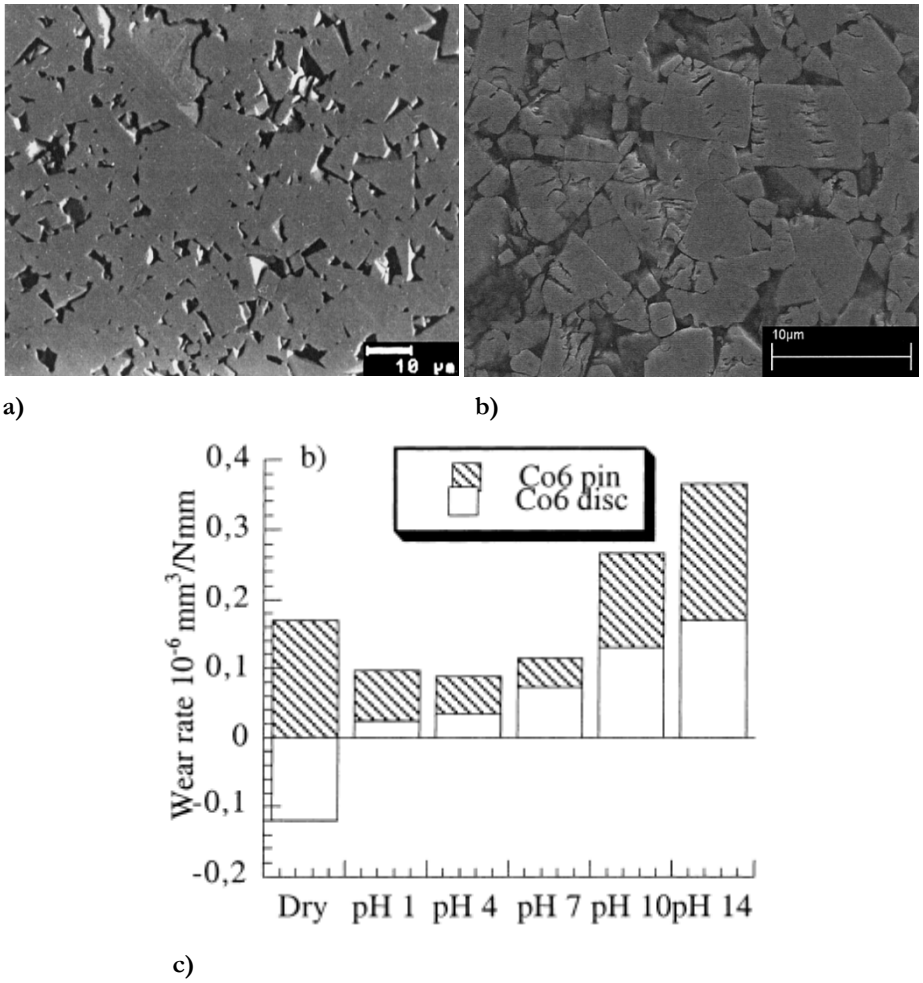

Figure 3-26: Corroded surfaces of WC-6Co following exposure to a) HCl pH 1 b) NaOH pH 14 and c) wear rates obtained from sliding tests across range of pH [117].

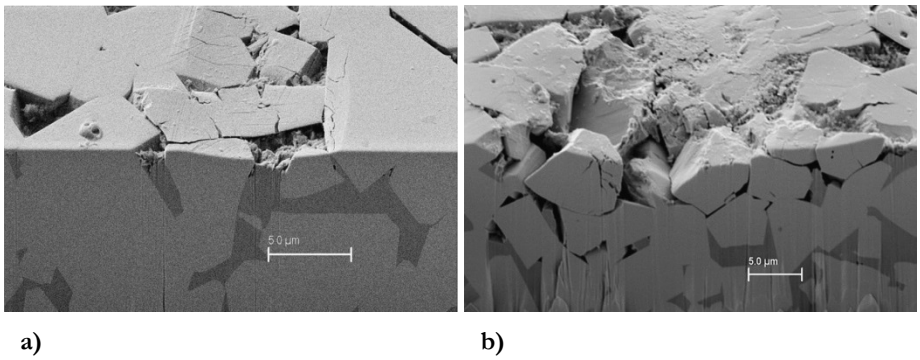

Figure 3-27: FIB section following scratch test on WC-11Co with exposure to 1M HCl after a) 1 pass and b) 50 passes [118].

Abrasion-corrosions tests which use acidic slurries have produced similar findings [105, 119]. Gant et al. [120] performed an investigation of various WC-Co grades in corrosive slurry, ranging from pH 1.1 to 13 using an ASTM G65 abrasion rig. In contrast to Engqvist, studies found immersion in more acidic media increased binder

removal and pluck out of small grains was observed, while wear rate decreased in alkaline solution. Further evidence was presented showing that microstructure seems to have a more prominent role than bulk material properties on the wear resistance, demonstrating that the material removal mechanisms are an important aspect when studying these systems. Wear was highest for fine grained WC across all pH levels tested, echoing results from Shipway and Howell discussed earlier (see Section 3.4.2).

Thakare et al. [121] developed a modified microabrasion test rig that is capable of performing *in situ* electrochemical measurements. By measuring corrosion further understanding of the degradation mechanisms beyond mass loss comparisons and visual inspection of the wear track can be made. Current measurements showed that there was a gradual increase as the wear scar increased in area. At the end of the test however currents did not return to the same levels as at the start of the test. Although results found that neutral and weak alkaline conditions had little effect on total wear rates, analysis of the worn area found the binder phase had been depleted in all solutions tested, ranging from pH 7 to 13. One of the limitations of microabrasion is that in order to achieve the desired mode of wear load has to be carefully controlled. Under low loads removal of the binder would make little difference as load is unable to initiate significant fracturing of the carbide grains.

3.5.3 Temporal Effects

It is important to appreciate that the rate of corrosion will often not be stable over time, especially in a tribocorrosion system where mechanical degradation of the surface is likely to alter the corrosion kinetics. This effect has been demonstrated by Olsson and Stemp [122] and Jemmely et al. [123] who studied the corrosion current of stainless steel and iron-chromium alloy samples in a reciprocating tribometer. From this mathematical and empirical models could be established to predict current over the duration of the experiment based on passive film growth kinetics. Under certain experimental conditions, models showed reasonable fit to experimental measurements. However, the extent to which passive films influence the corrosion of WC-Co is not well established and thus these models may be not that applicable to WC-Co.

3.6 Electrochemical Corrosion

3.6.1 Introduction

In the previous section (Section 3.5) corrosive degradation was introduced in the context of enhancing mechanical wear. Ponthiaux et al. [124] discussed the merits of combining a range of *in situ* electrochemical tests, namely open circuit potential, polarisation and electrochemical impedance spectroscopy (EIS), into an abrasion test to gain greater understanding of the underlying corrosion kinetics. In order to fully understand the results from Thakare et al. [121] and explore corrosion further, a thorough understanding of electrochemical theory is required. By doing this, greater understanding of chemical reactions and their effects the degradation mechanisms can be obtained.

3.6.2 Redox Reactions

The lower the value of the potential the more active the metal is and has a greater tendency to corrode. For two metals in contact the more active metal will become the anodic while the other will be cathodic. Anodic and cathodic site can also occur on the surface of one metal. In well-prepared samples these sites are close together and move with time, resulting in equal corrosion across the surface. However in samples with rough surfaces and varying features, anodic and cathodic areas can stabilise leading to local corrosion which can be significantly faster. The electrode potentials for elements of interest are listed in Table 3-1.

Table 3-1: Electrochemical series at 25°C for selected elements for common oxidation state, potential with respect to standard hydrogen electrode (SHE)

Element	Electrode reaction	Electrode potential *vs* SHE / V
Oxygen	$O_2 + 4H^+ + 4e^- \rightarrow 2H_2O$	+1.23
Hydrogen	$2H^+ + 2e^- \rightarrow H_2$	0
Tungsten	$WO_3 + 6H^+ + 6e^- \rightarrow W + 3H_2O$	-0.090
Cobalt	$Co^{2+} + 2e^- \rightarrow Co$	-0.277

Measurement of the transfer of electrons can allow the mass of the corroded material to be calculated using Faraday's laws of electrolysis. Assuming 100% current efficiency in anodic dissolution the mass loss per unit area per unit time, g cm^{-2} s^{-1}, can be defined by:

$$\frac{\Delta w_{\mathrm{m}}}{At} = \frac{j_{\mathrm{cor}} M_{\mathrm{m}}}{nF} \tag{3.21}$$

Where M_{m} is the molar mass of the metal and n is the charge number of the oxidation reaction. The corrosion current density, j_{cor}, is equal to the anodic current density, j_{a}, which depends on the anodic area, A_{a}:

$$j_{\mathrm{a}} = \frac{I_{\mathrm{a}}}{A_{\mathrm{a}}} \tag{3.22}$$

3.6.3 Oxide Layers

Under certain conditions the metallic cations which are released during the oxidation reaction can react with oxygen and hydroxides present in the surrounding solution to form an oxide film. Oxide layers which form stable, adherent and non-porous films are able to protect the surface from further corrosion, referred to as passivation. Such films inhibit corrosion by acting as a diffusion barrier, preventing further oxygen ions from reaching the surface [125]. They also increase the activation energy, thereby reducing dissolution of the metal. The formation of oxide layers is not considered in the electrochemical series or Faraday's law, therefore making accurate prediction of corrosion challenging.

The porosity of these oxide layers, and therefore an assessment of its ability to passivate, is the Pilling-Bedworth (P-B) ratio, PBR:

$$\mathrm{PBR} = \frac{M_{\mathrm{W(oxide)}} \rho_{\mathrm{(metal)}}}{\mathrm{n}\, A_{\mathrm{W(metal)}} \rho_{\mathrm{(oxide)}}} \tag{3.23}$$

Where $M_{\mathrm{W(oxide)}}$ and $\rho_{\mathrm{(oxide)}}$ are the molecular weight and density of the oxide; $A_{\mathrm{W(metal)}}$ and $\rho_{\mathrm{(metal)}}$ are the atomic weight and density of the metal; and n is the number of metal atoms in the oxide. For ratios below unity the volume of the oxide coating is less than that of the metal. This will result in the oxide being porous or continuously cracking and consequently providing little protection to the surface.

For values greater than two stresses can build in the oxide which lead to buckling and detachment from the surface, again providing limited protection. On the other hand, if the P-B ratio is between unity and two, the oxide layer has the possibility passivation. By comparing the P-B ratio of some of the oxides of interest, see Table 3-2, it can be seen that WO_3 and $Co(OH)_2$ are likely to provide minimal protection. Cobalt's other oxides CoO and Co_3O_4 have to potential to provide some protection, although they too are toward the upper end of the criteria. The P-B ratio, however, represents an idealised case and has limitations in its application as it does not consider factors such as adherence and non-stoichiometric films. Furthermore the effect of elastic and plastic deformation by external forces, as would be found in abrasion contacts, cannot be assessed.

Table 3-2: P-B ratio for selected oxides

Element	Oxide	P-B ratio
Tungsten	WO_3	3.6 [126]
Cobalt	CoO	1.9 [126]
Cobalt	$Co(OH)_2$	3.9*
Cobalt	Co_3O_4	2*

*Caculated from Equation (3.23)

Growth of the oxide film is also an important factor in determining its ability to passivate. For oxides that form at the oxide-solution interface, that is to say metal ions diffuse outward in preference to inward diffusion of oxygen, the oxide layer is unrestricted and more likely to form a protective layer, see Figure 3-28a. However for those that form at the metal-oxide interface the oxide is subject to compressive stresses and therefore cracking and spalling is more likely to occur, see Figure 3-28b. Visual observation by Human et al. [127] on tests conducted on Co(W,C) in sulphuric acid show the oxide layer retaining the holder shape suggesting that growth of the oxide occurs at the metal-oxide interface.

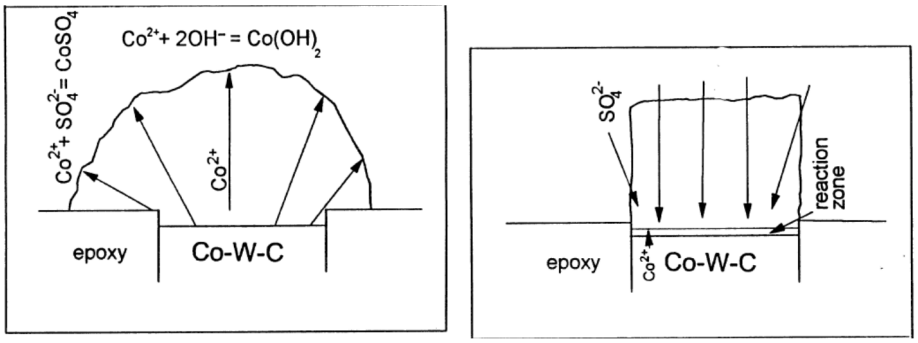

Figure 3-28: Schematic comparison of oxide growth mechanisms for Co-W-C in H_2SO_4 solution at a) oxide-solution interface and b) metal-oxide interface [127].

Observation of WC-Co used in percussive drill bits found evidence of oxide formation, see Figure 3-29. This loosely attached oxide, which the authors assumed to be tungsten oxide, is unlikely to provide any wear protection, although Thakare et al. [121] proposed that oxides could reduce the CoF which would result in reduced wear rates.

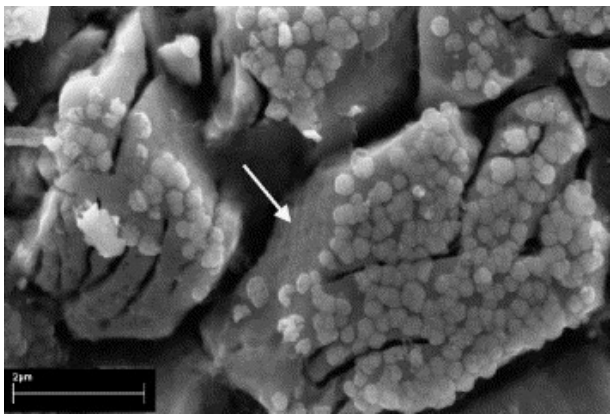

Figure 3-29: Evidence of oxide layer on WC grains from rock drilling [99].

3.6.4 Pourbaix Diagrams

One of the most important factors that determines the corrosion behaviour is the pH of the surrounding or adjacent environment. Thermodynamic understanding of the half-cell reactions, coupled together with understanding of the solubility of oxides in solution can be represented in the form of potential-pH equilibrium diagram, also often referred to as the Pourbaix diagram, see Figure 3-30 and Figure 3-31. These diagrams indicate the conditions at which metals are stable or form ions and oxides. By applying a cathodic potential or adjusting the pH it is possible to

prevent corrosion from occurring for a given surface, either through stabilisation of the metal or formation of a passive layer.

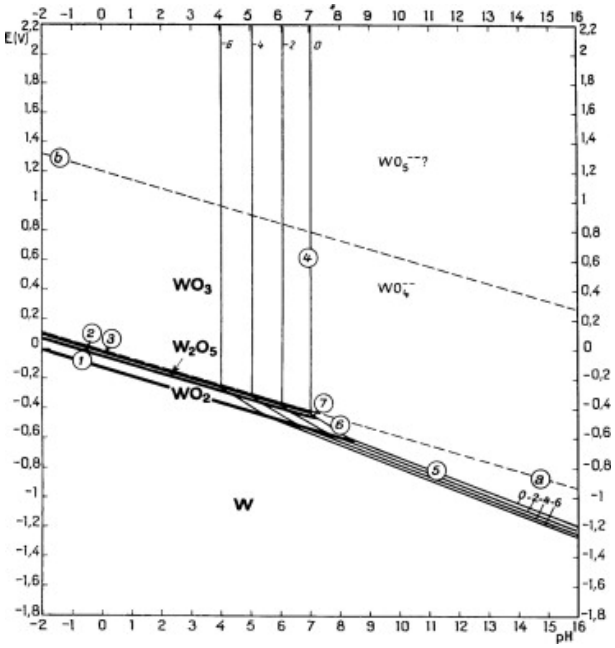

Figure 3-30: Potential-pH equilibrium diagram for tungsten-water at 25°C, potential with respect to standard hydrogen electrode [128].

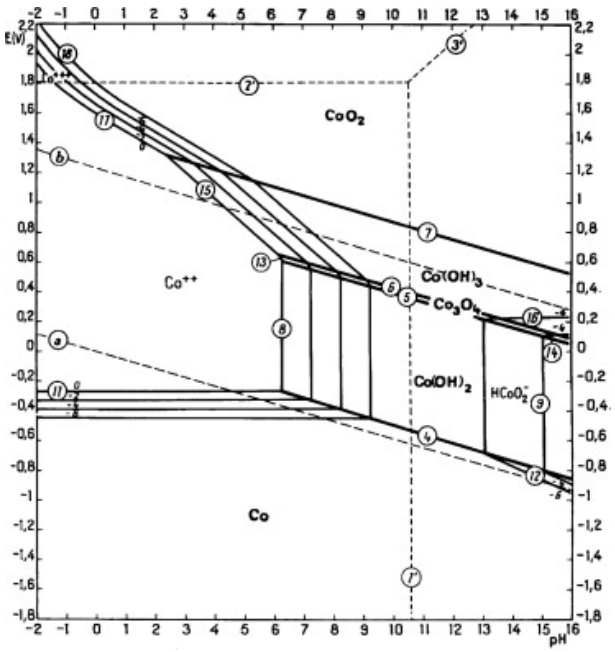

Figure 3-31: Potential-pH equilibrium diagram for cobalt-water at 25°C, potential with respect to standard hydrogen electrode [128].

The pH values indicated on the Pourbaix diagram is that of the solution in direct contact with the surface of the metal. This can differ to that of the bulk solution due to the presence of other anions or concentration of H^+ ions in specific areas.

Furthermore, there is an underlying assumption that below a given metal ion concentration no corrosion occurs. Metal cation concentrations (10^{-6} M, 10^{-4} M etc.) are represented in the diagram as lines labelled −6 and −4, respectively.

There are three distinct regions on the Pourbaix diagram that can be identified. The metallic region (i.e., W and Co regions in Figure 3-30 and Figure 3-31) indicate that metal is stable and has immunity to corrosion. $M_nO(H)_n$ (e.g., WO_3 and $Co(OH)_2$ on Figure 3-30 and Figure 3-31) show that a stable oxide layer is formed and, although this is required for passivation to occur, it does not indicate the effectiveness of corrosion inhibition as discussed in Section 3.6.3. M^{n+} (e.g. WO_4^{2-} and Co^{2+} on Figure 3-30 and Figure 3-31) indicates a driving force for corrosion to occur, although the diagram does not provide information on the rate of corrosion.

In order to study the effects of potential electrochemical techniques, such as potentiodynamic and potentiostatic polarisation, can be used to artificially apply potentials to a sample.

3.6.5 Potentiodynamic Polarisation

Changes to the surface and the solution will impact the corrosion process, moving it away from its equilibrium potential, E_0. Polarisation can also be induced by the application of an external potential or galvanic coupling. This is termed overpotential, P_η, defined by:

$$P_\eta = E_p - E_0 \tag{3.24}$$

Where E_p is the polarised potential. A similar term called overvoltage, P_ε, measures the difference between applied polarisation potential and the corrosion potential, E_{cor}, of a freely corroding system, see Figure 3-32. Overpotential, is related to the current, j, through the Tafel equation:

$$P_\eta = \beta \log \frac{j}{j_0} \tag{3.25}$$

Where j_0 is the exchange current density and β is the Tafel slope or constant. This can be determined from extrapolation of the linear section of the anodic and cathodic polarisation curves, β_a and β_c respectively. At the intersection of these lines j_0 or for mixed potentials j_{cor} can be determined allowing calculation of corrosion

rate using Faraday's law, see Figure 3-32. Combination of the anodic and cathodic Tafel equations gives the Butler-Volmer equation:

$$j = j_{\text{cor}}\left(\exp\left[\frac{2.303\left(E_{\text{P}} - E_{\text{cor}}\right)}{\beta_{\text{a}}}\right] - \exp\left[\frac{-2.303\left(E_{\text{P}} - E_{\text{cor}}\right)}{\beta_{\text{c}}}\right]\right) \quad (3.26)$$

A common technique to study corrosion of materials is linear potentiodynamic polarisation. A potential is applied to a sample in a solution and the current measured. From the resulting data, example shown in Figure 3-32, it is possible to calculate the Tafel constants and therefore understand the corrosion kinetics of the system.

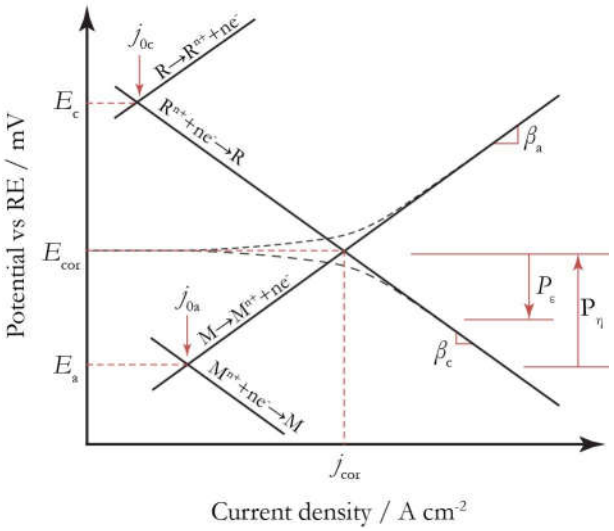

Figure 3-32: Potentiodynamic polarisation schematic showing the anodic and cathodic branches and major terms. E_a and E_c will be E_0 for the respective anode and cathode. Potentials are made in relation to a reference electrode (RE).

In passivating metals an oxide film begins to form and inhibit corrosion, this effect can be seen the polarisation curve by a reversal in the current density above a certain anodic potential. During this region current no longer changes as potential increases, see Figure 3-33. Further increase in the anodic potential will result in the oxide layer breaking down indicating the onset of corrosion pitting, termed transpassive region.

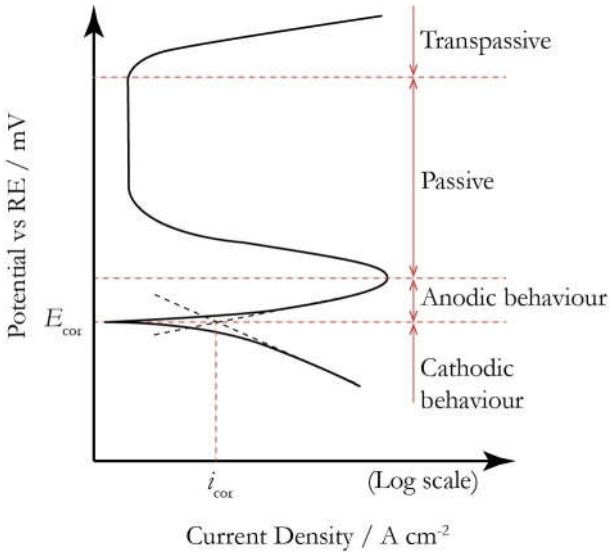

Figure 3-33: Potentiodynamic polarisation illustration for a material that exhibits passivity with main corrosion regions highlighted.

Human and Exner [129] studied the corrosion properties of WC-Co in sulphuric acid. Polarisation curves indicate that the corrosion of WC-Co in acidic media more closely follows the behaviour of Co than WC, see Figure 3-34b and Figure 3-34a respectively. Although, unlike pure Co a current peak is observed in the WC-Co samples. Potentiodynamic polarisation was carried out on a cobalt alloy with tungsten and carbon additions (Co-4W-0.02C) which was representative of the composition of the binder phase in WC-Co, as discussed in Section 3.1.4. A similar electrochemical response was reported to that of WC-Co, see Figure 3-34c, suggesting that the binder was the rate controlling factor for corrosion in acidic media. Investigations by Sutthiruanwong et al. [49] also showed clear correlation between electrochemical behaviour of binder phase and cemented carbides. Experiments also found higher tungsten content led to a slight increase in corrosion resistance [127, 130].

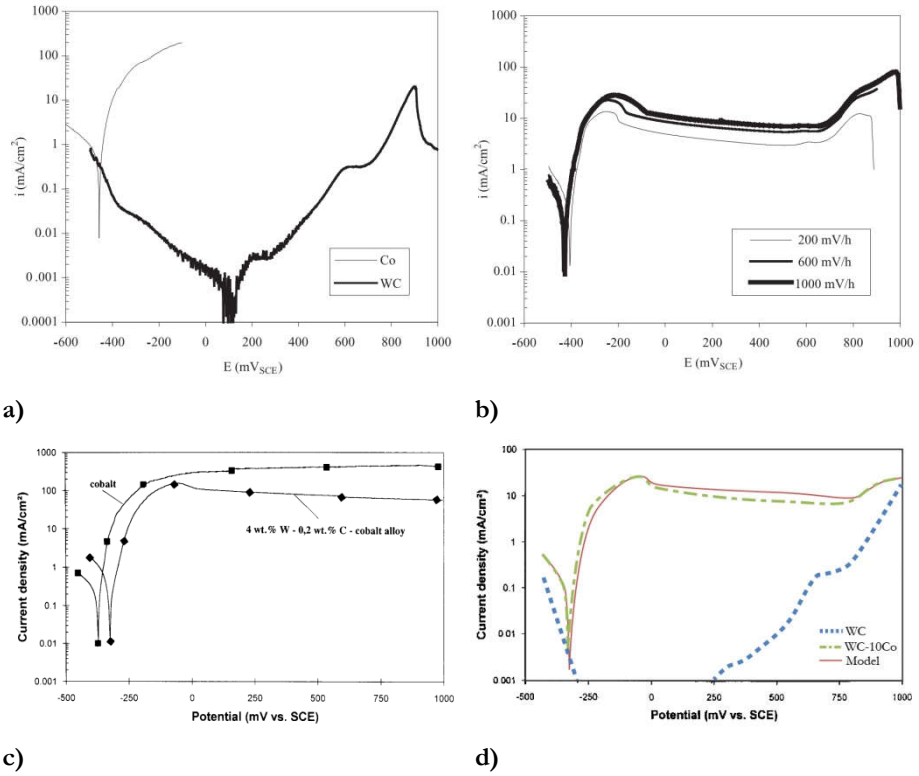

Figure 3-34: Potentiodynamic polarisation of a) Co *vs* WC, b) WC-9Co as varying scan speeds, c) Co *vs* Co-4W-0.02C and d) WC *vs* Co-4W-0.02C *vs* model (redrawn for clarity) in 1 N H_2SO_4 solution. Potentials *vs* SCE [129, 130].

This dissolution of the cobalt binder and formation of a tungsten oxide in acidic environments can be predicted by inspection of the Pourbaix diagram, see Figure 3-30 and Figure 3-31, which shows cobalt ion formation in solution pH 6 or lower and stabilisation of WO_3. Following polarisation of WC-Co samples Sutthiruangwong and Mori [130] observed formation of a tungsten oxide layer around 10 µm thick and cobalt depleted region below this of thickness 250 µm, see Figure 3-35. This was also observed by Ghandehari [131] in a phosphoric acid solution with pH of 0.56.

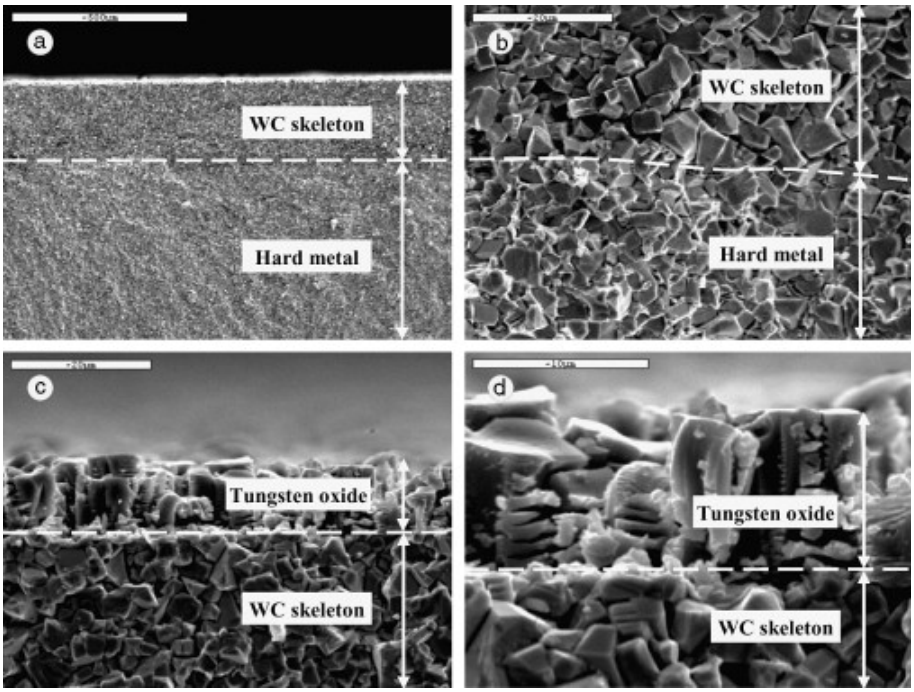

Figure 3-35: SEM cross sectional images of WC-9Co sample following polarisation in 0.5 M H_2SO_4 [130].

The region of lower current density in the potentiodynamic polarisation curve, which occurs following a peak current, is similar to passivation behaviour. The term 'pseudo-passivity' was proposed by Human and Exner [129] and although it is a phenomenon that has also been observed by others [130, 132], the authors pointed out the importance of current densities that are much higher than would be expected from truly passive materials. Human and Exner attributed this behaviour to the porous tungsten oxide layer that would restrict ionic mobility but does not passivate. Sutthiruangwong and Mori [130] offered a different explanation following chronoamperometric measurements at active and pseudo-passive potentials. Results suggest that corrosion inhibition is a result of the tungsten carbide skeleton that remains following oxidation of the binder which increases the diffusion path. Bozzini et al. [133] and Hochstrasser et al. [51] however reported no pseudo-passive behaviour. Bozzini explained this difference was because aerated and deaerated solutions provide different responses, although this was directly contradicted by Sutthiruangwong and Mori [130] who reported little difference in electrochemical behaviour when direct comparison was made, concluding that dissolved oxygen has little impact on the anodic behaviour.

Finally, as the anodic current is increased further the material exits the pseudo-passive region and corrosion current begins to rise again. This is due to the oxidation of WC rather than oxygen evolution, which will begin to have an impact on the corrosion of the sample overall around 800 mV, see Figure 3-34d.

However, water based drilling fluid pHs tend to range between 9 and 11. The corrosion resistance of WC-Co is known to have better performance in alkaline solutions and so analysis of WC-Co in alkaline solutions has had relatively little attention [134]. Analysis of the Pourbaix diagrams indicates that tungsten is unstable in alkaline conditions and is unable to form a stable oxide layer as described in earlier. Cobalt however is known to passivate in alkaline solutions, forming a layer of $Co(OH)_2$ [135, 136]. Further oxidation of these corrosion products to more complex Co_3O_4 and CoOOH increases the stability of the passive film. Theoretically this could provide some passivating behaviour of the bulk material. Potentiodynamic polarisation results by Kellner et al. [55] in very alkaline solutions found some passivation effects on WC-Co due to the formation of $Co(OH)_2$ on the surface, although corrosion of WC at higher potentials restricted the range, see Figure 3-36a. Although Hochstrasser et al. [51] also saw similar passivation of cobalt, this did not result in passivation of the WC-Co sample, see Figure 3-36b. Both experiments used a scan rate of 5 mV s^{-1} although samples were different compositions. However, given that the passivation behaviour appears to arise from the cobalt phase, it would be expected that the higher cobalt fraction used by Hochstrasser and co-workers could result in this difference in passivating behaviour.

When Hochstresser et al. compared the potentiodynamic polarisation plot between acidic and alkaline solutions, the authors found that as pH increased there was a trend of moving E_{cor} to more negative values, around 1000 mV difference, for Co, W and WC-Co samples. In general cobalt dominated WC-Co behaviour in acidic and neutral conditions, whereas WC dissolution played a more significant role in alkaline solutions. However, even although WC is more susceptible to corrosion in alkaline conditions the binder still influences the sample behaviour due to galvanic coupling.

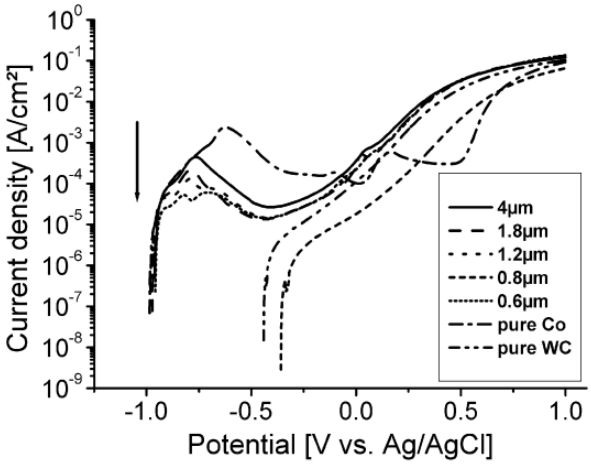

a)

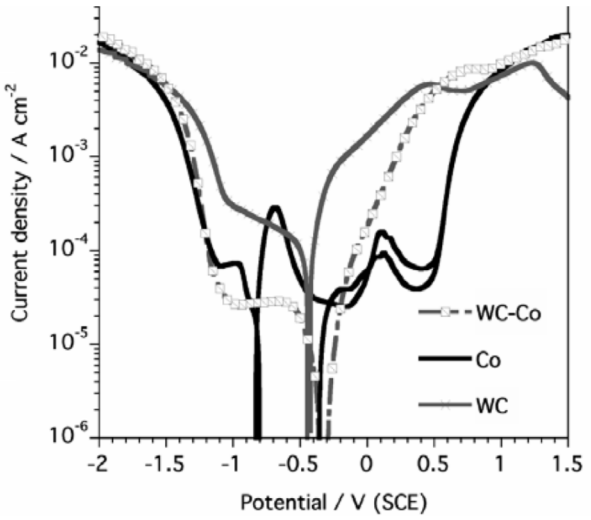

b)

Figure 3-36: Comparison of potentiodynamic polarisation of Co, WC and WC-Co in a) 1 M NaOH for range of WC grain size (WC-6Co) and b) 0.1 M NaOH (WC-15Co). Note differences in reference electrode [51, 55].

3.6.6 Galvanic Coupling

As WC-Co is a heterogeneous material and both materials are conductive (electrical resistivity 5 μΩ cm – 100 μΩ cm [32]) electrons can move between the two phases producing a corrosion cell. Polarisation scans have shown cobalt to be more anodic than tungsten carbide at all pHs which will cause the blinder to act as a sacrificial anode [51, 129, 130]. At open current or low applied potentials the binder phase is preferentially corroded leaving the skeletal structure of WC grains.

Hochstrasser et al. [51] used inductively coupled plasma mass spectroscopy to compare the corrosion products of WC-15Co, WC and Co. Despite WC-Co

showing similar corrosion kinetics to WC, when WC-Co corrosion products were measured significantly more cobalt was present in solution across the whole pH range indicated enhanced dissolution. The author attributed this to galvanic coupling, whereby the WC phase is cathodically protected by the binder phase.

The ratio of anode to cathode area is also an important factor in corrosion rates. A large anode to cathode ratio will increase corrosion rate while the opposite will reduce corrosion. In the WC-Co grade of interest the anodic binder region is typically much smaller than the cathodic region. Human and Exner [129] reasoned that although composites with higher binder fractions have higher current density, this is due to the larger exposed area, rather than because corrosion rate has increased. When only the exposed binder area is considered similar current densities were obtained. This hypothesis would suggest that the relative size of anodic and cathodic areas was not significant, indicating galvanic coupling is of such a small order of magnitude it does not affect corrosion rate of the binder. However, results from Sutthiruangwong and Mori [130] contradict this view, observing lower current density regardless of whether total surface area or binder surface area is used.

Olovsjö et al. [113] found evidence of this preferential dissolution near the surface of worn drill bits, see Figure 3-37. This could only have been a result of corrosion processes as material is removed significantly below the contact surface. Interestingly drilling environments are typically alkaline, where WC-Co is known to have better corrosion performance [134].

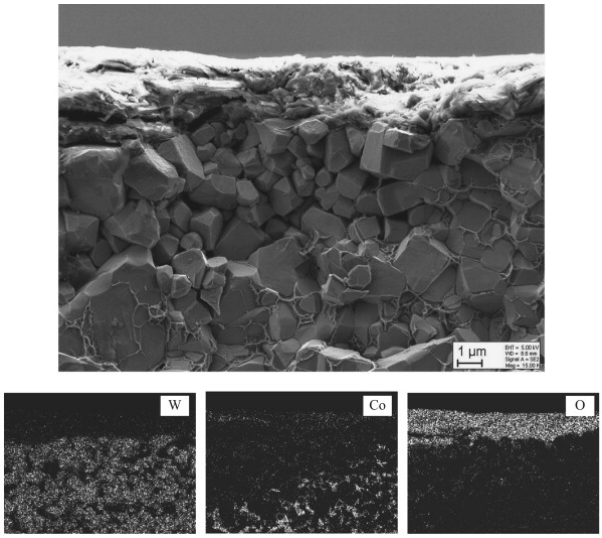

Figure 3-37: Cross section below of worn drill bit and EDX map showing presence of cobalt depleted zone near the surface. Evidence of rock transfer film can also be seen [113].

The presence of the binder depleted regions could be explained through galvanic coupling. However, another explanation of these features is the creation of microenvironments. It was observed that where these binder depleted zones occurred a rock transfer layer above was always present. This is significant as this could enable a microenvironment to exist which is different to that of the bulk solution.

3.6.7 Microenvironments

Microenvironments can create chemical concentration effects due to the restriction of mass transport of ions, an effect that is often associated with crevice or pitting corrosion. During corrosion processes the consumption of oxygen can lead to other chemical reactions which will change the chemistry of the microenvironment compared to that of the bulk electrolyte. Increased chloride concentration and lowering of the pH would create the conditions for accelerated corrosion that is uneven across the surface of the material.

Evidence of preferential corrosion of the binder has also been observed in worn drill bits by Beste and Jacobson [99] and reported to be a significant deterioration mechanism, see Figure 3-38a. The authors identified crack like features which start at the surface of the sample and are an example of local corrosion described earlier. In these crevices oxidation of the WC grains is also noted which is likely to weaken them further and make them more prone to cracking from mechanical stresses, see Figure 3-38b.

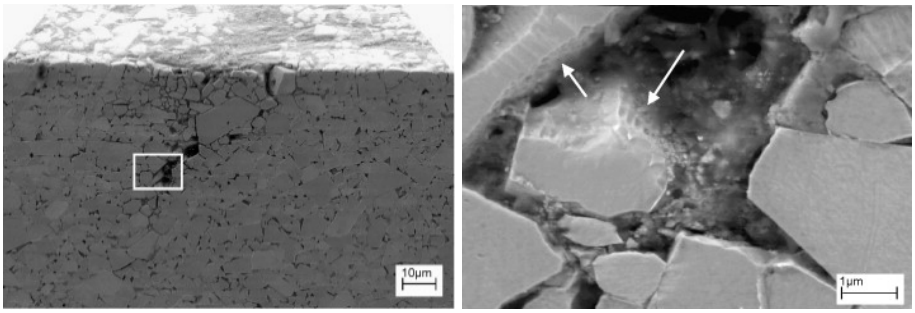

a) **b)**

Figure 3-38: Cross section of drill bit showing chemical degradation on bulk material. White arrows indicate corrosion of WC grains [99].

Corrosion which results in depletion of the binder will also have an impact on the mechanical properties of the material. This was investigated by Pugsley et al. [137]

and Tarrago et al. [138] who both found a significant decrease in strength of WC-Co samples after exposure to acidic solutions, seeing strength reduce by up to 70%. In addition to the depleted binder cross sections of the samples the authors also observed uneven corrosion which created stress raisers through corrosion pits, see Figure 3-39a. The use of FIB-FESEM cross sectioning by Tarrago also enabled a visualisation of the binder depleted network that exists post corrosion on the surface of the material to be created, see Figure 3-39b.

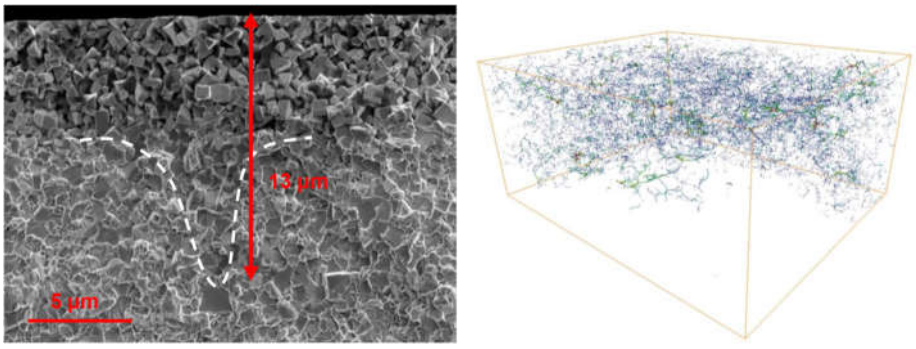

a) **b)**

Figure 3-39: a) Corrosion damage of WC-15Co after 24 h in synthetic mine water. Corrosion pit indicated by dashed line and b) 3D reconstruction of microcracked phases created from FIB-SEM [138].

3.7 Modelling

3.7.1 Current Approach to Understanding Tribocorrosion

An attempt to quantify the coupling effects of mechanical wear and corrosion has been proposed through the concept of 'synergy'. This has been applied to abrasion, erosion and sliding wear-corrosion systems. An ASTM standard (G119) [139] was published following the approach developed by Pitt [140, 141] and Madsen [142-144]. The method attempts to break material loss, V, down into its constituent parts:

$$V_{AC} = V_{PA} + V_{PC} + V_S \tag{3.27}$$

Where subscripts AC, PA, PC and S are wear associated with abrasion-corrosion, pure abrasion, pure corrosion and synergy respectively. Electrochemical mass loss, V_{PC}, can be calculated using Faraday's law of electrolysis, Equation (3.21) discussed in Section 3.6.2, although this is subject to significant error as corrosion is complex and often involves multiple reactions. V_{AC} and V_{PA} are typically calculated from experimental mass loss measurements, leaving V_S to be calculated by balancing the

equation. Synergistic wear has been further defined as the aggregate of change of abrasive wear due to corrosion, ΔV_A and change of corrosive wear due to abrasion, ΔV_C:

$$V_S = \Delta V_A + \Delta V_C \tag{3.28}$$

ΔV_A would describe processes such as increased mechanical wear as a result of the dissolution of the binder phase which would create unsupported carbide grains, such as that seen by Gant et al. [118] in Figure 3-27. ΔV_C would describe processes such as crevice corrosion which would occur in fractures initiated through mechanical interaction, a possible initiation of the feature observed by Beste and Jacobson [99] in Figure 3-38. Using *in situ* electrochemical measurements on tribology rigs, electrochemical and mechanical wear of the synergy equation can be measured under different operating conditions. One popular way of visualising this information is through the creation of tribocorrosion maps, see Figure 3-40.

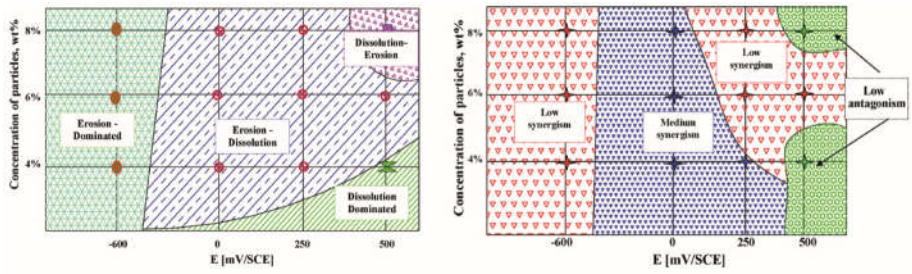

a) **b)**

Figure 3-40: Example of tribocorrosion maps for WC-Co-Cr coating a) erosion-corrosion mechanism map and b) erosion-corrosion synergism map [145].

These maps are considered to be a useful method for determining trends and delineating predominant degradation mechanisms in a tribocorrosion system [146]. Wear systems are often grouped together where similar levels of mechanical and corrosive degradation are obtained. This is typically done to highlight the extent of degradation due to a given mechanism, e.g. high, medium or low wear, or to describe transitions between degradation mechanisms, e.g. erosion dominant, erosion-passivation or passivation dominant [147].

However, the validity of such an approach is subject to debate. One of the primary difficulties with using this assessment of a system is to attain a baseline upon which synergy values can be added [63]. If baseline abrasion tests are conducted in dry

conditions, this will fail to take account of lubrication regime and will likely over predict material loss. The challenge is therefore trying to select an electrolyte which will provide a baseline. Deionised water is often used as the zero point, although this is not an inert environment and despite it not always yielding the lowest wear rate. Furthermore, as can be seen from the Pourbaix diagrams discussed in Section 3.6.4, chemical reactions are not linearly related to pH and different oxides can be deposited in acidic or alkaline solutions. Indeed numerous studies have found systems to have negative synergistic effects, sometimes referred to as antagonistic, even under a relatively small set of parameters [148-150].

Theoretically, under cathodic protection selection of electrolyte should make no difference as corrosion processes should be suppressed. The ASTM G119 method suggests using a potential of −1 V cathodic to the corrosion potential, to suppress metal dissolution thereby allowing measurement of material loss due to mechanical wear alone. Studies into this method have found weaknesses in this approach however, noting that application of cathodic potentials does not affect various materials equally. Under certain conditions cathodic protection has been found to have little effect on corrosion kinetics while others have reported the possibility of hydrogen embrittlement [151, 152].

Thus, while the synergy approach may be suitable as an assessment method of various mechanical parameters or for material selection purposes within a defined tribocorrosion system, uncertainty and the number of variables make it difficult to extrapolate findings across tribocorrosion systems or to service conditions.

Another approach to the problem has been suggested by Mischler et al. [153, 154], based on work by Uhlig [155] for fretting corrosion systems. This mechanistic approach uses the concepts of corrosion accelerated wear, V_{MECH}, and wear accelerated corrosion, V_{CHEM}. The chemical degradation can be approximated using Faraday's law while total wear, V_{TOT}, can the measured using volumetric or gravimetric approximations. From this V_{MECH} can be deduced:

$$V_{MECH} = V_{TOT} - V_{CHEM} \tag{3.29}$$

By removing the synergy parameters many of the problems with the synergy approach are negated. Mischler did note drawbacks in this approach however, as it is based on a simplified understanding of the contact [156]. Factors such as contact

area and wear debris are not accounted for in this approach, although modification to the equation would be possible. The reason that this approach has not been widely adopted however is likely due to it not explicitly providing any more information than that of the synergy approach.

3.7.2 Types of Models

The complexities of tribocorrosion have led to the pursuit of a model that can both elucidate physical phenomena and predict wear performance in a given environment. By ensuring that critical physical behaviours and interactions of the material are captured, such a model should in theory be able to model tribocorrosive wear entirely. Additionally, by being able to isolate individual parameters, the model could be used to explain synergistic outcomes. Current modelling approaches can be roughly classed into three types:

- empirical,
- mathematical and
- numerical.

3.7.3 Empirical Modelling

Previously wear models have been primarily empirically derived relationships, such as Archard's wear law discussed in Section 3.4.2, which use wear constants as a fitting parameter for a particular wear system. Modification of these equations has also been used to study other tribocorrosion systems such as chemical-mechanical polishing (CMP). An example of this approach is the modification of Preston's equation proposed by Luo et al. [157] who studied CMP of copper in both acidic and alkaline solutions, where polish rate, V_R, is defined as:

$$V_R = \left(a_3 P + a_4\right) v_l + a_5 \tag{3.30}$$

Where P is applied load, v_l is linear velocity and a_3, a_4 and a_5 are fitting parameters for experimental data. Another example of this approach is by Jia and Fischer [94], whose model was discussed in Section 3.4.2, and can be generalised to the form:

$$K_w = a_6 + a_7 d_{WC} \tag{3.31}$$

Where d_{WC} is WC grain size and a_6 and a_7 are fitting coefficients. One of the main advantages of the empirical modelling approach is its simplicity to apply. Fitting parameters can be applied to any set of experimental material loss measurement. Provided that the experimental setup is similar to the application, the material combinations tested can be ranked. Extension of this approach can also provide a service life estimation. However, its simplicity is also its main drawback. Materials typically go through a process of wear transitions before establishing quasi-steady state wear as was discussed in detail by Blau [158], see Figure 3-41. The duration of these transitions and severity of them varies by material, environment and contact geometry, which wear coefficients cannot capture. These conditions are also difficult to accurately replicate outside of service conditions, meaning that even for quasi-steady state wear the accuracy of extrapolating material loss is uncertain.

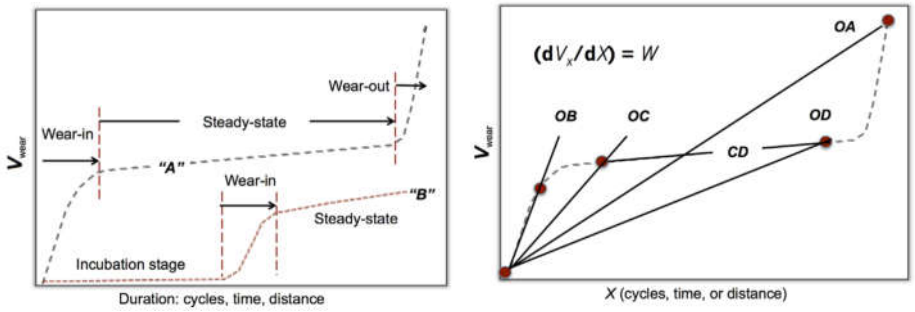

a) b)

Figure 3-41: a) Example of non-linear wear going through wear transitions and b) highlighting the danger of extrapolating wear rate from a single material loss measurement [158].

3.7.4 Mathematical Modelling

Mathematical models use an analytically derived understanding of interactions to predict an outcome. An example of this is the tribocorrosion model presented by Jiang et al. [159, 160] and later developed by von der Ohe et al. [161], which drew on a number of studies to combine mechanical wear and corrosion processes. Starting with the synergy approach described earlier and expanding the terms using analytical solutions, resulting in the following material loss expression when stable passive film is formed:

$$V_{AC} = \frac{\pi D_d^2 N_C A_a f_c t_s}{6} g_r + \left[\frac{A_W l_s t_s}{z_e F \rho}\right] a_g l_w \sqrt{\frac{P_n}{H}} \left(j_0 - j_p\right) f_c \tau_0 \left[1 - \exp\left(\frac{-1}{f_c \tau_0}\right)\right] + \frac{\pi D_m^2 N_c A_a f_c t_s}{6} g_R + \frac{\pi D_m^2 N_c A_a f_c t_s}{6} \left\{g_{CFS}\left[1 - \exp\left(\frac{-1}{f_c \tau_i}\right)\right] + g_S\right\} \quad (3.32)$$

Explanation for these terms can be found in the nomenclature. While the models from Jiang and von der Ohe did bring together analytical solutions from both tribology and electrochemistry field, which could form that basis for a more general description of tribocorrosive wear, their complexity makes wider adoption challenging. In both cases no validation was presented, which was due in part to the difficulty of measuring some terms within the equation, such as crack growth rate terms, *g*. Furthermore, it is not clear if other major interactions, such as what happens to wear debris in the contact and affect of microenvironments on corrosion, could be described analytically and added to the model. Even if all such interactions of a complex wear system were incorporated, validation of the model would become even more difficult. As with empirical models, mathematical models deal with global behaviour and cannot be used to study interactions at the grain level, an important factor as discussed earlier in Section 2.1, in which Beste et al. [5] compared the effects of loose *vs* bulk quartz. Neither approach directly explains what mechanisms are involved in degradation and subsequently how they can be minimised.

3.7.5 Numerical Modelling

With the advent of advanced computing technology, the restriction of being able to apply material physics directly at the microscale is lifted. By combining degradation mechanisms on a fundamental level with modelling at the microscale this may assist understanding the relationship between scratch and microabrasion testing. Such complex interaction and physics do not have analytical solutions and would be difficult for a mathematical model to capture. This suggests the need to move towards a numerical solution.

Rather than trying to model global behaviour, numerical modelling starts with the fundamental interactions. Using computing power this is then scaled up to analyse global behaviours. Current modelling of cemented tungsten carbide has therefore concentrated on the interface between the phases at the grain level. One of the

drawbacks of this approach is that it is currently unable to provide an estimate of material loss rate. Modelling of tungsten carbide is significantly behind that of our understanding of the material wear processes. One explanation of this is that appropriate numerical methods are not widely available to capture brittle failure, a major degradation mechanism in tungsten carbide. However, promising numerical methods have arisen recently as well as the computational resources needed run them.

The numerical modelling approaches employed to study cemented tungsten carbide can be categorised into three types:

- hypothetical geometries,
- idealised geometries and
- accurate geometries.

Hypothetical geometries are the most simplified models, often bearing little resemblance to real geometries, see Figure 3-42a. Geometries are usually simplified to squares, rectangles and circles or their 3D equivalents. These are the most computationally efficient method and easiest to perform parametric studies, as variables of these simple shapes are easy to define. However, because these geometries are simplified so much, they are difficult to validate when new combinations are brought together. This modelling approach was used by Livescu et al. [162] to study residual stresses in the microstructure. Simulations were able to obtain a similar strain response behaviour to that of experimental results, although significantly underestimated residual strains.

Idealised geometries simplify microstructures, although use more complex shapes than hypothetical geometries, see Figure 3-42b. They are often used to investigate specific aspects of the microstructure. An example of this approach is by Poech et al. [163] who examined the global response of a domain to parametric variables. The difficulty with this method is that it is harder to define the variables compared to hypothetical geometries, but also does not represent a microstructure which can be achieved.

Accurate geometries attempt to mimic the microstructures as close as possible and are the most computationally expensive of the three methods, see Figure 3-42c. While it is difficult to perform parametric studies due to the arbitrary geometries

modelled, this approach is the easiest to validate against experimental results. Early modelling studies of cemented tungsten carbide looked to use finite element modelling to predict the elastic properties of the bulk material. Rather than use general expressions to describe the material properties of a bulk material, such as the rule of mixtures, Jaensson and Sundstrom [164] proposed that modelling could provide specific material properties for any given microstructure of interest. SEM images were used to create accurate geometries based on real microstructures with WC and Co properties applied to the individual phases. Simulation results of Young's modulus were within the upper and lower bound predicted by the rule of mixtures across a range of binder contents between 11.4% and 35%. Plane stress and plane strain conditions did produce different values, although the differences were small, suggesting that using a 2D model to a 3D microstructure is a reasonable approach.

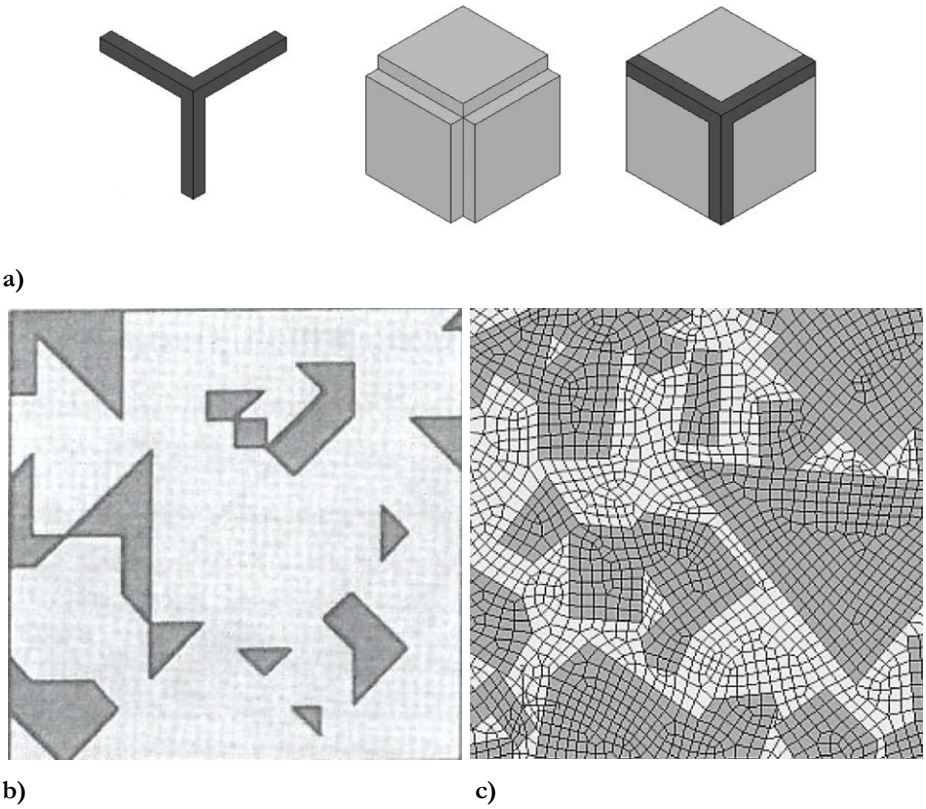

Figure 3-42: Examples of the three numerical modelling approaches used in the literature a) hypothetical approach showing binder, carbide and composite b) idealised microstructure and c) full microstructure [162, 163, 165].

3.7.6 Continuum Approaches

Continuum based approaches are the most widely used method used in engineering software for thermal system to fluid dynamics and solid mechanics. The computational domain is discretised into regions that are defined by nodes at which the constitutive laws are solved. The finite element method (FEM) is the most widely used for solid mechanics problems. It is a well-developed and rigorous technique and is flexible enough to deal with a wide variety of common engineering problems including being able to cope with complex geometries, heterogeneous materials and nonlinear behaviour.

One of the first attempts at modelling fracture of WC-Co was performed by Sigl and Schmauder [166], using the 2D FEM software ASKA (Automatic System for Kinematic Analysis), to study the stress of the binder phase. A mesh was created based on the microstructure of a sample subjected to a three point bend test by Sigl and Exner [85], as discussed in Section 3.3.5, see Figure 3-43.

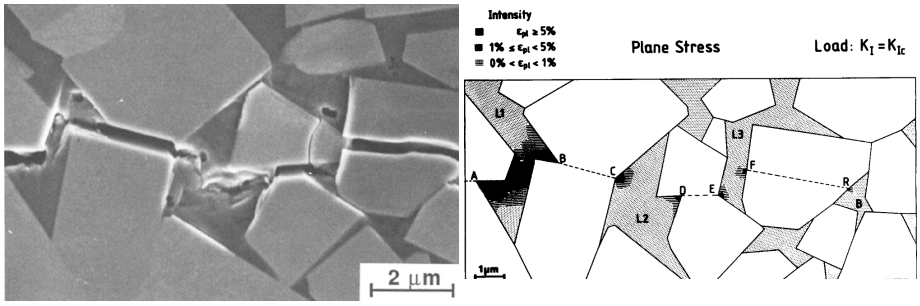

a) **b)**

Figure 3-43: a) Fracture path from WC-10Co sample from three-point bend test and b) results from FEM showing stress distribution in binder region [166].

Simulations were able to show stress is distributed across the binder phase between carbide phases as load was applied. The stress distribution was found to be greatly affected by the geometry of the carbides which acted as stress raisers. This caused greatest stresses closest to fractures in the carbide phases, suggesting that voids will nucleate from this point. Plasticity was restricted to binder directly in the crack plane. This supports previous finding from Sigl and Exner [166] that the plastic zone is on the same order of magnitude as binder mean free path. This model was restricted to small strains, meaning that only the initial stages of ligament formation could be studied. Furthermore, explicit simulation of the fracture could not be performed using this method and so voids along carbide grains which represent

fracture in the WC phase had to be assumed initially in order to study the stresses in the binder phase.

McHugh and Connolly [167] extended this approach to idealised geometries by using Abaqus finite element software with the addition a modified Rice and Tracey [168] damage model which was implemented through the use of a subroutine. This introduced the effect of ductile failure in the Co phase through the use of a damage parameter in order to predict void growth based on the stress and strain of an element. During the simulation finite elements were effectively removed from the domain once a critical value of the damage parameter had been reached, thereby allowing the model to explicitly simulate crack propagation in the binder phase. A model of an idealised multiligament zone (MLZ), which forms in the binder phase in the wake of crack propagation through the ceramic phase, was used to perform a number of parametric studies. The study used an interesting mix of homogeneous and heterogeneous modelling of the WC-Co structure, nevertheless it was able to demonstrate the toughening effect of the binder in WC-Co through a series of crack resistance curves (R-curves). These showed binder ligaments increased fracture toughness by arresting crack propagation.

Dębski and Sadowski [169] compared the Rice and Tracey modelling approach used by McHugh and Connolly with the extended finite element method (XFEM) in Abaqus which used a traction-separation law. The focus of this study was micropores which are created during the manufacturing process and how they lead to void growth. This meant that modelling was restricted to the analysis of the WC/Co interface. The mesh used was based on a very low binder content composition with WC grains surrounded by a thin layer of Co. The two methods approached a qualitative convergence for varying levels of porosity and both indicated a non-linear relationship between porosity and mechanical properties. Although this result was in agreement with other studies no quantifiable validation was presented and the structure modelled could be described as an idealised geometry.

While there has been some research into the fracture of WC-Co, published literature has focused primarily on Co fracture. One of the few times that WC fracture has also been considered is in studying the similar but different field of fracture fatigue. Özden et al. [170, 171] performed FEM simulations using Abaqus and applied

similar formulations to the tensile fracture simulations. Similar to McHugh and Connolly, a subroutine removed elements once a fatigue failure criterion had been met, see Figure 3-44, with separate failure criterion for WC and Co phases. Failure of the brittle WC phase was based on a maximum tensile stress while a non-linear damage law based on the accumulation of plastic strains was used for the cobalt. The model applied this to a real microstructure which was used in an experimental study.

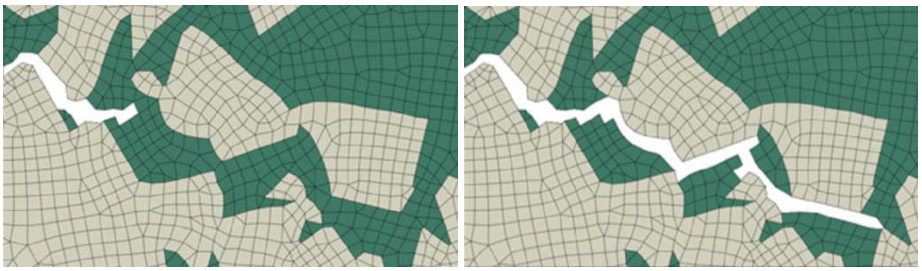

a) b)

Figure 3-44: Evolution of fracture propagation after a) 50 cycles and b) 244 cycles [171].

Interestingly very high tensile strength was used for the carbide phase of 4000 MPa, much higher than that generally expected. This highlights one of the key problems surrounding the modelling of WC-Co behaviour, that of uncertainty in material properties of the constituent phases. This is also an issue for yield stress of the cobalt binder. Values of between 279 MPa [165] to 2180 MPa [172] have been used in literature across a variety of simulations. Despite these uncertainties, Özden et al. obtained good agreement between fracture paths generated experimentally and simulation results, see Figure 3-45. A fairly high binder content of 25 wt.% was used which resulted in fracture propagating primarily through the binder phase with few carbide fractures observed. Similar to the approach used by Sigl and Schmauder [166], this method of validation was able to both give a visual indication of the accuracy of the simulation and aids understanding of fracture propagation.

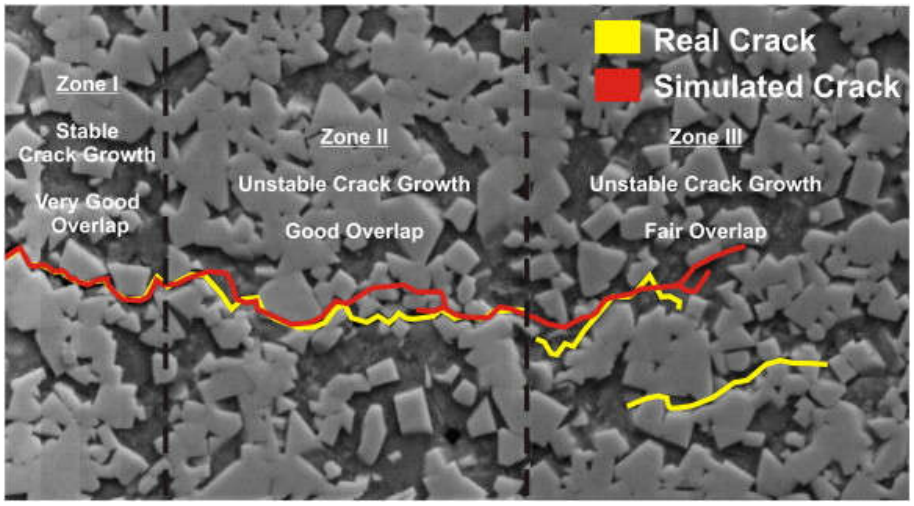

Figure 3-45: Comparison between experimental and simulated fracture paths [171].

3.7.7 Combined Finite-Discrete Element Method

The discrete element method (DEM) was developed to overcome some of the limitations of continuum approaches. The method was first developed by Cundall and Strack [173] using spherical particles and designed for non-cohesive media such as powder and sand. In this approach the domain is composed of individual particles that are assembled to form a geometry. The physics of these individual elements are based on interactions laws. Motion of the particles was described using Newton's second law while contact between elements is represented through a spring-dashpot system. Originally derived for granular applications, this technique is able to capture physics not possible using continuum approaches, such as flow behaviours observed in hoppers including: funnel flow that occurs due to areas of stagnant particles; or bridging cause by agglomeration of particles at the discharge nozzle, see Figure 3-46. However, DEM is computationally more expensive which limits its application to either small length scales or few particles. This makes it generally unsuitable for study of solid materials.

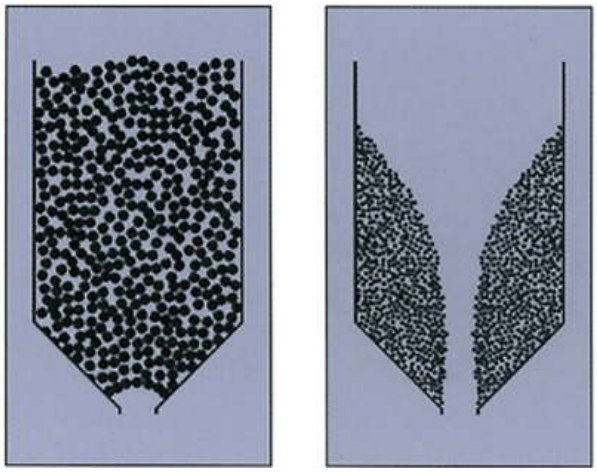

a) b)

Figure 3-46: Flow problems associated with granular material a) bridging and b) funnel flow [174].

More recently, the research software Y-Geo has emerged as a powerful two-dimensional solver that uses a hybrid finite-discrete element method (FDEM) allowing it to model both continuum and discrete element behaviour. This builds on the FEM by adding the ability to simulate particle dynamics through the DEM, leveraging the advantages of each approach. The transition from continua to discontinua enables the software to simulate fractures explicitly without predefining fracture paths. Originally developed by Munjiza [175], Y code was further developed by research groups at Queen Mary University/Imperial College London and University of Toronto. The former collaboration between Munjiza and Latham [176] resulted in the creation of the Virtual Geoscience Workbench (VGW) which focused on developing a 3D DEM solver with coupled CFD. The latter, developed by Mahabadi et al. [177], created Y-Geo which focused on the 2D solver, providing some enhanced capabilities as well as adding a graphical user interface (Y-GUI) to simplify and speed up the set-up of simulations [178]. Y-GUI is then able to export an input file which can be read by an adapted Y code solver. Further information on the pre-processor Y-GUI and associated solver, Y-Geo, are available in papers published by Mahabadi et al. [177, 178], while a detailed description of the algorithms used in Y code can be found in a textbook authored by Munjiza [175]. While combination of two modelling techniques is not unique, CFD-DEM (computational fluid dynamics) has already been incorporated into commercially available software such as STAR-CCM+ and ANSYS Fluent, FDEM codes have remained researched based only. VGW and Y-Geo have primarily focused on geomechanical applications

such as concrete and rock core strength modelling, however similar modelling issues such as simulation of brittle fracture and heterogeneous materials suggest that this numerical method has the potential to yield insightful information on ceramic type material failure.

The Y code mesh consists of linear triangular elements that are created in a standard way using a coordinate matrix which defines nodes and element matrix defined by nodes. Prior to initialisation of the simulation, the software adds in a joint or cohesive element between all elements, see Figure 3-47.

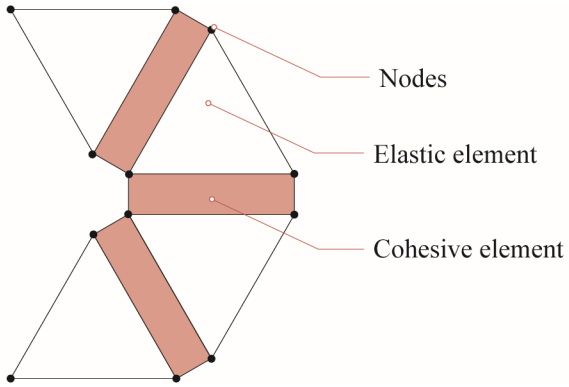

Figure 3-47: A simple model showing mesh structure and element types.

Elastic behaviour is simulated using the FEM approach of constituent laws. All material properties are assumed isotropic and linear elastic. The addition of cohesive elements enables explicit simulation of fracture. This is performed through the removal of cohesive elements once a failure criterion has been met. Once cohesive elements are removed this will alter how stresses are distributed within a domain. However, as there is no adaptive mesh refinement algorithm, meshing of the domain needs to be sufficiently fine at the outset in order to obtain an accurate stress solution around geometric stress raisers and thereby predict fracture behaviour.

The fracture model handles the transition between continua and discontinua. This process is implemented through a cohesive zone model (CZM), a concept first introduced by Barenblatt and Dugdale [31]. To maintain numerical stability as well as computational optimisation, the stress-strain curve is split into two sections, see Figure 3-48. The first section being relatively simple to implement in the standard way through the constitutive law (i.e. stress-strain relation) until element stresses reach a critical stress value, σ_c; the second section is formulated using a stress-displacement relation. This approach is similar to the traction-separation failure

criterion that was implemented in XFEM simulations by Debski and Sadowski and the McHugh and Connolly approaches discussed earlier. The latter, however, used a slightly different approach through a gradual reduction in stress and stiffness based on time steps rather than displacement. Using this framework crack paths are not predefined and fracture initiates through the breaking of cohesive elements whose properties are defined by neighbouring elements. This definition of properties based on neighbouring elements enables Y code to simulate both intergranular and transgranular fracture.

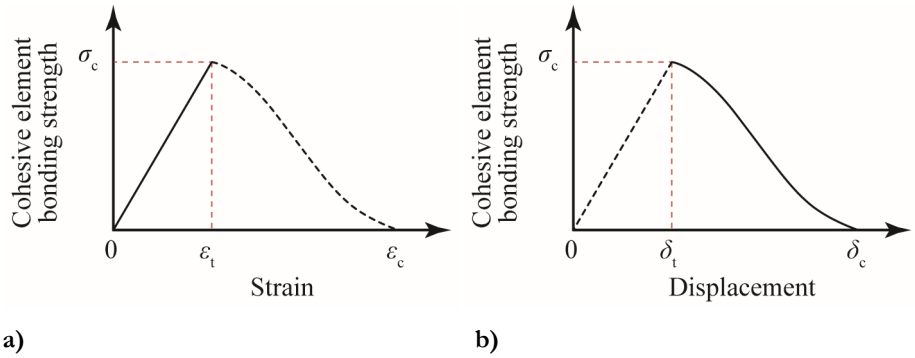

Figure 3-48: Stress-strain relationship until element stress equals tensile stress b) Stress-displacement relationship until element hits critical displacement.

Mahabadi et al. [179] demonstrated Y-Geo's ability to model both macro and micro scale through two case studies on rock material. In the macro case study cliff recession was simulated which was able to reproduce accurate failure mechanisms including interactions along defined discontinuities in the rock and toppling. At the micro scale model simulations for a Brazilian test set up which indirectly measures tensile strength closely matched experimental results. In the latter case material properties of individual phases were applied to elements to create a heterogeneous mesh based on a material map of a real sample. This allowed direct comparison between fracture paths of experimental and simulation results. The model accurately reproduced failure mechanisms observed in experimentation, specifically, tensile fracture along loading axis and shear failure near the loading platens, see Figure 3-49. Fractures were found to propagate in a similar manner along intact grains and along grain boundaries. One of the problems faced with implementing the simulation was use of accurate material properties. Typically these values are given as averaged properties of a bulk material. In order to obtain reliable results for the bulk, material parameters of *in situ* phases are required. Furthermore properties of the interface (tensile and shear strengths) of different phases have been difficult to assess. In the

rock specimen estimated values based on the properties of the individual phases was used.

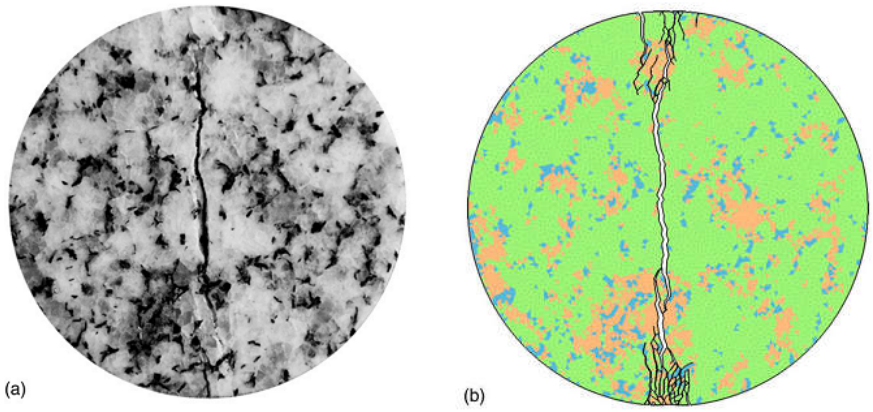

Figure 3-49: Fracture patterns of Brazilian disc a) sample disc from experiment and b) simulation using Y-Geo solver [177].

A similar FDEM method was employed by Kraft et al. [180, 181] to study the compressive and tensile loading of ceramic material aluminium oxide (Al_2O_3). Discretisation of grains allowed simulation of both intergranular and transgranular fracture, see Figure 3-50a. Analysis of the fracture found that fracture toughness of the specimen was affected by the grain boundary distribution with an average difference of 44% between strongest and weakest structures simulated. This seemed to correlate with a difference in percentage of fractures that were transgranular between the two structures, 69.3% cf. 12.6%. As properties for the cohesive elements are the same, this result demonstrates that microstructural effects on the bulk properties can be modelled explicitly.

Kraft et al. also demonstrated the effect that grain morphology has on fracture toughness. Elongated grains were found to increase failure strength, although fracture did not follow the expected fracture path along grain boundaries. When attempting to promote one fracture mode (intergranular) another was initiated instead (transgranular). Instead of the fracture toughness being increased through increasing fracture path tortuosity, the fracture had to penetrate through the Al_2O_3 grains which have a higher fracture toughness compared with grain boundaries. This highlights the importance of trying to obtain a full understanding of microstructural effects and although not the same material, the study shows that FDEM simulations could be useful to studying technical ceramics.

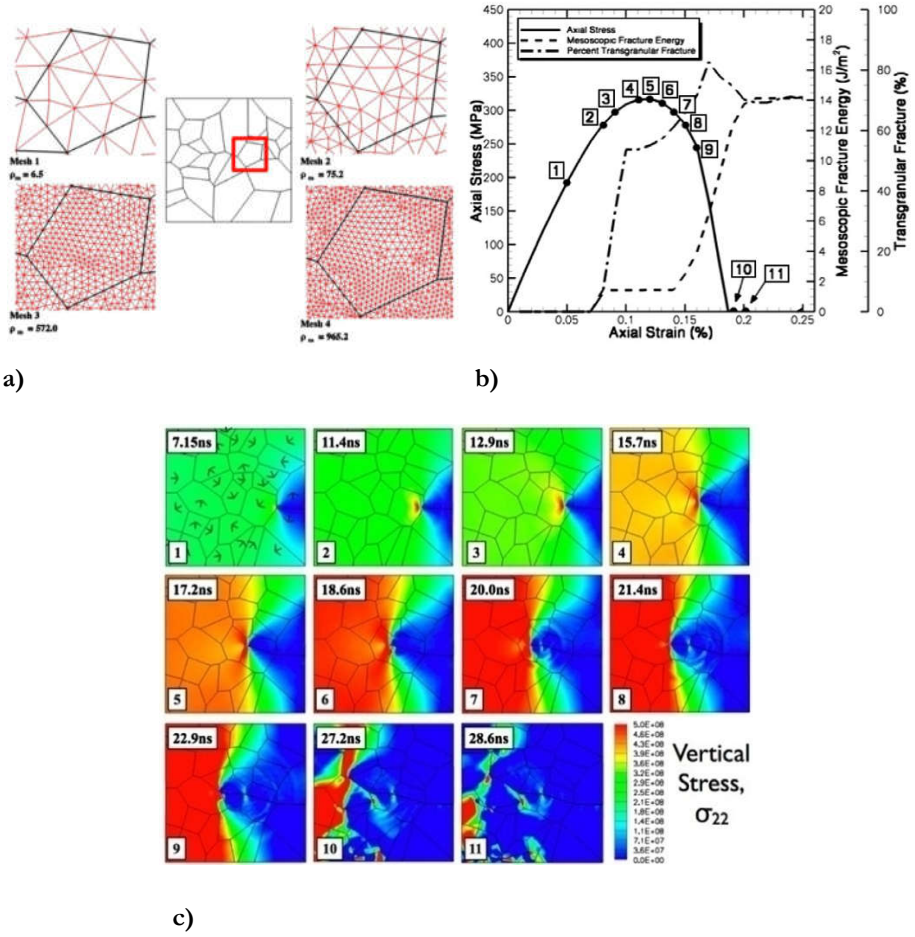

Figure 3-50: Simulation of transgranular fracture of Al_2O_3 a) mesh structure of multi element grains, b) tensile simulation stress-strain response from crack propagation (from right to left) and c) corresponding simulation output for labelled points on curve [180].

3.8 Concluding Remarks and Summary

Cemented tungsten carbide is used in a number of high wear application including oil and gas drilling, due to their high hardness and reasonable fracture toughness which results in high abrasion resistance. Control of manufacturing variables in the sintering process has enabled manipulation of microstructural variables such as grain size and is able to achieve production of an almost flaw free cemented carbide with homogeneous distribution of carbide and binder phases. There has been extensive research into the wear mechanisms of these composite materials, which identified two important factors that affect the wear performance: the composition and the microstructure. These define not only the bulk properties but also the degradation mechanism which dominates. A summary of these wear mechanisms is provided in Table 3-3.

Table 3-3: Summary of principle mechanical wear processes for WC-Co

W1	Binder depletion through extrusion or cutting
W2	Build-up of plastic strain in WC grains, observed as slip planes
W3	Fracture and spalling of carbides
W4	Pull out of carbide grains
W5	Creation of tribolayer composed of wear particles

Not only is the binder vulnerable to mechanical wear, the most commonly used binder material, cobalt, also has weak corrosion resistance. This results in preferential dissolution of the binder which will reduce the ability of the surface to distribute stresses resulting in reduced fracture toughness. Furthermore, evidence of crevice corrosion suggests microenvironments can form on the surface, significantly altering the chemical solution. A summary of the corrosion mechanisms is provided in Table 3-4.

Table 3-4: Summary of principle corrosion processes for WC-Co

C1	Preferential corrosion of binder phase
C2	Formation of weak oxides
C3	Crevice/pitting corrosion behaviour

Tribocorrosion systems add further complexity through addition of many more variables. This means that materials optimised for one degradation mechanism, may not be optimum in one exposed to both processes, for example selection of an optimal binder material. Nickel may be more appropriate in static corrosion experiments, but its poor performance in tribocorrosive environments can be attributed to either its passive layer being no longer effective, or its intrinsic material properties being inferior. Understanding of these interactions is therefore important to selection and development of suitable materials.

Synergy has been commonly used to describe the effects of combined mechanical and corrosive wear mechanisms. This approach has been used as a foundation for experimental tribocorrosion experiments on many WC based systems. However, synergistic quantification can be unreliable where wear-corrosion interactions are

small. The addition of multiple mechanisms compounds uncertainties from other more commonly studied variable such as surface finish and geometric changes, leading to a high degree of error in predicted performance. Furthermore, it is not evident that using the synergy approach in a mathematical model will provide further insight to wear processes. This suggests that it is important to focus on the possible mechanical and corrosion interaction and subsequent degradation mechanism that underpin these synergistic effects, a summary of which is presented in Table 3-5.

One way to address these uncertainties and quantify these variable is through numerical modelling. This approach changes the focus from global wear measurements to studying isolated behaviours and bringing them together under a common platform. By building models from the ground up it is possible that by simulating individual interactions accurately, it could be possible to simulate synergy effects explicitly. Modelling the effects of degradation, such as the changing material properties or the dissolution of the binder phase, would result in changing how forces are distributed. This would alter the dominant wear mechanisms that is simulated, such as moving from WC grain fracture to plucking of WC grains. However, the accuracy of models are dependent on fundamental the understanding of material properties and behaviours which are established through experimental work.

Table 3-5: Mechanical and corrosion interactions for WC-Co mapped to existing tribocorrosion synergy model (Equation (3.28))

Synergistic mechanisms	Abrasion assisted corrosion (ΔV_C)	• Fracture initiated by mechanical interaction leading to increased crevice corrosion. • Mechanical removal of oxide layer. • Creation of tribolayers which enable microenvironments on the surface resulting in increased crevice corrosion.
	Corrosion assisted abrasion (ΔV_A)	• Preferential corrosion of binder leading to unsupported WC grains and increased pull out. • Creation of stress raisers leading to increased fracture initiation and propagation.
Antagonistic mechanisms	Abrasion inhibited corrosion ($-\Delta V_C$)	• Re-embeddment of wear fragments in the surface which will prevent corrosive solution attacking surface of bulk material. • Creation of additional rock layers which protect bulk material from corrosive attack.
	Corrosion inhibited abrasion ($-\Delta V_A$)	• Creation of oxide layer which acts as a solid lubricant and results in reduced mechanical wear. • Dissolution of binder leads to loosening of WC grains which can increase surface compliance and reduces point stresses, therefore reducing mechanical wear.

This project will look to explore three key areas which have been identified as weaknesses in the present open literature. By studying both numerical modelling and experimental methods it is hoped that this project can help to bridge the gap between these two fields. The main objectives aspects of this project can be summaries in Table 3-6.

Table 3-6: Objectives of project

Section	Problem identified in literature review	Objective of project
3.7	Numerical modelling approaches are currently unable to simulate fracture accurately enough to predict material loss of brittle materials, a critical mechanism in the degradation of WC-Co.	Demonstrate the ability of FDEM to simulate the fracture mechanisms of WC-Co as described by experimental studies discussed in Section 3.3.5.
3.6	There are a number of conflicting results and conclusions on the corrosion behaviour of WC-Co in acidic and alkaline solutions.	Conduct electrochemical analysis of commercially available WC-Co sample discussed in Section 3.6.5 and understand the subsequent physical effects on the microstructure using SEM and EDX analysis.
3.5	The current approach to studying tribocorrosion relies on abrasion and scratch testing, which is unable to provide useful input to a numerical model.	Investigate the influence of acidic and alkaline conditions on the material properties (hardness and Young's modulus) and fracture behaviour (fracture toughness and geometry) of WC-Co using nanoindentation as well as the Palmqvist Method discussed in Section 3.3.4 and analysis techniques discussed in Section 3.3.5.

Chapter 4 – Simulation Methodology

Chapter Highlights

In this chapter a numerical modelling methodology is proposed which can overcome the limitations of the synergy approach (Section 3.7.1). The modelling process used in this project is explained, including mesh generation and modelling parameters.

- Modelling at the mesoscale allows individual material properties and microstructure to be defined explicitally rather than using fitting parameters.
- A series of smaller validation steps are taken before a mesoscale fracture simulation is performed.
- Dynamic simulation and fracture add additional complexity through additional modelling parameters, which are not required in static simulations.

4.1 Objectives

The literature review highlighted that while understanding of the principle wear mechanisms of WC-Co is well established through experimental studies, modelling is currently unable to simulate the underlying physical processes and no rigorous tribocorrosion models were found in the open literature. Current modelling approaches tend to be based on the synergy approach or empirical methods discussed in Section 3.7. This breaks down wear into its constituent parts:

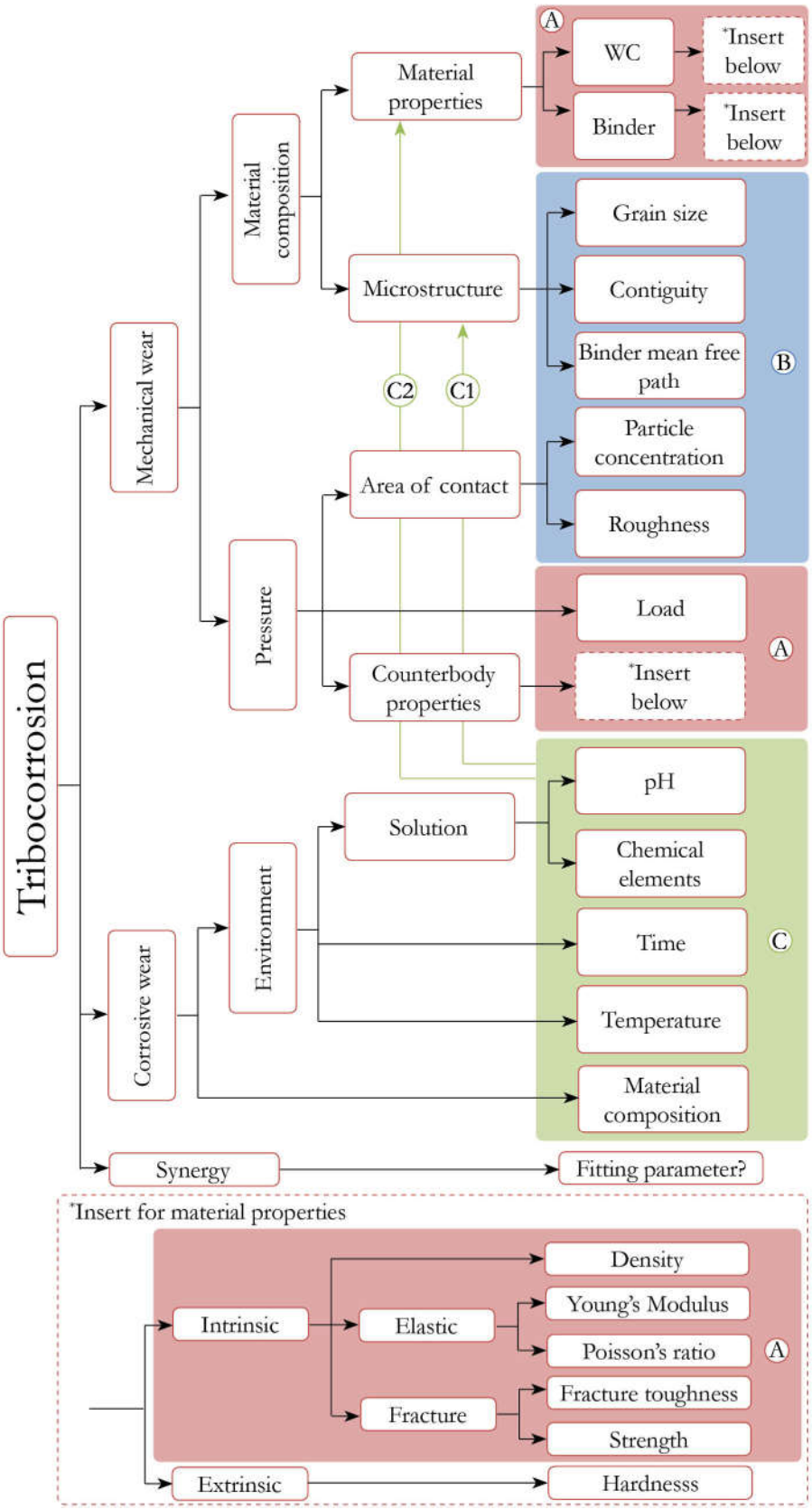

Figure 4-1: Breakdown of tribocorrosion into constituent parts. A: Modelling inputs B: modelled explicitly C: Integrated through modification of microstructure (C1) and material properties (C2).

- mechanical wear,
- corrosive wear and
- synergy or antagonism (mechanically accelerated corrosion and/or corrosion accelerated wear).

Extension of this approach then breaks these constituent wear mechanisms down further by establishing relationships between material or environmental parameters and wear rate, for example between hardness and mechanical wear rate. This method is visualised in Figure 4-1.

One of the major difficulties with the synergy approach is the number of variables which affect the wear rate, listed on the right hand side of Figure 4-1. Trying to find a relationship between mechanical wear and an individual variable such as binder mean free path can itself be difficult. The addition of over 20 other variable therefore makes relationship almost impossible to establish and validate. Furthermore, synergy effects do not appear to be constant, nor has any empirical relationship been established between synergy and another variable. This suggests a new approach to the tribocorrosion of WC-Co is required which brings us to the use of numerical modelling methods.

The chosen numerical method should be capable of simulating the wear processes summarised in Table 3-3 and corrosion processes summarised in Table 3-4. By studying these interactions, it is thought that the tribocorrosion synergistic and antagonistic mechanisms, summarised in Table 3-5, can be simulated directly without fitting parameters or other experimental specific data. In order to create a rigorous model it is important that the primary interactions are simulated accurately. With the number of complex interactions involved in a tribocorrosion contact discussed in the literature review, attempting to create a numerical model incorporating all of them is not currently possible. Not only are the necessary building blocks not in place for a tribocorrosion model, they are also not in place for a dry contact wear model for WC-Co. What does seem to be established is modelling using FEM. As discussed in Section 3.7.5, numerous studies have managed to demonstrate elastic response of the bulk material through using separate WC and Co elements and combining them in a domain. FEM is capable of simulating wear processes W2 (build-up of plastic strain in WC grains, observed as slip planes) and to some extent W1 (binder depletion through extrusion or cutting)

described in Table 3-3, in which linear and non-linear stress-strain behaviour is the dominant physics. The challenge is therefore to bridge the gap between this work and a dry contact wear model. One of the challenges in modelling WC-Co is not having the appropriate numerical method to capture the brittle fracture behaviour, a major driver for degradation as discussed in Section 3.4. While fracture models of WC-Co models have been presented in the literature, they are currently not robust enough to capture fracture behaviour fully. With many studies using hypothetical and idealised geometries it is difficult to validate results against experimental data.

Selection of the right scale is important. By maximising the number of explicitly modelled parameters this can reduce the number of empirical variables for which relationships need to be established. The mesoscale, whereby individual phases and microstructure is modelled, is seen as a good compromise between computational intensity and being focused on material defined properties rather than empirical variables. This would mean that variables highlighted as B in Figure 4-1 would be explicitly modelled, requiring no empirical relationship to be established. Modelling inputs would be reduced down to intrinsic material properties, highlighted as A in Figure 4-1. In comparison, at the macroscale there is not sufficient resolution for microstructural variables such as WC grain size and binder mean free to be modelled explicitly, therefore still requiring empirical data. The mesoscale is also a scale at which both numerical modelling and experimental fields overlap. This enables simulations results to be validated directly against experimental results.

Accurate simulation of fracture behaviour during tensile loading is therefore going to be the focus of simulation work in this project. This will be similar in approach to that use by Özden et al. [170, 171] for simulating fracture fatigue discussed in Section 3.7.6. The modelling will concentrate on intrinsic material properties and microstructure, drawing on literature from Sections 3.1, 3.2 and 3.3 that is able to describe the material physics rather than use of empirical relationships. Looking at the mechanical wear processes this work is especially significant to W3 (fracture and spalling of carbides) and W4 (pull out of carbide grains) wear mechanisms described in Table 3-3.

This path towards a tribocorrosion model can be visualised as key milestones shown in Figure 4-2. Although the current work focuses on fracture behaviour, the platform could accommodate the other mechanical and corrosion aspects seen in

tribocorrosion degradation of WC-Co. Corrosion effects, highlights as C in Figure 4-1, can be integrated through changing the microstructural or material properties of the model. Experimental techniques which could help inform this process are explored in Chapters 8, 9 and 10. Chapter 9 focuses on microstructural effects while Chapter 10 focuses on mechanical effects, C1 and C2 respectively in Figure 4-1.

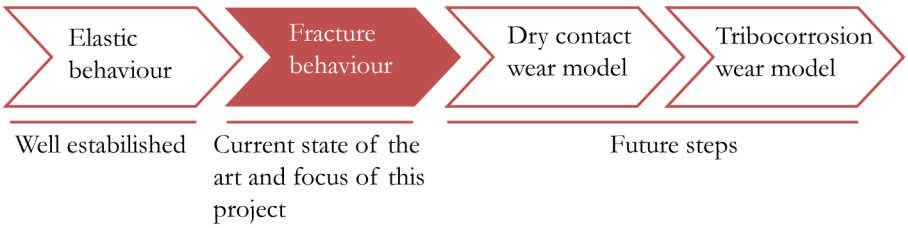

Figure 4-2: Major milestones on road to a tribocorrosion model.

4.2 Modelling Plan

In order to build up to a full mesoscale fracture simulation of WC-Co, a series of smaller steps are taken in order to validate each part of the model, see Figure 4-3. Firstly, in Chapter 5, domains consisting of only one set of material properties is studied. This is validated against an analytical solution for stress concentration. In Chapter 6, domains consisting of both ceramic and binder material are simulated. This is validated against both an elastic analytical solution and the rule of mixtures. Finally, in Chapter 7, a mesoscale fracture simulation is performed and validated against experimental results.

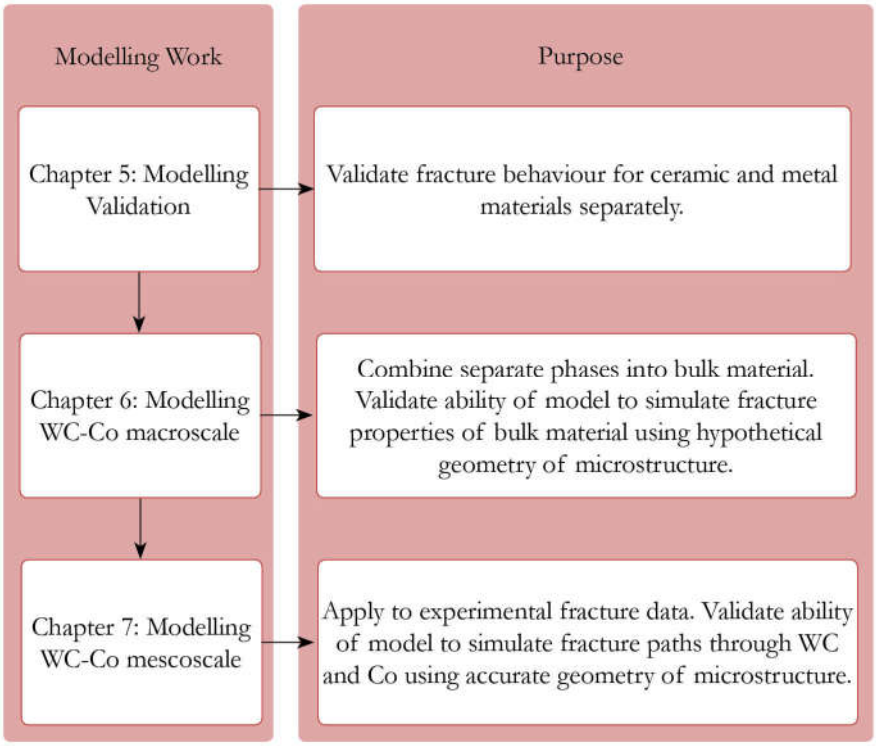

Figure 4-3: Steps required to build up to mesoscale fracture model of WC-Co.

The research software Y-Geo [178], introduced in Section 3.7.7, was chosen due to its ability to explicitly model fracture and assign properties to individual elements. In previous publications the use of this code has been focused on geomechanical and concrete applications. These brittle materials share some key physics to ceramic based material and so this project will look to expand the use of this software to WC-Co material.

Y-GUI v2.8.5 and associated Y-Geo solver have been used for all simulations and are publically available [178]. The original open source C++ code that Y-Geo was based on, Y-code, created by Munjiza, is also publically available for download [175].

One of the limitations of the Y-GUI is that does not include a well-developed mesh generation package, therefore Abaqus is the primary method used to generate meshes. The node and element matrices that are created by Abaqus can then be imported into the Y-GUI software. Assignment of material properties, boundary/initial conditions and simulation parameters is performed in the Y-GUI environment. A summary of the modelling process is shown in Figure 4-4.

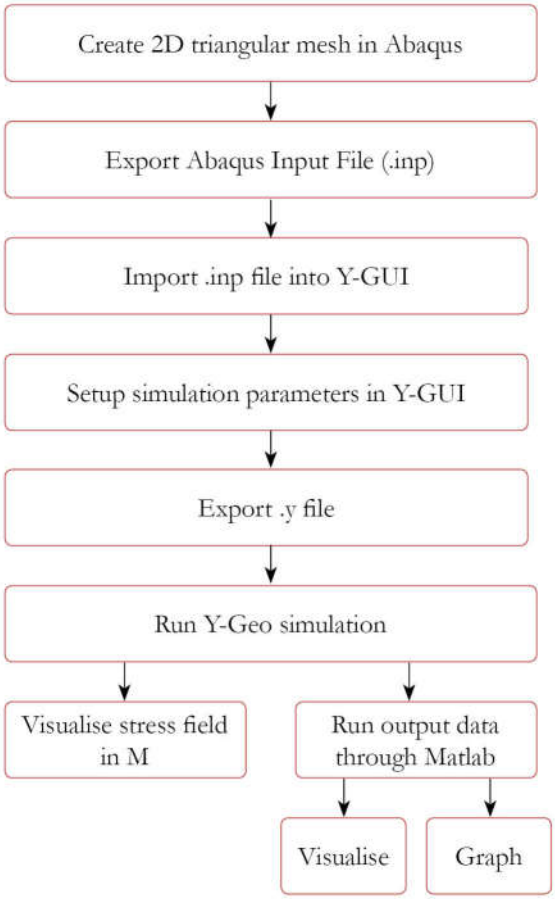

Figure 4-4: Modelling process summary. Dashed lines indicating optional steps in process.

4.2.1 Y-GUI and .y File

The .y file is a text file and is the input for Y-Geo, which reads in the data to run the simulation. This can be coded manually or created through the Y-GUI interface, see Figure 4-5. The Y-GUI interface makes setting up complex models simpler and quicker compared to writing of the .y file directly. This is further aided through the visualisation of the model which helps to reduce errors in set up. Y-GUI is also able to import meshes by reading Abaqus input files (.inp), making it easier to model complex geometries. Y-GUI extracts the node and element matrices from the .inp file, reformatting it into a readable .y format.

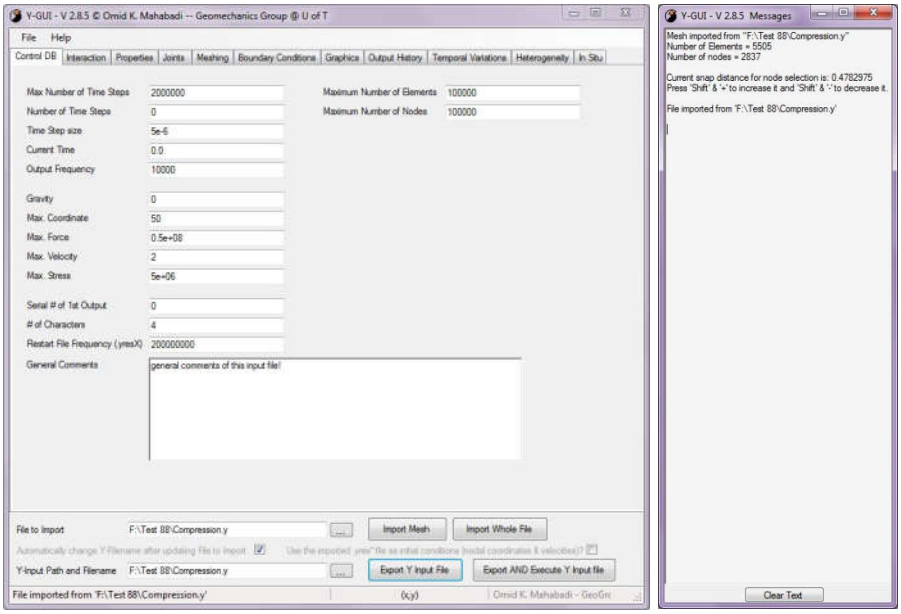

a) **b)**

Figure 4-5: Y-GUI interface a) main window and b) message window.

User simulation inputs is performed through a series of tabs that split up the modelling databases, those being: simulation parameters, material properties, initial and boundary condition and output history points. Y-Geo does not require the specification of units, therefore input values can take the form of any consistent set of units, with output history in corresponding units. Once set up is complete Y-GUI is able to automatically generate the .y file, see Figure 4-6. Sections within the .y file correspond to the tabs in Y-GUI and are marked accordingly.

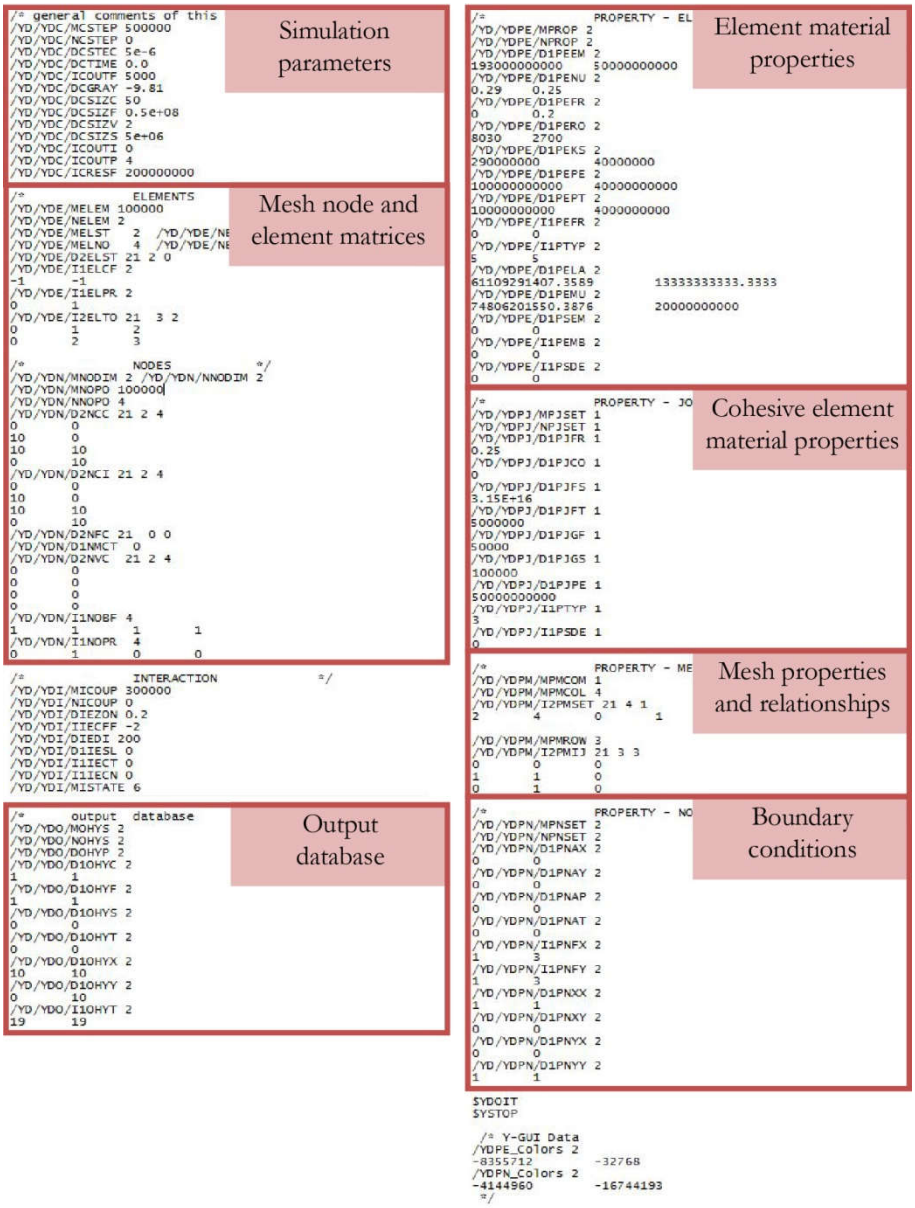

Figure 4-6: Example of .y input file for a simple simulation.

Although Y-GUI is able to generate .y files much faster than manually typing it does have some limitations. For this reason it was sometimes necessary to modify the .y file manually, for example to combine meshes from multiple objects. It was also sometimes quicker to create sections of the code outside of Y-GUI. Output data, such as the force at each node, needs to be defined prior to simulation. As the exact coordinate for each node has to be manually entered this is time consuming for multi element features. A Matlab script was therefore written which could generate this section of code using mesh data from the Abaqus .inp file.

4.2.2 Simulation Parameters

Dynamic modelling brings about a number of numerical complications, for example due to the number of variables regarding element positions, orientations and vectors, implicit time integration would be almost impossible to implement. Instead, Y-Geo uses an explicit time integration scheme. This causes the solution be become conditionally stable and requires small enough time steps to be taken in order to achieve stability. This restricts the mesh density as finer meshes would significantly increase computation time.

Y-Geo solves problems through dynamic simulation which creates stress oscillations and reflections. This can lead to inaccurate solutions for static and quasi-static problems. In order to reduce these dynamic effects a dynamic relaxation is used on the elements called viscous damping. Time step size is also dependent on the viscous damping. For higher values of damping the time step size needs to be decreased in order for numerical stability to be achieved. A compromise therefore needs to be made between viscous damping and time for simulation for solve. Using critical damping ensures stress reflections and oscillations are minimised while also maximising the time step size. Munjiza [175] found the critical viscous damping, ζ_c, for elements to be:

$$\zeta_c = 2h_e\sqrt{E\rho} \tag{4.1}$$

Where h_e is the element size. Elements smaller than h_e will be critically damped. As discussed in Section 3.7.7, FDEM simulates fractures through the use of cohesive elements which are removed once they meet a failure criterion. This is defined through displacement, δ_c, as:

$$\delta_c = \max\begin{cases} 2\delta_t \\ 3\dfrac{G_{IC}}{\sigma_c} \end{cases} \tag{4.2}$$

δ_t is the critical yield displacement defined by the critical stress criteria, σ_c, and through the use of a fracture penalty term, p_f, which defines how stresses are distributed in an element:

$$\delta_t = \frac{2h_e\sigma_c}{p_f} \tag{4.3}$$

When $\delta_t < \delta < \delta_c$ a strain softening function is used which is defined through the bonding stress between elements, σ_b, defined as:

$$\sigma_b = z\sigma_t \tag{4.4}$$

Where z is a scaling function defined:

$$z = \left[1 - \frac{a_9 + a_{10} - 1}{a_9 + a_{10}} \exp\left(D \frac{a_9 + a_{11}a_9}{(a_9 + a_{10})(1 - a_9 - a_{10})}\right)\right] \times \left[a_9 (1 - D) + a_{10} (1 - D)^{a_{11}}\right] \tag{4.5}$$

Where a_7, a_8 and a_9 are constants and D is the normalised displacement defined:

$$D = \frac{\delta - \delta_t}{\delta_c - \delta_t} \tag{4.6}$$

This results in strain softening curve as seen in Figure 3-48b which is similar to that seen in experimental fracture of WC-Co as shown in Figure 3-10.

Once elements become discrete elements interaction between them is modelled using a contact detection algorithm. This is implemented using the Mujiza-NBS (no binary search) linear contact detection algorithm. Contact penalty functions used to define allowable overlap or penetration between elements. The amount of overlap or penetration permissible is dictated by the contact penalty, p_c. The smaller the overlap desired the higher the contact penalty, therefore as overlap $\rightarrow 0$, contact penalty $\rightarrow \infty$. The resulting contact force is also dictated by the amount of overlap between the elements. Although minimal overlap is desired this comes at a computational cost, requiring smaller time steps to pick up the smaller penetration. For linear elastic material the change in length of an element, ΔL, is described through Hooke's law and can be written as:

$$\Delta L = \varepsilon h_e = \frac{\sigma h_e}{E} \tag{4.7}$$

Similarly the allowable element penetration, d_a, of two elements is given by:

$$\delta_a = \frac{\sigma h_e}{p_c} \tag{4.8}$$

Therefore p_c can be expressed in terms of E for a given material. By using this method numerical error of the displacement can be controlled. A summary of the

terms and how values are calculated are provided in Table 4-1. These values were validated by Tatone and Grasselli [182] and will be used in all simulations.

Table 4-1: DEM property values

Parameter	Values used
Viscous Damping	$2h_e\sqrt{E\rho}$
Contact Penalty	E
Tangential Penalty	$10E$

The plane strain assumption is used in all simulations in this project. This presumes that strains perpendicular to the plate are constrained by neighbouring material and are relatively small compared to other strains, therefore causing a triaxial stress state near the crack tip. This appears reasonable given that a rigid carbide skeleton structure as described by Dawihl, see Section 3.1.5, would be surrounding any domain of interest.

4.2.3 Y-Geo Output

The Y-Geo solver creates a number of output files when run, a summary is provided in Table 4-2.

Table 4-2: Y-Geo files created during simulations

File extension	Description
.y#	Data from output history for each time step in the form of text file. Outputs collected for the simulations were stress (xx, yy) and force (x, y). The data type and coordinate have to be defined in the model setup. For each output point specified file generated will be .y0, .y1, .y2 etc.
.ym	For geometry outputs which are produced from each defined in the simulation parameters which can be visualised in using an associated OpenGL executable which has been written for Y-Geo.
.yhSFK	List of elements which have yielded in the form of text file including mode type, time of failure and coordinates of element
.yhBRK	List of elements which have fractured in the form of text file including mode type, time of failure and coordinates of the element.

4.2.4 Matlab Post Processing

Post processing of .y#, yhSFK and .yhBRK files is done through Matlab. This was required for two reasons. Firstly it enabled more useable matrices to be created by reducing their size or reformatting the data so that it could be analysed. This is required as any change of value at an output point is recorded. With the small time steps required for numerical stability of the dynamic simulation, this can result in very large matrices being written. Secondly, Matlab is also able to visualise data through input of coordinate and mesh data. This expanded the analysis that can be performed on simulations compared to the .ym files alone. Further details of this process is discussed in Section 6.4.5.

Chapter 5 – Modelling Validation

Chapter Highlights

A series of simple simulations were conducted in the FDEM software to look at the most basic fracture interactions, which are limited to domains of a single set of material properties. This chapter demonstrates how fracture is modelled in FDEM and how various parameters affect the results.

- By changing elastic and fracture properties, stress-strain response can simulate either brittle materials (ceramics) or ductile materials (metals).
- The mesh has a significant effect on the simulated fracture behaviour and path.
- Simulation of stress concentration effects caused by geometry accurately replicates the analytic solution.

5.1 Modelling Objectives

Validation of computational models is a critical step in assessing the accuracy of simulation solutions. Before more complex models are created a series of simple simulations are conducted on domains of a single material property to obtain an understanding of how fracture is simulated in Y-Geo and the effects of modelling parameters. Results can be compared quantitatively to assess solution convergence

and also against analytical solutions where appropriate. These modelling parameters will be explored in isolation with a view to bringing this understanding together to analyse the fracture of WC-Co material in later chapters. Furthermore, to be able to model at the mesoscale properties of brittle and ductile materials need to be modelled separately, rather than treating the domain as a homogeneous structure. However, as modelling parameters are the focus of this part of the project results are normalised to demonstrate that behaviour would be the same regardless of material values chosen. Any set of consistent units can therefore be assumed, for example kg/m/s/N/Pa or g/mm/s/μN/Pa.

5.2 Simple Fracture

Fracture simulation is a critical element in this study. Although transition from continua to discontinue is not a unique feature to Y-GUI, the way in which this transition is dealt with is important to understand. In order to explore this an initial study was completed to by simulating the most basic interaction between two triangular elements joined with a cohesive element along one edge, see Figure 5-1. The bottom node boundary condition is fixed ($v_y = 0$), a tensile force is created by applying a velocity in the y-axis ($v_y = 0.2$) to the top node and the middle nodes have force in y-axis set to zero ($f_y = 0$). In order to prevent movement in the y-axis, all nodes have horizontal velocity fixed ($v_x = 0$).

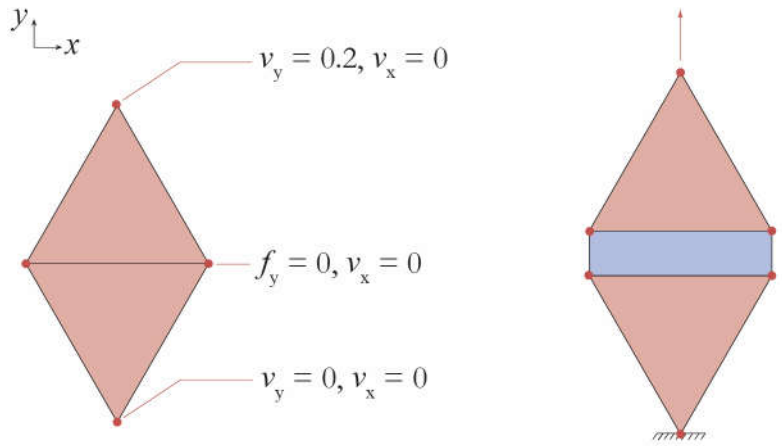

Figure 5-1: Fracture validation test of cohesive element a) Mesh input and boundary conditions and b) mesh during simulation with cohesive element generated.

Two material properties are tested, designated material A and material B. Although properties selected would be indicative of WC and binder properties respectively, at

this stage the focus is on simulation behaviour rather than the values themselves. With element size h_e = 20 (unit length), viscous damping, contact and tangential penalty can be calculated from equations in Table 4-1.

Properties of the cohesive element, which represent fracture properties, are slightly harder to define. Typically experimental studies of WC-Co measure fracture of the bulk material rather than the individual phases. This is problematic using the approach taken as each phase is defined separately. The following manipulation of the fracture parameters discussed in Section 4.2.2 is therefore required in order to solve this problem.

If an appropriate value of p_f is chosen, the value of δ_c will default to the second condition in Equation (4.2). To apply a critical strain value to the cohesive elements, the equation needs to be rearranged to incorporate this term. From the definition of strain, displacement of a single element at fracture can be described as:

$$\delta_c = \varepsilon_c h_e \tag{5.1}$$

Where ε_c is critical strain. Substitution into the second conditions of Equation (4.2) yields:

$$G_{IC} = \frac{\varepsilon_c h_e \sigma_c}{3} \tag{5.2}$$

In order apply the material's ε_c Equation (5.2) is used to calculate G_{IC}. When creating a mesh, often mesh density is varied across the domain in order to achieve good resolution in critical areas of the geometry while minimising computation time. In this case however, as fracture is a function of h_e, without over complicating element properties element size will need to be equal over the whole domain. As viscous damping is also a function of element size, Table 4-1, this approach also allows a single value to be defined for each material property. By using this definition it is possible to use critical strain values obtained from experimental studies of pure materials.

Fracture penalty from Equation (4.3) must also be defined. By rearranging this equation in terms of p_f we get:

$$p_f = \frac{2 h_e \sigma_c}{\delta_t} \tag{5.3}$$

From substitution of δ_t using same form as Equation (5.1) and definition of Hooke's law given in Equation (4.7), p_f can be defined in terms of E:

$$p_f = 2E \tag{5.4}$$

This allows the element properties to be defined from the terms shown in Table 5-1. These cover the material properties required from the insert shown in Figure 4-1.

Table 5-1: Material properties

Property	Material A	Material B
Young's Modulus	E_1	½ E_1
Density	ρ	½ ρ
Poisson's ratio	0	0
Tensile Strength	σ_c	½ σ_c
Critical strain	ε_c	5 ε_c
Fracture Penalty	$2E_1$	E_1

Results from the simulation of the two materials are compared to the manual calculation using the equations discussed in Section 4.2.2, see Figure 5-2. Although strain softening is modelled using a stress-displacement relationship for numerical stability, in order to make comparison easier this is converted to an equivalent stress-strain relationship.

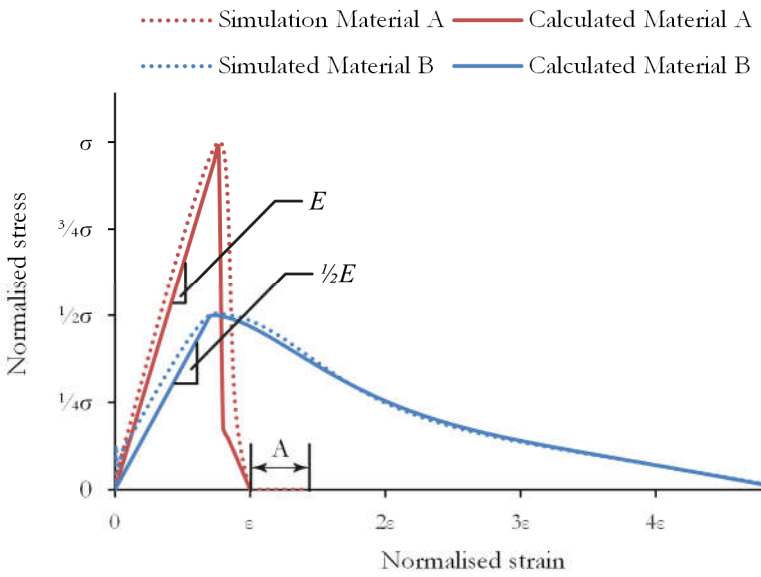

Figure 5-2: Tensile simulation comparing behaviour of Material A and B with calculated behaviour.

We can see there is a slight deviation between simulation results and the manual calculations for the stress-strain relationship. This is likely due to relaxation in the dynamic model required for numerical stability. Despite this, the critical points along the stress-strain relationship are the same, principally: maximum stress, the stress-strain relationship to maximum stress, and maximum strain prior to cohesive element breaking.

The different shape of the two curves indicates the differing behaviour between the two materials. The gradient of the curves prior to maximum stress indicate the Young's modulus with material B being half of that of material A. The tensile strength meanwhile affects when the transition to strain softening occurs, with material A requiring twice the stress compared to material B. Finally, fracture energy defines how large the strain softening section of the curve is, with material B requiring five times higher strain than material A before the cohesive element is broken. Finally, viscous damping, Equation (4.1), of the element prevents stress oscillations in the element throughout the loading cycle, as well as post fracture as indicated by A and B on Figure 5-2.

5.3 Mesh Density

Mesh density is an important factor to consider in modelling as a balance between accuracy and computational cost has to be made. The first condition that has to be

met is accurate modelling of the geometry. For more complex geometries a higher mesh density is required to accurately represent edges and surfaces. The second condition is that there is sufficient concentration of elements to approximate the continuous function, in this case stress distribution in the domain. A third condition that is specific to the FDEM simulations is ability to represent and simulate fracture accurately. Since fracture is generated through the breakage of cohesive elements that are only present between triangular elements, without adaptive mesh refinement this imposes a natural constraint on the simulation as a result of the initial mesh geometry.

In this simulation a comparison between the fracture behaviour of six simulations with various mesh densities is performed. Two triangular elements are used to compress a square object which is allowed to fracture. The number of elements which represent the square varies between 8 and 8192 elements, see Figure 5-3. The simulation parameters, geometries and material properties for all simulations are identical, although viscous damping and fracture toughness are adjusted accordingly for mesh density defined by Equation (5.2) and Table 4-1. An arbitrary boundary condition velocity is set at the loading element nodes in order to induce a compressive load on the square object until fracture is achieved. The effect of changing the compression velocity is discussed later in Section 6.4.3, at this point only the mesh parameters are considered.

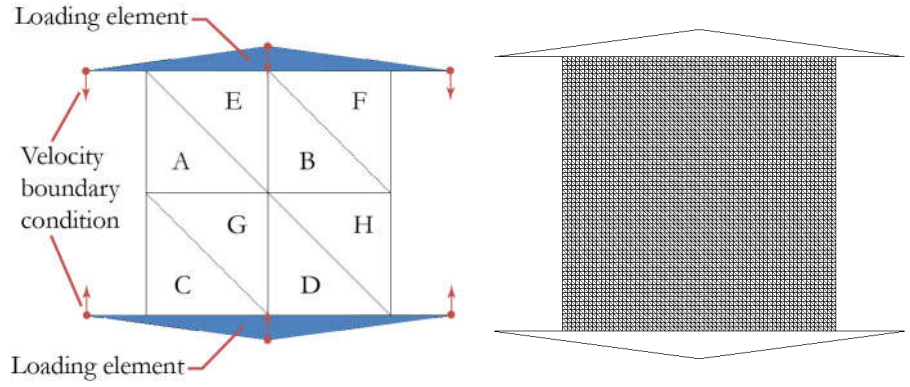

Figure 5-3: Comparison between coarsest and finest meshes simulated a) labelled regions of an 8 element mesh and b) 8192 element mesh.

In the first instance material A properties (representative of a brittle material) from the simple fracture simulation in the previous section were used. Comparing the loading response shows slightly differing behaviour of the six simulations, see Figure 5-4. Initial load-strain response is similar for all mesh densities except for the coarsest

mesh used. This would be expected given that elastic properties are the same in all scenarios. The coarsest mesh has too few elements to accurately resolve stresses in the domain resulting in the different behaviour. A slight oscillation in the load response can be observed, primarily in the coarsest mesh, but also in the finest mesh. Although viscous damping is adjusted for mesh density this result suggests it is more difficult to control for very coarse or very fine meshes.

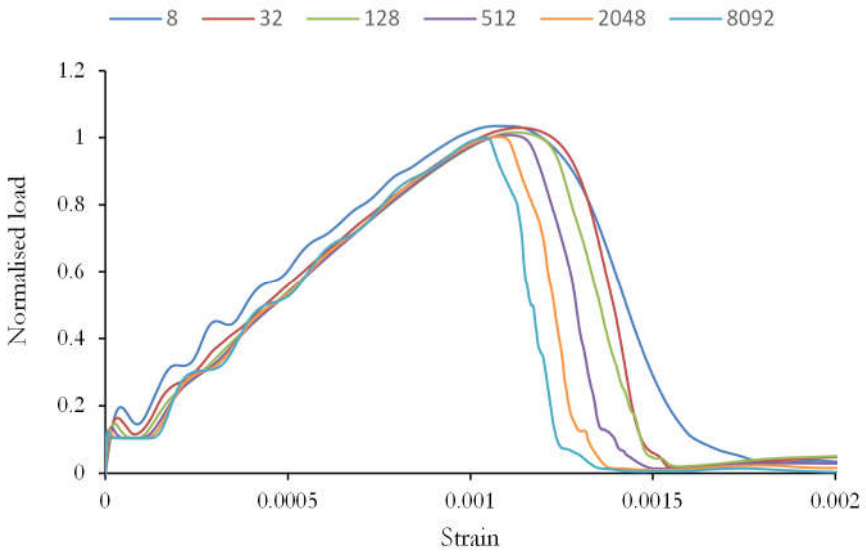

Figure 5-4: Comparison of load response between varying mesh densities for material A. Force normalised by converged maximum force at highest mesh density.

Despite load-strain behaviour being similar, maximum load is slightly different in each with coarsest mesh giving a 3.5% higher load compared to the finest mesh. As the mesh is refined maximum load converges on the load from the finest mesh as shown in Figure 5-5. A similar convergence was also observed for material B properties with highest load 2.4% higher. As elastic response is the same this effectively delays fracture initiation until a higher strain is applied. Load response during fracture (after maximum load is achieved) also appears similar for all the mesh densities once the differing strain rates at onset of fracture is accounted for.

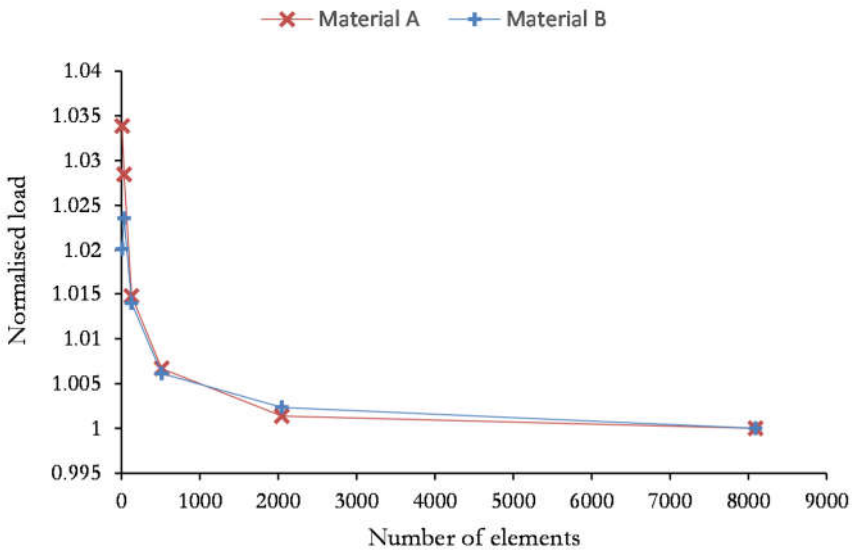

Figure 5-5: Convergence of maximum load for material A and B, normalised by converged values at highest mesh density.

As this is a dynamic simulation it is possible to analyse how fracture propagates in each of the simulations. The sequence of images in Figure 5-6 illustrates how stress distribution and fracture evolve over the duration of the simulation. They also help explain why the maximum measured load is different for each mesh density.

Generally, there is similar behaviour between all meshes simulated. Compressive stresses build up in the domain until shear fracture is initiated at the top left and bottom right hand corners which propagates toward the centre until a continuous fracture is created along regions A-E and D-H (designated on Figure 5-3). Once this fracture splits the domain into two, compressive stress is initially relieved as elements can be displaced. Upon further compression the two halves can no longer be displaced and stresses build up in opposing corners, elements C and F. Once enough stress has built up fracture is initiated in corner elements. Whereas the fracture location for the initial fracture is the same, the location of the secondary fractures depends on location of cohesive elements in region C-G and B-F.

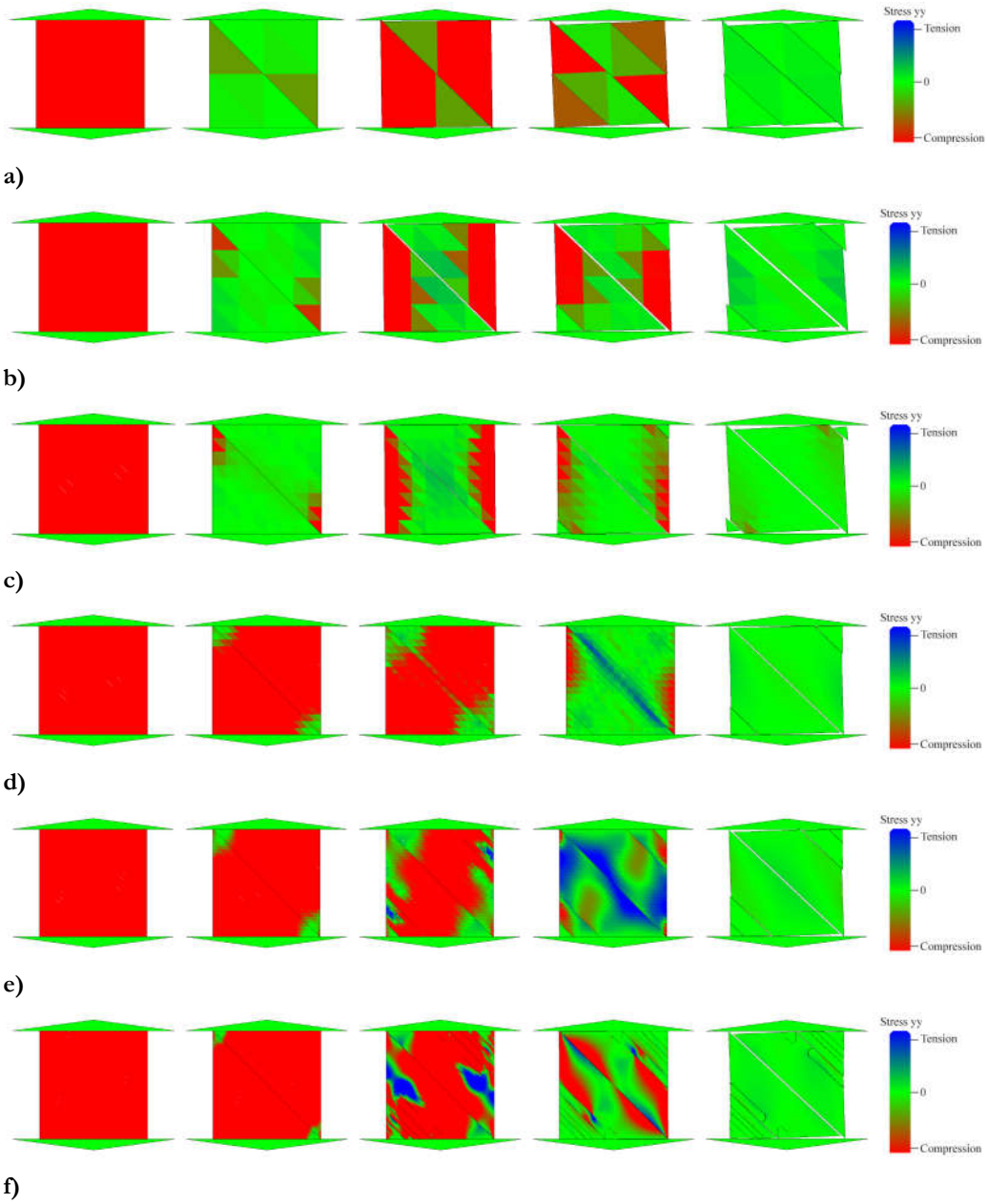

Figure 5-6: Comparison of stress distribution and fracture for material A properties between domains comprised of a) 8 b) 32 c) 128 d) 512 e) 2048 and f) 8092 elements.

The effects of insufficient damping can be seen most clearly in the two highest mesh densities, Figure 5-6e and Figure 5-6f, as stress waves as seen to propagate and reflect. The effect of this is initiation of multiple fractures at the same time as a result of stress propagation waves which increase local stresses. This means that while initiation of fracture is more accurate through improved resolution of local stresses, the accuracy of simulating fracture propagation is poorer. Although viscous damping could be increased, very small time steps would be required which results in long simulation times. Furthermore, viscous damping that is too high effectively stiffens the elements

and would create a different elastic response. Therefore, so long as loading oscillations and stress waves are negligible, it can be assumed that viscous damping is sufficient.

A similar set of images for stress distribution and fracture behaviour can be obtained for material B properties which show similar behaviour with initial propagation of a diagonal fracture along A-E and D-H, followed by subsequent smaller fractures, see Figure 5-7. Analysis of the stress distribution from the simulation shows that while stress waves still propagate through the material, they do not result in multiple fracture initiation points at higher mesh densities indicating that higher critical strains result in a more stable crack propagation simulation.

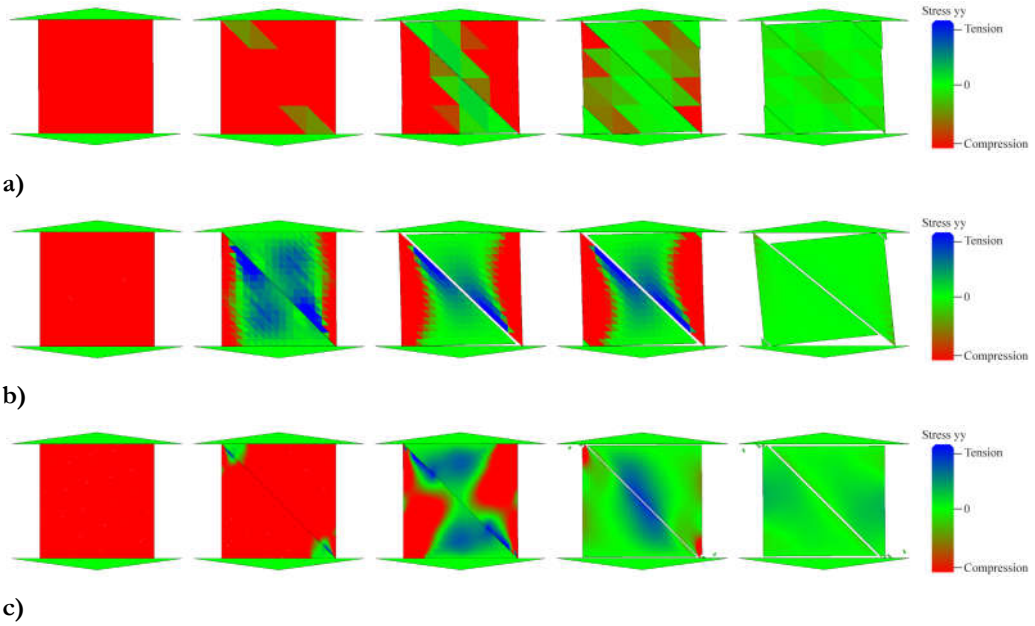

Figure 5-7: Comparison of stress distribution and fracture for material B properties between domains comprised of a) 32 b) 512 and c) 8092 elements.

The difference in load carrying capacity results from improved stress resolution at the corners. Whereas in coarse meshes the stresses are averaged over a larger area, the critical stress criteria will be reached earlier where stress concentration in the corners are more accurately modelled. Overall, this results in the coarser simulations displaying slightly higher strength. Similarly, the ability for fracture to initiate closer to the corners of elements C and F in the finer meshes effectively reduces the stress required to overcome the critical fracture criteria. This effect can be further illustrated by reviewing the strains at which initial and secondary fractures occur, see Figure 5-8.

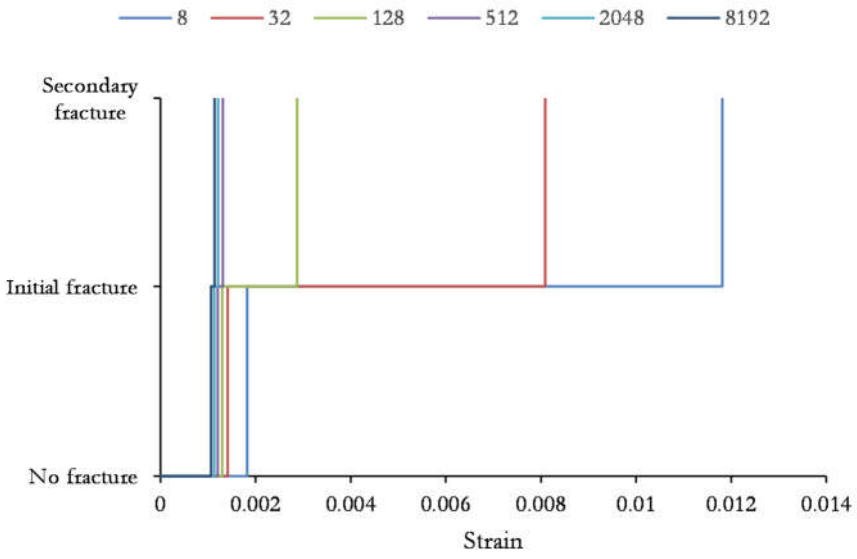

Figure 5-8: Strain required to induce fracture for material A.

Although fractures propagated in the same location, there is a significant difference in the timings of these fractures. It can be seen that as mesh density increases the strain required to induce the initial fracture reduces, with convergence around a strain of 0.001. This effect is even more significant in the propagation of the secondary fractures, with the coarsest mesh requiring a strain of 0.012 compared with 0.001 for the finest mesh. As the mesh is refined, secondary fractures occur at almost the same time as the initial fracture. This would be the expected result in an experiment for a genuinely homogeneous material as stresses would be symmetrical. The reason for fracture initiating along A-E and D-H is due to inherent mesh bias which will be reviewed next.

5.4 Meshing Bias

Meshing bias which results from the numerical approximation of the domain is an important factor to consider. In fracture modelling this is particularly important as fracture modes and paths can become highly depended on mesh orientation. A comparison of structured and unstructured meshes was conducted to understand the influence on failure behaviour, see Figure 5-9. The number of elements in each mesh used is about the same, 3202 for structured mesh and 3296 for unstructured mesh.

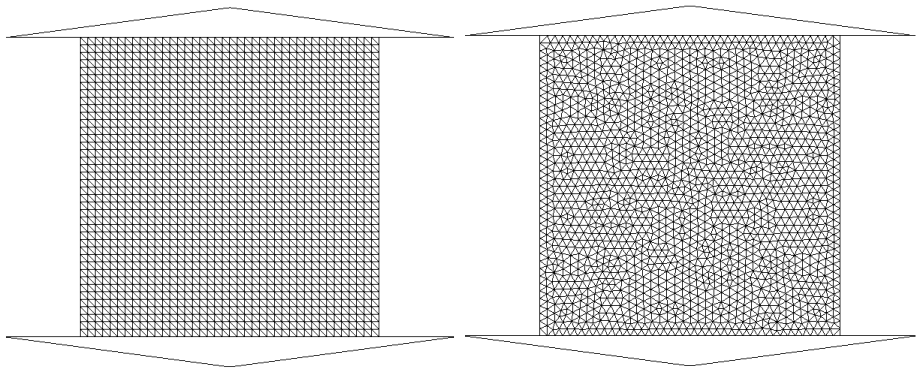

a) b)

Figure 5-9: Comparison of meshes for a) structured mesh b) unstructured mesh.

The force response of the loading plate is shown in Figure 5-10, with values normalised by the same converged load measured from the previous section (maximum load for the structured mesh therefore equal to unity).

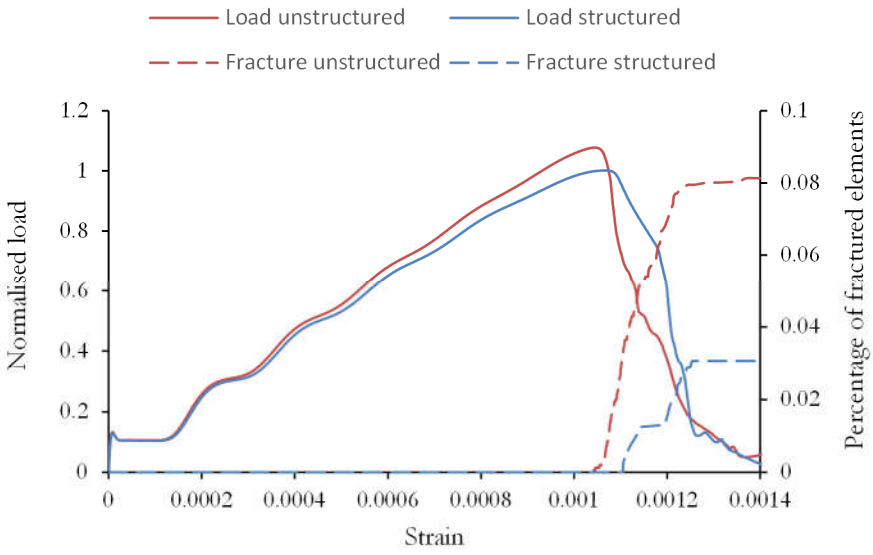

Figure 5-10: Comparison of force and elements fractured response for structured and unstructured mesh. Force normalised by maximum force in structured mesh.

Loading behaviour is very similar for both meshes with slight load oscillations in both suggesting this is not affected by mesh bias. There is a slight difference in load-strain response, with the unstructured mesh being stiffer. This could be due less compliance in the random orientation of elements.

The onset of fracture causes the dramatic reduction in load carrying capacity of the object in both. A slightly higher maximum force of approximately 7% is applied to the unstructured mesh indicating a higher strength. This difference can be explained

by having a mesh orientation having a higher propensity for fracture to propagate as is the case in the structured mesh. Furthermore, alignment of elements along fracture path allows the fracture to propagate quickly, resulting in an underprediction in a material's strength. In the unstructured mesh there is a natural restriction to this propagation as fractures cannot propagate along a single axis. This would be similar to the behaviour of homogeneous materials as phase properties, grain boundaries and manufacturing defect result in non-linear fracture paths. Depending on the nature of loading and failure, Mode I or Mode II, bias meshes are likely to either over or underestimate the material strength of heterogeneous materials. Failure simulations are therefore highly sensitive to mesh orientation in Y-Geo that cannot be overcome with mesh refinement alone. The final fracture paths, as shown in Figure 5-11, show a stark difference between fracture paths in the two meshes.

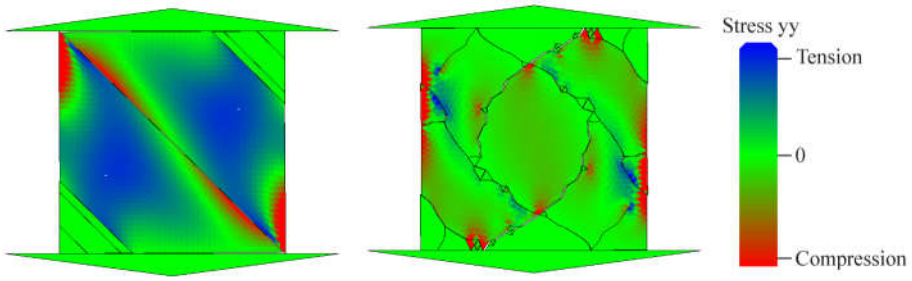

Figure 5-11: Comparison of fracture behaviour between a) structured mesh and b) unstructured mesh.

In both meshes the object's primary failure mode is in shear, however there are clear differences in their behaviour. In the structured mesh fractures propagate along these planes with little interaction causing discrete bands to form in the object. This is in contrast to the unstructured mesh where propagation is much more random and results in fractures interacting with one another.

5.5 Simulation of Stress Concentration Around a Hole

Understanding of modelling fracture parameters can be brought together with elastic response through validation of simulation results against the analytical solutions of stress distribution in a geometry. In this simulation stress concentration around a hole is compared to Kirsch's linear elastic solution discussed in Section 3.3.1.

A plate with a hole (modelled as a void) at the centre with a radius of a is modelled with length of sides $10a$, as shown in Figure 5-12a. An unstructured triangular mesh

was generated with element size $h_e = {}^{a}/_{10}$ over the whole domain, which was found to provide good accuracy and created a domain with 21668 elements, see Figure 5-12b. In order to create uniaxial tensile loading, velocity boundary conditions are applied to all nodes along top and bottom of the domain (E_2 and E_4) creating a displacement controlled simulation. Nodes along the right and left side of the domain (E_1 and E_3) are restricted to vertical movement by applying $V_x = 0$ and $F_y = 0$ boundary conditions. Remaining nodes are given zero force boundary conditions in both axis ($F_x = 0$ and $F_y = 0$). Material A properties were used in the simulation, although results are normalised as results and discussion are independent of the material properties.

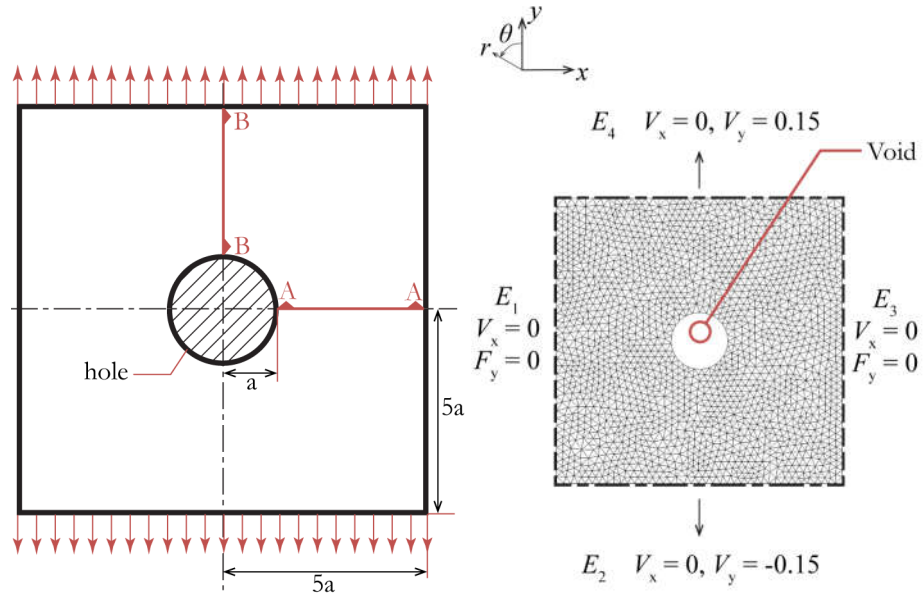

Figure 5-12: a) Plate with a hole simulation parameters and b) Mesh.

The simulation results of the stress distribution show how both FEM and DEM parts of the software work together. Snapshots of the dynamic simulation before and after fracture initiation are shown in Figure 5-13.

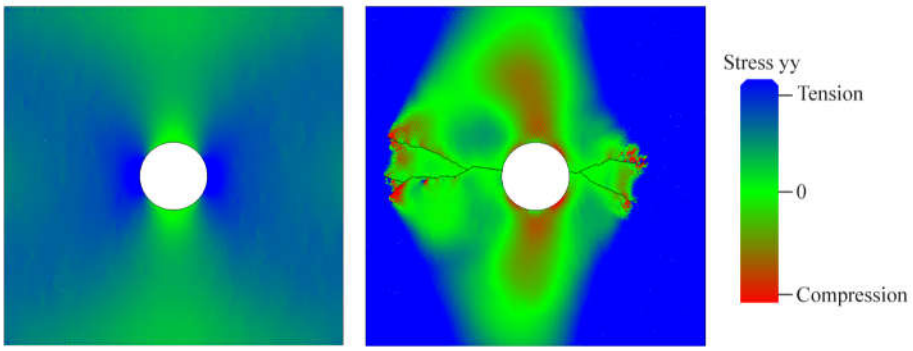

a) b)

Figure 5-13: Transition between continuum and discontinuum behaviour a) stress builds as tensile force applied to top and bottom edges and b) fractures propagate outward from the point of maximum stress.

As discussed previously, stress concentration occurs around geometric features ultimately leading to fracture initiation at a remote stress lower than that of the failure stress. It can be seen from Figure 5-13a that as a tensile force is applied tensile stresses slowly build either side of the hole. This result would be similar to that of a standard FEM simulation. Once stresses exceed the tensile strength fracture initiates from the edge of the hole at the point of maximum stress, see Figure 5-13b. Stresses in the plate redistribute around this fracture as the fracture itself becomes a point of stress concentration. This causes the fracture to propagate outwards along the edges of elastic elements.

This simulation demonstrates the advantage of FDEM modelling. While FEM is able to simulate elastic behaviour, failure of the component is assumed by the user when reported stress value in the domain exceeds that of the yield strength, or other predefined failure criteria, of the material. FDEM, on the other hand, is able to continue to simulate the next phase in this process by simulating fracture initiation and propagation.

Further analysis can be performed by comparing simulated stress distribution in the domain with the analytical solution by Kirsch. Along A-A and B-B (indicated in Figure 5-12a) stress distribution defined by Equations (3.8) and (3.9) can be simplified to:

$$\sigma_{\theta\theta} = \sigma_{\infty}\left(1+\left(\frac{a}{r}\right)^{2}\right) \tag{5.5}$$

$$\sigma_{rr} = \sigma_{\infty}\left(1-\left(\frac{a}{r}\right)^2\right) \tag{5.6}$$

Results from the simulation stress distribution along A-A and B-B is compared with the analytical solution using Cartesian coordinates, see Figure 5-14. The simulation shows good agreement with Kirsch's analytical solution for σ_{yy} and σ_{xx} along both axes.

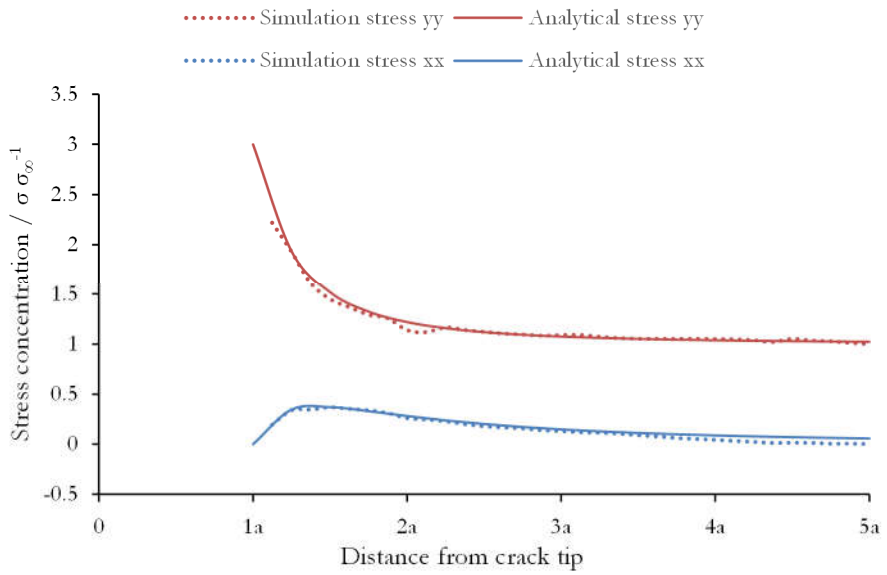

Figure 5-14: Stress concentration comparison along A-A between analytical solution and simulation results of normalised stress concentration just before fracture.

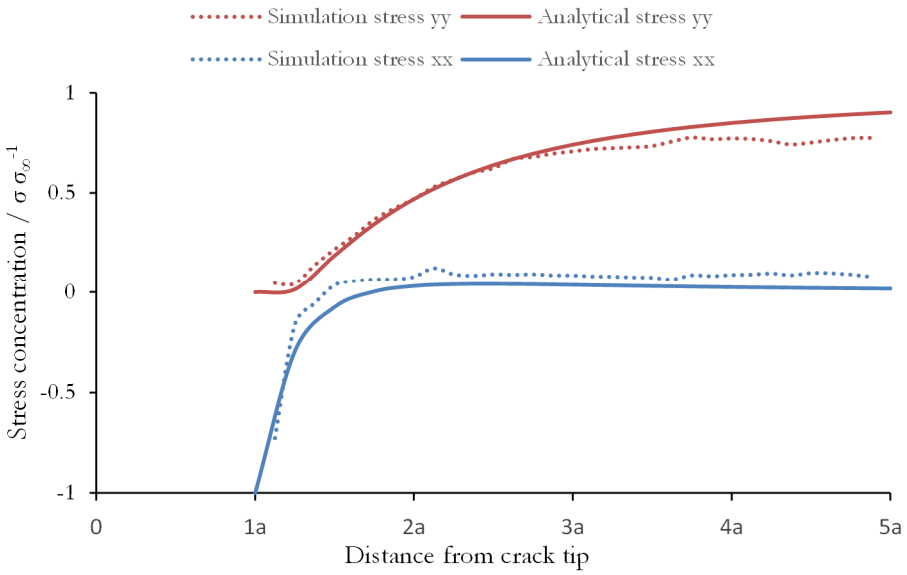

Figure 5-15: Stress concentration comparison along B-B between analytical solution and simulation results of normalised stress concentration just before fracture.

From Kirsch's analytical solution, the hoop stress value at the point of highest concentration is three times that of the remote stress (when $r = a$ and $\theta = \pi/2$). This is located at the edge of the hole along A-A and is accurately predicted in Figure 5-14a. Difference arise between simulation and analytical results as stress on each element is averaged across its area, essentially providing the stress at the centre point of the triangular element. Because an unstructured mesh is used these centre points do not align with the output points. Furthermore, due to the unrefined mesh, the measured stress distribution is unable to pick up the high concentration near the hole. This is particularly evident across A-A where stress concentrations are the highest. However, it is still possible to infer the failure load by measuring the remote stress, which is within 5% of $\frac{1}{3}\ \sigma_c$ when fracture initiates.

One of the limitations of the method employed is the lack of dynamic mesh refinement. This becomes very apparent in fracture propagation where bifurcation occurs much more frequently in simulations than would be expected in reality. It typically happens when the corner of an element is in line with the fracture path with each edge angled symmetrically along the fracture path, see Figure 5-16a. This makes mesh biasing a very important consideration in this type of simulation. Typically mesh bias is avoided in numerical studies as it can result in erroneous stress distribution, however in fracture modelling it could be used to provide a more accurate solution when they mimic naturally occurring weaker interfaces such as grain boundaries and slip planes within a crystal lattice. For example, when a bias mesh is used on the same geometry with elements aligned along anticipated fracture path, a horizontal fracture path with no branching can be achieved, see Figure 5-16b.

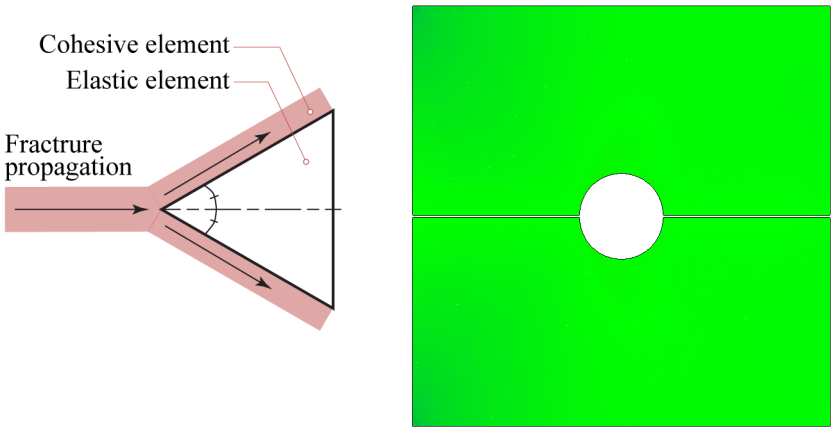

a) **b)**

Figure 5-16: Mesh bias a) showing how it can result in fracture branching and b) simulated fracture path with no bifurcation using bias mesh.

5.6 Conclusions

These results have been able to demonstrate the ability for Y-Geo to accurately reproduce elastic behaviour through validation of stress distribution in a domain and simulation of fracture propagation under compressive and tensile loading scenarios.

The mesh density has been shown to have a significant impact on the behaviour of fracture within an object. Finer meshes are able to resolve stress concentrations more accurately, although are more difficult to suppress the effects of dynamic simulation. These stress wave propagations are more problematic in brittle property elements than ductile ones as the critical strains are small. This can result in very fine meshes creating a less stable simulation. The effects on computational time also need to be considered, especially as the model becomes more complex. Typically in FEM mesh density is varied over the domain in order to overcome these issues, however in Y-Geo the definition of viscous damping and critical strain require domains to have consistent element size over the whole domain. Clearly unstructured meshes are more representative of the homogeneous structures as fracture is initiated at random locations with the domain. However, mesh bias could also be used to mimic naturally occurring weaknesses in microstructures, such as the interface between grains or even slip planes. It also manages to restrict the problem of fracture bifurcation.

Simulations in this chapter were restricted to domains consisting of one material which is not representative of the heterogeneous structure of WC-Co. In the next chapter the effect of combining brittle and elastic material properties into one domain will be investigated.

Chapter 6 – Modelling Fracture of Composite Material at the Macroscale

Chapter Highlights

One of the key aspects to WC-Co is the clear separation of ceramic and binder phases (Section 3.1.2) and the proportion of each phase plays an important role in determining the bulk material properties. These bulk properties can be predicted by the rule of mixtures based approach (Section 3.1.5). However, to model at the mesoscale, individual properties have to be assigned to the elements. This chapter combines brittle and ductile elements into one domain to show that bulk fracture properties can be simulated.

- Dynamic loading effects can alter the measured bulk material properties.
- By assigning different proportions of brittle and ductile properties to individual elements, the simulated tensile strength of the bulk material can replicate estimation by the rule of mixtures.
- Post processing of output files enables analysis of where fractures are occurring in the microstructure.

6.1 Modelling Objectives

In the previous chapter Y-Geo was validated against some basic geometries. Different behaviours could be seen between brittle and ductile materials although only domains of a single material property were investigated. The next step is to introduce composite behaviour by studying the effect of combining brittle and ductile elements into one simulation replicating the effect of separate WC and Co properties. As discussed in Section 3.7.5, previous numerical modelling studies of WC-Co using FEM were able to simulate bulk material elastic properties by applying separate material properties to individual elements. FDEM also allows a similar approach to be used, with the added ability to simulate bulk material fracture properties. In order to study this a Brazilian disc test simulation is performed, a compression test similar to the setup used for validating meshing parameters in Sections 5.3 and 5.4. This approach was successfully used by Mahabadi et al. [177, 178] on rock materials (see Section 3.7.7) to investigate the effect of combining different types of rocks into a single system. Further analysis techniques are also developed to help analyse the behaviour of the simulated fracture propagation.

6.2 The Indirect Tensile Test

Due to the difficulties of conducting a uniaxial tensile test, an indirect method called the Brazilian disc test was developed to measure the tensile strength of brittle materials. In this test a cylindrical specimen is compressed between two loading platens until failure occurs, as shown in Figure 6-1a.

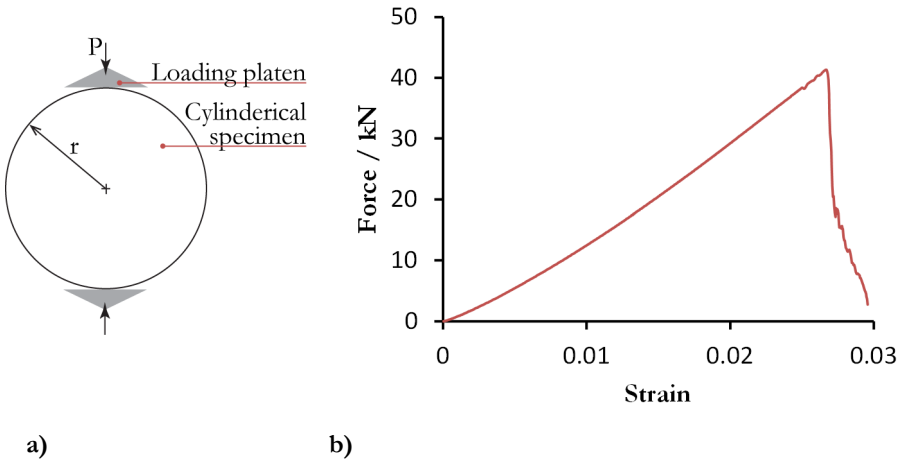

Figure 6-1: a) Schematic of Brazilian disc test setup and b) example of loading curve.

The applied stress induces a tensile stress across the centre of the specimen that is perpendicular to the loading direction. It is assumed that the material is isotropic and homogeneous resulting in failure occurring at the centre of the specimen at the point of maximum stress. By measuring the load applied at the loading platen the tensile strength, σ_{UTS}, of the specimen can be calculated from:

$$\sigma_{UTS} = \frac{P_{max}}{\pi r s} \tag{6.1}$$

Where P_{max} is the maximum load prior to failure, r is the radius of the specimen and s is the thickness, set to unity for the simulations as they are 2D.

6.3 Simulation Set-up

Simulation of a 2D Brazilian disc test was performed in Y-Geo following the flowchart described in Figure 4-4. A disc shape with triangular elements top and bottom was sketched in Abaqus with a radius of 25 mm. An unstructured triangular mesh with element size 1 mm was applied to the disc, creating a domain with 5503 elements, see Figure 6-2.

A compressive load is applied to the disc by applying displacement boundary conditions to the three nodes that defined the A and B loading platens. As all nodes in the domain required to have boundary conditions, elements that define the disc are given zero force boundary conditions.

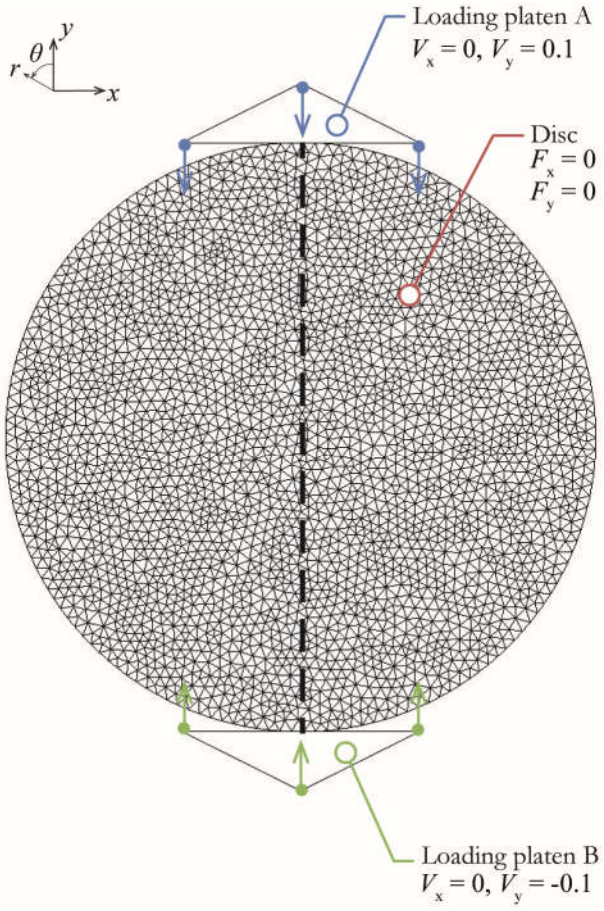

Figure 6-2: Mesh created for Y-Geo simulation. Dashed line indicates central loading axis.

Each element in the disc was assigned either Material A or B properties. The percentage of each element can be controlled using a function in Y-GUI which allows the user to prescribe the percentage each element and apply randomly to selected domain.

6.4 Results and Discussion

6.4.1 Stress Distribution

Similar to the stress concentration around a hole in Section 5.5, the simple geometry used allows stress distribution in the domain to be compared against an analytical solution, which allows further validation of elastic behaviour prior to fracture. In this instance homogeneous material properties are used. Stress distribution along the central loading axis (see Figure 6-2) of the disc was calculated by Hondros [183] to be:

$$\sigma_\theta = \frac{P}{\pi r s \theta_\alpha}\left\{\frac{\left[1-\left(\frac{r_r}{r}\right)^2\right]\sin 2\theta_\alpha}{1-2\left(\frac{r_r}{r}\right)^2\cos 2\theta_\alpha+\left(\frac{r_r}{r}\right)^4}-\tan^{-1}\left[\frac{1+\left(\frac{r_r}{r}\right)^2}{1-\left(\frac{r_r}{r}\right)^2}\tan 2\theta_\alpha\right]\right\} \quad (6.2)$$

$$\sigma_r = \frac{-P}{\pi r s \theta_\alpha}\left\{\frac{\left[1-\left(\frac{r_r}{r}\right)^2\right]\sin 2\theta_\alpha}{1-2\left(\frac{r_r}{r}\right)^2\cos 2\theta_\alpha+\left(\frac{r_r}{r}\right)^4}+\tan^{-1}\left[\frac{1+\left(\frac{r_r}{r}\right)^2}{1-\left(\frac{r_r}{r}\right)^2}\tan 2\theta_\alpha\right]\right\} \quad (6.3)$$

Where θ_α is the half central angle related to the distributed load applied and r_r is the radial distance from the centre of the disc; tensile stresses are positive. At a given displacement, d, of the loading platens half central angle can be calculated using geometry of a circular segment:

$$\theta_\alpha = \arccos\left(1-\frac{d}{r}\right) \quad (6.4)$$

A comparison between Hondros's analytical solution and simulation result from Y-Geo are presented in Figure 6-3. Results have been normalised by ($P/\pi rs$).

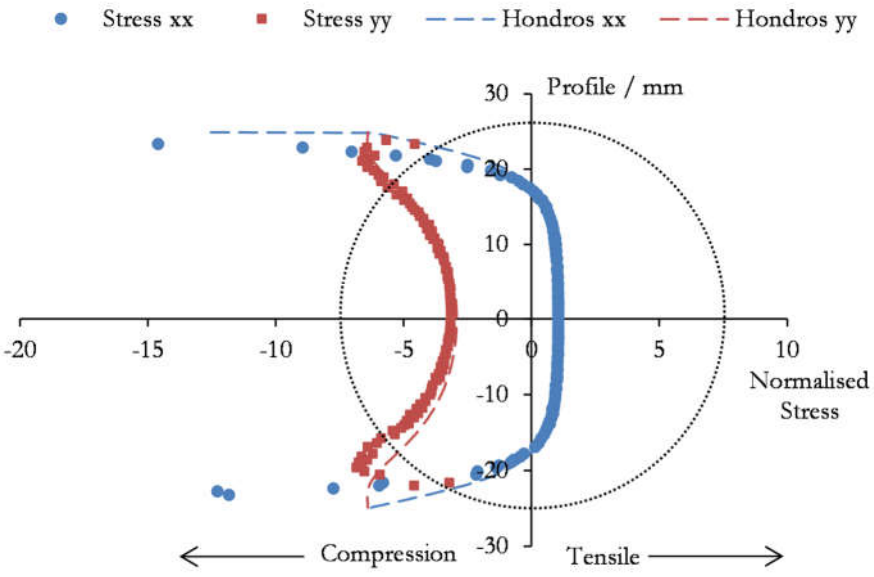

Figure 6-3: Comparison between normalised stresses σ_{xx} (blue) and σ_{yy} (red) from Y-Geo simulation (bold lines) and Hondros solution (dashed lines). Dashed circle represents disc specimen.

Highest tensile stresses (stress xx) are generated along the centre of the disc with an equal distribution across the majority of the domain. There is very good correlation between simulated and analytical solution of the stress distribution, with a slight overestimation of maximum stress by the simulation of 15% of normalised stress. This is likely due to an overestimation of the contact area between loading platen and disc, which was performed manually using Equation (6.4). Compressive stress distribution (stress yy) is also well replicated by the simulation, with 7% difference in normalised stress at the centre of the disc. These results provide further validation of elastic behaviour in the model.

6.4.2 Failure Mode

Y-Geo can simulate mode I, mode II and mixed mode fracture mechanisms. By modifying the properties of individual elements initiation of different macro failure mechanism can be simulated. For example, by changing the shear strength of the elements differing macro behaviour can be observed, which indicates the type of failure mode, see Figure 6-4. Under shear failure fracture initiates from the loading element whereas in tensile failure initiation is from the centre of the specimen.

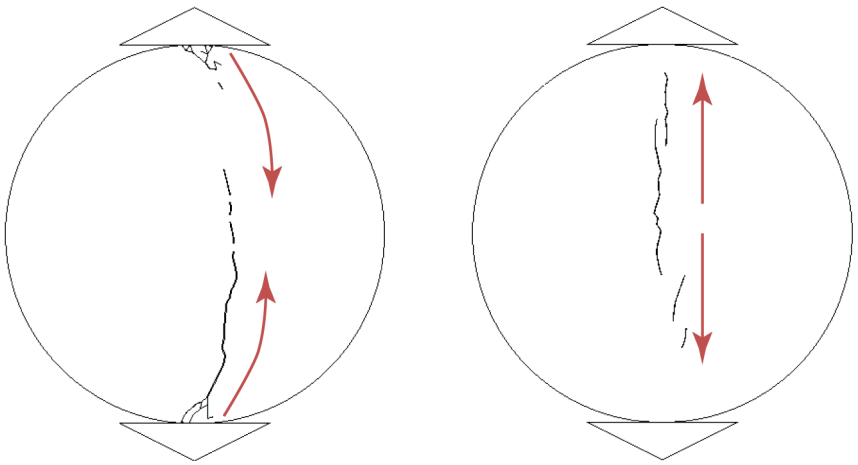

a) b)

Figure 6-4: Comparison of different failure patterns simulated through changing element fracture properties (arrows indicating direction of fracture propagation) a) shear failure and b) tensile failure.

The Brazilian disc test is only valid for measuring tensile strength so any materials whose failure initiates in shear cannot be assessed. In order to prevent Mode II fracture from occurring the shear strength was set to a value one order of magnitude higher than the tensile strength in subsequent simulations. This will result in failure

only being initiated through Mode I failure and thus allowing calculation of the tensile strength of the bulk material to be made using Equation (6.1).

6.4.3 Dynamic Loading Effect

The calculated strength of a material varies in accordance with the loading rate used which has been observed experimentally. It is well known that higher strain rates result in higher material strength being recorded. To understand this effect in Y-Geo simulations were performed for varying loading rates for the same microstructure, see Figure 6-5. Simulation time was taken as wall clock time from simulation initiation till failure of the specimen at maximum applied load. Tensile strength was normalised by the tensile strength measured at the lowest strain rate while simulation time was normalised by the fastest simulation which was obtained at the highest strain rate.

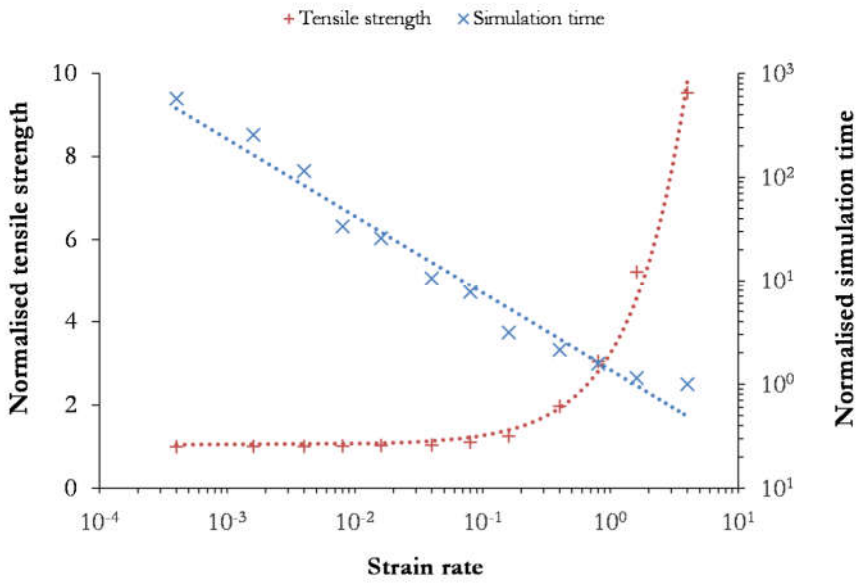

Figure 6-5: Comparing tensile strength and simulation time vary with loading rate.

The simulation results are able to replicate a similar dynamic loading as would be expected experimentally with strength increasing as strain rate increases. As strain rate is reduced measured strength converges on a single value. Simulation time meanwhile increases with lower strain rate and displays a power-law relationship, as indicated by the linear log-log relationship. A balance between accuracy of solution and simulation time is therefore required. Although high strain rates were quickest to simulate, a measured tensile strength up to ten times higher than the converged solution is too high of an error. However, the slowest strain rate takes almost 600

times longer to simulate. A strain rate of around 0.04 s^{-1} only has a difference of 4% in tensile strength, while at the same time is able to simulate fracture initiation 50 times quicker than at of the slowest strain rate of 0.0004 s^{-1}.

No assessment is made as to whether the relationship is the same as would be seen experimentally although it is likely that due to the critical damping assumption used in order to obtain quasi-static loading condition, that it will overpredict the effects of strain rate on tensile strength. However, typically experimental tensile tests are conducted at quasi-static conditions so as not induce these dynamic loading behaviours which is a field of research in itself. As such, for the purpose of this project it is only required that quasi-static loading is simulated and dynamic loading effects minimised. This behaviour however could be an avenue of future research for investigation of strain dependent properties.

6.4.4 Tensile Strength

Having validated elastic behaviour, accounted for Mode II failure and the effects of dynamic loading the material strength of a disc with a mixture of elements with different properties can be reviewed. Generic material properties A and B from Chapter 5 are used in the first instance, see Table 5-1. Now that elements are used together fracture properties at the interface between these two elements must also be defined. As discussed in Section 3.3.5, Sigl and Exner [85] found fracture to occur alongside carbide/binder interfaces in the binder phase rather than exactly on it. This would suggest that the cobalt binder properties would dictate fracture at this interface, therefore ductile material properties are applied to interface elements. The scale is such that the microstructure is not accurate or meaningful, therefore differences between intergranular and transgranular WC fracture is not considered. Load-displacement curves obtained from the simulation output allows tensile strength to be calculated using Equation (6.1). Simulations were run which varied the quantity of each material and resulted in changes to the measured tensile strength of the disc, as shown in Figure 6-6. Tensile strength is normalised by the tensile strength of material A elements. These are plotted against a theoretical bulk strength based on the rule of mixtures approach discussed in Section 3.1.5.

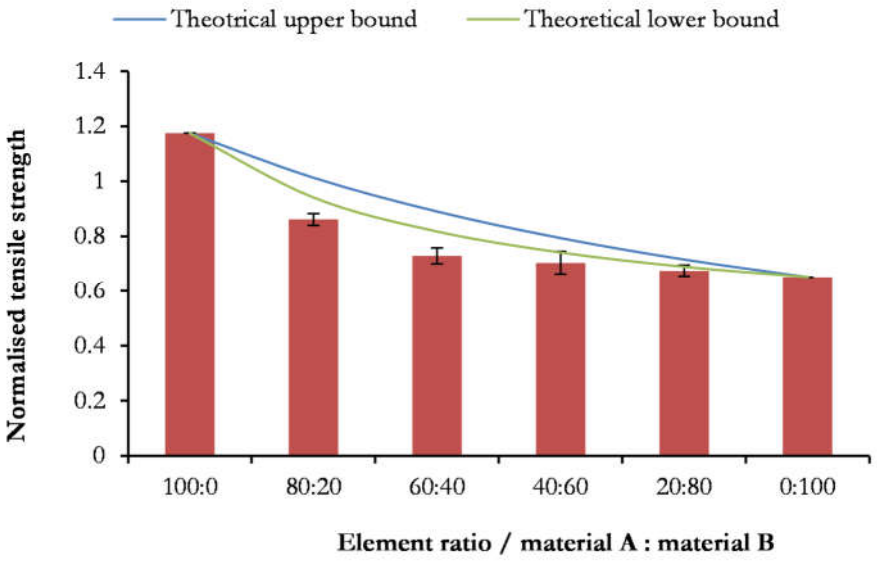

Figure 6-6: Average tensile strength from tensile tests for varying ratios of material A and B, error bars representing maximum and minimum values calculated. Theoretical upper and lower bounds calculated using rule of mixture approach and adjust for increase in bulk material strength due to dynamic effects.

The simulation results show a gradual decrease in tensile strength as the percentage of material B elements increases. The measured strengths for domains that are 100% material A or B calculated from simulation results are higher than that of the tensile strength of the individual elements by around 15%. This suggests that even although low stain rates are used, dynamic loading still affects the results. However, reducing strains rates further is computational intensive and therefore not viable. As the effective increase in simulated tensile strength is the same for both homogenous domains (100% of either material), it is assumed that the effect of dynamic loading is equal in any given ratio of material A and B. Therefore, in order to make a better comparison with the simulation results the upper and lower bounds of the theoretical strength is increased to account for dynamic loading effects in Figure 6-6.

The measured strengths for the heterogeneous simulation approximately follow the lower bound estimation. The difference between these values increases as material A percentage increases. One possible reason for this is that the domain is not at a sufficient resolution to model an accurate microstructure and therefore stress distribution in the domain will not be representative of a real material. Amplification of stress concentration effects from this approximation will cause fracture to initiate earlier and consequently reduce bulk material strength.

To demonstrate the advantage of applying material properties of individual phases the heterogeneous mixtures simulations were run five times each with randomised element composition, a function which is built into Y-GUI. For each simulation there is a slight change in tensile strength, with the largest variance of 6% occurring at 60% Co content. This is an indication of the microstructural influences on material strength, a result that could not be achieved through averaged properties such as the rule of mixtures based approach. Although the simulation results do not fall within the theoretical strength values, they do demonstrate the ability for global fracture properties to be simulated in Y-Geo through the use of separate brittle and ductile element properties.

6.4.5 Post-Processing

One of the limitations of the Y-Geo is its lack of post processing analysis tools. Stresses, strains and velocities visualisation is handled through OpenGL code M and .ym files that can be extracted to bitmap files, however this cannot be interrogated.

Due to this restriction Matlab code was written to support analysis of simulation data. One of the important aspects of fracture behaviour that needs to be validated is the interaction between phases, including intergranular and transgranular behaviour. In order to observe this interaction yield and fracture data from the .yhSFK and .yhBRK files were plotted onto the domain including element properties, see Figure 6-7. From this it can be seen where fractures are initiating and propagating with relation to the phases of the material.

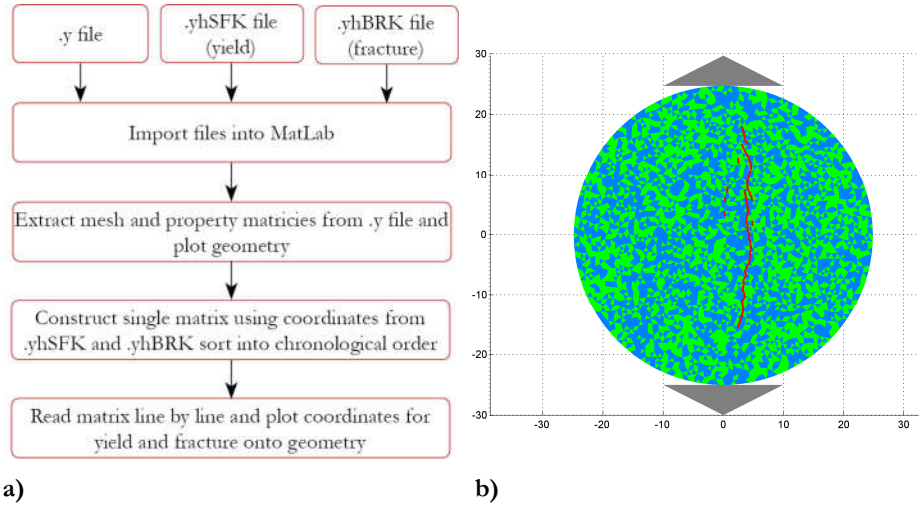

a) b)

Figure 6-7: Plotting of fracture in Matlab a) Code structure and b) Plot of mesh and element properties, WC (blue), Co (green) with fracture path (red) shown.

Extending this code analysis of fracture visualisation of fracture propagation can be done. By reading and plotting the yield and fracture elements line by line an animation of fracture propagation can be created, see Figure 6-8. They will also aid in the validation of simulation data by comparison to experimental behaviour.

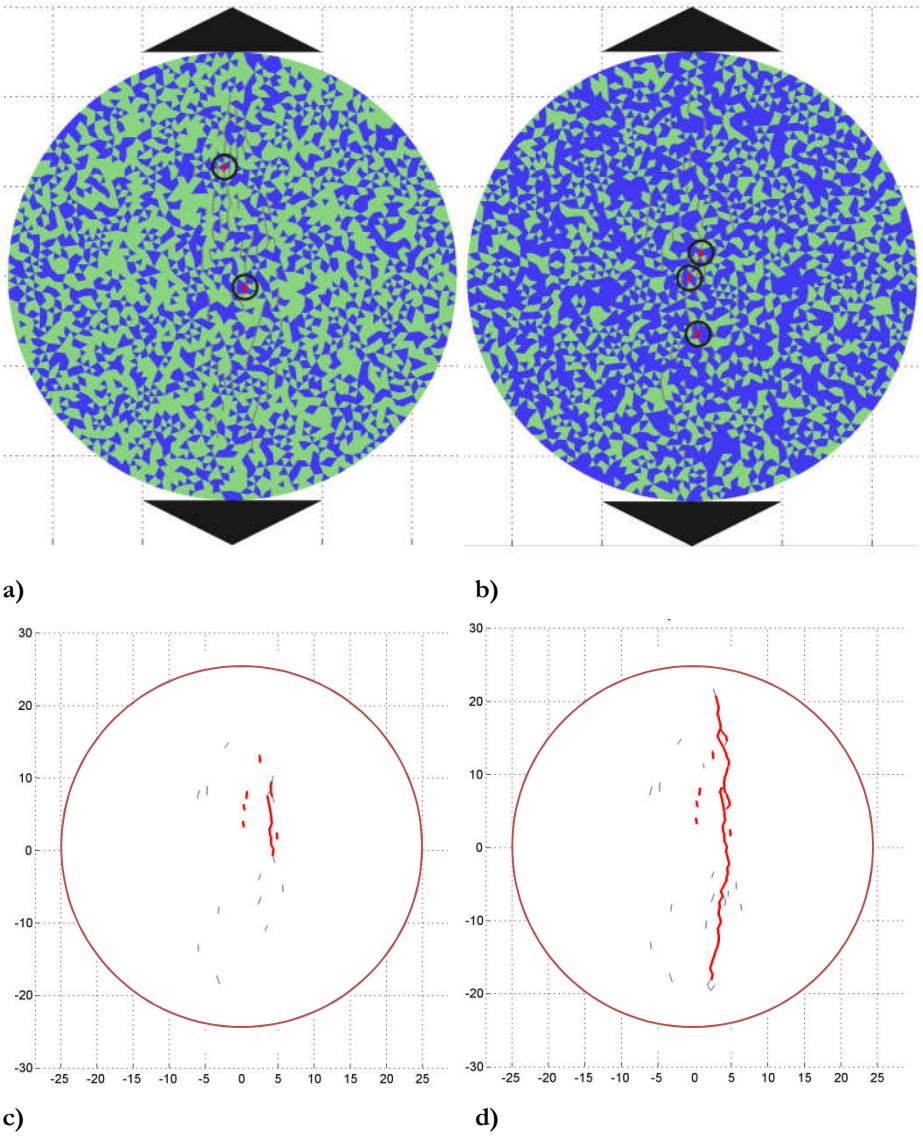

Figure 6-8: Plots of fracture propagation showing yield (grey) and fracture (red). Brittle material elements (blue) and ductile martial elements (green). Examples of fracture initiation in brittle elements circled for domain with a) 60:40 ratio and b) 40:60 ratio b). c) and d) show fracture propagation in 80:20 ratio simulation with few yielded elements outside of the main fracture path.

The results show that there are multiple points where yield will occur in the disc and there are multiple fracture initiation points typically within the brittle material even when significant yield has occurred in the ductile material, see Figure 6-8a and Figure 6-8b. These are not necessarily initiated in the centre of the specimen as would be

expected from a homogeneous sample, as discussed in Section 6.4.1. The heterogeneous mesh results in stresses not being equally distributed in the domain due to the differing properties of brittle and ductile elements. Furthermore, as the distribution of the elements in the domain is changed for the heterogeneous simulations, fracture is initiated in slightly different locations of the specimen for each simulation run resulting in the varying strengths recorded in Figure 6-6.

Upon further applied load additional microcracks are formed, generally in the vicinity of existing fracture points. This is likely due to stresses being altered in the vicinity of broken cohesive elements as elements are no longer able to carry load. Some of these microcracks join together while propagation of others is suppressed, predominantly where the fracture neighbours the binder phase. Once enough microcracks merge sufficient global stress concentration effect occurs, such that a single fracture propagates outwards toward the loading platens.

Each time a different allocation of elements is run a slightly different fracture path emerges as a result of the differing stress distributions, see Figure 6-9. However, the final fracture for all simulations will have the appearance of a single vertical fracture around the centre of the disc indicating tensile failure.

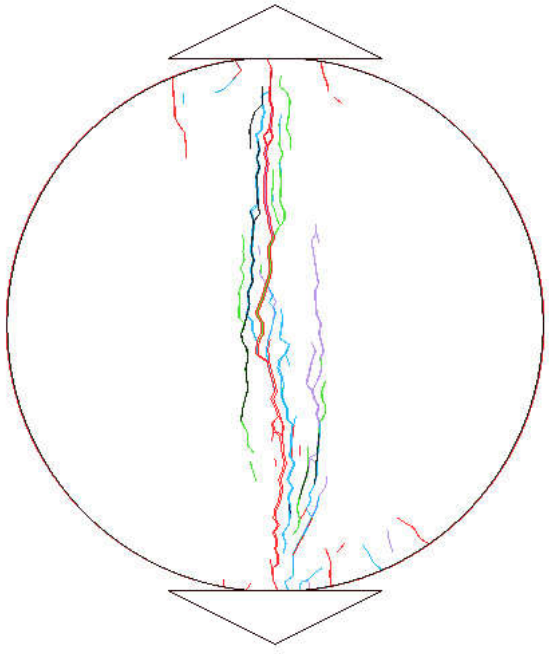

Figure 6-9: Overlay of five fracture paths from WC-20Co simulations (each colour representing one simulation).

In order for LEFM analysis to be valid a small plastic zone size is required, see Section 3.3.2. Experimental data found very little yield or fracture outside of the main fracture path. Furthermore, Sigl and Exner [85] saw no microcracking or crack branching in the carbide phase. Looking at the plots of yield elements shows that in high percentages of ductile material there is significant failure outside of the main fracture path. However, in high percentages of brittle material which would be typical of WC-Co grades of interested there is little failure around the crack tip which indicates a small plastic zone, see Figure 6-8c and Figure 6-8d.

6.5 Conclusions

Simulations demonstrate the ability of Y-Geo to model bulk material fracture properties, such as tensile or shear failure and strength of composite materials, by applying specific material properties of individual phases. Simulation of the Brazilian rock test was able to show a change in tensile strength as fractions of the ceramic and binder phase were changed. Furthermore, an initial assessment of microstructural changes through random dispersion of elements in the mesh was able to capture differing values of tensile strength of the specimen. This supports the influence of the microstructure on the behaviour of the bulk material.

Further analysis of the simulation was performed using Matlab which enabled propagation of the fracture to be analysed. This allowed fractures propagation to be observed in relation to the material phases, something that could not be done natively using Y-Geo and associated visualisation tools. This will aid in validation of behaviour against experimental results.

The scale of this simulation, however, is unable to represent the microstructure of WC-Co accurately. Consequently, microstructural effects discussed in Section 3.2 and the resulting stress concentrations will not accurately capture fracture behaviour. This aspect will be the focus of the next chapter where modelling at the grain scale is used.

Chapter 7 – Modelling WC-Co Fracture at the Mesoscale

Chapter Highlights

Microstructure plays a key role in determining the bulk properties of WC-Co (Section 3.2). By modelling at the mesoscale, this enables both material properties of individual phases to be assigned to elements as well as being able to capture the geometry of the microstructure explicitly. This is performed by modelling a real microstructure to validate fracture behaviour and path against experimental results. This chapter also demonstrates the insight that FDEM offers beyond conventional FEM techniques.

- Highlight the importance of measuring intrinsic material properties and need for fracture properties to improve models.
- The model was able to simulation the discrete steps in fracture process which was described previously from observation of experimental results. The final simulated fracture path was also close to the experimental result.
- Stress raisers are created at the angular interface between WC grains which affect the direction of fracture propagation.

7.1 Modelling Objectives

Although the Brazilian disc model was able to simulate fracture in a composite material composed of brittle and ductile elements, it does not capture a number of important material behaviours. One of the main being microstructural interactions that was discussed in Section 3.2.

Having used a simulation to show that applying brittle or ductile material properties to individual elements can mimic bulk behaviour, the next step is to validate results against experimental results. The approach used by Sigl and Schmauder and Özden et al. [170, 171], whereby phenomenological observations from an experimental fracture path through the microstructure is compared and contrasted against numerical results will be used in this chapter. This is performed at the mesoscale, using a real microstructure to validate the model against phenomenological observations and current understanding of the fracture process discussed in Section 3.3.5. One of the most interesting findings was that fracture in WC-Co progressed in discrete steps. Sigl and Exner [85] described these steps as:

i. Initially, there is the formation of fracture in the WC phase ahead of the crack tip;

ii. This is followed by deformation of the Co binder which forms voids and ligaments;

iii. Finally, these voids coalesce to form the final fracture path.

This behaviour however has not been described in fracture modelling studies so far.

7.2 Simulation Set up

Fracture experiments conducted by Sigl and Exner [85] provide a good reference as SEM images provide a clear picture of how fracture interacts with microstructural features. A Chevron notched WC-10Co sample (35 mm × 6 mm × 2 mm) was subjected to a loading in three-point bend test, rollers 28 mm apart, and the resulting fracture analysed. The sample microstructural properties are given in Table 7-1.

Table 7-1: Sample microstructural properties [85]

Microstructural property	Value
Volume fraction / %	16.5 ± 2.1
Average grain size / μm	2.18 ± 0.02
Mean free binder path / μm	0.84 ± 0.02

Stable crack propagation was obtained using very slow loading-rate control, 20 N s^{-1}, allowing the fracture to be arrested before propagating through the whole sample and provide a snapshot in time. A SEM image of the fracture path obtained from the experiment is shown in Figure 7-1a.

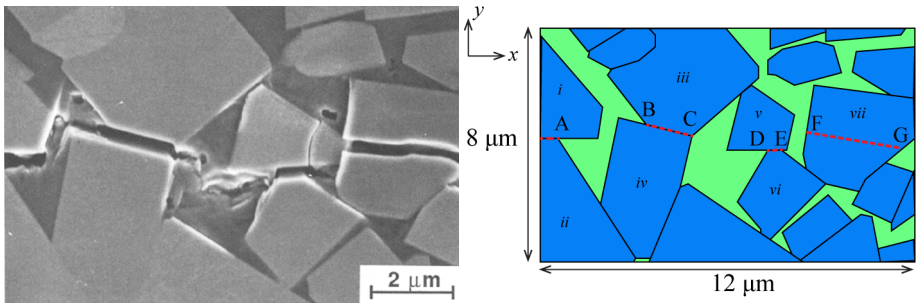

a) b)

Figure 7-1: a) SEM image of fracture path (propagating left to right) in WC-Co [85] and b) skeleton structure used for mesh and annotated with key WC grains and fracture locations: WC (blue) and Co (green).

A triangular mesh based on the microstructure see Figure 7-1b was created in Abaqus and imported into the Y-Geo environment which represents a domain of approximately 8 μm × 12 μm. This mesh is slightly different to the mesh used in a follow-on FEM study by Sigl and Schmauder [166] in two respects. Firstly, for unknown reasons the microstructure differed slightly to the experimental images. Secondly, in the FEM model it was assumed that fracture had already formed ahead of the main fracture in the carbide phase and therefore fractures at A, B-C, D-E and F-G were introduced, see Figure 7-1b. This was performed by introducing voids in the domain to create pre-existing stress raisers. As FDEM can explicitly model fracture, only a single void is introduced into the domain at A by preventing cohesive elements from being introduced between grain *i* and *ii*. This is similar to the experimental study where a Chevron notch introduces a stress raiser.

WC-Co is modelled as a heterogeneous material using intrinsic material properties as per Table 7-2 and Table 7-3. WC and Co material was discretised further effectively allowing simulation of the four types of fracture in WC-Co classified by Sigl and Exner, namely:

- fracture along WC and Co interfaces (WC/Co)
- intergranular fracture along WC grain interfaces (WC/WC)
- transgranular fracture within WC grains (WC)
- transgranular fracture through the Co phase (Co)

There is assumed to be WC/WC interaction between WC grains, this aligns with the established theory that there is a continuous carbide skeleton as proposed by Dawihl [58]. Furthermore, continuity of WC grains is assumed i.e. the interface properties between WC/WC are the same as between WC elements within a single grain. As discussed in Section 5.4, mesh bias can provide more accurate simulation of fracture paths. In this model mesh bias is introduced by meshing WC and Co phases separately, as well at individual WC grains thereby creating cohesive elements along these interfaces when model is initialised. The mesh and associated boundary condition described is shown in Figure 7-2.

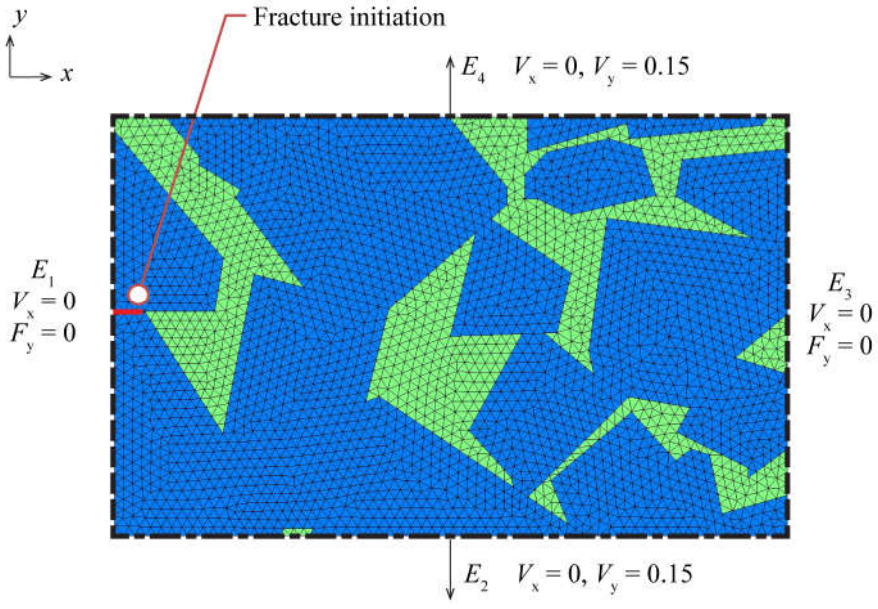

Figure 7-2: Mesh created for Y-Geo simulation based on micrograph, using heterogeneous microstructure: WC (blue) and Co (green).

Similar to the plate and hole model in Section 5.5, loading is introduced to the domain along the top and bottom edges (E_2 and E_4) in order to create a tensile stress through the application of a velocity boundary condition. The magnitude needs to be low enough for stresses to stabilise while considering computational time to induce a large enough force to initiate fracture. Vertical edges (E_1 and E_3) are constrained in the x-axis by applying a zero $\boldsymbol{x}$ direction velocity. This is chosen as the carbide skeleton extend through the material and therefore constrain the domain of interest. Element size is h_e = 200 nm, creating a domain of 8343 elements.

7.3 Material Properties

7.3.1 Elastic Properties

There have been many studies on the mechanical properties of WC-Co, along with the many literature reviews which summarise these findings [31, 41, 88, 184]. The majority of studies which focus on WC-Co material properties however only consider the bulk material response. In order to model at the mesoscale material properties for the constituent phases is required. Nanoindentation has been shown to be a suitable technique for determining the properties of individual phases in-situ [185].

The Young's modulus for the binder phase, E_{Co}, has been found to be similar to its bulk material properties 200 – 250 GPa [45, 57]. WC grains, which have an irregular hexagonal structure, one basal {0001} and two prismatic {10–10}, have been found to be anisotropic. Studies using nanoindentation have found basal facets exhibit approximately ×1.5 higher elastic modulus compared to prismatic facets, 400 – 700 GPa and 500 – 900 GPa respectively [45, 47].

However, indention results are restricted to Young's modulus measurements and hardness measurements. Furthermore, the latter is not an intrinsic material property, but rather a material behaviour that is a result of a complex interaction between multiple material properties. Hardness can be described through other mixture of parameters such as toughness and ductility making modelling using this value next to impossible and therefore cannot be used directly as a modelling parameter.

The elastic material property values used in similar numerical studies have tended to fall within the same order of magnitude. Co properties have ranged from 176 GPa

to 227 GPa for Young's modulus and Poisson's ratio typically ranging from 0.3 to 0.32.

Although anisotropy of WC has been shown, with such a large scatter in results in the literature and no clear consensus on the magnitude of difference between the planes, implementing this aspect would be challenging and create even more unknown variables. To date, numerical studies have modelled WC as an isotropic material with Young's modulus ranging from 600 GPa to 714 GPa and Poisson's ratio between 0.18 and 0.25. Simulations were performed using the elastic material properties of WC and Co as shown in Table 7-2, which generally represents average values found in experimental and numerical studies.

Table 7-2: Elastic material properties used in simulation [32, 165]

Elastic Property	WC	Co
Young's modulus / GPa	700	210
Poisson's ratio	0.24	0.31
Density / g cm^{-3}	15.6	8.9

7.3.2 Fracture Properties

Although elastic properties are fairly well established, there is much less consensus for the material failure criteria. Values used in simulations appear to vary significantly in the literature especially for the Co phase, with yield strength ranging from between 279 MPa and 2950 MPa. The lower values are approximately equal to the expected values for pure Co (295 – 485 MPa [32]), while upper estimates are based on a one-third hardness value assumption, a factor which has been found approximately true for most metals [186]. This difference has not fully been explained in the various studies although hypothesis put forward for this difference include: alloying of the binder during the sintering process with modifies the composition, size effects, FCC crystal structure as a result of the sintering process which holds Co in its high-temperature structure compared to HCP in its pure form, and the physical effect of the surrounding WC skeleton. These factors have yet to be reconciled.

A numerical investigation by Sadowski and Nowicki [165] into the mechanical properties of each phase a Co yield value of 279 MPa was used. A similar value of 297 MPa was also used by Dębski and Sadowski [169].

There have been some studies on fracture properties of WC-Co. During the sintering process the cobalt binder mixes with tungsten and carbon from the WC powder creating a Co-W-C alloy [50]. Tensile tests were performed by Roebuck et al. [56] on specimens with this composition. Unfortunately no yield properties were reported, however tensile strength values of alloy compositions of interest were the range of 700 MPa to 950 MPa and fracture strain of between 4 – 12% which is similar in value to those of pure Co.

Although there has been significantly less modelling of WC fracture, likely due to numerical issues discussed earlier, a similar discrepancy of critical stress values has occurred for the WC phase. In fatigue studies of WC-Co by Özden et al. [170, 171] an ultimate tensile strength value of 4000 MPa was used. This is significantly higher than that of WC which is generally quoted by manufacturers of between 350 and 550 MPa [32]. A value within this range, 356 MPa, was used by Dębski and Sadowski as the failure stress of the WC/Co interface.

As the premise of this modelling approach is that the interaction between the individual phases creates the bulk material behaviour, critical stress values are assumed to be within the range of the original material properties. This assumption also agrees with the elastic properties which appear to be similar to their bulk material properties. Simulations were performed using the fracture material properties for WC and Co, as shown in Table 7-3.

Shear strength is calculated using the von Mises yield criterion which takes shear yield stress to be $3^{0.5}$ of the tensile strength. The critical shear strain is assumed to be equal to the critical tensile strain.

As reasoned in the previous chapter, Co joint properties are also applied to elements at the WC/Co interface. This follows findings from Sigl and Exner [85] (discussed in Section 3.3.5) who found fracture to occur alongside carbide/binder interfaces in the binder phase rather than exactly on it, suggesting that the cobalt binder properties would dictate fracture at this interface.

Table 7-3: Fracture material properties used in simulation [32, 165]

Fracture Property	WC	Co
Critical Tensile Stress / MPa	450	280
Critical Shear Stress / MPa	260	160
Critical strain / %	0.1	8

7.4 Results

The previous numerical simulation by Sigl and Schmauder only studied the stress distribution in the binder phase for reasons discussed earlier. This, combined with the assumption of linearly elastic elements means that the stress distribution is therefore only valid for small scale yielding. On the other hand, FDEM is a dynamic simulation and the progression of the fracture through the domain can be visualised. Figure 7-3 shows a sequence of images from simulation result plotting stress (σ_{yy}) distribution across the domain. Together they illustrate key stages of the crack propagation process.

As force is applied stress throughout the microstructure increases, with stresses mainly being transferred through WC grains. Local stress concentrations are naturally formed at the interface between grains which are angular due to the shape of the WC crystal, see Figure 7-3a.

The initiation notch creates a local stress concentration which starts to propagate along the WC/Co boundary, see Figure 7-3b. This propagation halts when it reaches the Co phase which is much more ductile than the ceramic phase. Stress continues to build at the crack tip, but fracture in the Co phase is prevented as the surrounding WC structure constricts displacement. Forces are therefore required to disperse through the adjacent WC grain structure until stresses are sufficiently high enough to cause fracture along a nearby WC/WC interface between grains *iii* and *iv*, see Figure 7-3b. Fracture initiates between two grains where a natural stress raiser is created at the interface between two angular grains. Redistributed stresses from the crack tip can initiate fracture at this point and causes the crack to jump across the Co region.

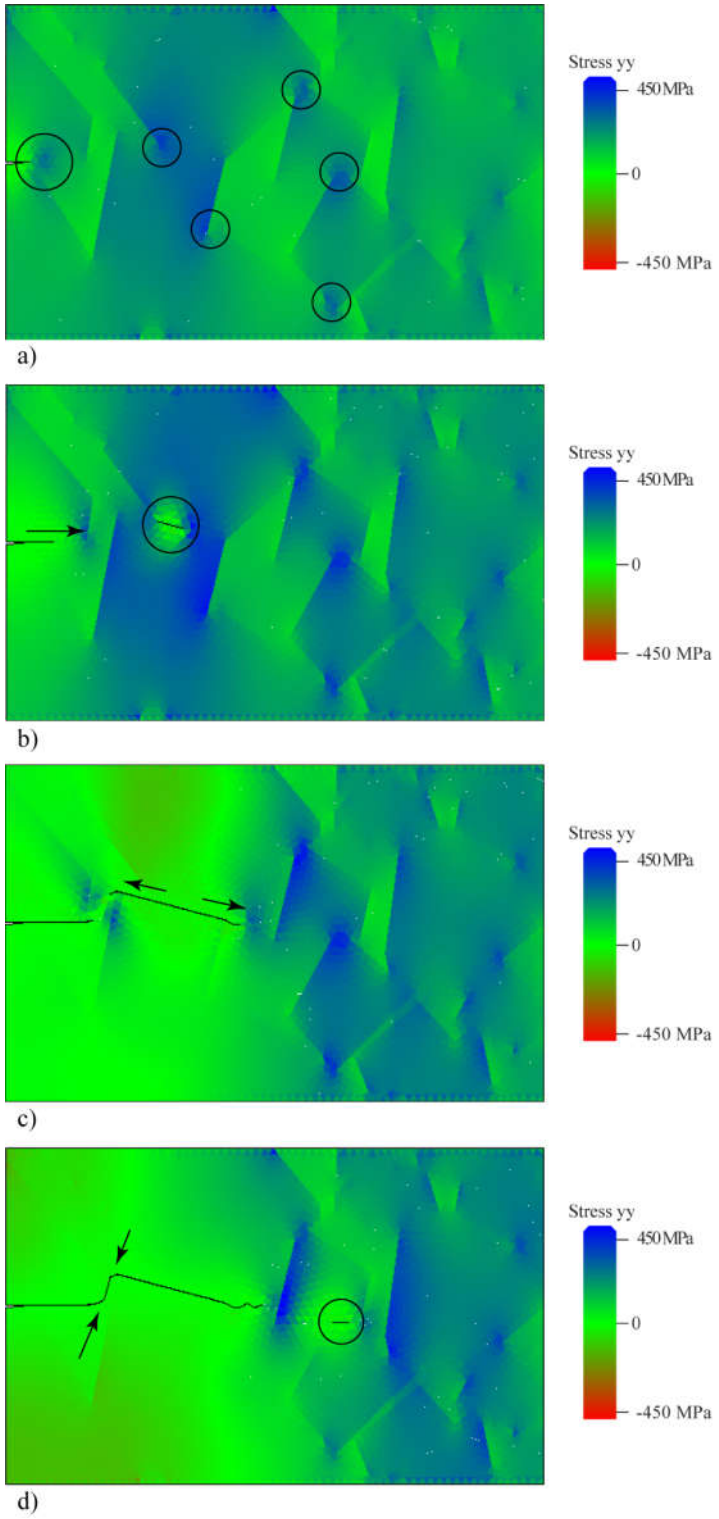

Figure 7-3: Simulation visualisation results of fracture propagation process, showing stress yy. Circles and arrows highlighting a) stress concentration in WC grain interfaces b) fracture propagating along WC/Co interface and jumping across binder region creating microfracture ahead of main crack tip c) microfracture propagating ahead of crack tip and d) microfracture joining up with main fracture and repeat of microfracture process ahead of main crack tip.

This second fracture propagates along the WC/WC and WC/Co interfaces in both directions, see Figure 7-3c. Stresses are once again redistributed in the microstructure ahead of the crack as the primary load bearing structure is removed.

Fracture also propagates through the Co phase towards the initial fracture until it finally connects creating a continuous fracture. The whole process is repeated as once again the fracture appears to jump across the binder phase and initiates ahead of the crack front at a WC/WC interface, see Figure 7-3c.

The discrete nature of this fracture process can also be seen from analysis of the element fractures as tensile load is applied, see Figure 7-4. This demonstrates that fracture is not propagating in a linear relationship to applied load, with flat areas (highlighted) indicating parts of the simulation where fracture is not propagating despite strain linearly increasing.

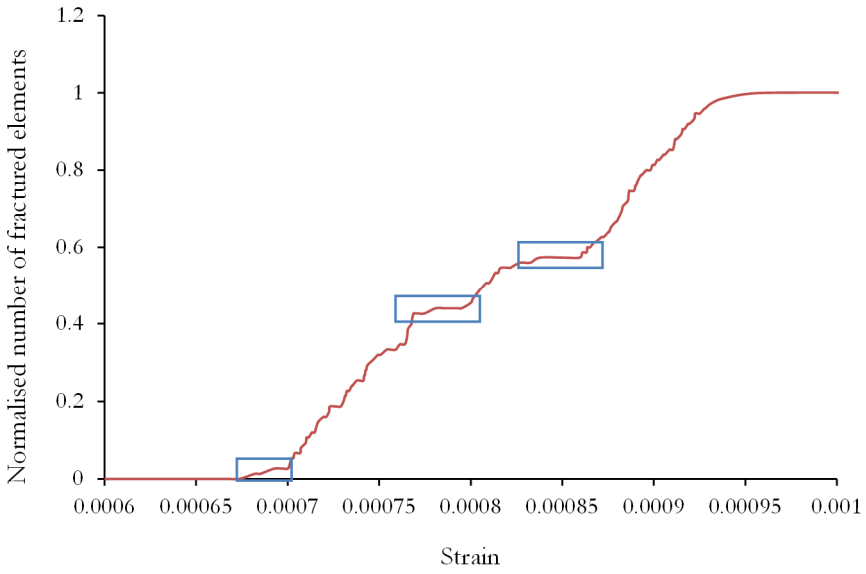

Figure 7-4: Demonstrating fracture propagating in start-stop way. Number of fractured elements normalised by number of fractured elements at end of simulation. Highlighted regions indicate regions of little propagation despite increasing strain.

A visualisation of the final fracture path, as well as comparison with experimental results, is provided in Figure 7-5. Key fracture locations along WC grains at B-C and D-E, as well as connecting fractures through the Co phase between A-B, C-D and E-F are replicated exactly by the simulation. The final fracture path along F-G is not so accurately simulated, reasons for which will be discussed later.

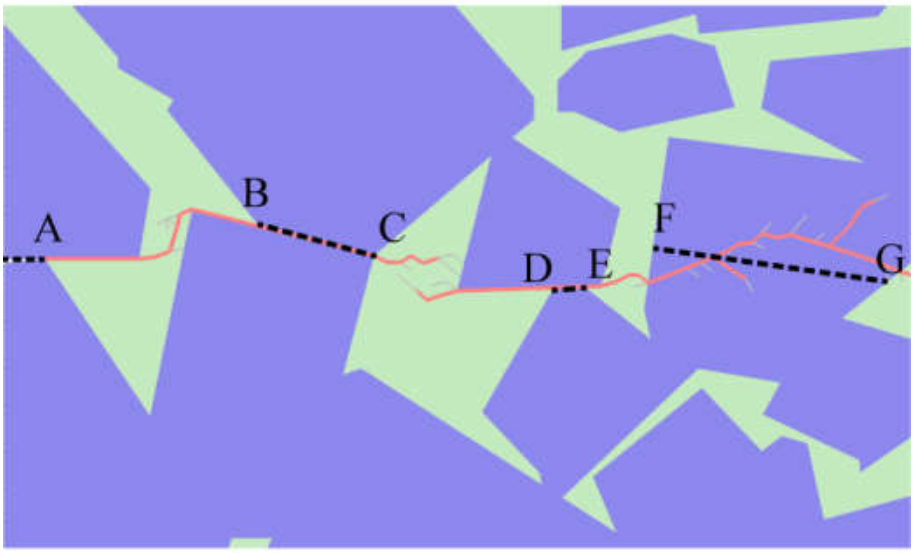

Figure 7-5: Final simulated fracture path (red) with respect to microstructure phases WC (blue) and Co (green). Compared with results from experimental fracture of WC denoted by dashed lines.

7.5 Discussion

7.5.1 Elastic Behaviour

In the simulation transfer of stress is initially through the carbide structure, with some stress concentrations occurring in the binder phase at WC grain corners. This indicates that WC-Co behaviour is dominated by WC initially. This result is counter to the behaviour described by Sundstrom whereby the stress-strain relation was first controlled by plastic deformation of the binder phase, followed by yielding of the carbide network. This result would only be possible if the binder can detach from the WC. Furthermore, this behaviour was not observed in fracture experiments which found only slight deformation to the binder phase outside the fracture path and was only found less than the binder mean free path away.

One of the major drawbacks of only considering elastic behaviour is restricting the time that the simulation is valid for to very small displacements. Although good correlations between areas which would enter the plastic regime and the location of voids in the binder phase from experimental studies can be obtained, as highlighted by Fischmeister et al. [172], only statistical estimates of where fracture is likely to initiate can be established. Without a method of incorporating the discontinuous nature of fracture the stress redistribution within the domain that follows cannot be

captured. Stresses will therefore change as the domain changes and is a significant advantage of the FDEM approach.

7.5.2 Fracture Behaviour

The dynamic simulation results correspond well to experimental observations of the fracture process as described by Sigl and Exner as discussed in Section 3.3.5, principally that smaller carbide fractures advance ahead of the crack tip followed by failure of the Co phase which links these fractures, therefore supporting this hypothesis. Furthermore, the final simulated fracture path through the microstructure closely resembles that obtained from the experiment.

The effect of localised stress concentration was observed by Lee and Gurland [67] as a result of compressive loading by hardness tests. FEM simulations by Sigl and Schmauder also highlighted the effect that angular grains had on the stress distribution within the binder phase when subjected to tensile loading. However, relatively little credit has been given to the importance of the geometry in determining the initiation point of fracture in the advancing WC phase microcracks. With stresses concentrated in the WC phase, areas of reduced cross section in the continuous carbide skeleton result in stress raisers being formed. These sections of the microstructure are first to fracture. This initial point then plays a major role in determining the final fracture path as it will dictate the stress field in the surrounding microstructure. Once fracture occurs in the carbide its load carrying capacity reduces to zero, forcing load to be taken up by either surrounding WC grains or in the binder phase. As previously highlighted in previous FEM studies the combination of an existing fracture and increased stress caused by the geometry of the microstructure leads to fracture in the binder phase.

Despite the assumption that fracture properties at the interface between WC grains are assumed equal to the grain itself, the simulation still predicts fracture at these interface points as a result of localised stress concentrations. Once again this lends weight to the importance of microstructure over material properties in determining fracture path. One fracture toughening mechanism that can be created in the microstructure is through increasing fracture tortuosity; that is to say, that the microstructure prevents the fracture from propagating linearly by diverting it around features in the microstructure thereby increase effective fracture length.

However, the simulation deviates from experimental observations in grain *vii* along path F-G, which could be due to a few of reasons. Firstly, because it is a 2D model certain physical characteristics are not captured accurately enough such as where grains are located in the z-axis which then affects how they interact with one another. More likely however is that the domain is not large enough to correctly model the fracture. As demonstrated by fractures across B-C and D-E, the surrounding carbide skeleton affects how stresses are distributed around a fracture. Because this is the primary mode in which stresses are transferred through the structure the absence of a modelled microstructure adjacent to the fracture along F-G is likely to impact how stresses are distributed in this area of the domain. Although a fixed boundary condition is applied along both vertical edges, this is not sufficient to overcome this restriction.

Bifurcation is also seen much more in the simulation than in experimental studies which have found little evidence of this. As discussed earlier, this is a result of mesh bias and lack of dynamic mesh refinement. Although mesh bias was introduced along WC/WC grain interfaces, mesh bias was not used to mimic the naturally formed slip planes in the WC crystals. This results in a much more irregular fracture path fracture which propagates where stresses are highest in the WC grain rather than propagating along the weaker crystal planes.

7.6 Conclusion

The study successfully demonstrates the suitability of FDEM to analyse the fracture behaviour of the two-phase composite material WC-Co at the mesoscale. Validation against fracture paths obtained using experimental techniques on WC-10Co and 2 μm grain size show good agreement. This is the first time that the discrete fracture steps in WC-Co, which has been described using experimental images, has been replicated through simulation. As the model uses fundamental material properties this is important in two respects. Firstly, it supports this fracture process description without having coded it directly. Secondly, it allows this method to be used across any microstructure of interest without multiple variables.

The numerical modelling studies discussed in Section 3.7.6 focused on the effects of the binder in improving bulk fracture toughness through improved understanding of ligament formation. By modelling fracture of both phases this study has enabled understanding of the initial phase of fracture whereby load is primarily distributed

in the carbide skeleton. Stress concentrations due to the geometries of this phase then lead to the initiation of fracture which precedes the effect of binder ligament formation studied by other models.

These results support the hypothesis that degradation mechanisms can be simulated through simulation of intrinsic material properties without the need for empirical values. Extension of this method would enable other physical wear processes such as pull out of carbide grains (W4 in Table 3-3). The ability to model properties and microstructure gives numerically modelling a clear advantage over empirical and mathematical models discussed in Sections 3.7.3 and 3.7.4 which are either too simplified to describe all the physical mechanisms or become so complex that they are difficult to validate. Furthermore, the validation against a real microstructure is a good test for models to understand if interactions between the various properties and parameters mimic those seen experimentally, which is difficult to do for hypothetical and idealised geometries (discussed in Section 3.7.5).

In this study only one domain is studied to demonstrate the potential of FDEM, however in order to fully validate the accuracy further simulation would need to be conducted on a range of domains with experimental data to validate results. These would also need to include the study of simulation parameter independence such as mesh density effects, domain size and DEM parameters discussed in Section 4.2.2. Further details about how to improve the accuracy of the simulation is discussed in the Future Work Chapter (Section 11.4.1).

Chapter 8 – Experimental Methodology

Chapter Highlights

The numerical modelling approach proposed requires knowledge of both the microstructure and mechanical properties of the individual phases. This chapter proposes experimental techniques that can be used to help inform modelling fracture behaviour at the mesoscale, with new ways of integrating conventional test outputs.

- The effects of corrosion of WC-Co on the microstructure is investigated using the standard three-cell electrode and SEM analysis to understand corrosion behaviour.
- The mechanical properties of corroded samples is tested using nanoindentation and indentation.
- Palmqvist fracture measurements are a way of validating simulated fracture behaviour of corroded samples.

8.1 Objectives

The literature review and computational section of this thesis have highlighted some key gaps in our understanding of WC-Co, which makes it difficult to model the physics accurately. These shortcomings are attributed partly to the experimental approaches that have been adopted which have helped our fundamental

understanding of wear processes but has little impact in the modelling community as findings are described in terms of global behaviours, such as mass loss, or visual inspection of surfaces which describe differences in appearance. In modelling it is relatively easy to model a single interaction or relationship, for example the stress-strain relationship of a single element. However, as the number of interactions is increased this becomes more difficult to incorporate. This is in contrast to experimental studies where it is extremely difficult to isolate a single parameter, but it is comparatively easier to extract data from a sample that has undergone multiple interactions, as would be the case for in-service components. The differences between the two fields can be visualised in Figure 8-1 which highlights the difficulty in bringing them together.

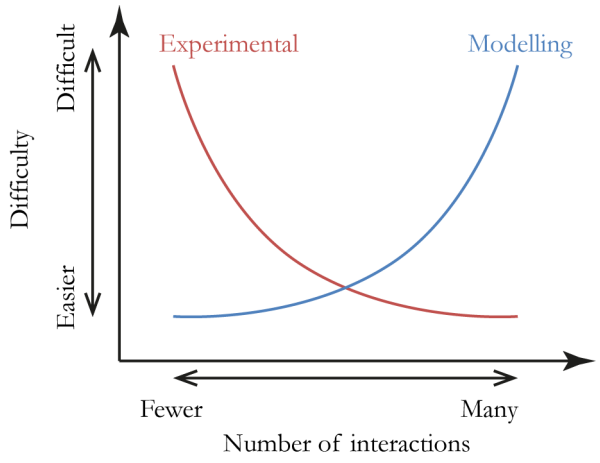

Figure 8-1: Comparing difficulty of experimental vs modelling approach.

As discussed in Section 3.5.2, current experimental approaches for studying tribocorrosion use scratch or microabrasion testing. However, working at this length scale is not practical for modelling due to the number of interactions involved combined with the current limitations of models. This disparity has resulted in divergence in approach of modelling and computational fields. In order to move towards a greater collaboration between the modelling and experimental sides of the field a new experimental focus on intrinsic material properties is therefore proposed.

As shown in Chapter 7, modelling at the mesoscale is beneficial as it is suitable length scale for both experimental and computational approaches. It allows both material properties, composition and microstructure to be considered explicitly. Furthermore, computational results can be directly compared against experimental results. This is therefore chosen as the length scale at which to conduct experimental studies.

Studying these three experimental inputs: microstructure, material properties and validation data therefore forms the basis of the experimental work, see Figure 8-2.

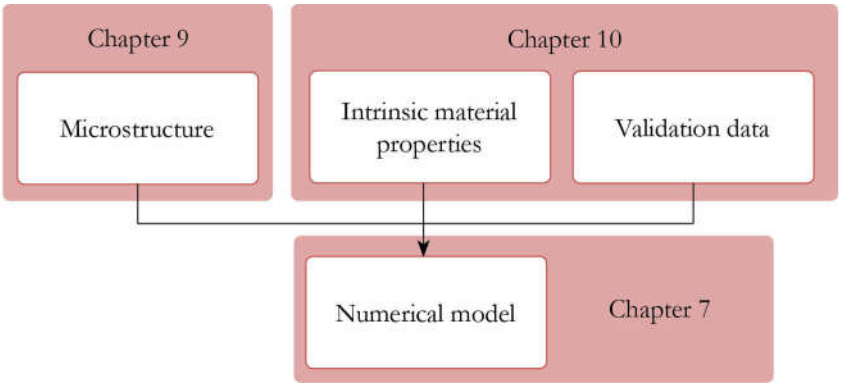

Figure 8-2: Experimental inputs required for numerical model.

The literature review suggested that there is still significant discrepancy regarding the electrochemical behaviour of WC-Co, see Section 3.6.5. In particular, whether pseudo-passivation occurs in WC-Co and if so, what causes this effect? Additionally, more focus has been made of electrochemical behaviour in acidic compared to alkaline conditions. The corrosion study will therefore seek to clarify these two issues by studying electrochemical behaviour for both acidic and alkaline solutions and analyse the corresponding effects on the microstructure.

It was observed that experimental tests on WC-Co are typically approached from either a material science or corrosion science approach. However, the most insightful studies were those two are brought together. From the material science approach there has been significant study of hardness and fracture analysis. In the corrosion science field, most of the focus has been on electrochemical behaviour in acidic conditions. In order to build upon these, the effects of corrosion will be linked to impact on material properties and fracture behaviour.

This chapter discusses the experimental methods used in this project. A description of the materials and solutions used in the project, as well as the methods used for preparation is discussed first. This is followed by the methodology of experimental electrochemical and mechanical testing techniques. Further experimental parameters are detailed in the relevant chapters. Finally, post-test analysis methods are described.

8.2 Experimental Plan

The experimental work is split into two pieces of work which explore novel methods that can be used to inform the modelling of a tribocorrosion system for the numerical

modelling approach which has been proposed. These focus on the two main modelling inputs: microstructure and material properties, see Figure 4-1. In Chapter 9, effects of corrosion on the microstructure are studied. In Chapter 10 mechanical properties of these corroded samples are tested, along with a technique which could enable simulations of corroded samples to be validated.

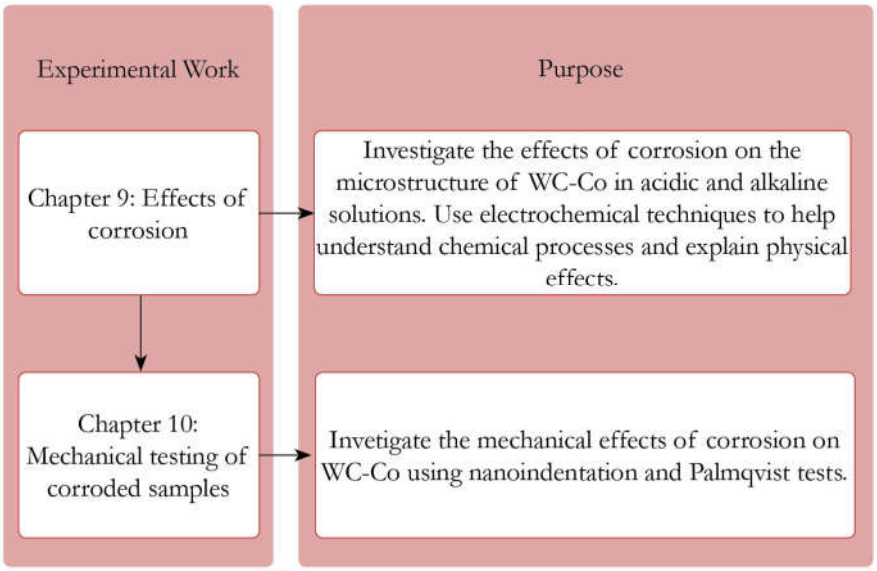

Figure 8-3: Experimental section is split into corrosion and mechanical testing.

Samples used were restricted to WC-Co grades only with no additional alloying elements. Alloying elements typically change the mechanical and corrosive properties of the material, so this was a way of reducing the complexity and reduce variables within the system. All experiments were carried out at room temperature to provide simplification to the system.

Static corrosion tests are conducted in both acidic and alkaline solutions, which span the pH range from pH 0 to pH 13. Although drilling fluids are typically between pH 8 and 11 (Section 2.5), the possibility of microenvironments of the surface, discussed in Section 3.6.7, could result in acidic conditions being experienced by the drill bits. It is therefore important to understand corrosion across the full pH range. However, the complex composition of drilling fluids can make isolation of chemical reactions challenging therefore solutions were restricted to common compounds, NaOH and H_2SO_4, so that chemical reactions are simplified. NaOH is a common additive used in drilling fluid as a sulphur scavenger, increase the viscosity of drilling fluids and maintain alkaline conditions downhole. Acids can also be found in downhole environments. These can be naturally occurring, for example oxidation of sulphide

material results in H_2SO_4, or by injection of acids such as HCl during the drilling process to dissolve rocks. The electrochemical behaviour can be compared against the different solutions, as well as conducting post analysis SEM and ESBD on the corroded surfaces to understand their effect on the microstructure. Use of both techniques will help in forming a clearer understanding of the processes involved and can to be used to support findings from each other, thereby strengthen hypothesises. This method of analysis was employed by Human and Exner [129] and Sutthiruangwong et al. [49] in acidic solution (H_2SO_4).

Once electrochemical corrosion tests have been conducted mechanical testing of the corroded surfaces will be done. This will attempt to make an important connection between electrochemical corrosion, mechanical properties and microstructure. Mechanical properties are measured using nanoindentation which can measure the properties of individual WC grains. In addition, to understand how fracture behaviour is altered the Palmqvist method, discussed in Section 3.3.4, is performed post corrosion to measure fracture toughness. As corrosion is a surface effect this approach has the benefit of being able to measure this corrosion layer without interference with the uncorroded bulk material below. Further understanding is achieved by characterisation of the cracks employing a similar method to that used by Sigl and Exner [85] who did this for fracture characterisation from three point bend tests, see Section 3.3.5.

While this approach might not be able to answer all of the questions raised in the numerical modelling, it does take a step forward in bringing computational and experimental approaches together.

8.3 Sample Preparation

Commercial grades of cemented tungsten carbide are chosen which are typically used in oil and gas drilling applications, see Section 3.1.1. Samples are cylindrical with diameter of 10 mm and depth of 5 mm. WC-11Co samples were supplied by Boart Longyear and WC-6Co by Marshalls Hard Metals Ltd. Composition and properties are given in Table 8-1.

Table 8-1: Sample composition

Composition	Co / wt.%	Hardness / HV	Density / g cm^{-3}
WC-6Co	6	1419	14.95
WC-11Co	11	1370	14.43

Indentation and corrosion tests are very sensitive to surface defects so surface preparation is critical in achieving consistent results. This is also necessary when conducting corrosion tests so that contaminants are removed from the surface and minimise stabilisation time of anodic and cathodic regions. All samples were lapped on a Kemet 15 diamond lapping machine using diamond paste at 25 μm and 14 μm for 20 minutes each then polishing on 6 μm and 1 μm diamond paste for 2 minutes and 1 minute, respectively. Between each stage samples were ultrasonically cleaned in propan-2-ol for 10 min to remove any diamond paste. A mirror finish was obtained with roughness values of R_a = 7.5 nm ±1 nm. SEM images of uncorroded WC-6Co and WC-11Co samples are shown in Figure 8-4.

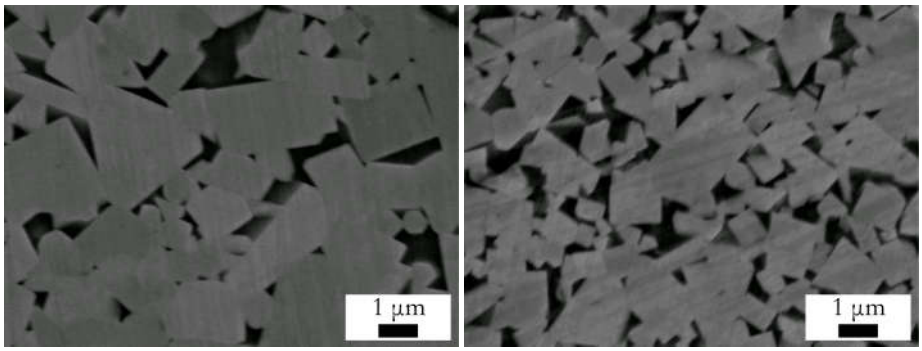

a) **b)**

Figure 8-4: SEM backscatter image of a) WC-6Co sample and b) WC-11Co sample.

As discussed in Section 3.2, microstructural parameters are also important in defining the bulk material properties. Using the linear intercept method and Equations (3.4), (3.6) and (3.7) microstructural parameters are calculated for the two samples, results shown in Table 8-2. 1000 counts were taken for N_{CC} and N_{BC} to minimise error.

Table 8-2: Microstructural properties of WC-Co samples. Errors are 1 standard deviation

Composition	Mean grain size / μm	Contiguity	Binder mean free path / μm
WC-6Co	1.25 ± 0.30	0.61 ± 0.17	0.30 ± 0.17
WC-11Co	0.84 ± 0.16	0.46 ± 0.15	0.22 ± 0.09

8.4 Electrochemical Techniques

8.4.1 Solution Preparation

Sulphuric acid (H_2SO_4) was chosen as it is a solution that is commonly used in the literature and therefore allows easier comparison of results. Sodium hydroxide (NaOH) was used as the alkaline solution. This is again commonly used in literature but is also an additive used in drilling fluids, see Section 2.5. Solutions were prepared from reagent grade chemicals supplied by Fisher Scientific and diluted down using distilled water to the required concentration. Required concentration of each solution was calculated from:

$$V_s = \frac{V_R\left[\frac{10\exp(-1pH)}{N_s}\right]}{\frac{c_{MR}\rho}{MW}} \tag{8.1}$$

Where V_s is volume of stock solution required, V_R is required volume of solution, N_S is normality and c_{MR} the stock solution mass ratio. pH values of diluted solutions were corroborated using a Hanna Instruments pH 211 meter. Solutions used in experiments are shown in Table 8-3.

Table 8-3: Test solutions

pH	Solution	Molecular Formula	Concentration
0.3	Sulphuric acid	H_2SO_4	0.5 M
4	Sulphuric acid	H_2SO_4	0.05×10^{-3} M
10	Sodium hydroxide	NaOH	0.1×10^{-3} M
13	Sodium hydroxide	NaOH	0.1 M

8.4.2 Potentiodynamic Polarisation

A standard three-cell electrode setup was used consisting of the specimen with 6 mm diameter exposed area (28.3 mm^2) as the working electrode, silver-silver chloride reference electrode with Luggin capillary and graphite counter electrode. All potentials presented here are reported with respect to silver-silver chloride (Ag/Ag/Cl) electrode. Other common electrodes that are used experimentally are listed in Table 8-4.

Table 8-4: Electrode Potentials for selected reference electrodes at 25°C, potential with respect to standard hydrogen electrode

Reference Electrode	Abbreviation	Electrode potential
Saturated Calomel Electrode	SCE	+244 mV
Silver/Silver chloride electrode (3.5 M)	Ag/AgCl	+205 mV
Standard Hydrogen Electrode	SHE	0

Experiments were carried out at room temperature and the corrosion cell was placed inside a Faraday cage to minimise electrical interference. Data was collected using a Gamry Instruments Reference 600 potentiostat and Gamry Framework software v6.33.

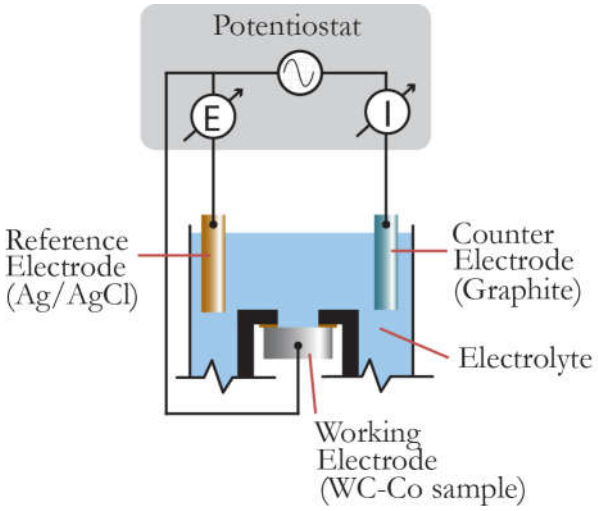

Figure 8-5: Schematic diagram of three cell electrode setup.

E_{OCP} measurements were collected at 1 Hz for 3 h while the surface stabilised to see how long it took to reach quasi-steady state conditions. Generally three scans of each combination were performed, unless there was a significant difference in values obtained. In this case additional experiments were performed in order to be confident that the behaviour had been accurately captured. For instance, in the example shown in Figure 8-6, Test 1 and Test 2 settled at around −290 mV. In Test 3 it was −250 mV, so a fourth test was performed which also obtained an open-circuit potential of −290 mV so this value is taken. These differences are likely to arise from surface imperfections that give rise to localised corrosion events which have a significant impact on the overall surface. For clarity, in the results section only one of the correct scans is shown for combination of sample and solution. Equilibrium conditions were obtained before further electrochemical techniques.

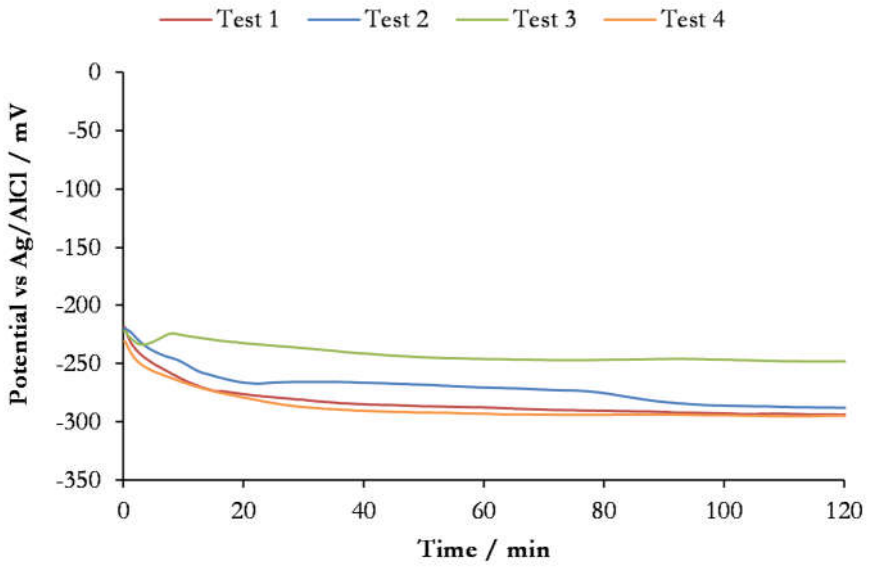

Figure 8-6: Reproducibility Open-circuit Potential for WC-6Co in 0.5 M H_2SO_4.

Polarisation scans were conducted starting from an overvoltage of −200 mV *vs* E_{OCP}. This was found to provide enough information for Tafel constants to be calculated whilst not having hydrogen evolution occurring. This was increased to +1500 mV *vs* E_{OCP} in order to fully capture anodic behaviour whilst not inducing oxygen evolution. Scan rate was performed at 1 mV s^{-1}, although the effect of scan rate is has also been reviewed in Sections 9.3.2 and 9.5.2. Gamry Echem Analysis software v6.33 was used to determine Tafel constants and the corrosion current performed automatically using a non-linear least square fit of the Butler-Volmer Equation, see Section 3.6.5. These values were then verified manually using approximation methods.

8.5 Mechanical Techniques

8.5.1 Nanoindentation Testing

Nanoindentation is able to characterise the mechanical properties of materials at very fine resolution and has been used successfully to measure the mechanical properties of WC-Co [45, 47, 57, 185]. Unlike macro and micro indentation, the size of the residual impressions are too small to measure directly using visual techniques, therefore the contact area is derived from depth of penetration. Accurate geometry measurements of the indenter then allow size of the area contact to be determined from which hardness and Young's Modulus can be calculated.

These parameters are commonly derived using the Oliver-Pharr method [187-189]. The indentation modulus is determined from the gradient of the unloading of the load-displacement response. In an ideal set up indentation modulus would be equal to Young's modulus, see Figure 8-7. However factors such as pilling up will alter the accuracy.

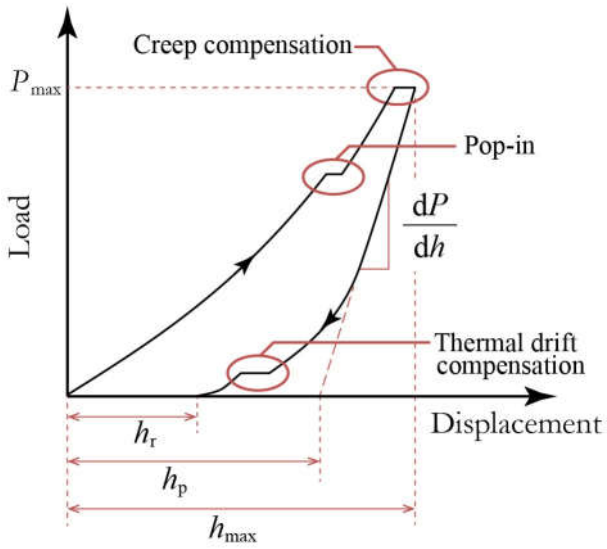

Figure 8-7: Typical load-displacement response from nanoindentation test, showing elastic-plastic loading followed by elastic unloading.

Nanoindentation was carried out using a NanoTest Platform 2 nanoindenter (Micro Materials Ltd., Wrexham, UK) using a Berkovich diamond indenter. Indentations were performed in load-controlled mode. Samples are mounted with adhesive onto an aluminium stub and attached to a motorised three axis stage. Setup is mounted on granite frame which is placed on an anti-vibration table. This is all housed inside a cabinet and located in an air-conditioned laboratory to minimise environmental noise and temperature fluctuations.

The system is based on a pendulum which is controlled through an electromagnet. An image of the setup is shown in Figure 8-8. By applying a DC current to the coil a precise load can be applied to the indenter. The corresponding displacement is measured through capacitor plates located directly behind the indenter. One plate is fixed while the other is attached to the pendulum and will move with the indenter. By measuring the change in capacitance and equivalent displacement can be calculated.

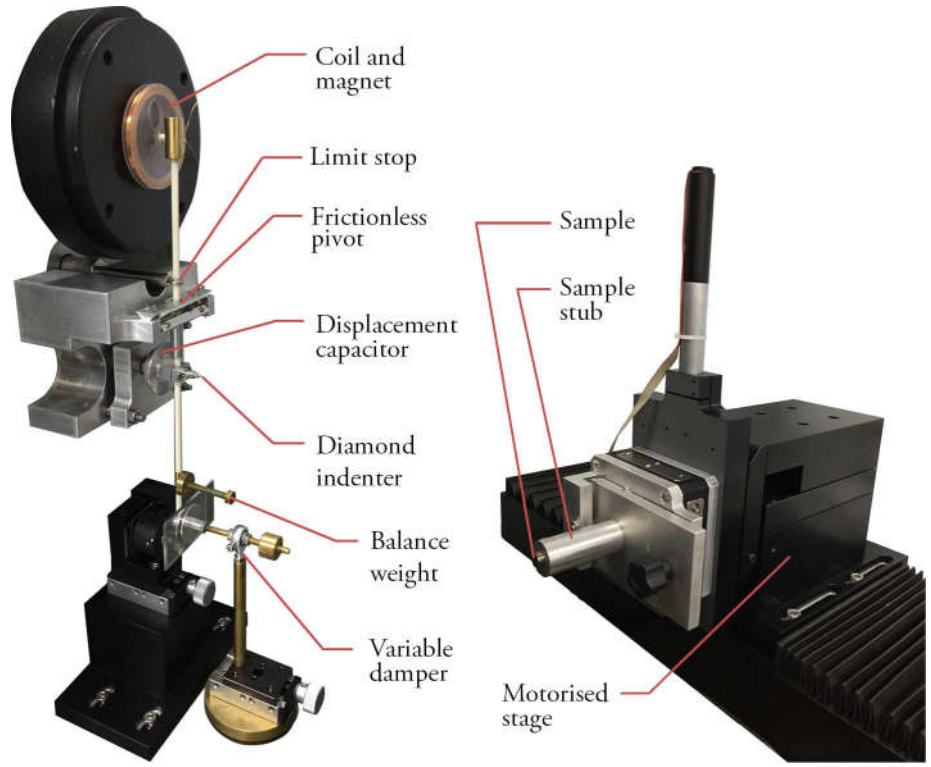

Figure 8-8: NanoTest Vantage setup. a) Pendulum and b) Stage.

For an ideal Berkovich indenter, the plastic depth of the indent, h_p, is related to the projected area, A_c, by:

$$h_p = \sqrt{\frac{A_c}{24.5}} \tag{8.2}$$

For loads of between 1 mN and 30 mN, depths were in the range of 10 nm to 250 nm. However, calibration is required to account for actual tip geometry which can vary over the lifetime of an indenter tip as it is worn from repeated testing. This is performed by applying the diamond area function:

$$A_c = a_{12} h_p^{\,2} + a_{13} h_p \tag{8.3}$$

Where a_{10} and a_{11} are fitting parameters which account for deviation from an ideal Berkovich indenter and rounding of the tip respectively. These values are obtained by running a calibration routine on a silica sample which has known properties. The reduced modulus of the sample can then be calculated from:

$$E^* = \frac{dP}{dh} \frac{\sqrt{\pi}}{2\beta_{BERK}\sqrt{A_c}} \tag{8.4}$$

Where β_{BERK} is the indenter geometry shape factor which is 1.034 for Berkovich. The indentation modulus, E^*, is related to the elastic properties of the two materials in contact (sample and indenter):

$$\frac{1}{E^*} = \frac{\left(1-\upsilon_1^2\right)}{E_1} + \frac{\left(1-\upsilon_2^2\right)}{E_2} \tag{8.5}$$

Young's modulus of the sample can be calculated using Equation (8.5) by knowing the indenter properties, shown in Table 8-5, as well as v of the sample.

Table 8-5: Indenter properties

Indenter type	Material	Young's Modulus / GPa	Poisson's ratio
Berkovich	Diamond	1141	0.07

Loading and unloading were performed over a 25 s period, and thermal drift compensation was performed for 60 s post-test. Hold at maximum load was completed for 20 s to compensate for creep. Analysis of data for calculation of material properties was performed using Nanotest Vantage software v40.52.

8.5.2 Hardness and Palmqvist Testing

Indention at higher loads allows understanding of the larger scale effects and how the ceramic and binder phase interact. Surfaces of the WC-Co samples are indented with a Vickers pyramid indenter (Vickers Limited) with applied loads of between 10 kgf and 50 kgf, equivalent to a range of 100 N – 500 N. The applied load is held for 10 s. At each load measurements are taken as an average of diagonal lengths, d, from at least five indents (10 measurements), which were typically in the range of 100 μm – 300 μm. From these measurements Vickers Hardness value can be calculated:

$$H_V = 0.1891\frac{P}{d^2} \tag{8.6}$$

Where P is the applied load and d the diagonal length. This can then be converted to metric using:

$$H = 0.009807 H_V \tag{8.7}$$

This method also allows the fracture toughness of brittle materials to be measured using the Palmqvist method by measuring the length of the cracks that nucleate at the corners of the diamond impression, as discussed in Section 3.3.4. Fracture toughness is calculated using the crack resistance term, W, originally defined by Exner [87] and later modified by Ogilvy et al. [81] and Perrott [82] to include the threshold indentation load, P_0:

$$W = \frac{\left(P - P_0\right)}{4\bar{a}} \tag{8.8}$$

Where $\bar{a}$ is the mean length of the four lateral vent cracks, which typically averaged between 5 μm – 125 μm. Measurements are taken as an average of lengths are taken from at least 4 indents (16 measurements). The geometry of the impression left by the indentations is shown in Figure 8-9.

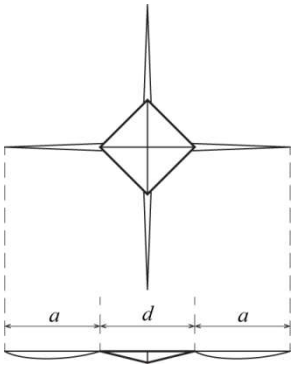

Figure 8-9: Geometry of Vickers indentation with Palmqvist cracks shown diagonal length '*d*' and lateral vent crack length '*a*'.

Fracture toughness, K_{IC}, is then calculated from the derivation by Shetty et al. [83], Section 3.3.4, using the geometry of the indenter:

$$K_{IC} = 0.0889\left(HW\right)^{0.5} \tag{8.9}$$

This equation was also found to be the most accurate by Spiegler et al. [84] when compared to other models, although due to assumptions about the crack type it only retains accuracy for fracture toughness above 8 MPa $m^{0.5}$, below which median cracks may occur which are not considered in this model. Similarly, the minimal pileup and elastic compression of the plastic zone is assumed, restricting it to fracture toughness up to 15 MPa $m^{0.5}$.

8.6 Post Test Analysis

8.6.1 3D Optical Microscopy

Optical microscopy and surface profilometry was performed using the Alicona InfiniteFocus. This is a 3D optical microscope that is able to provide high resolution images and uses light to infer the topography of a surface in order to generate a 3D model of the surface. Objective magnification ranges between ×2.5 and ×100. From this it can perform roughness measurements in accordance with EN ISO 25178. It was also used to measure the diagonal lengths of Vickers pyramid indents discussed in Section 8.5.2 and Palmqvist fractures.

8.6.2 SEM (Scanning Electron Microscopy)

SEM images are made using a JEOL JSM-6500F in both secondary and backscatter electron mode (BEM), see Figure 8-10.

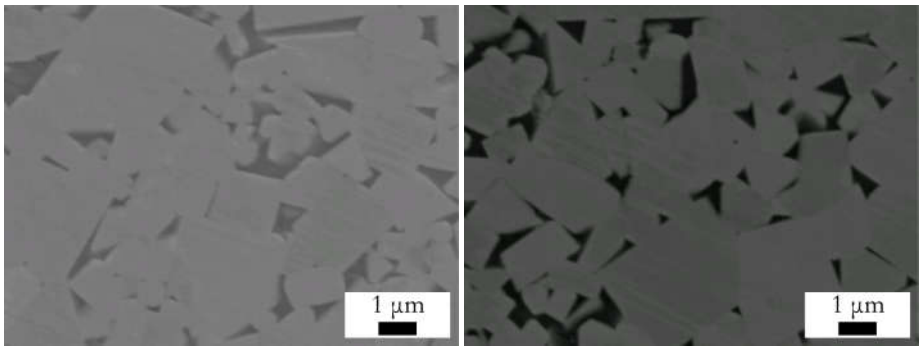

a) **b)**

Figure 8-10: SEM image of WC-6Co sample comparing a) secondary electron and b) backscatter electrons.

Accelerating voltages of 15 kV and beam current of 91 µA were found to provide the best image quality. The working distance was set to 10 mm which provides good compromise between high depth of field and resolution. The electron range or depth of electron penetration, R_{KO}, was described by Kanaya and Okayama [190] as:

$$R_{KO} = \frac{0.0276 A_W E_a^{(5/3)}}{\rho Z_a^{(8/9)}} \tag{8.10}$$

Where A_W is the atomic weight, E_a is the beam energy and Z_a atomic number. For WC and Co the R_{KO} for the voltage used is 0.65 µm and 0.85 µm respectively.

8.6.3 EDX/EDS (Energy Dispersive X-ray Spectroscopy)

EDX allows chemical characterisation of bulk material by analysis of x-ray patterns deflected from the surface at depths between 300 nm and 3000 nm. This was performed on samples post corrosion testing to understand the chemical composition of products on the surface. The analysis was run for 60 s to obtain a clear spectrum from which the elements could be identified. This was also performed using the JEOL JSM-6500F with the same parameters as SEM imaging. An EDX area spectrum of the two samples is taken so that comparison can be made with corroded samples.

Table 8-6: EDX analysis of uncorroded samples wt.%

	Tungsten	Cobalt	Carbon
WC-6Co	90.4	6.37	3.23
WC-11Co	83.7	12.4	3.89

8.6.4 Fiji

Fiji is a distribution of ImageJ, an open source image processing software. It is used to extract coordinates from SEM images of Plamqvist fractures. Images are first scaled using scale bar and the multi-point tool is used to outline the fracture manually. The coordinate data can then be exported for processing.

8.6.5 Matlab

A Matlab script was created to characterise the fracture path using technique similar to that described by Sigl and Exner [85], discussed in Section 3.3.5. They used three parameters to categorise fractures: length distributions $N(l_d)$, angular distribution $N(\alpha_d)$ and linear roughness R_L as defined by:

$$R_L = \frac{\sum l_d}{L_{pr}} \tag{8.11}$$

Where L_{pr} is the profile length of the fracture. Fracture parameters are shown in Figure 8-11.

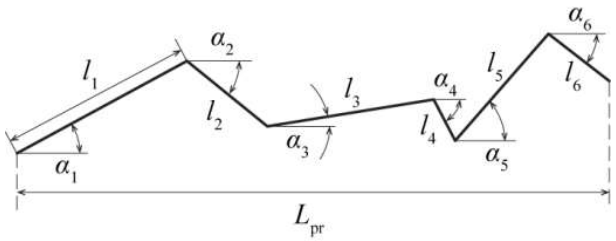

Figure 8-11: Fracture profile, after Sigl and Exner [85].

These parameters are obtained by importing the coordinates file from Fiji into Matlab and processing them using a script. The SEM image of the fracture is unlikely to be captured with the fracture running horizontal. This will change the projected length and angle of fracture. In order to align the coordinates linear regression is performed on the coordinate points. The coordinates are then rotated around the centroid of the fracture, see Figure 8-12. This script also orientates the four fractures which propagate outwards from the indentation into a common direction making it easier to process.

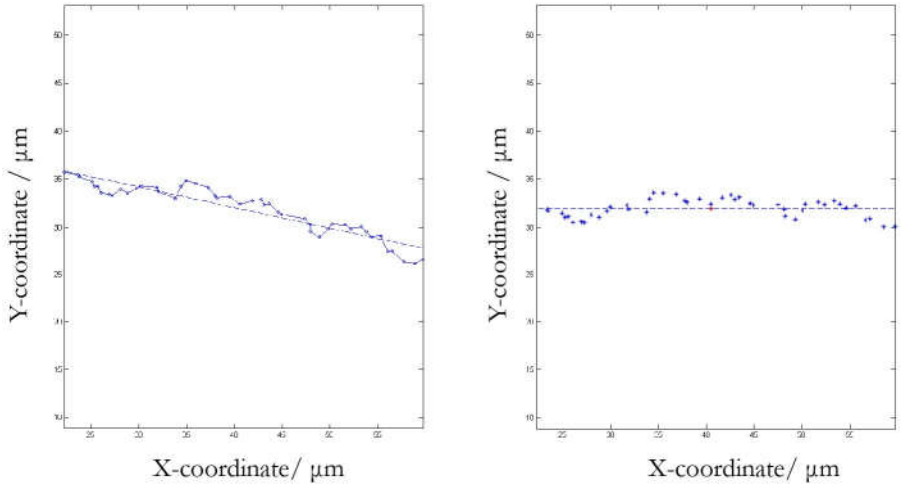

Figure 8-12: Rotation of fracture with linear regression a) input coordinate and b) after rotation.

Once alignment is performed l_d and α_d, as described in Figure 8-11, can be calculated for each section of the fracture from coordinate points from:

$$l_d = \sqrt{(x_2 - x_1)^2 + (y_2 - y_1)^2} \tag{8.12}$$

$$\alpha_d = \tan^{-1}\left(\frac{y_2 - y_1}{x_2 - x_1}\right) \tag{8.13}$$

Characteristic fracture profiles are then generated through average profiles from at least four Palmqvist fractures (12 fractures), typically consisting of between 400 and 1000 measurements. The full characterisation process is shown visually in Figure 8-13.

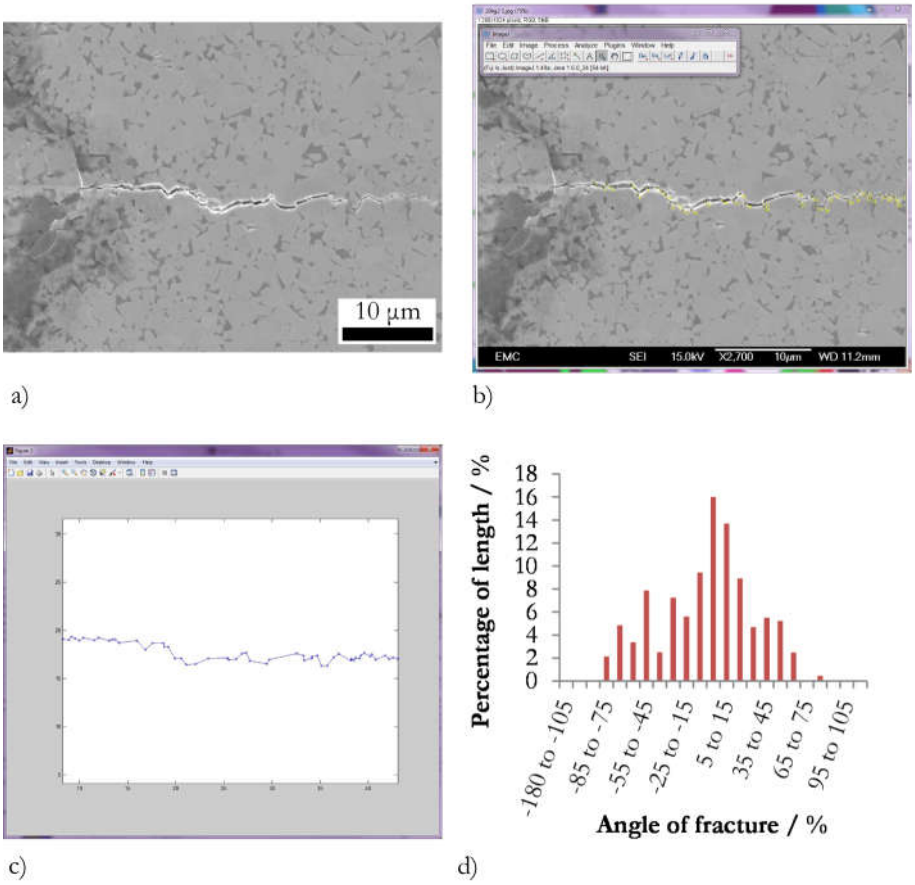

Figure 8-13: Process for characterisation of Palmqvist fracture a) SEM image of fracture from 20 kgf on uncorroded WC-6Co b) outline fracture using Fiji c) Matlab processing d) Graph histograms and average multiple fractures.

Chapter 9 – Electrochemical Response of WC-Co Exposed to Acidic and Alkaline Solutions

Chapter Highlights

Good modelling of fracture behaviour is reliant on accurate representation of the microstructure (Chapter 7). However, corrosive environments have been seen to alter this microstructure (Section 3.6). This chapter seeks to understand what microstructural changes occur and why they happen.

- Electrochemical analysis is able to help understand physical effects.
- Acidic corrosion is characterised by preferential dissolution of the binder, leaving a WC skeleton, whereas alkaline corrosion is characterised by pitting behaviour.
- Pseudo-passivation behaviour is limited to very acidic environments (pH 0) which results from binder depletion and is influenced by the microstructure.
- Modelling the effects of corrosion should reflect these microstructural changes, while modelling of oxide is not a priority as it will have little impact in a tribocorrosion system.

9.1 Experimental Objectives

In the literature review differences were found in the understanding of corrosion behaviour of WC-Co, as well as absence of a comprehensive review of the effects of different corrosive solutions, see Section 3.6.5. In order to understand and explain these results electrochemical tests are combined with post analysis techniques of the surface.

Rather than comparing multiple grades and alloying additions of cemented tungsten carbide only two grades are used, both of which have no alloying additions, WC-6Co and WC-11Co. Quiescent corrosion tests (no mechanical stirring or agitation from aeration) were performed in on the lapped samples which were immersed in naturally aerated acidic (0.5 M H_2SO_4 and 0.05×10^{-3} M H_2SO_4, pH 0.3 and pH 4; respectively) and alkaline solutions (0.1×10^{-3} M NaOH and 0.1 M NaOH, pH 10 and pH 13; respectively) to see how the material performed under a range of chemical conditions. Relating electrochemical behaviour (open-circuit potential, potentiodynamic polarisation and potentiostatic polarisation) with SEM and EDX analysis of the surface enables greater understanding of the corrosion effects on the individual phases of the microstructure which can aid modelling at the mesoscale.

9.2 Immersion in Acidic and Alkaline Solution

9.2.1 Surface Analysis

Extended immersion tests were performed on WC-6Co samples over a number of 3 or 7 days. Samples were placed in a beaker with 150 mL of corrosive solution which was covered with parafilm. SEM images of the sample exposed to 0.5 M H_2SO_4 show clear evidence of preferential depletion of the binder phase while the WC has little sign of degradation after three days, see Figure 9-1a. After seven days the binder has been completely removed and WC grains which were previously underneath the binder are uncovered, see Figure 9-1b. WC grains still show little sign of corrosive attack, with the polished and faceted WC grains on the surface still evident.

Unlike the more corrosive solution formation of a substance, likely oxide, was found on the sample exposed to 0.05×10^{-3} M H_2SO_4 solution, see Figure 9-1c. Initially the oxide is sparse, although after seven days a larger oxide formed which covered the majority of the surface, see Figure 9-1d.

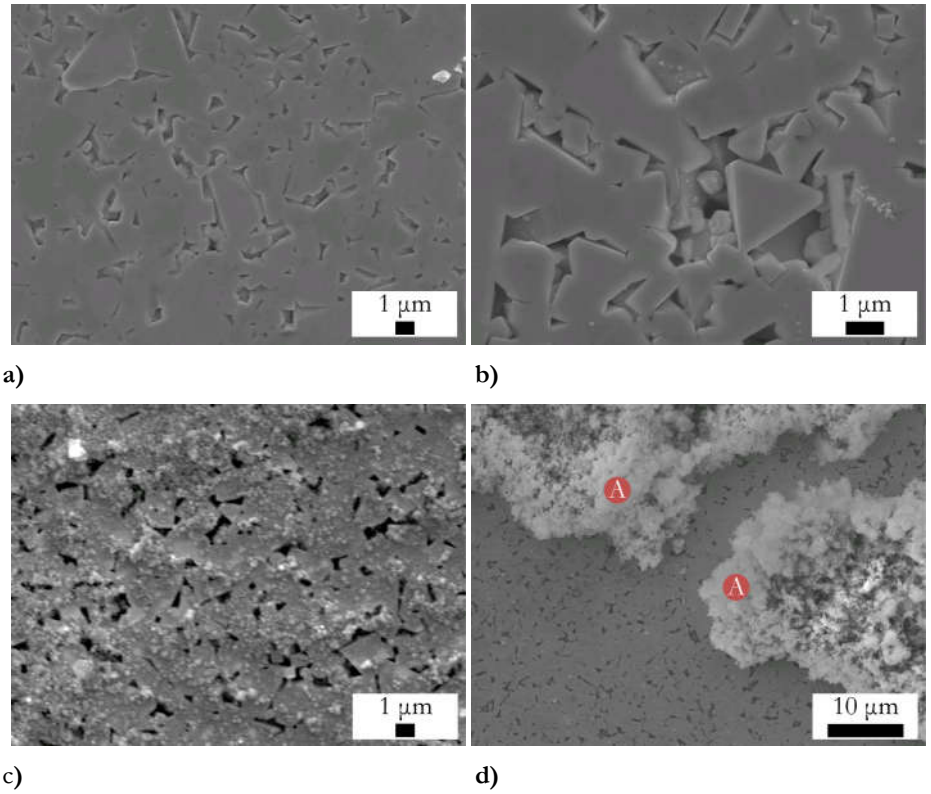

Figure 9-1: Immersion test of WC-6Co in acidic solution after a) 3 d in 0.5 M H_2SO_4 b) 7 d in 0.5 M H_2SO_4 c) 3 d in 0.05×10^{-3} M H_2SO_4 d) 7 d in 0.05×10^{-3} M H_2SO_4 A: Corrosion product.

There was little difference between three and seven day immersion in the alkaline solutions. An oxide film can be observed on the surface of the 0.1×10^{-3} M NaOH sample which was similar in appearance to that of the oxide in 0.05×10^{-3} M H_2SO_4, see Figure 9-2a. In the 0.1 M NaOH solution two scales of oxide were observed. A thin oxide covering the whole surface, see Figure 9-2b, and at the larger scale more substantial oxide region had formed, see Figure 9-2c and Figure 9-2d. The use of BEM helps to distinguish the larger oxide clusters from bulk material and thinner oxide on the surface, see Figure 9-2d. Adhesion of the oxide layer in both cases was very weak and light abrasion of the surface could remove the film.

To understand the overall effects on the microstructure, removal of the oxides formed was required (specifically for samples in 0.05×10^{-3} M H_2SO_4 and 0.1 M NaOH solutions). This was performed by light manual polishing with 1 µm diamond paste, for less than 5 s, to remove any oxide followed by ultrasonic cleaning in propan-2-ol for 10 min.

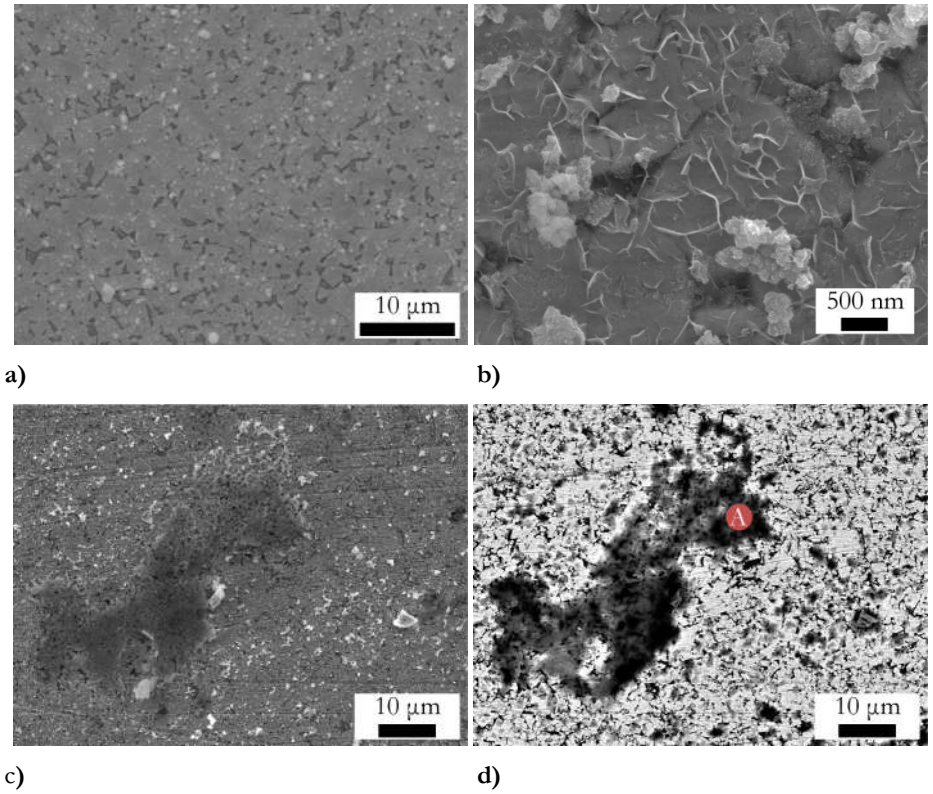

Figure 9-2: Immersion test of WC-6Co in alkaline solution after a) 7 d in 0.1×10^{-3} M NaOH b) 3 d in 0.1 M NaOH c) 3 d in 0.1 M NaOH d) 3 d in 0.1 M NaOH BEM image clearly showing formation more substantial oxide layer (indicated by A).

Taking a closer look at the binder itself a roughened surface in the binder regions can be seen in 0.5 M H_2SO_4, which has receded below the original polished surface, see Figure 9-3a. In the less acidic solution this roughened binder can also be seen, although to a lesser degree, see Figure 9-3b. Even after 7 d immersion the binder regions are not as depressed as after 3 d in the more acidic solution. Additionally, there appears to be preferential corrosion at the WC/Co interface. This effect is even more prominent in the 0.01×10^{-3} M NaOH solution leaving 'binder islands' in the binder regions, see Figure 9-3c. Unlike the acidic environment however the remaining binder material does not have a roughened surface. The surface of the 0.1 M NaOH sample is more akin to the 0.5 M H_2SO_4 surface than the less alkaline solution with binder regions significantly degraded, see Figure 9-3d. Furthermore, WC grains do not display their polished form suggesting that there has been corrosive attack.

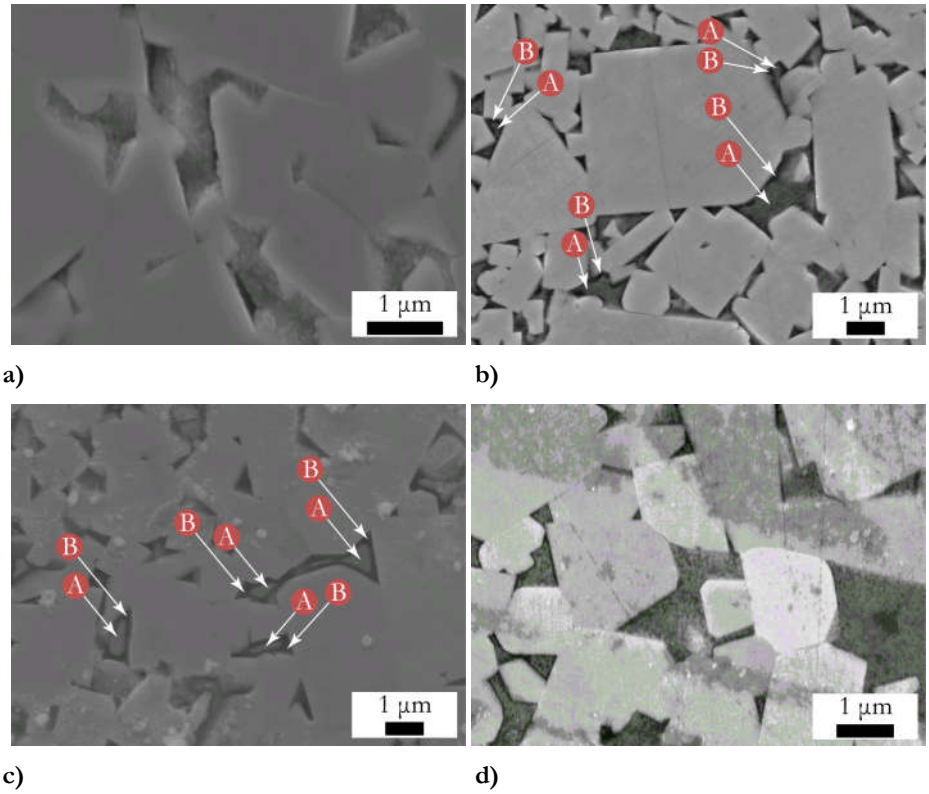

Figure 9-3: Comparing corrosion of binder phase in WC-6Co samples after immersion test a) 3 d in 0.5 M H_2SO_4 b) 7 d in 0.05×10^{-3} M H_2SO_4 A: binder and B: WC/Co interface c) 7 d 0.01×10^{-3} M NaOH A: binder and B: WC/Co interface and d) 7 d 0.1 M NaOH.

EDX analysis was performed on the corroded surfaces, the results of which can be seen in Figure 9-4 and Table 9-1. The analysis of the 0.5 M H_2SO_4 surface confirms a significant reduction in binder content, with a small presence of oxygen. In the binder regions minor amounts of cobalt was detected, with a low percentage of oxygen. The significant amount of oxygen in the layer that formed on the sample exposed to 0.05×10^{-3} M H_2SO_4 confirms the assumption that an oxide layer has formed. Additional, the high percentage of cobalt detected suggests that this is a cobalt oxide rather than tungsten oxide. Similarly, high levels of cobalt and oxygen were detected on the fragments found on the surface of the 0.01×10^{-3} M NaOH sample. The binder regions still indicate high cobalt content with some oxygen. In the 0.1 M NaOH sample Co percentage is still relatively high.

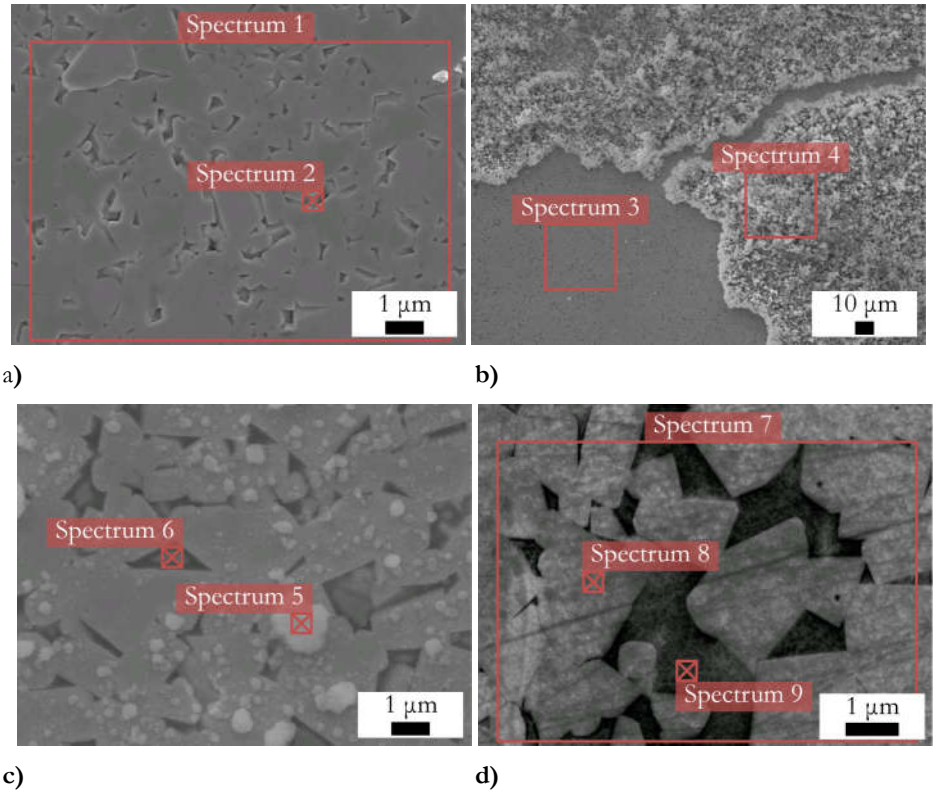

Figure 9-4: EDX sites of interest on WC-6Co samples a) 0.5 M H_2SO_4 b) 0.05×10^{-3} M H_2SO_4 b) 0.01×10^{-3} M NaOH and d) 0.1 M NaOH.

Table 9-1: EDX spectrum immersion test WC-6Co wt.%

Location	Solution	Tungsten	Cobalt	Oxygen	Carbon
Site 1	0.5 M H_2SO_4	93.91	nil	1.97	4.12
Site 2	0.5 M H_2SO_4	86.47	2.12	7.78	3.63
Site 3	0.05×10^{-3} M H_2SO_4	85.7	5	5.1	4.2
Site 4	0.05×10^{-3} M H_2SO_4	2.27	62.41	30.67	4.64
Site 5	0.1×10^{-3} M NaOH	25.66	54.59	19.75	nil
Site 6	0.1×10^{-3} M NaOH	11.04	84.61	4.35	nil
Site 7	0.1 M NaOH	86.13	7.29	1.53	5.04
Site 8	0.1 M NaOH	91.07	nil	1.26	7.67
Site 9	0.1 M NaOH	31.11	64.35	1.11	3.43

9.2.2 Open-Circuit Potential Measurements

Further understanding of corrosion when immersed in corrosive solution was undertaken by performing open-circuit potential measurements over a 3 h period. Samples stabilise at more negative potentials in the 0.5 M H_2SO_4 solution, see Figure 9-5. Furthermore, the higher content binder appears to stabilise at more positive potentials compared to WC-6Co. WC-6Co stabilises at around −295 mV and −260 mV in 0.5 M H_2SO_4 and 0.05×10^{-3} M H_2SO_4 respectively. This compares with −265 mV and −215 mV for the WC-11Co sample. However, the general behaviour of the two samples is similar. Results also show rapid stabilisation of the sample in 0.5 M H_2SO_4, reaching quasi-steady state within 30 min for both WC-6Co and WC-11Co samples, see Figure 9-5. This compares to nearly 1 h to stabilise in 0.05×10^{-3} M H_2SO_4 for both WC-Co grades.

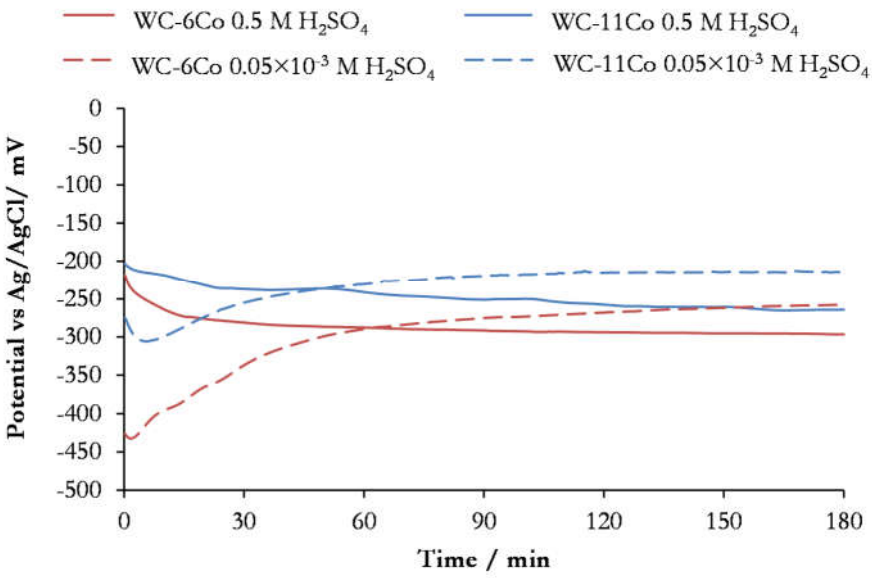

Figure 9-5: Open circuit potential for samples exposed to acidic solution.

In alkaline solutions behaviour is also similar between the two samples. A constant potential of around −234 mV was achieved in around 15 min for both WC-Co samples exposed to 0.1 M NaOH, see Figure 9-6. This compares to around 100 min in 0.1×10^{-3} M NaOH, although there is still a clear gradual tendency of the potential to become more positive. Small instability was also observed on the to 0.1 M NaOH samples, with sudden reductions and recovery of potential.

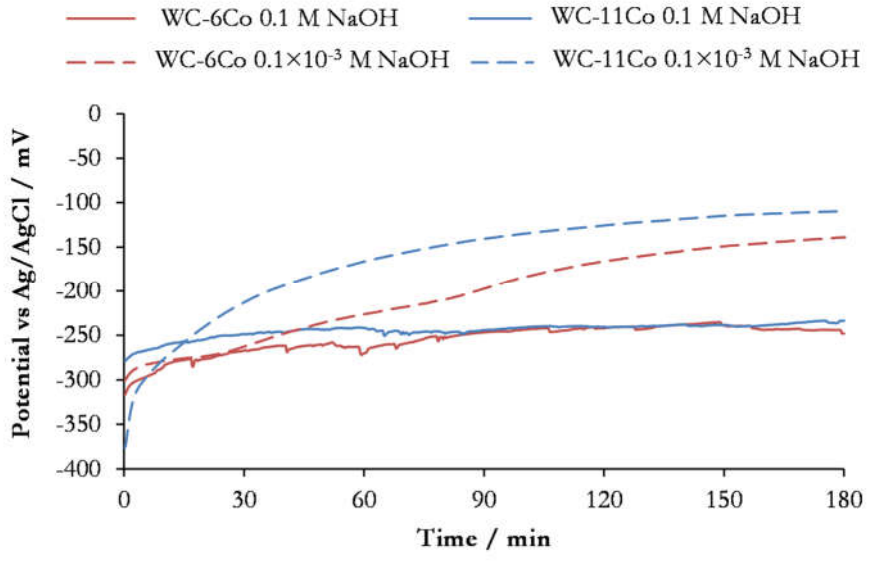

Figure 9-6: Open circuit potential for samples exposed to alkaline solution.

The instability of the samples is highlighted when comparing the change in potential per minute against the other solutions, see Figure 9-7. Usually samples tend to

gradually reach stability, defined here as when change in potential is less than 1 mV min^{-1}, and remain stable over time. However, in the 0.1 M NaOH solution samples continue to have short periods of high instability, seen as peaks above the stability line, even after the potential change has reached the initial 1 mV min^{-1} criteria.

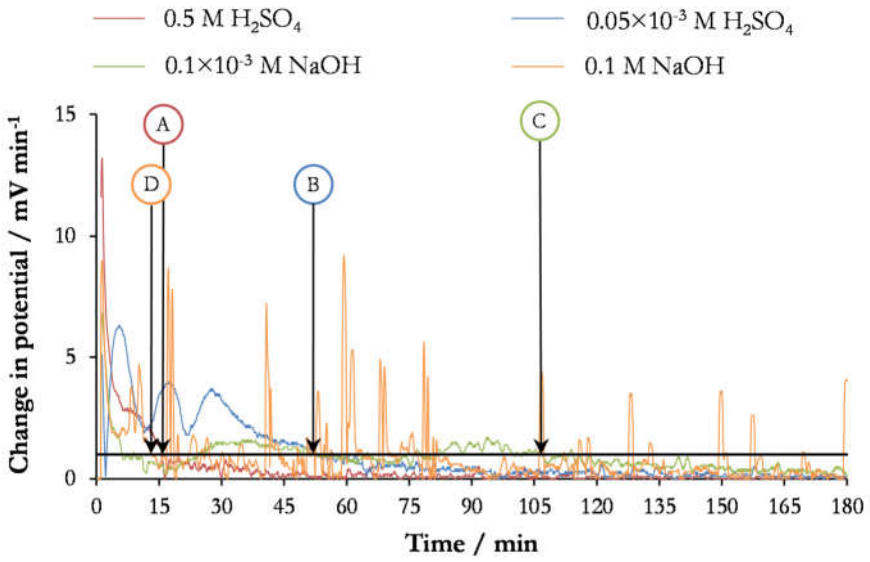

Figure 9-7: Time till stabilisation, defined as less than 1 mV min^{-1} (black line) for WC-6Co sample in A: 0.5 M H_2SO_4, B: 0.05×10^{-3} M H_2SO_4, C: 0.1×10^{-3} M NaOH and D: 0.1 M NaOH.

9.2.3 Discussion

The highly corrosive environments (0.5 M H_2SO_4 and 0.1 M NaOH) have faster kinetics which quickly leads to fast stabilisation of the open-circuit potential in less than 30 min. This compares with stabilisation after 60 mins for the less corrosive environments (0.05×10^{-3} M H_2SO_4 and 0.1×10^{-3} M NaOH). Furthermore, increased percentage of dissolved solids in the highly corrosive environments will reduce the resistance of the solution according to Ohm's law. Dissolved solids will also increase the amount of dissolved oxygen in the solution which can further increase the rate of corrosion.

Detection of oxygen in the sample exposed to 0.5 M H_2SO_4 suggests that not only is cobalt preferentially corroded, but isolated oxide is formed in the binder voids. This would explain the roughed appearance of the binder. This also supports the hypothesis by Human et al. [127] that the reaction occurs at the metal-oxide rather than oxide-solution interface, see Section 3.6.3. This would be in agreement with the Pourbaix diagrams, Figure 3-30, which suggest this could be WO_2, W_2O_5 or WO_3.

This oxide appears to provide little protection of the surface and by 7 d the oxide has likely dissolved into the solution leaving just the WC skeleton. As the WC grains have no evidence of corrosive attack, the tungsten oxide is therefore likely to have been formed from tungsten in the Co-W-C binder. The fragmented oxide that forms in the 0.05×10^{-3} M H_2SO_4 solution is likely to provide little protection to the surface. The high cobalt content, however, suggests this is not the same oxide that was found on the 0.5 M H_2SO_4 samples and likely to be $Co(OH)_2$. As with the 0.5 M H_2SO_4 solution no evidence of corrosion of the WC was seen.

One of the limitations of EDX is the spatial resolutions that can be obtained. Electrons analyse a volume around a point below the surface whose depth is dependent on the beam voltage and the material (see Section 8.6.2). This is particularly influential when measuring the binder phase which is relatively small and isolated. It is therefore likely that when measuring the binder phase, not only will alloyed tungsten in the binder be measured, but also the tungsten from the surrounding WC grains. EDX measurements which target the binder will therefore not be measuring the binder composition alone and will see a higher percentage of tungsten, for example Site 6 in Table 9-1. Similarly, on thin oxides the material below can influence the measured elements, for example Site 4 and Site 5 in Table 9-1. However, despite this drawback, EDX provides a good indication of the elements in a given area allowing identification of WC, binder or oxide.

The corrosion potential of the samples stabilise at between −295 mV and −215 mV which lie between the exchange potential of cobalt (−482 mV vs Ag/AgCl) and tungsten (−205 mV vs Ag/AgCl), see Section 3.6.2. This is in agreement with findings of other studies [51, 129]. Although a general stabilisation can be said to occur quickly in 0.1 M NaOH, instabilities suggest that local effects are happening across the surface which results in small but rapid decreases in potential. Recovery is also rapid, taking around a minute to return to the stabilised potential. This behaviour is often typical of materials that are prone to pitting behaviour, whereby localised corrosion events impact the bulk corrosion behaviour. This would correspond with SEM images of the binder islands which were very prevalent in the 0.01×10^{-3} M NaOH solution. These regions would have the potential to create pit and it is likely this behaviour would also be repeated in the 0.1 M NaOH, although corrosion product has now been created.

The preferential corrosion at the WC/Co interface is likely to result from differences in composition in the binder. Auger mapping by Kellner et al. [55] found that W and C are not evenly distributed in the binder and instead higher at the WC/Co where diffusion of the WC grains has occurred during the sintering process. A schematic of this is shown in Figure 9-8. Previously, increases in W content were associated with increases in corrosion resistance and the authors used this to explain higher corrosion resistance of samples tested in NaOH solution. However, this statement was originally made by Human et al. [127] in the context of acidic solutions. In alkaline solutions W in unstable, as can be seen from the Pourbaix diagram, and as such corrosion at the WC/Co will occur. The binder islands that are left are therefore likely to be the unalloyed Co which is more stable in alkaline solutions.

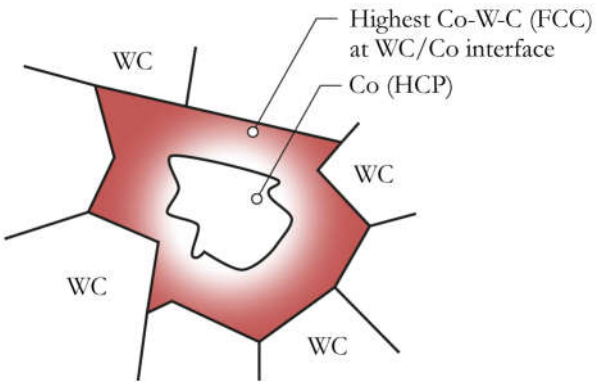

Figure 9-8: Schematic of distribution of alloying elements in binder as found by Kellner et al. [55].

Even although stabilisation occurs in the 0.01×10^{-3} M NaOH after 60 min for both samples, the tendency toward more positive potential over the test duration suggests that the surface is continuing to evolve over time. This behaviour is often associated with slow oxide formation on the surface which is more visible on the 0.1 M NaOH sample.

WC-11Co samples stabilise at higher potentials than WC-6Co samples in all solutions and expect for 0.1 M NaOH which stabilises around the same potential. As discussed, increases in W and C in the binder have been associated with corrosion resistance of the binder in acidic solutions. Furthermore, due to the effect of diffusion during sintering, Kellner et al. [55] also found small grain size results in an increase in W and C content. As the WC-11Co sample has an average grain size 0.84 μm compared to 1.25 μm for the WC-6Co this would suggest that the binder in the WC-11Co has higher proportions of alloying elements, thereby increasing the corrosion resistance

of the WC-11Co sample. This relationship however does not apply in the 0.1 M NaOH solution where WC grains are seen to be subject to corrosive attack. Despite WC-6Co having a slightly higher proportion of WC, in both grades the ceramic is the dominant phase and as such have similar corrosion rates. Galvanic coupling effects are therefore also likely to be more significant in 0.1 M NaOH when WC is unstable. This would then result in the cobalt oxide, likely $Co(OH)_2$, that forms from the release of Co ions.

9.3 Potentiodynamic Polarisation in Acidic Solution

9.3.1 Electrochemical Behaviour Results

Once initial stabilisation of the surface was reached, potentiodynamic polarisation scans were performed between −200 mV to +1500 mV *vs* E_{OCP} in the two acidic solutions. Results of scans are shown in Figure 9-9.

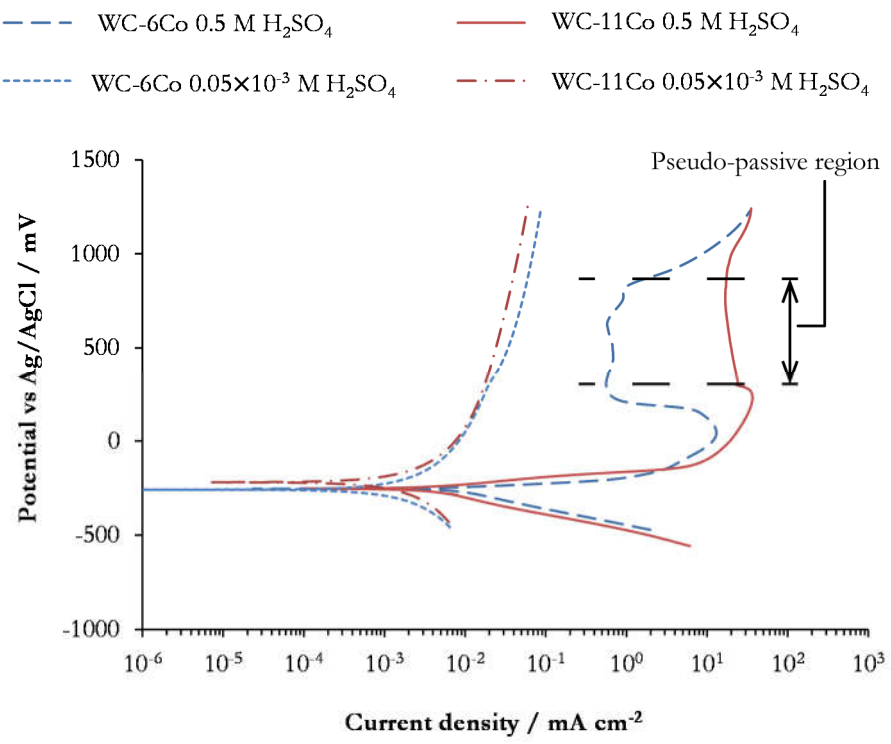

Figure 9-9: Potentiodynamic polarisations for WC-Co sample to assess the influence of acidic solutions (H_2SO_4). Scan rate of 1 mV s^{-1}.

Corrosion potential is around −255 mV in both acidic solutions. As expected this is between the corrosion potential of cobalt and WC and represents an average potential of the two phases. This value however is slightly more positive than that reported in the literature which tends to be in the region of −350 mV to −290 mV [49, 129, 130,

191]. This could be a result of differences in manufacturing technique which will affect the relative composition of Co-W-C binder.

For the WC-6Co sample in 0.1 M H_2SO_4 solution there is a clear drop in current density in the anodic region of nearly two orders of magnitude at a potential of 60 mV. After a maximum current density of 13 mA cm^{-2}, this is followed by stabilisation at around 0.6 mA cm^{-2}, before increasing again at around 800 mV. A similar behaviour is seen in the WC-11Co sample, although pseudo passivation occurred at a more positive potential of around 230 mV and suppressed current is only about half the maximum current density at 18 mA cm^{-2}. Corrosion currents in the 0.05×10^{-3} M H_2SO_4 solution are around one or two orders of magnitude lower than in 0.5 M H_2SO_4 for both samples and passivation behaviour is not observed. A summary of the electrochemical parameters measured from the polarisation curves are presented in Table 9-5.

Table 9-2: Electrochemical parameters from Figure 9-9 of WC-Co in H_2SO_4

Concentration	Sample	E_{COR} / mV	j_{COR} / mA cm^{-2}	β_a / mV $decade^{-1}$	β_c / mV $decade^{-1}$
0.5 M	WC-6Co	−255	6.26	90	−25
0.5 M	WC-11Co	−255	2.9	85	−35
0.05×10^{-3} M	WC-6Co	−260	0.35	70	−75
0.05×10^{-3} M	WC-11Co	−220	0.53	115	−100

9.3.2 Effect of Scan Rate

Within the open literature there is disagreement on the corrosion kinetics of WC-Co in corrosive solutions due to differences in potentiodynamic polarisation curves as discussed in Section 3.6.5. One of the explanations for this could be the range of scan rates applied. In order to explore this effect a series of potentiodynamic polarisation tests were conducted on WC-6Co in 0.5 M H_2SO_4 across a range of scan rates that were present in the literature, between 5 mV s^{-1} and 0.167 mV s^{-1}, see Figure 9-10. Overall trends are similar for all scan rates used, obtaining similar corrosion potentials and pseudo-passive behaviour is observed in all three cases.

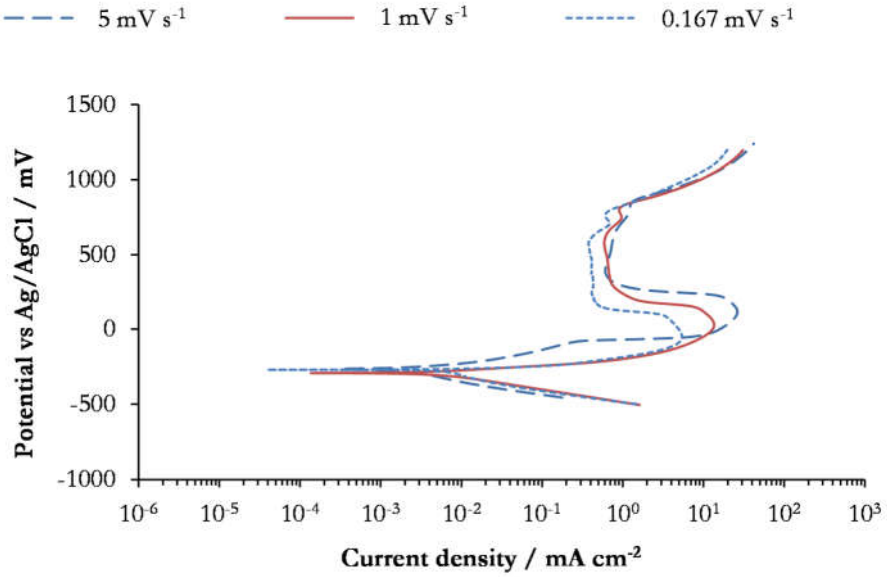

Figure 9-10: Potentiodynamic polarisation for WC-6Co in 0.5 M H_2SO_4 (pH 0) for range of scan rates.

9.3.3 Surface Analysis

SEM images of both the WC-11Co and WC-6Co exposed to 0.5 M H_2SO_4 surfaces show a similar cracked oxide layer has formed, see Figure 9-11. An oxide was seen on the surface of the sample of around 45 μm thick on the WC-11Co sample, see Figure 9-11c. Extensive cracking of the oxide was attributed to dehydration of the corrosion product under vacuum in the SEM.

By comparison, at the larger scale evidence of pitting was seen on samples which were exposed to 0.05×10^{-3} M H_2SO_4, see Figure 9-12a. At smaller scales only a patchy oxide had formed and did not form a cohesive layer. SEM images also suggested that there had also been dissolution of the cobalt binder in pit areas, see Figure 9-12b. This is highlighted in Figure 9-12c where an unpolished carbide can be seen as the original binder covering it has been removed.

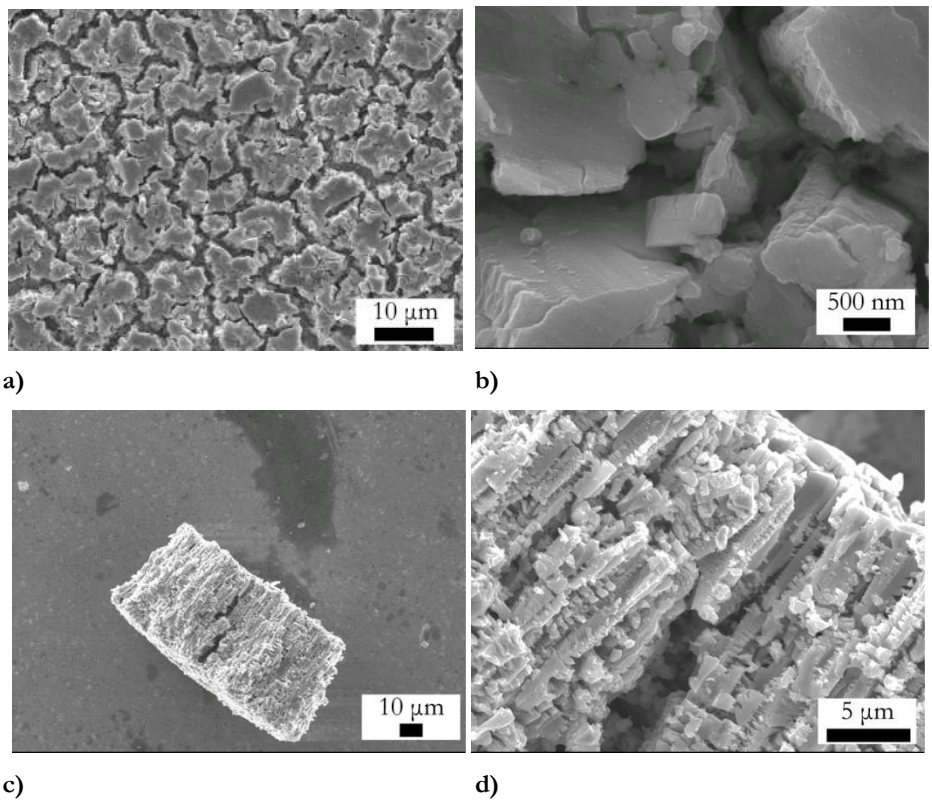

Figure 9-11: SEM images of post polarisation of samples showing tungsten oxide layer formed in 0.5 M H_2SO_4 solution a) WC-6Co surface and b) magnified WC-11Co surface, c) and d) tungsten oxide fragment on WC-11Co sample.

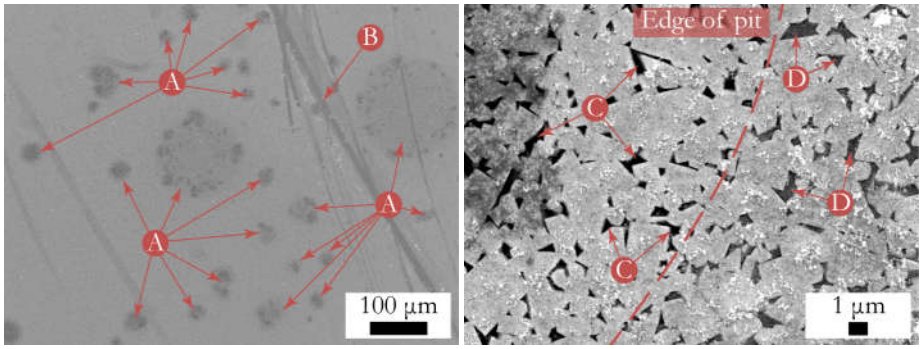

a) b)

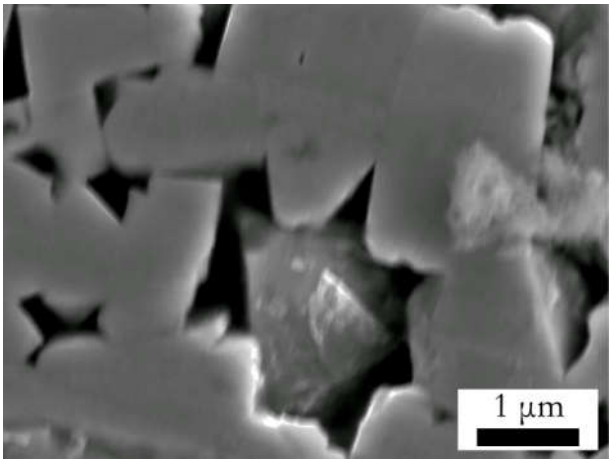

c)

Figure 9-12: SEM images of surfaces exposed to 0.05×10^{-3} M H_2SO_4 a) WC-6Co A: multiple pits on surface B: weak oxide detached during removal of sample from holder b) WC-6Co at edge of pits shows clear distinction between surfaces C: areas of binder depletion D: areas where binder is still visible and c) WC-11Co surface showing unpolished carbide being exposed after binder has been preferentially corroded.

Analysis of the surface of sample exposed to 0.5 M H_2SO_4 using EDX found no cobalt present and increased levels of oxygen, confirming the presence of tungsten oxide, WO_3, see Figure 9-13a. Even under the spalled fragments of oxide no cobalt was detected indicating the presence of a cobalt depleted region. EDX of samples exposed to 0.05×10^{-3} M H_2SO_4 confirmed visual inspection of SEM images, showing substantially reduced levels of cobalt, around 5.5 wt.% in both samples, see Figure 9-13b.

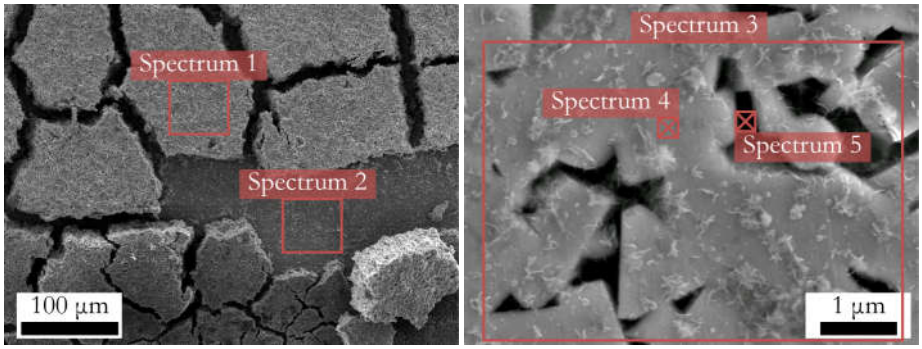

a) b)

Figure 9-13: EDX spectrum of WC-11Co surface after polarisation in a) 0.5 M H_2SO_4 and b) 0.05×10^{-3} M H_2SO_4.

Table 9-3: EDX analysis of surfaces exposed to acidic solution, wt.% of elements

Sample	Concentration	Site	Tungsten	Cobalt	Oxygen
WC-11Co	0.5 M	Spectrum 1	77.56	nil	22.44
WC-11Co	0.5 M	Spectrum 2	90.12	nil	9.88
WC-6Co	0.05×10^{-3} M	Spectrum 3	91.59	5.65	2.76
WC-6Co	0.05×10^{-3} M	Spectrum 4	95.66	2.3	2.04
WC-6Co	0.05×10^{-3} M	Spectrum 5	94.06	3.72	2.22

9.3.4 Discussion

As seen in the potentiodynamic polarisation curves linear behaviour between −500 mV and −100 mV on the semi-log plot is observed, see Figure 9-9. This is equivalent to exponential behaviour for both cathodic and anodic reactions which indicates activation controlled processes. Tafel constants (β_a and β_c) are comparable with results from literature for WC-9Co in the same solution which was 97 mV decade^{-1} and 50 mV decade^{-1} for anodic and cathodic constants respectively [130]. There is little variation in electrochemical parameters between the WC-6Co and WC-11Co samples suggesting that neither composition nor microstructure is rate controlling during cathodic or anodic regions.

The stabilisation of current density at around 0.6 mA cm^{-2} and 18 mA cm^{-2} for the WC-6Co and WC-11Co samples in 0.5 M H_2SO_4, respectively, is evidence of pseudo-

passivity as reported in literature [49, 127, 130], although also contradicts findings in other studies [51, 133]. Studies which have also this seen this behaviour in various corrosive media have reported current densities of between 0.1 mA cm^{-2} and 20 mA cm^{-2} [129, 132, 192]. Human and Exner [129] proposed that pseudo-passive behaviour resulted from the build-up of an oxide layer, although which is porous enough to allow the electrolyte to penetrate to the surface. A similar oxide to that seen by Human and Exner could be seen on the surface of polarised samples, see Figure 9-11. Sutthiruangwong and Mori [130] suggested pseudo-passivity resulted from the cobalt depleted region, which was also seen from the EDX measurements. As the region increases in depth so does the cobalt diffusion path. The laying of oxide and cobalt depleted region is comparable to the composition seen by Sutthiruangwong and Mori [130], see Section 3.6.3.

Electrochemical behaviour was generally unchanged for the three scan rates used with pseudo-passive behaviour still evident. The fast scan on 5 mV s^{-1} does modify the anodic behaviour slightly by increasing the potential required before pseudo-passive behaviour begins. This is caused having insufficient corrosion of the surface to modify its behaviour to pseudo-passivation before the potential is increased. Once sufficient corrosion of the surface has happened current density falls to similar levels seen in the 1 mV s^{-1} scan rate. The reverse effect occurs in the slower scan whereby modification of the surface results in pseudo-passivation occurring at a more negative potential. Furthermore, the pseudo-passivation effect is increased and current density in this region is slightly lower at 0.4 mA cm^{-2} compared to 0.6 mA cm^{-2} for the 1 mV s^{-1} scan rate.

The increase in potential after the pseudo-passive region is similar to results from Human and Exner [129] who saw a rise at 750 mV *vs* SCE. This was attributed to oxidation of WC at higher potentials rather than oxygen evolution which would be expected to occur at higher potentials (1500 mV *vs* Ag/AgCl). Corrosion of more prevalent ceramic phase will dominate the overall current measured from the bulk material.

Lower current densities are observed in the samples polarised in 0.05×10^{-3} M H_2SO_4 of at least one order of magnitude. The oxide that formed on the surface was much more fragmented, although there was still evidence of the binder depleted region. The implications of preferential corrosion of the binder on the microstructure will be

significant. As discussed in Section 3.1, the binder plays an important role in improving the fracture toughness of the material by making the bulk material more ductile and arresting fracture. Therefore, removal of this phase will not only remove these benefits but also introduces voids into the material. The effect on the mechanical properties of the samples will be investigated further in Chapter 10 using nanoindentation and Palmqvist tests.

Potentiodynamic polarisation tests found no evidence of pseudo-passivation behaviour in 0.05×10^{-3} M H_2SO_4 solution. Initially, this would suggest that the tungsten oxide is influencing pseudo-passivation behaviour as this is one of the primary observable differences between the two solutions. However, given that a significant tungsten oxide was found on both WC-6Co and WC-11Co samples, this would not explain the one order of magnitude difference between pseudo-passivation current density. Having seen that scan rate has little effect on the general behaviour, this factor can also be excluded from the reason why some studies have not observed pseudo-passivation. Further understanding of pseudo-passivity is undertaken in the next section using potentiostatic polarisation in order to provide explanation for these differences in behaviour. The large increase in potential that was seen at 800 mV was also not replicated. This suggests that WC is much more stable and therefore does not corrode sufficiently at higher potentials to affect the overall corrosion kinetics as it did in the 0.5 M H_2SO_4 solution.

From analysis of both immersion and potentiodynamic polarisation tests a summary of the corrosion processes that occur in acidic solution is shown in Figure 9-14 and Table 9-4.

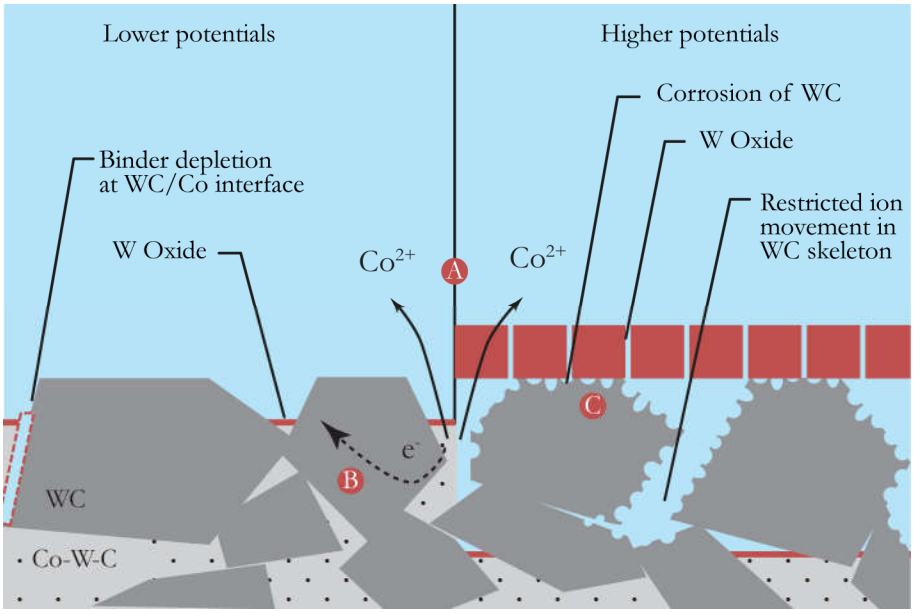

Figure 9-14: Corrosion on surface of WC-Co in acidic solutions.

Table 9-4: Chemical reactions relating to Figure 9-14

Site	Description	Reaction
A	In acidic solutions the binder preferentially corrodes leaving behind a binder depleted zone. This process occurs in parallel to formation of a thin tungsten oxide layer primarily found in the binder regions. The oxidation of the Co-W-C binder and formation of the tungsten oxide layer can be described from the following reactions [192].	$Co \rightarrow Co^{2+} + 2e^-$ $W + 3H_2O \rightarrow WO_3 + 3H_2$ $C + 2H_2O \rightarrow CO_2 + 2H_2$
B	The corresponding reduction reactions.	$O_2 + 4H^+ + 4e^- \rightarrow 2H_2O$ $2H^+ + 2e^- \rightarrow H_2$
C	At higher potentials oxidation of WC grains dominates, as discussed by Human and Exner [129], which will form the oxide layer shown in Figure 9-13 through the following process.	$WC + 3H_2O \rightarrow C + WO_3 + 3H_2$

9.4 Potentiostatic Polarisation in Acidic Solution

9.4.1 Electrochemical Behaviour Results

Pseudo-passivity has been given relatively high attention in the literature, with multiple studies observing this behaviour and trying to explain this effect. Human and Exner [129] proposed that pseudo-passive behaviour to the build-up of a porous oxide layer, allowing electrolyte to penetrate to the surface. On the other hand Sutthiruangwong and Mori [130] suggested pseudo-passivity resulted from the cobalt depleted region which restricted diffusion. To study this effect further potentiostatic

polarisation is performed at three potentials of interest based on the potentiodynamic polarisation plots, those being: −100 mV for the anodic reaction; +500 mV for the pseudo-passive region; and +1000 mV for post pseudo-passive region, see Figure 9-15.

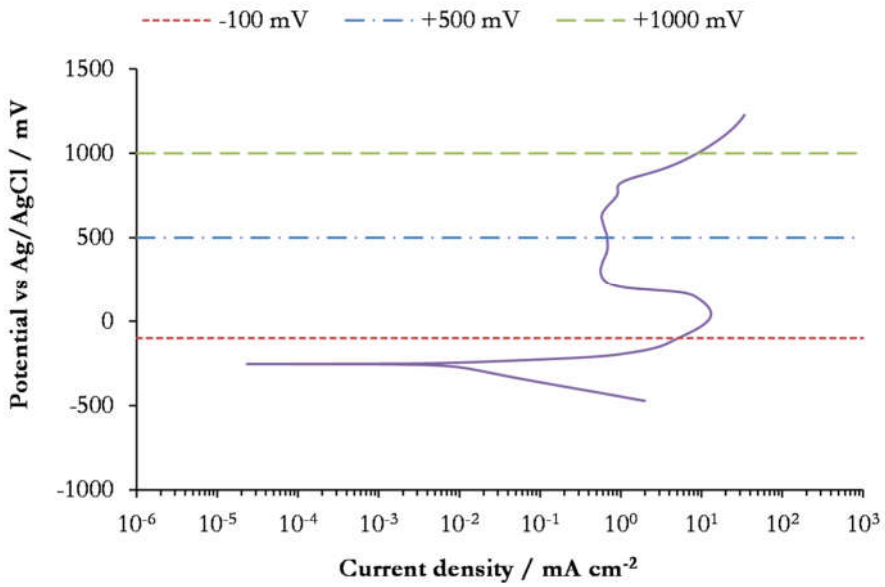

Figure 9-15: Areas of interest selected from potentiodynamic polarisation plot of WC-6Co in 0.5 M H_2SO_4. Scan rate of 1 mV s^{-1}.

Once stabilisation of the samples had happened potential were held for 1 h. Results from this is shown in Figure 9-16 and compared against the current density obtained from the potentiodynamic results.

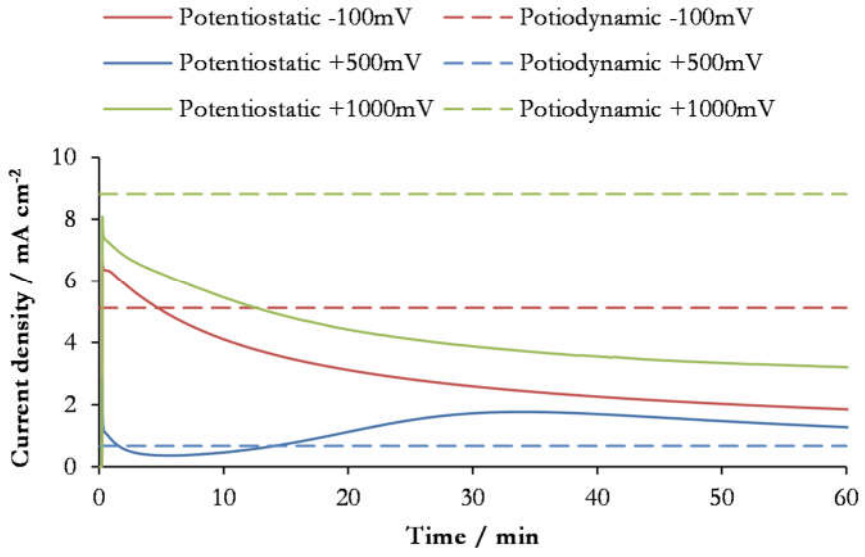

Figure 9-16: Potentiostatic polarisation of WC-6Co in 0.5 M H_2SO_4.

In the anodic region current logarithmically decays from 6.6 mA cm^{-2} to 1.8 mA cm^{-2} over the duration of the 60 min. In the pseudo-passive region currents fluctuate around the 0.68 mA cm^{-2} obtained in the potentiodynamic polarisation experiment. Initially rising then falling after 30 min. The post pseudo-passive region has a similar behaviour to the anodic region as current decreases in a logarithmic manner, starting at just over 7 mA cm^{-2} and falling to 3.2 mA cm^{-2}.

9.4.2 Surface Analysis

After potentiostatic corrosion of the samples SEM images were taken of the three surfaces, see Figure 9-17.

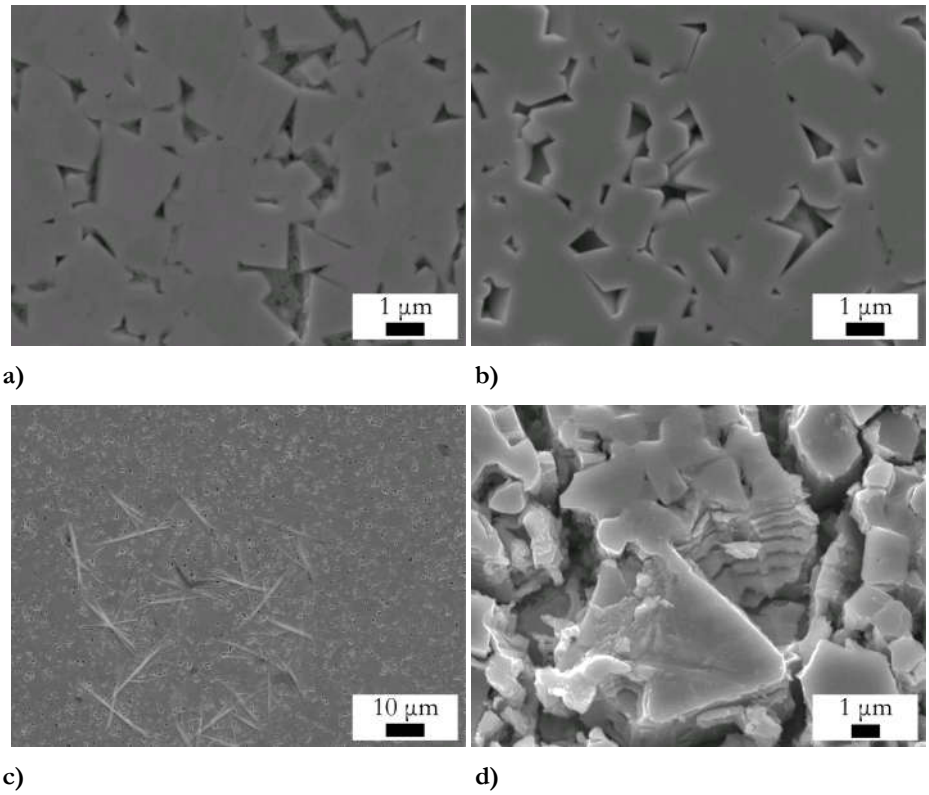

Figure 9-17: SEM of WC-6Co post potentiostatic polarisation a) -150 mV *vs* E_{OCP} b) +500 mV *vs* E_{OCP} c) oxide on +500 mV *vs* E_{OCP} and d) +1000 mV *vs* E_{OCP}.

The sample which was held at a potential of -150 mV *vs* E_{OCP} still has clear carbide and binder phases, see Figure 9-17a. Corrosion appears to have little effect on the carbide phase. The binder, however, is recessed from the surface and has a roughened appearance. The surface held at a potential of +500 mV *vs* E_{OCP} shows further preferential corrosion with complete removal of the binder phase, see Figure 9-17b. This is similar in appearance to immersion after 7 d, see Figure 9-17b. There is still no evidence of corrosion on the carbide phase with well defined facets. Some oxide

was observed on the surface in isolated locations, example shown in Figure 9-17c, but it was very sporadic and would have little effect on the overall corrosion behaviour. At +1000 mV *vs* E_{OCP} the surface is very similar to that of the sample subjected to potentiodynamic polarisation in Section 9.3 where a clear tungsten oxide layer has formed.

9.4.3 Discussion

The surface of the -150 mV *vs* E_{OCP} sample is similar to the immersed sample after 3 d, see Figure 9-3a. Binder is present, although clear evidence of preferential corrosion. Current is initially high then levels off which suggests that the corrosion process is slowing over time. This can be explained through corrosion of the binder and build up of an oxide layer, as was seen in the immersion tests. The oxide will offer some protection to the binder underneath, although is still porous enough for corrosion to continue.

For the potential in the pseudo-passive region (+500 mV *vs* E_{OCP}) the current density is similar to that obtained for pseudo-passive in the potentiodynamic polarisation tests, for the whole duration. It is also the lowest of the three potentials tested. SEM images indicate no oxide layer apart from isolated areas of non-cohesive oxide which are likely to change the corrosion kinetics. Preferential corrosion of the binder increases the distance between solution at the surface and uncorroded binder over time and leaves behind a carbide network which restricts movement of ions, thereby turning an activation controlled process to a diffusion controlled process. This process would also explain why slower scan rates result in lower pseudo-passive current densities, as more binder will be depleted over time. This suggests pseudo-passivity is a consequence of the binder depleted region rather than the oxide layer creating a semi-protective barrier. This supports the conclusion made by Sutthiruangwong et al. [130] and contradicts the hypothesis by Human et al. [129] and Tomlinson and Linzell [132]. The inability of WO_3 to passivate the surface also agrees with the P-B ratio, discussed in Section 3.6.3, which suggests that stresses in the oxide are likely to lead to buckling and detachment. With this understanding the reason for the significant difference in pseudo-passivity between the WC-6Co and WC-11Co samples can be explained. In the WC-6Co sample cobalt content is less and therefore the carbide network that remains will be more tortuous, restricting ion movement more than in a WC-11Co WC network. Furthermore, tortuosity will also function of

the microstructure and therefore it would be expected that corrosion will be a function of contiguity. Lower continuity means that there is more dispersion of WC, therefore pseudo-passive effects would be minimised as diffusion is less restricted by the carbide network and current densities increase as a result. Similarly, higher binder mean free paths would result in bigger gaps between carbides once the binder is corroded, which would also have higher pseudo-passive current densities. This theory can be extended further to explain why pseudo-passivity has not been observed by all authors which were using different microstructures, even although compositions were the same. However, it is difficult to evaluate the published literature against this hypothesis as typically authors in corrosion science typically only provide composition of the samples and not microstructural parameters.

Polarisation at +1000 mV *vs* E_{OCP} has a similar surface to full potentiodynamic polarisation, see Figure 9-13. Analysis of the surface suggests that in the post pseudo-passive region there is rapid oxidation of WC grains. This process forms the large tungsten oxide layer that is observed in potentiodynamic and potentiostatic polarisation tests. The current density is similar to the behaviour of that of the anodic region (-150 mV *vs* E_{OCP}) suggesting the same corrosion processes are occurring, whereby the oxide provides some protection of the surface. However the current density never falls to that obtained during pseudo-passivation which further supports the conclusion that this behaviour is caused by binder depletion.

Having established that pseudo-passivation is a result of the binder depleted region, an explanation as to why this behaviour was not seen in the 0.05×10^{-3} M H_2SO_4 H_2SO_4 solution is required as binder depletion also observed. Current densities were much lower than in 0.5 M H_2SO_4, even compared to the most significant pseudo-passivation effect in WC-6Co. This could mean that corrosion kinetics are slow enough that diffusion of ions through the WC skeleton is not rate limiting in this solution.

9.5 Potentiodynamic Polarisation in Alkaline Solution

9.5.1 Electrochemical Behaviour Results

Potentiodynamic polarisation is conducted in alkaline solutions for the two compositions. The same experimental setup as the acidic solution was used, with

potential scan of between −200 mV to +1500 mV *vs* E_{OCP}, results shown in Figure 9-18.

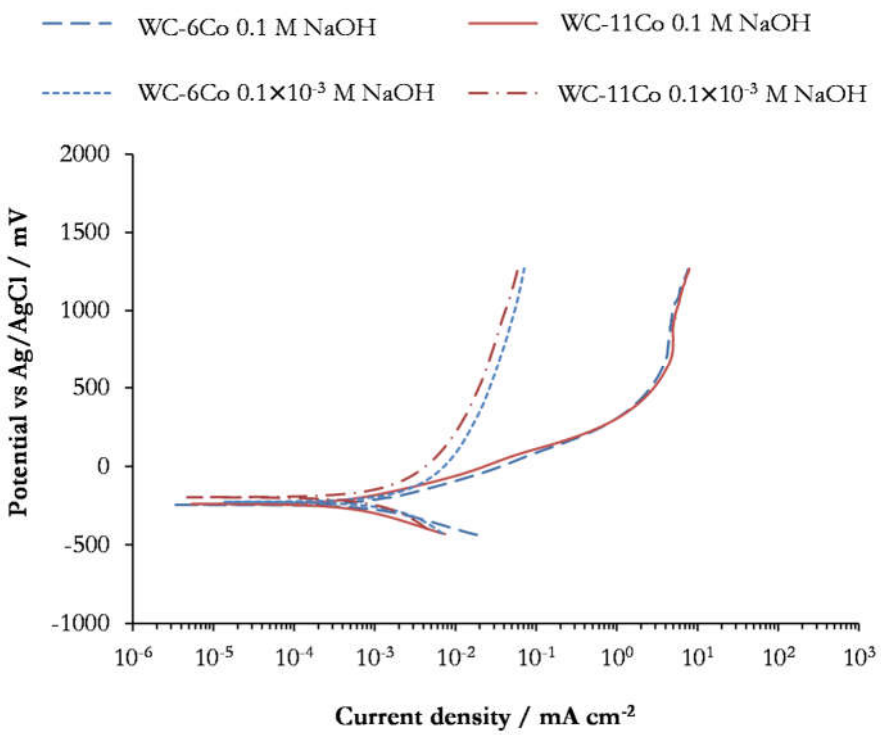

Figure 9-18: Potentiodynamic polarisations for WC-Co sample to assess the influence of alkaline solutions (NaOH). Scan rate of 1 mV s^{-1}.

General behaviour and current densities are the same for both WC-6Co and WC-11Co in the solutions tested. Compared to acidic solutions corrosion potential are slightly more positive by around 10 mV to 20 mV. No passive or passive like behaviour was observed in either alkaline solution.

Although current density in 0.1 M NaOH solution is lower than that of 0.5 M H_2SO_4 for the majority of the polarisation curve, the current density is higher in the WC-6Co sample during the pseudo-passivation period. A linear relationship between current density and potential on the semi-log plot indicates both anodic and cathodic branches are charge transfer controlled.

Behaviour and current density obtain in 0.1×10^{-3} M NaOH is similar to that in 0.05×10^{-3} M H_2SO_4. Furthermore, two distinct types of behaviour were observed, see Figure 9-19. Type A behaviour had a constant increase in current density as potential increases, typical of diffusion controlled process. Type B behaviour had a similar behaviour, up to around 230 mV, after which a sharpe increase in current density was observed.

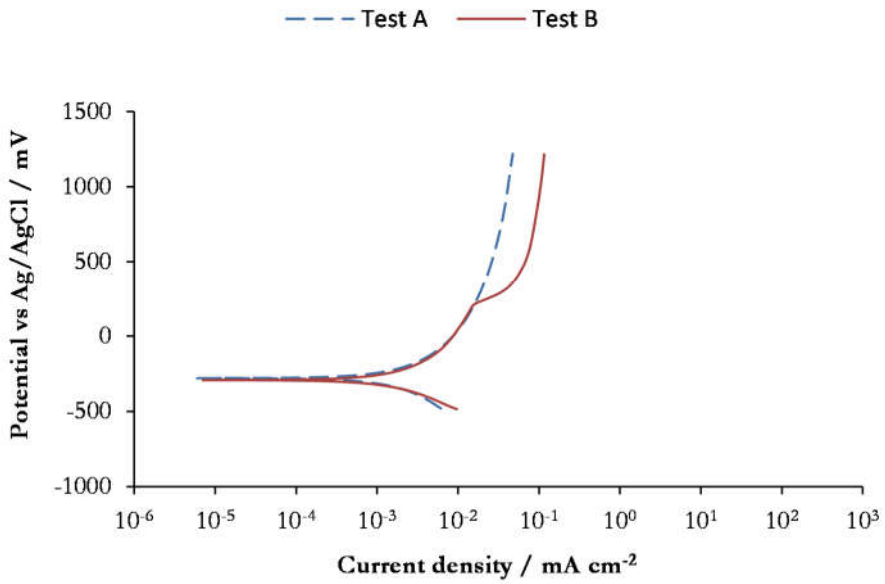

Figure 9-19: Two behaviours identified in 0.1×10^{-3} M NaOH. Scan rate of 1 mV s^{-1}.

A summary of the electrochemical parameters measured from the polarisation curves are presented in Table 9-5.

Table 9-5: Electrochemical parameters from Figure 9-9 of WC-Co in NaOH solution

Concentration	Sample	E_{COR} / mV	j_{COR} / mA cm^{-2}	β_a / mV $decade^{-1}$	β_c / mV $decade^{-1}$
0.1 M	WC-6Co	−245	3.64	155	−155
0.1 M	WC-11Co	−240	1.77	140	−165
0.1×10^{-3} M	WC-6Co	−260	27.52	1145	−1135
0.1×10^{-3} M	WC-11Co	−200	10.26	665	−655

9.5.2 Effect of Scan Rate

As with the acidic solution, scan rate was investigated for WC-6Co in alkaline solution. This time the lower alkaline solution was chosen 0.1×10^{-3} M NaOH was used due to its more characteristic curve and those tests which displayed type B behaviour compared. Scan speeds of between 5 mV s^{-1} and 0.167 mV s^{-1} were used, results shown in Figure 9-20.

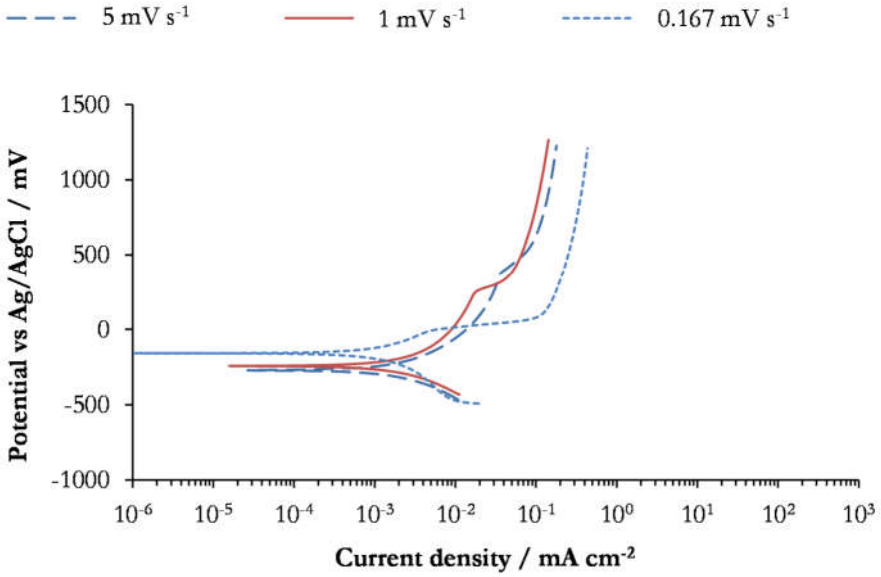

Figure 9-20: Potentiodynamic polarisations for WC-6Co in 1×10^{-3} M NaOH (pH 10) for range of scan rates.

Corrosion potentials are fairly consistent, ranging from −340 mV to −240 mV. The fastest scan delays the increase in current density to higher potentials of 320 mV, likely due to a delay in the response of the surface to the changing potential. This is similar to the effect seen in the acidic fast scan rate test in Section 9.3.2. In the slower scan rate a dramatic increase in current density occurs much earlier around 0 mV before stabilising around 100 mV.

9.5.3 Surface Analysis

Analysis of the surface of the polarised sample in 0.1 M NaOH shows a very different morphology to that of the acidic solution, with structures on the surface much larger allowing image by optical microscopy techniques, see Figure 9-21. These were seen in both WC-6Co and WC-11Co samples. Although polarisation parameters are the same the craters on the surface indicate evidence of pitting corrosion.

SEM images of these pits provide further insight, see Figure 9-22. There is a build up of corrosion product at the centre of the crater, above the pit. Around this area are seen WC grains which are exposed and are irregular in shape, indicating this is not the original polished surface, suggesting they have been subject to corrosion. Surrounding this area is more extensive corrosion product.

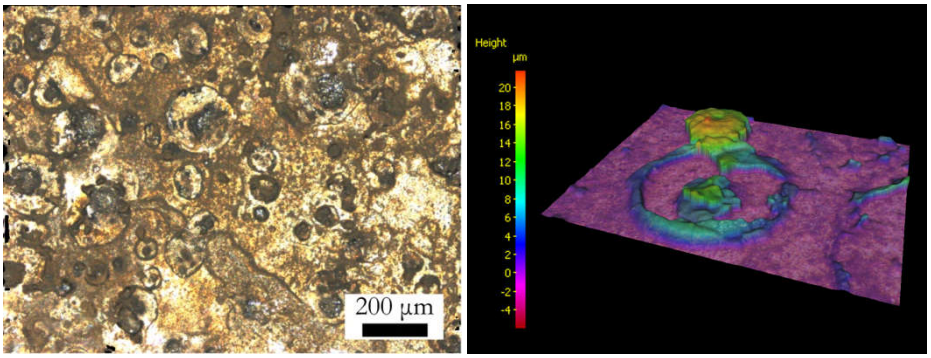

a) b)

Figure 9-21: Alicona images of polarised WC-11Co surface exposed to 0.1 M NaOH.

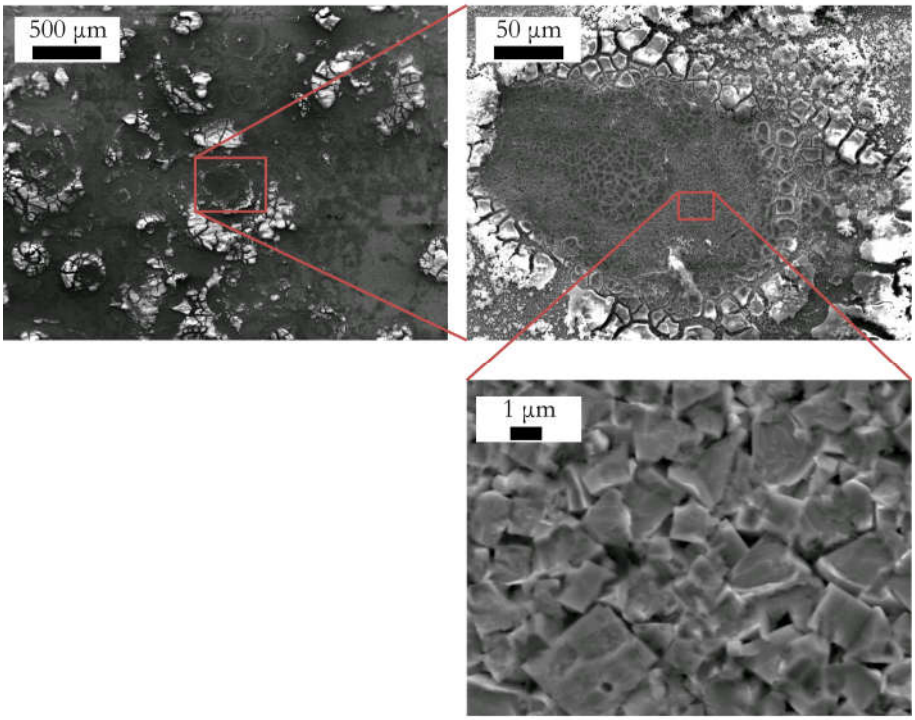

Figure 9-22: WC-11Co surface exposed to 0.1 M NaOH.

By comparison, samples exposed to 0.1×10^{-3} M NaOH only formed a thin oxide layer. On samples which displaced type B behaviour significant local depletion of the binder phase was more prevalent, suggesting that pitting had occurred, see Figure 9-23. This is similar to behaviour observed in 0.05×10^{-3} M H_2SO_4, although this is more localised, being only a few microns in diameter.

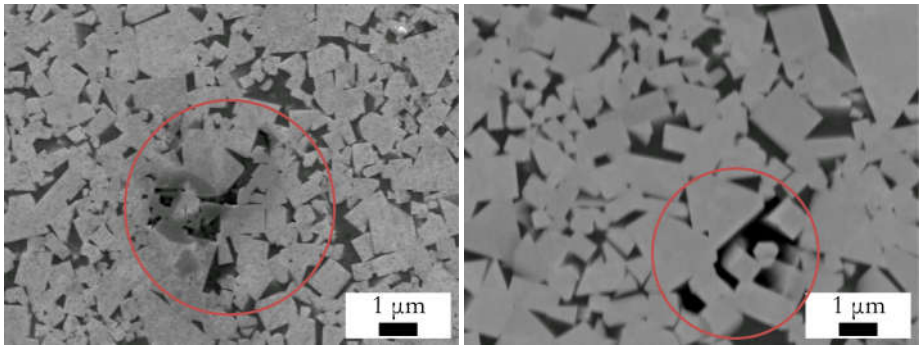

a) b)

Figure 9-23: Evidence of pitting corrosion in WC-11Co surface exposed to 0.1×10^{-3} M NaOH a) increased corrosion in localised area and b) complete removal of binder.

EDX was performed on both polarised samples, see Figure 9-24 and Figure 9-5. Significant levels of cobalt and oxygen are seen on the surface on 0.1 M NaOH samples suggesting the formation of cobalt hydroxide. In the area surrounding the pit the percentage of cobalt is significantly lower, although still indicate presence of a thin hydroxide. Cobalt in the 0.1×10^{-3} M NaOH solution has been reduced overall. Binder regions still display higher levels of cobalt, although within the pits this percentage is reduced significantly, along with an increase in oxygen.

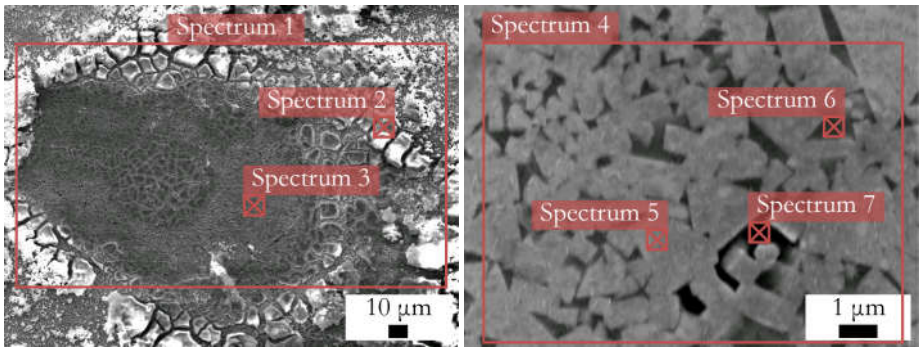

a) b)

Figure 9-24: EDX spectrum of surface after polarisation in a) WC-6Co 0.1 M NaOH and b) WC-11Co 0.1×10^{-3} M NaOH.

Table 9-6: EDX of samples exposed to NaOH

Sample	Concentration	Site	Tungsten	Cobalt	Oxygen
WC-6Co	0.1 M	Spectrum 1	22.12	58.03	19.86
WC-6Co	0.1 M	Spectrum 2	8.63	70.39	20.98
WC-6Co	0.1 M	Spectrum 3	79.25	11.07	9.68
WC-11Co	0.1×10^{-3} M	Spectrum 4	75.76	22.91	1.33
WC-11Co	0.1×10^{-3} M	Spectrum 5	93.27	3.64	3.09
WC-11Co	0.1×10^{-3} M	Spectrum 6	18.11	80.72	1.17
WC-11Co	0.1×10^{-3} M	Spectrum 7	51.76	37.79	10.27

EDX element mapping can also be used to visually represent how elements are distributed on the surface around the pit formations in 0.1 M NaOH solution. The higher tungsten areas become evident at the centre of the feature, along with less oxygen and cobalt.

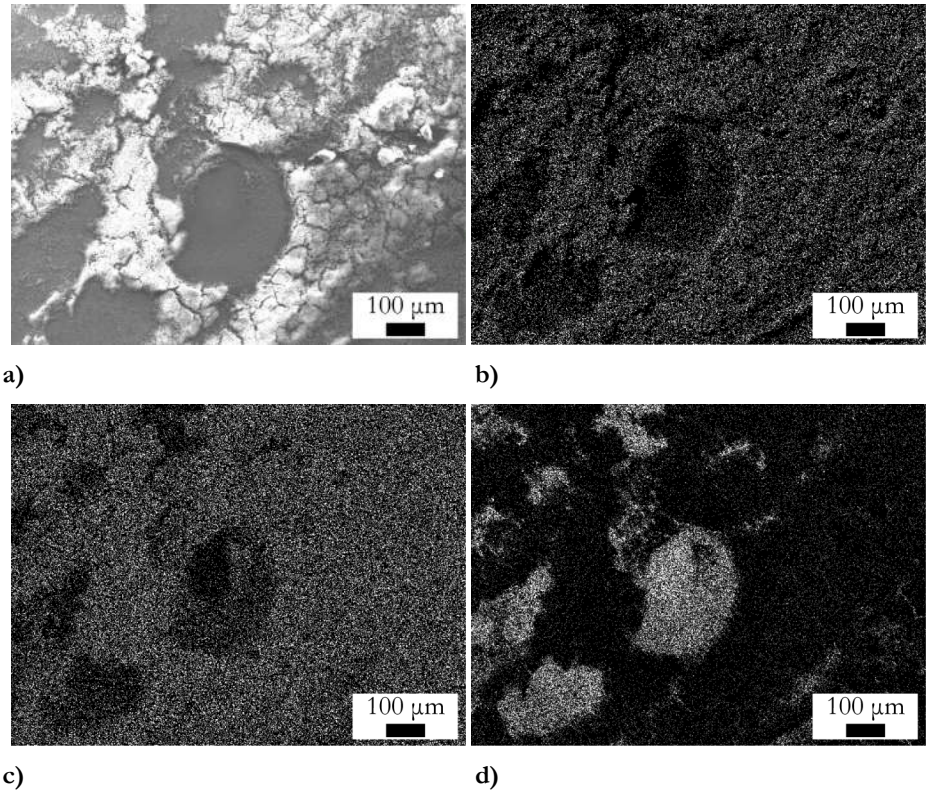

Figure 9-25: EDX map of elements around feature in WC-6Co exposed to 0.1 M NaOH (lighter indicating where elements are detected) a) SEM image, b) Oxygen map, c) Cobalt map and d) Tungsten map.

9.5.4 Discussion

The similarities in potentiodynamic polarisation and surface images of WC-6Co and WC-11Co samples suggest that neither cobalt nor microstructural parameters affect the corrosion behaviour in NaOH solution. Previous electrochemical tests found cobalt to have some passivating behaviour in alkaline solution from an oxide layer. This would suggest a continuous non-porous oxide would be formed, such as the thin film observed in SEM images. However, as seen from the potentiodynamic polarisation curves this film appears to make little appreciable difference to the overall behaviour of the bulk material.

Pitting appeared to be a significant effect in both alkaline solutions, although clearly to a lesser extent in the 0.1×10^{-3} M NaOH solution. Pitting is often considered more dangerous than uniform corrosion as it is both more difficult to predict and also detect. This behaviour could explain why the distinct Type A and Type B behaviours were observed in potentiodynamic polarisation in the less alkaline solution only. This hypothesis was reinforced by SEM images which showed localised corrosion of the binder. At lower alkalinity pitting become more unpredictable, requiring local defects

such as pores, impurities or even higher local W alloy in the binder to initiate corrosion pits. Once a pit is formed this will dominate over small local anodic and cathodic regions, making it is to easier for other pits to form. Furthermore, as the corrosion potential of W is higher than that of Co, higher potentials are required until corrosion of will W will dominate the overall corrosion kinetics. This would explain why there is an increase in corrosion potential around the same value of −230 mV. This behaviour is similar to that discussed by Human and Exner [129] explaining the increase in current after the pseudo-passive region is due to oxidation of WC which occurs at similar potentials regardless of binder composition thus will only influence the overall reaction at higher potentials.

Tafel constants obtained for the 0.1×10^{-3} M NaOH solution are much higher than that of the acidic solutions or 0.1 M NaOH solution, suggesting a diffusion controlled reaction whereby the reaction rate is limited by the rate of mass transport of ions in the solution to the reaction site. The corrosion rates obtained are therefore subject to significant error. Tafel slopes assume activation (or charge-transfer) controlled corrosion, which is seen as a linear relationship on the semi-log plot. This can introduce significant error to the corrosion current densities calculated in diffusion controlled reactions as the Butler-Volmer equation relies on this value.

Pitting behaviour is very clear in the 0.1 M NaOH solution. The pits themselves will be local anodes, with surrounding areas cathodic. In these cathodic areas little binder is present and WC grains show evidence of corrosive attack. While corrosion of the WC grains is not surprising given that it is not stable in alkaline environments and absence of cobalt suggests that galvanic coupling takes place. The binder acts a sacrificial anode and once the binder is depleted, WC grains are no longer protected and start to be attacked. These processes can be described from the following reactions for both the binder and carbide grains respectively:

$$W + 4H_2O \rightarrow WO_4^{2-} + 8H^+ + 6e^- \quad (9.1)$$

$$WC + 6H_2O \rightarrow WO_4^{2-} + CO_2 + 12H^+ + 10e^- \quad (9.2)$$

As can be seen from both Equations (9.1) and (9.2) hydrogen is a product of these reactions. This could lead to an increase in hydrogen ions in the pit creating a local acidic solution. As has been discussed, acidic solutions are particularly detrimental to the binder, therefore increasing the rate of binder depletion. As WC dominates the

corrosion process it is unsurprising that passivating behaviour is not observed. In acidic solutions the binder is chemically corroded and therefore diffusion effects are increased as the binder depleted region increases. This process only ends when oxidation of WC dominates at higher potentials. In alkaline conditions, once WC is no longer galvanically protected by the binder it will be chemically attacked by the alkaline solution. As the binder is only depleted due to galvanic coupling Co will not give up elections when WC grains are stable in solution. This would help to explain why it was only the 0.1×10^{-3} M NaOH solution which saw no signs of binder corrosion during immersion tests in Section 9.2. Whereas in the acidic environment the Co is attacked directly, binder depletion only occurs in alkaline conditions when WC is attacked. When WC grains are relatively stable the binder will remain.

From analysis of immersion and potentiodynamic polarisation tests a summary of the main electrochemical reactions can be constructed along with the chemical reactions, see Figure 9-26 and Table 9-7.

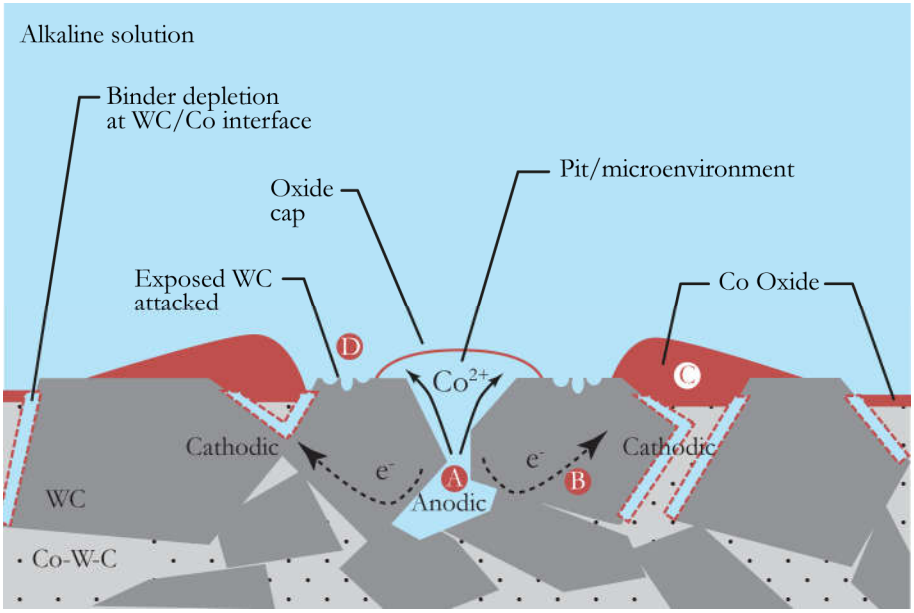

Figure 9-26: Corrosion on surface of WC-Co in alkaline solutions.

Table 9-7: Chemical reactions relating to Figure 9-6

Site	Description	Reaction
A	Initially there is preferential depletion of the binder at WC/Co interface, where there is higher W alloy. Furthermore, the binder acts as a sacrificial anode which initially protects the WC grains.	$W + 4H_2O \rightarrow WO_4^{2-} + 8H^+ + 6e^-$ $Co \rightarrow Co^{2+} + 2e^-$
C	Cobalt can also form cobalt hydroxide on the surface.	$Co + 2H_2O \rightarrow Co(OH)_2 + 2H^- + 2e^-$
D	Complete depletion of binder leads to removal of galvanic protection of WC grains and leads to corrosive attack of WC. Furthermore, tungsten oxide is not created in alkaline environments.	$WC + 6H_2O \rightarrow WO_4^{2-} + CO_2 + 12H^+ + 10e^-$
B	The corresponding reduction reaction.	$O_2 + 2H_2O + 4e^- \rightarrow 4OH^-$

9.6 Conclusions

Results from corrosion experiment show that oxides are weakly adhered to the surface and do not offer passivation behaviour in both acidic and alkaline solutions. As such, they are will have little effect on the tribocorrosion of WC-Co. Modelling of these oxides is therefore not a priority.

Apart for highly acidic 0.5 M H_2SO_4, there appeared to be little difference in electrochemical behaviour or surface appearance of the two grades of material tested. Surface analysis indicated the same effect of corrosion for both grades.

In very acidic solutions pseudo-passive behaviour, as described by Human and Exner [129] and Sutthiruangwong et al. [49], was observed as a dominant mechanism from potentiodynamic polarisation curves. Physical examination of samples subject to potentiostatic polarisation suggests that this behaviour was caused by creation of the binder depleted region rather than the tungsten oxide. Furthermore, difference in the microstructure between the two samples would explain the difference in passivation as well as findings from other studies.

In alkaline solution no pseudo-passive behaviour was observed, but pitting became a significant factor. The WC grains were found to have had corrosive attack. This indicates corrosion has a very different effect on the material properties and microstructure depending on the solution the surface is exposed to. This shows a need for both acidic and alkaline solutions to be considered when studying the effect of corrosion on WC-Co material.

In both solutions cobalt depletion is observed, although likely caused by different effects. In acidic solutions binder is unstable and therefore corrodes preferentially. In alkaline solutions, the binder acts as a sacrificial anode and therefore also preferentially corrodes. Additionally, instability of W in alkaline causes preferential deletions of the binder at the WC/Co interface, which can initiate pitting behaviour. These microstructural changes would be necessary to incorporate into a mesoscale model through adapting the geometry of the mesh. For example, removal of binder elements around WC grains mimics the effect of immersion in 0.1×10^{-3} M NaOH, see Figure 9-27.

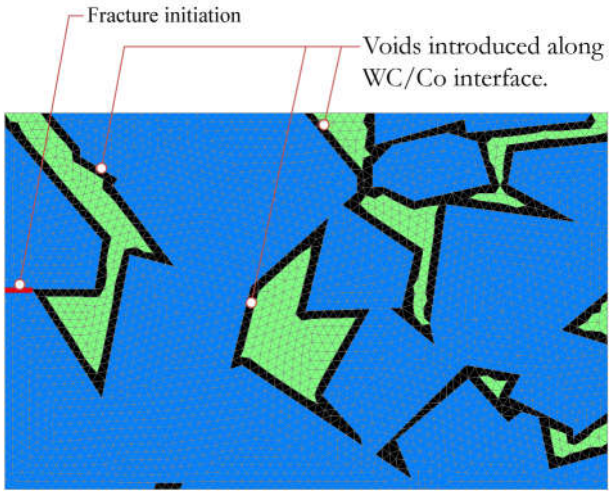

Figure 9-27: Example of how corroded microstructure could be modelled. WC (blue) and Co (green).

Having conducted and reviewed the effect on the microstructure, hypothesis about corrosion seen in the literature can be offered. Taking a closer look the corrosion observed by Olovsjö et al. [113], discussed in Section 3.6.6, there is evidence of a binder depleted region near the surface with WC grain being very angular, see Figure 3-37. These characteristics match findings obtained in acidic environments. In comparison corrosion observed by Beste and Jacobson [99], discussed in Section 3.6.7, the long narrow binder depleted region is evidence of pitting, see Figure 3-38. In addition to attack of the WC grains suggest that this happened in an alkaline environment.

Chapter 10 – Effects on the Mechanical Properties of WC-Co Exposed to Acidic and Alkaline Solutions

Chapter Highlights

This chapter examines the effect of corrosion on the mechanical properties of WC-Co studied in Chapter 9. As well as an understanding of the microstructure and material properties the numerical modelling approach used requires experimental test data to assess the accuracy of the model. An experimental technique that uses analysis of Palmqvist fractures (Section 3.3.4) is demonstrated to be a way of studying fracture behaviour of corroded samples and validating future simulations.

- Nanoindentation shows little change in hardness and elastic modulus after exposure to corrosive solution indicating that intrinsic material properties of the WC grains remain constant.
- Palmqvist fractures demonstrate a measurable reduction in bulk fracture toughness after exposure to corrosive solution.
- Characterisation of the Palmqvist fractures visualises changes in fracture behaviour between different microstructures and corroded surfaces.

10.1 Experimental Objectives

While an understanding of the effects of corrosion on the microstructure of WC-Co can be used to model hypothetical geometries of corroded samples, it is also important to understand how the mechanical properties of the material are altered by corrosion. However, as discussed in Section 3.8 standard tribology tests such as scratch or microabrasion tests are not able to provide sufficient level of detail of properties or interaction between the phases required to model at the mesoscale.

An innovative mixture of existing experimental techniques is used for the first time to understand corrosion of WC-Co which can complement mesoscale modelling. These tests are performed on uncorroded and corroded WC-6Co and WC-11Co samples from Chapter 9. Firstly, nanoindentation is used to study the effects of corrosion on the hardness and Young's modulus. Secondly, the Palmqvist method, discussed in Section 3.3.4, is used to examine fracture properties and behaviour. One of the primary advantages of using this approach is that it measures the fracture toughness at the surface only. As corrosion only affects the surface of the sample this makes this testing method an ideal solution compared with the SNEB three-point bend test which is traditionally used to measure fracture toughness of WC-Co. Using Equations (3.16) and (3.17) and applying geometric values of the indenter allows fracture toughness of the samples to be calculated by:

$$K_{IC} = 0.0889\left(HW\right)^{0.5} \tag{10.1}$$

Characterisation of the fractures will extend the value of this data and bring further understanding. This will be performed using the same method as employed by Sigl and Exner [85], discussed in Section 3.3.5.

10.2 Uncorroded Samples

10.2.1 Nanoindentation

An initial test was performed on uncorroded polished WC-6Co samples to assess the ability of the nanoindenter to produce accurate and precise results. Lower loads are preferable as they can measure individual phases of the microstructure, but are more prone to size effects and sensitive to environmental factors such as noise and surface roughness. Loads were varied between 1, 10 and 30 mN and with a loading time of 25 s. A series of 10 indents were performed for each load and spaced 10 μm apart so

that deformation of one indent did not affect the result of another. Tests were conducted overnight to reduce vibration from daytime activities in the surrounding area. Load-displacement curves from the test are presented in Figure 10-1.

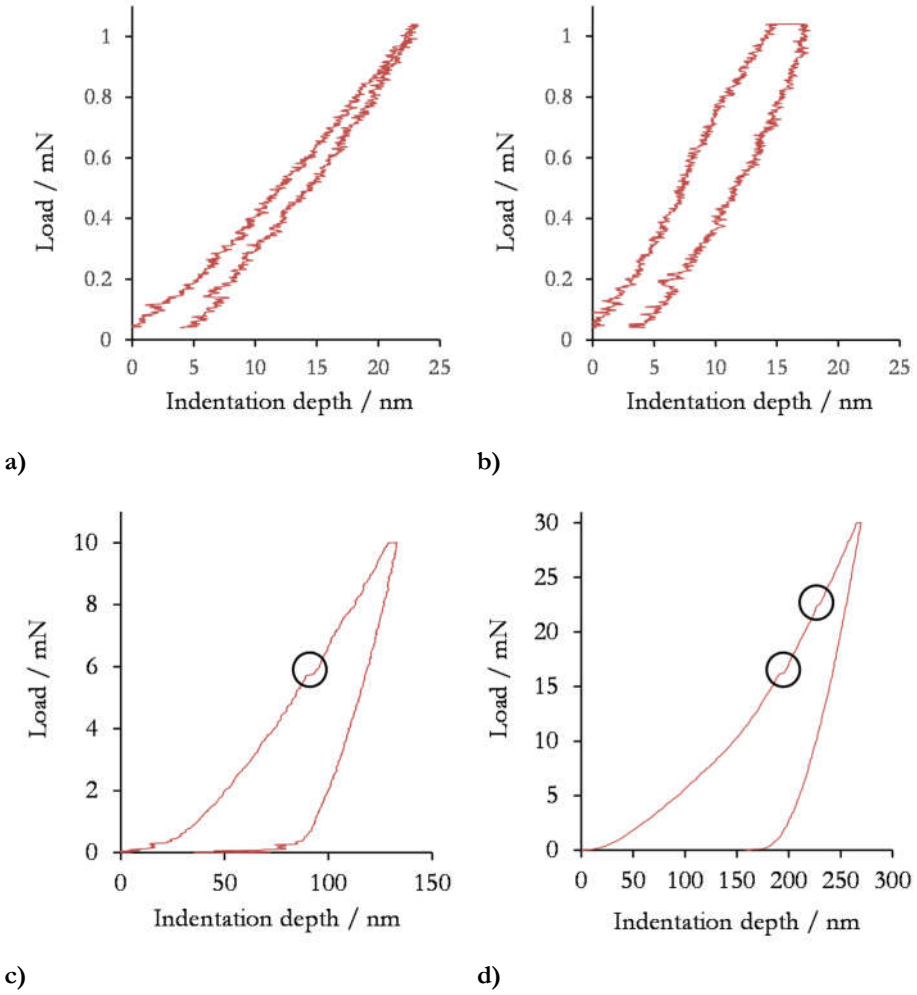

Figure 10-1: Load-displacement curves for indents made on lapped WC-6Co samples. a) and b) at 1 mN, c) at 10 mN and d) at 30 mN load. Pop-in events highlighted.

At the lowest low tested of 1 mN measurements produced comparable results to those at higher loads, although noise is significant which produces a large scatter in the data. Loads at 10 mN and 30 mN suffered from less noise which allowed pop-in events to be observed, seen as small plateaus in the load-displacement curve, highlighted in Figure 10-1c and d. These were commonly found at applied loads of between 15 mN and 25 mN. The measured hardness and Young's modulus from these results is shown in Figure 10-2. Young's modulus was calculated from Equation (8.5) for each indentation. These show that measurements at higher loads are more consistent, although average values are about the same, with a measured hardness of around 20 GPa and Young's modulus of 500 GPa.

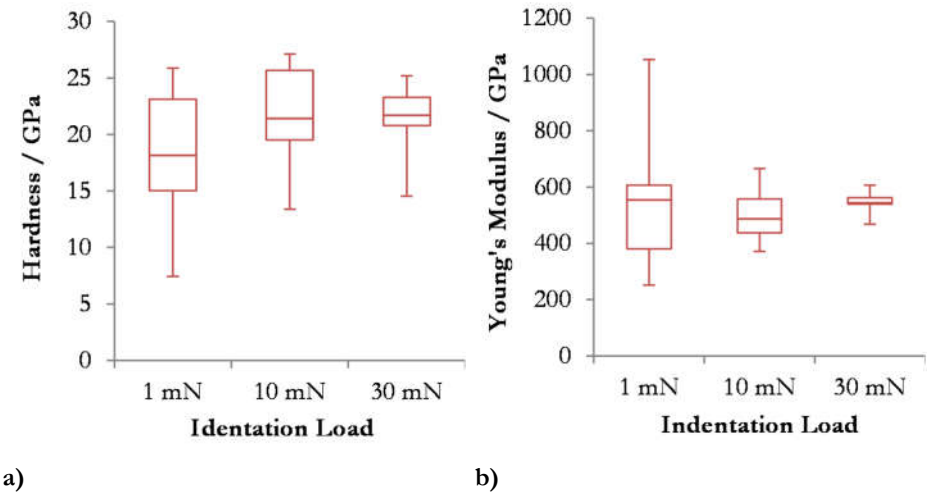

Figure 10-2: Nanoindentation results from initial test a) hardness and b) Young's modulus.

A more detailed analysis of WC-6Co samples was performed by creating a map of indentations of 10×10 (100 indentations) spaced 10 μm apart at loads of 10 mN and 30 mN. The distribution of the measured hardness and Young's modulus is shown in Figure 10-3 and Figure 10-4 respectively. The average hardness and Young's modulus decreases for the lower load as well as having a larger distribution in measured values, as was seen when comparing the three loads.

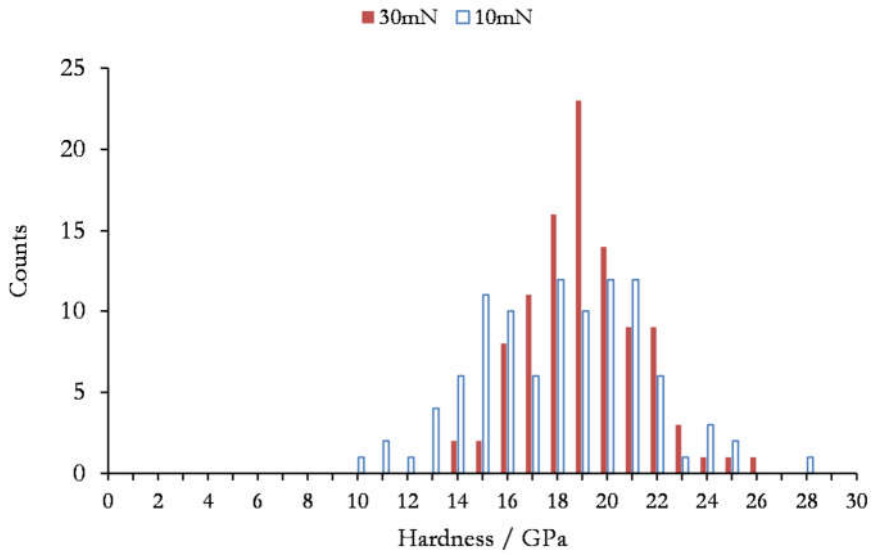

Figure 10-3: Measured hardness of uncorroded WC-6Co samples comparing 10 mN and 30 mN load.

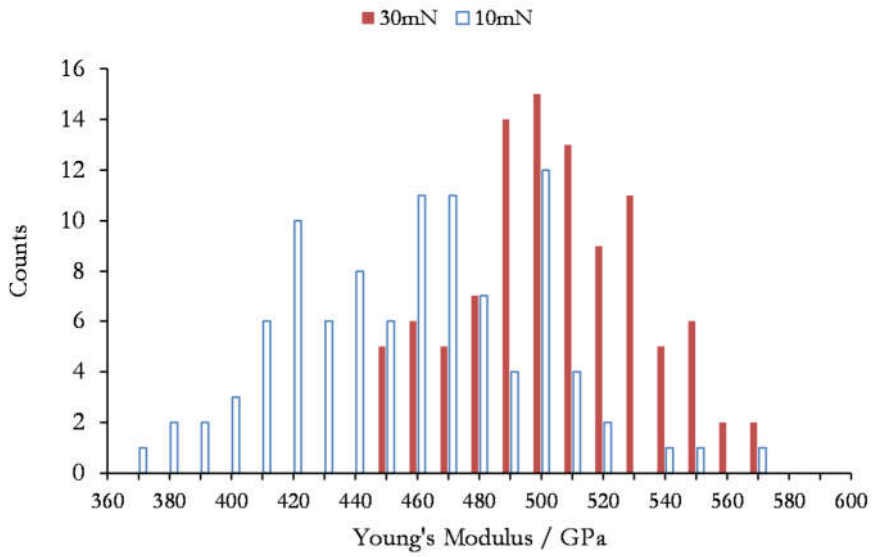

Figure 10-4: Measured Young's modulus of uncorroded WC-6Co samples comparing 10 mN and 30 mN load.

Nanoindentations using loads of 30 mN were performed to WC-11Co samples so that they could be compared with the WC-6Co, see Figure 10-5 and Figure 10-6. The distribution of measurements is similar for both samples, although the WC-11Co shows a reduction in both hardness (19 GPa *vs* 16 GPa) and Young's modulus (500 GPa *vs* 460 GPa).

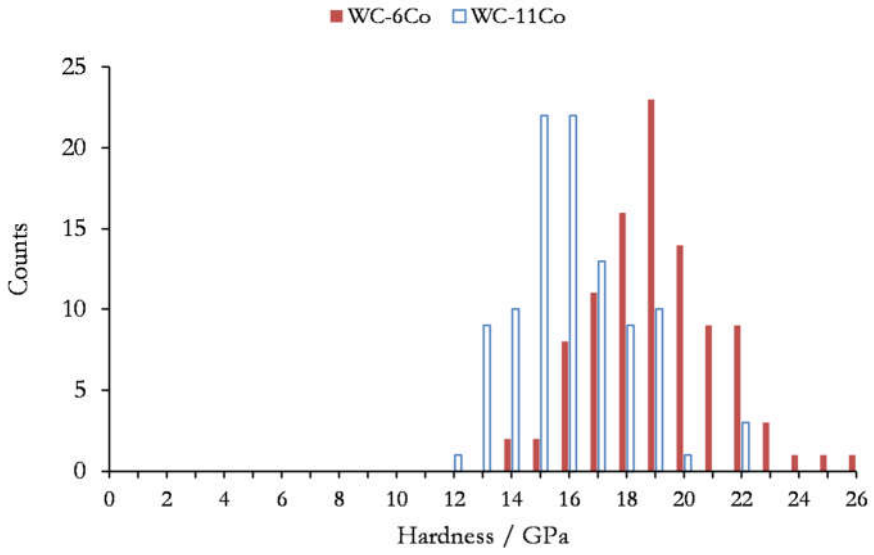

Figure 10-5: Measured hardness of uncorroded samples at 30 mN, comparing WC-6Co and WC-11Co.

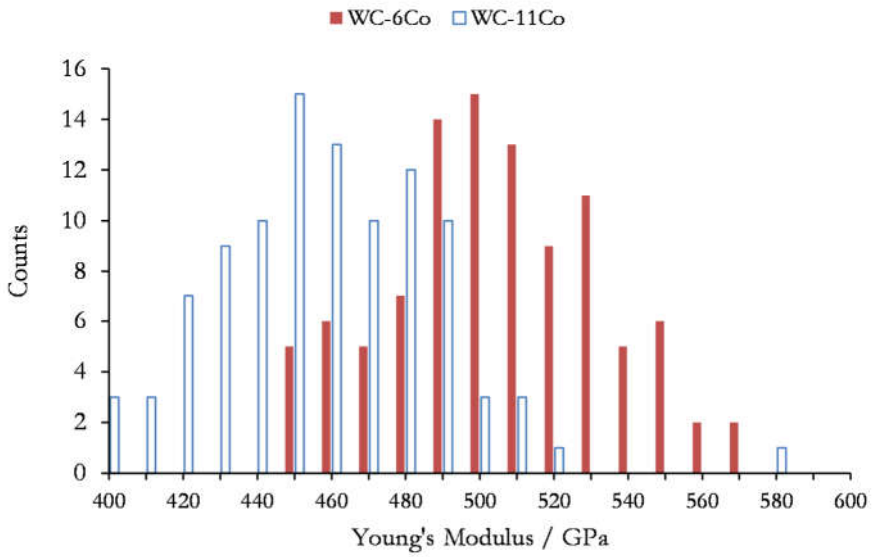

Figure 10-6: Measured Young's modulus of uncorroded samples at 30 mN, comparing WC-6Co and WC-11Co.

A summary of the measured values from the nanoindentation tests are shown in Table 10-1.

Table 10-1: Summary of material properties of uncorroded samples obtained from nanoindentation tests

Sample	Load	Hardness / GPa	Young's modulus / GPa
WC-6Co	1 mN	18.7 ± 6.0	538.0 ± 210.3
WC-6Co	10 mN	18.1 ± 3.4	459.2 ± 45.8
WC-6Co	30 mN	19.1 ± 2.2	504.8 ± 28.9
WC-11Co	30 mN	16.1 ± 2.0	458.6 ± 29.5

10.2.2 Fracture Properties

Vickers hardness test is performed on a range of loads between 10 kgf and 50 kgf. This produces indents that are between 110 μm and 250 μm and Palmqvist fractures up to 120 μm. Indentations were placed approximately 10 mm apart to prevent interaction between them. Measurements of the diagonal length of the pyramid

indentation and Palmqvist crack length are obtained using the Alicona 3D optical microscope. A typical set of images obtained is shown in Figure 10-7.

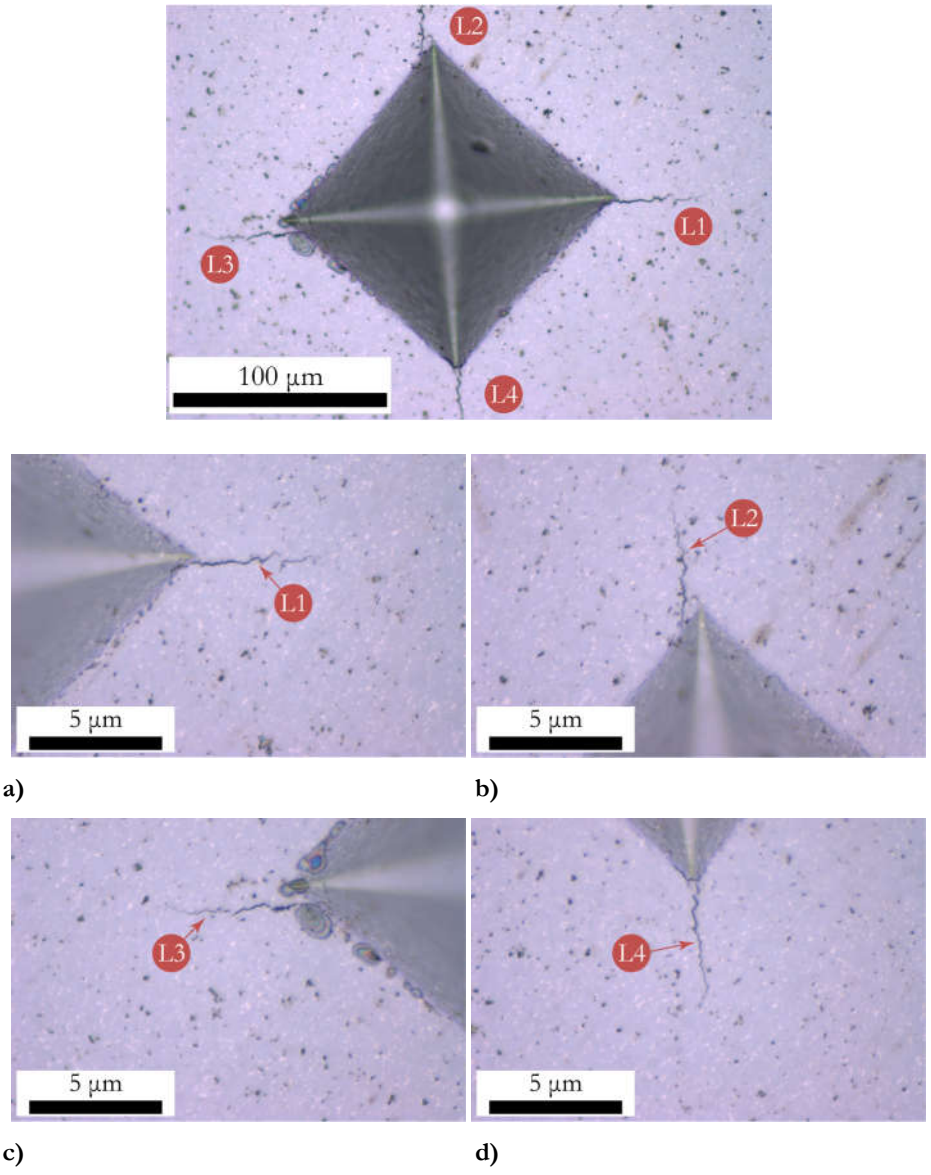

Figure 10-7: Alicona image of a) 20 kgf Vickers indent b) Palmqvist fracture at L1 c) Palmqvist fracture at L2 d) Palmqvist fracture at L3 and e) Palmqvist fracture at L4.

The hardness values obtained from five indents is shown in Figure 10-8. Results are very consistent across the different loads for both samples with an average hardness of 14.5 GPa and 12.8 GPa obtained for the WC-6Co and WC-11Co samples respectively and an error of less than 1% in each case.

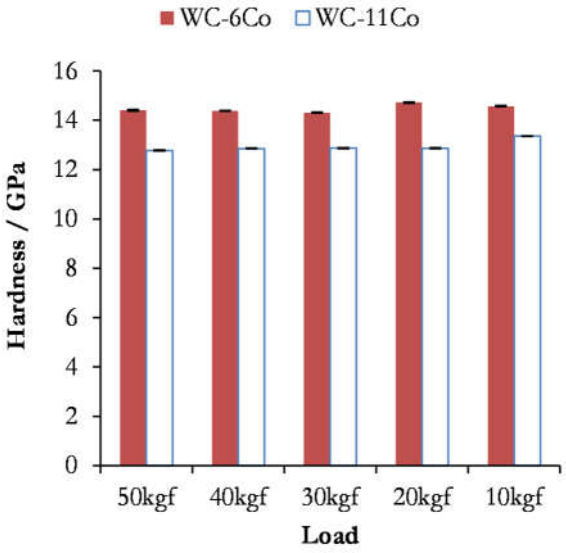

Figure 10-8: Hardness measurement of uncorroded samples.

Palmqvist crack measurements from a minimum of four sets of indentations (12 fractures) for the uncorroded polished sample is shown in Figure 10-9. Whereas hardness measurements are quite consistent (standard deviation of not more than 2 μm) the standard deviation for crack lengths is around 20 μm.

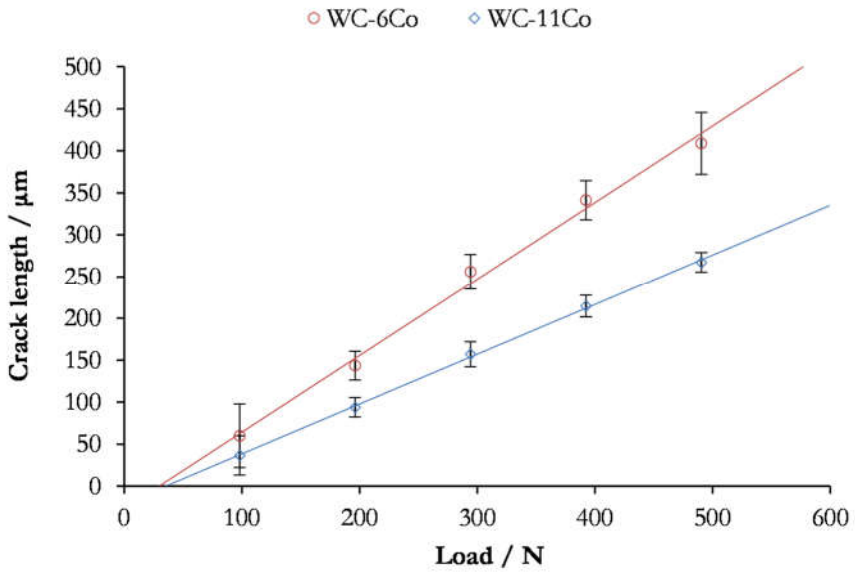

Figure 10-9: Palmqvist measurements of WC-Co uncorroded samples.

A linear relationship between applied load and crack length is obtained, which corresponds to the Palmqvist crack model as shown by Shetty et al. [83]. For a given load the crack length is longer for the WC-6Co than the WC-11Co sample indicating lower fracture toughness. Both samples intersect the x-axis at 35 N which gives P_0

values for Equation (8.8). The Palmqvist toughness can then be calculated for each load using this equation, see Figure 10-10.

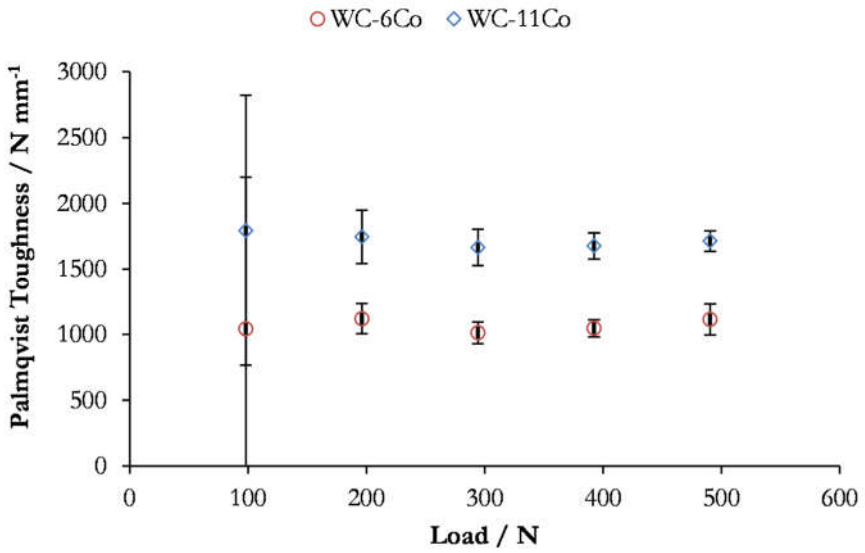

Figure 10-10: Calculated Palmqvist toughness values.

Although there is variability in experimental error across the five loads ranging from 5% at the higher loads up to 57% at 10 kgf, average values for all loads converge on similar Palmqvist fracture toughness values of 1065 N mm^{-1} and 1720 N mm^{-1} for WC-6Co and WC-11Co, respectively. A summary of the material properties obtained for the two samples is given in Table 10-2, including fracture toughness calculated from Equation (10.1). As would be expected the lower binder content sample has a higher hardness value but lower fracture toughness, and the opposite is true for the higher binder composition.

Table 10-2: Fracture toughness of uncorroded samples

Composition	H / GPa	W / N mm^{-1}	K_{IC} / MPa $m^{0.5}$
WC-6Co	14.5	1065	11.1
WC-11Co	12.8	1720	13.2

10.2.3 Fracture Characterisation

Using SEM to image the fractures, it is possible to identify typical fracture features that have been described in the literature from three point bend test fractures:

- Intergranular fracture of WC grains, see Figure 10-11a,
- Transgranular fracture of WC grains, see Figure 10-11b,
- Binder ligaments, see Figure 10-11c and
- Microfractures ahead of crack tip, see Figure 10-11d.

These features are important to identify in the context of being able to validate numerical modelling of fracture at the mesoscale. Intergranular fracture tended to result in deflection of the fracture when the WC/WC was not aligned with the fracture direction. Transgranular fracture on that other hand tended to be parallel to the fracture direction.

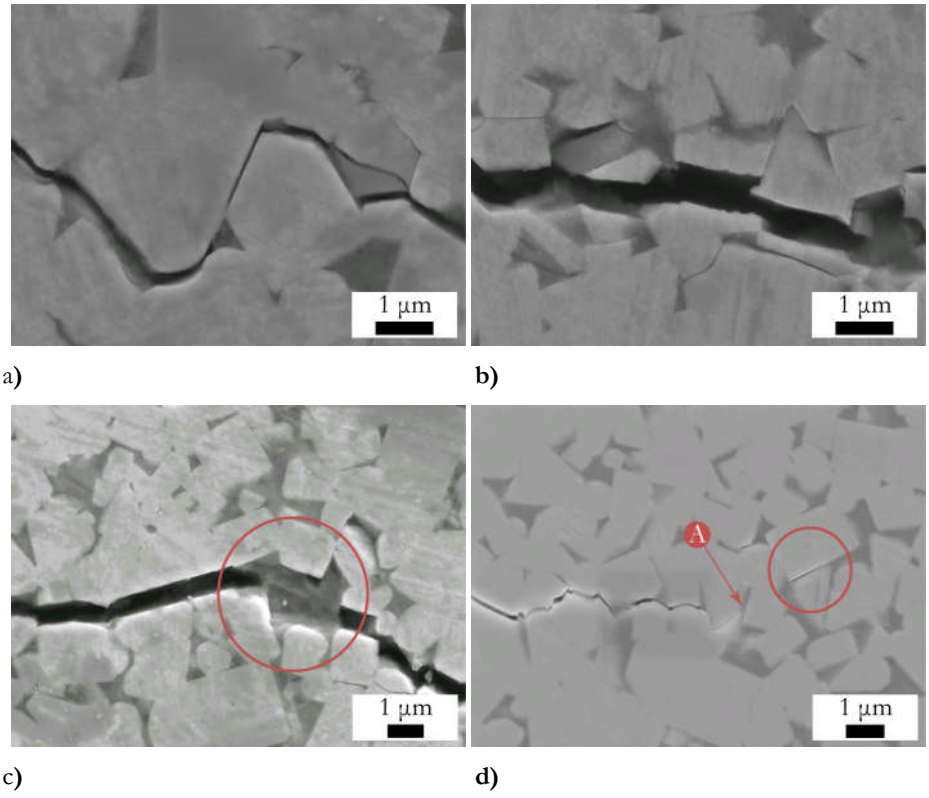

Figure 10-11: Examples of fracture features a) intergranular fracture b) transgranular fracture c) binder ligaments in binder phase and d) microcracks ahead of main fracture tip (A). Fractures propagating left to right in all images.

The Palmqvist cracks obtained from the 30 kgf loads are imaged in SEM and characterised using the technique discussed in Section 8.6.5. Results are shown in Figure 10-12.

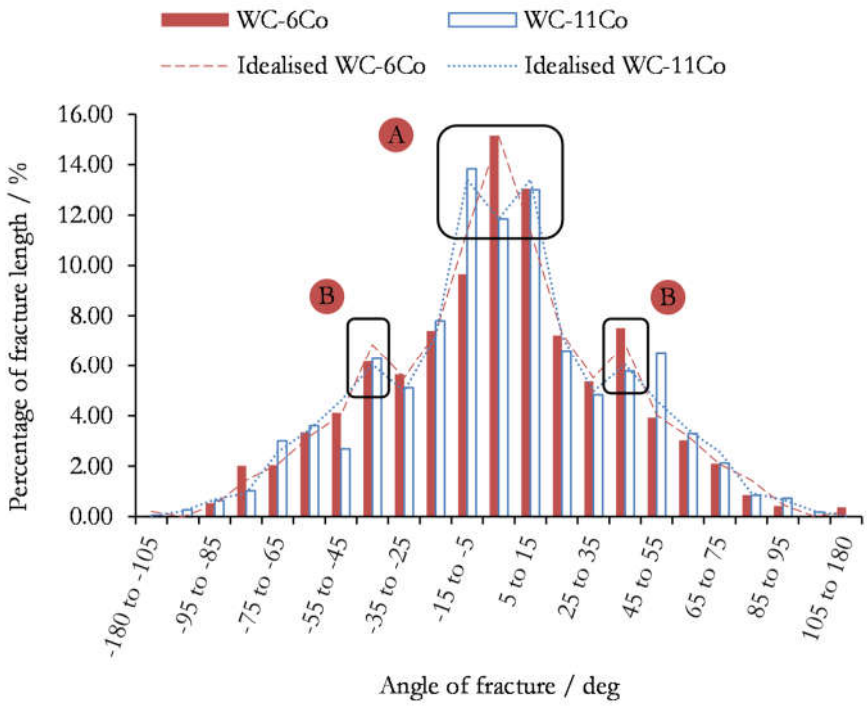

Figure 10-12: Characterisation 30 kgf Palmqvist fractures for uncorroded WC-6Co and WC-11Co samples. A: Propensity to fracture perpendicular to load. B: additional peak observed at 35° to 45°.

The deflection angle histogram has the typical appearance of a bell curve but with notable features. Fractures tend to propagate between 5° and −5° to fracture direction for the WC-6Co sample. The preferential fracture direction is modified slightly in the WC-11Co sample and tends to propagate at 5°–15° to the fracture direction, highlighted as A in Figure 10-12. In both samples there is also another preferential fracture direction at 35°–45°, highlighted as B in Figure 10-12. By taking the absolute angle of fracture an idealised fracture characterisation can be created which retains the features described previously. These will be used later to compare corroded with uncorroded fracture paths. For both samples and loads tested, the relationship between projected length and the total length of the fracture remained constant at 20 kgf and 30 kgf, see Figure 10-13. This results in a fracture roughness of approximately 1.23 ± 0.04.

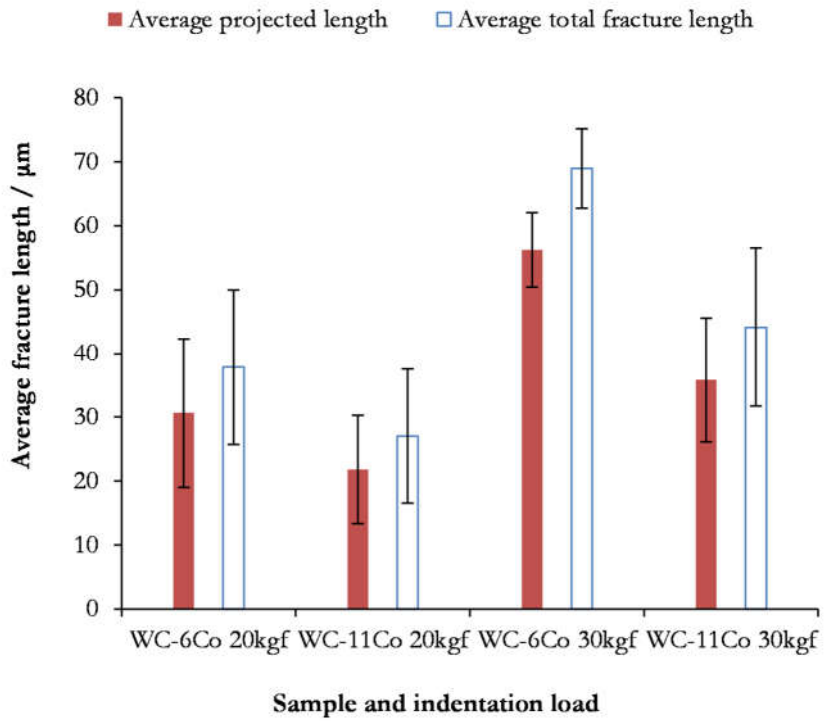

Figure 10-13: Uncorroded project fracture length vs total fracture length.

10.2.4 Discussion

Noise in the load-displacement data of nanoindentation experiments at 1 mN led to high variation in hardness and Young's modulus values, with the relative standard errors of 30% and 40% respectively. The scatter in results could be due to a mixture of factors which will have a larger impact at lower loads, including environmental disturbances such as change in temperature, surface effects such as surface stresses induced by polishing and tip geometry of the indenter. Although calibration was performed to account for tip geometry, imperfections such as tip bluntness and asymmetry will contribute to experimental error and have a larger impact at shallower depths. Furthermore, on corroded samples the non uniformity of the surface will add further scatter to the results which will be difficult to separate from the existing variability. These factors mean that the 1 mN loads are unable to provide sufficient precision for meaningful comparisons to be made between samples.

Lower noise in the 10 mN and 30 mN load-displacement data enabled pop-in events to be identified in around 1 in 10 indentations. These are attributed to dislocations nucleation and so require enough energy to initiate. This explains why pop-ins consistently appear at similar loads of between 15 mN and 25 mN as they relate to intrinsic material properties. The energy required to initiate a dislocation is also

depended on the crystallography of the carbide grain. As discussed in Section 3.1.3, WC grains are anisotropic, which means that depending on the grain orientation relative to the surface, differing properties would be measured. This material property difference results in whether pop-in events occur and at what load.

In the literature studies were able to take distinct measurements of binder, basal and prismatic planes. These required lower loads to be used, typically between 0.2 mN and 2 mN [45, 57, 185, 193] or large grain sizes more than 5 μm to be used [57, 194, 195]. These enable indentation depth to be no more than 10% of WC grain size. These results could not be replicated in the experiments as grains sizes are around 1 μm for both samples and indentation depths are 15% and 30% of the grain size for 10 mN and 30 mN loads. Furthermore, small binder mean free paths of 0.3 μm makes targeting binder phases without interference from adjacent WC grains impossible as imprints are approximately 0.67 μm and 1.29 μm for the 10 mN and 30 mN loads respectively. Although a wider distribution was observed at 10 mN compared to 30 mN (Figure 10-3 and Figure 10-4), which would be expected if differing phase properties were being measured, distribution of values is even across the range which means that individual phases cannot be identified. Additionally, the range is narrower than would be expected for the individual phases which have been reported as hardness of around 23 GPa and 14 GPa for basal and prismatic facets [47] and binder hardness of 8 GPa. This would suggest that neighbouring phases are still influencing measured values.

As well as the experimental errors discussed earlier for the 1 mN load, physical effects also have an impact on the measured properties. Typically as indentation depth decreases measured hardness increases slightly due to size effects. This has been observed in many engineering material, referred to as indentation size effect (ISE), including WC-Co [47, 196]. This effect was mathematically described by Abu Al-Rub and Voyiadjis [197, 198] through understanding of the dislocation process which depends on the scale of measurement. A larger penetration depth will result in initiating a greater number of dislocations and the material will therefore appear to have lower hardness. This results in a characteristic exponential decay function relationship between measured hardness and load with hardness approaching a minimum value. These size effects can also be observed when comparing the average hardness values from nanoindentation which are around 25% – 30% higher compared to the Vickers test. At the macroscale little difference in average hardness

was observed when comparing results from 10 kgf to 50 kgf loading. One of the implications of this is that hardness obtained from nanoindentation cannot be used to calculated fracture toughness from Palmqvist tests unless a mathematical relationship is created to account for size effects.

However, when comparing the 10 mN and 30 mN loads measured hardness reduces slightly. One explanation for this contradiction is that at lower loads the binder phase can become more influential on the indentation behaviour. Loads distributed through the carbide phase will be more resistant to plastic deformation than that distributed in the binder phase. As the load increases load is primarily distributed through the carbide skeleton which would increase the average hardness. This highlights one of the challenges with trying to obtain in-situ measurements of the individual phases in WC-Co, which are highly dependent on both size effects and the local microstructure.

As expected the hardness of the WC-6Co is higher than that of the WC-11Co due to the higher content of ceramic phase, as discussed in Section 3.2.1. The hardness values obtained are similar to that obtain in literature which typically range between 13 GPa to 16 GPa for similar WC-6Co grades and 10 GPa to 14 GPa for WC-11Co grades. Using the relationship between binder fracture and contiguity developed by Lee and Gurland [67] discussed in Section 3.2.3 (Equation (3.5)) WC-6Co and WC-11Co would have a predicted hardness of 13.2 GPa and 10.4 GPa respectively. Although smaller WC grain size typically increase the hardness according to a Hall-Petch relationship, see Section 3.2.2, the small difference between the two samples results in a less than 0.5% difference (from Equation (3.3)) in predicted hardness. As a result the difference in composition and continuity which describes the WC microstructure will have the greatest affect on mechanical behaviour. The dominant ceramic phase in WC-6Co also results in a lower fracture toughness as would be expected, see Section 3.3.3. Fracture toughness values calculated from the Palmqvist test are also similar to that obtained in literature for comparable compositions, with Spiegler et al. [84] reporting fracture toughness of 11.68 MPa $m^{0.5}$ for WC-6Co with grain size of 0.83 μm and 13.06 MPa $m^{0.5}$ for WC-12Co with grain size of 0.69 μm.

Both Palmqvist relationships converge on the same P_0 values and is similar to values obtained by Shetty et al. [83] which range between -87 N and 86 N. Exner [80] attributed this critical load to surface stresses created during grinding, suggesting

sample preparation created a similar surface stress state in both samples post polishing. Exner suggested that removal of the ground surface through polishing would result in critical load converge to zero. Despite extensive lapping and polishing of the samples this critical load remained. Given that other author also had critical loads not equal to zero and the inclusion of P_0 in Palmqvist toughness, it is unlikely that this will impact calculated fracture toughness values.

Obtaining similar Palmqvist toughness for each load suggests that fracture toughness measured is independent of applied load. Fracture roughness is also independent of load suggesting that fracture behaviour is the same allowing analysis of fracture produced by any load. However, fracture roughness remains constant for both samples which is a surprising result as they have different compositions and microstructure. This could be due to one of two reasons. Firstly, that the differences in microstructure and composition cancel each other out, resulting in similar behaviour. The other explanation is that fracture profile will always remain constant. Given that the material properties of the phases are the same and that microstructure is the only difference then dissipation of fracture energy in a given phase would be the same. If the energy required to deflect the fracture is too high, fractures would become transgranular rather than intergranular, thus reducing fracture roughness. This would be dictated by microstructural properties, which may be too similar in the samples tested to perceive this difference in behaviour.

Analysis of the fracture found that WC grains are the driving force behind fracture path, as was also concluded from simulation of fracture behaviour in Chapter 7. Intergranular fracture between either WC/WC or WC/Co increases tortuosity of the fractures. WC grains had to be both sufficiently large in order for deflection to occur and at an angle such that transgranular fracture was not initiated. Grain size therefore becomes a driving factor to tortuosity.

10.3 Samples Immersed in Acidic and Alkaline Environments

10.3.1 Nanoindentation

Indentation maps (10×10) at loads of 30 mN were performed on the WC-6Co samples from Section 9.2, which has been immersed for 7 d. The results for hardness and Young's modulus are shown in Figure 10-14 and Figure 10-15 respectively.

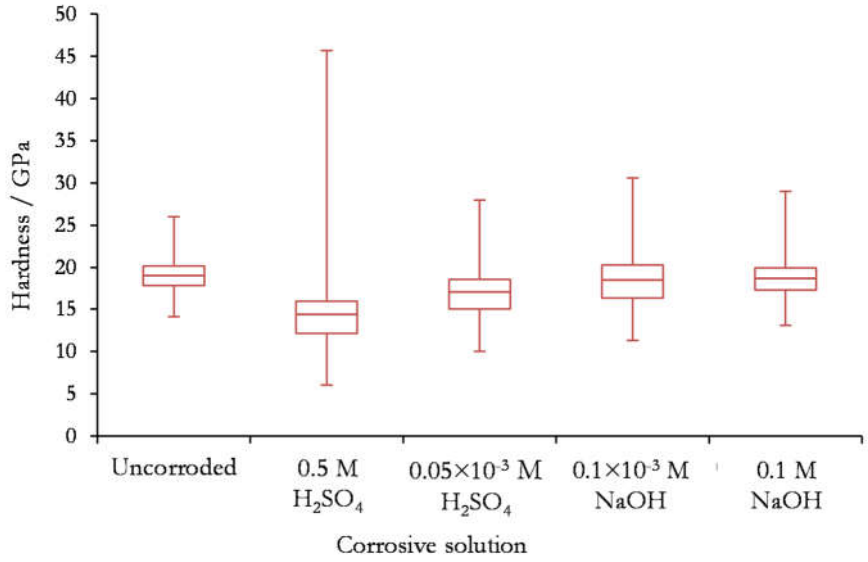

Figure 10-14: Comparing hardness of corroded samples WC-6Co after immersion for 7 d.

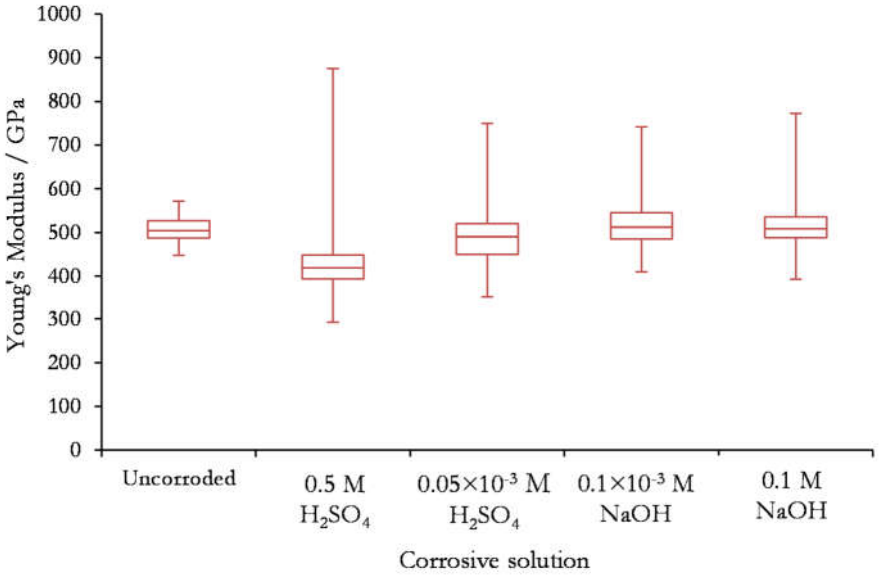

Figure 10-15: Comparing Young's modulus of corroded samples WC-6Co after immersion for 7 d.

There is little change to the hardness and Young's modulus for samples exposed to corrosive solution except for the 0.5 M H_2SO_4 sample which has a slight reduction in both, hardness from 19 GPa to 14 GPa and Young's modulus from 505 GPa to 425 GPa. In the other solutions hardness reduced to 18 GPa and increased Young's modulus to 510 GPa. The data is also has a larger distribution, although the interquartile range is consistent across all tests, see Figure 10-16 and Figure 10-17.

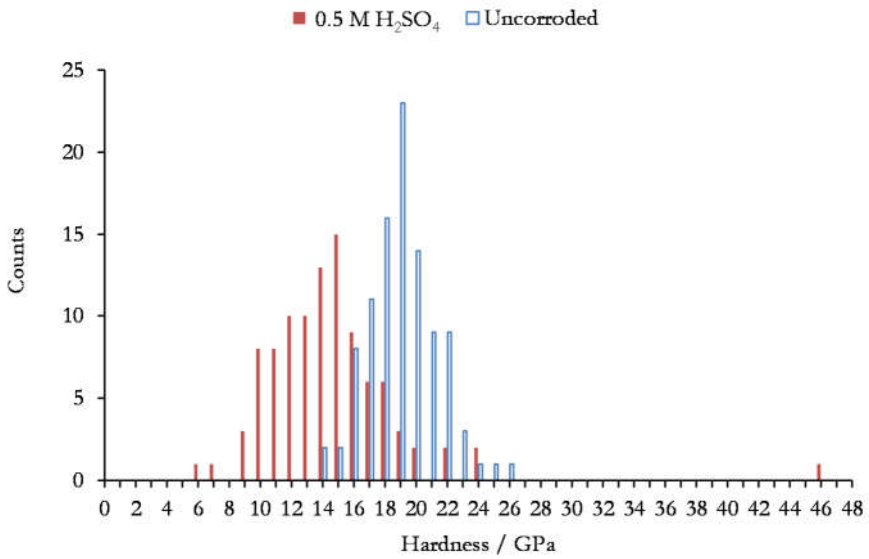

Figure 10-16: Measured hardness of WC-6Co samples at 30 mN, comparing uncorroded with sample immersed in 0.5 M H_2SO_4 for 7 d.

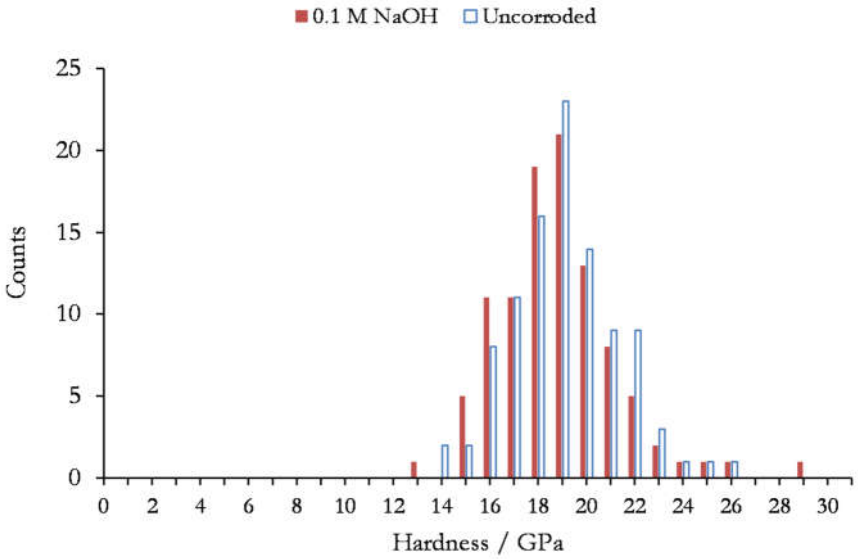

Figure 10-17: Measured hardness of WC-6Co samples at 30 mN, comparing uncorroded with sample immersed in 0.1 M NaOH for 7 d.

10.3.2 Fracture Properties

Fracture properties of the corroded samples were calculated from measurement of Palmqvist fractures. The hardness, calculated from the Vickers indentations, is little changed compared to the uncorroded sample and all four immersion tests.

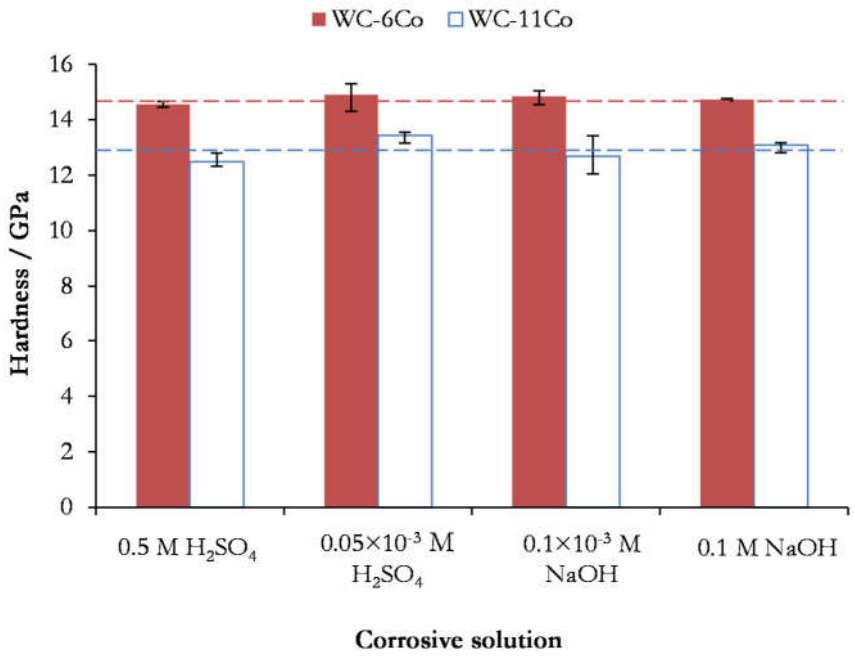

Figure 10-18: Comparison of hardness after immersion in corrosive solution, lines indicating uncorroded hardness for WC-6Co (red) and WC-11Co (blue).

Unlike the uncorroded polished samples it was more difficult to identify the fracture length using the Alicona. This was caused by both damage created by corrosion which reduced the contrast between fracture and surface and also a reduction in the fracture opening. This leads to an underprediction in fracture length and therefore increase in fracture toughness. For corroded samples the SEM was used to analyse the fractures created by loads at 20 kgf. The measured fracture toughness for WC-6Co and WC-11Co post corrosion is shown in Figure 10-19. The hardness of the corroded layer was assumed to be the same as for uncorroded samples. There is a clear reduction in the calculated fracture toughness for all samples, with the highest reduction for the sample immersed in 0.5 M H_2SO_4 which was reduced to 4 MPa $m^{0.5}$.

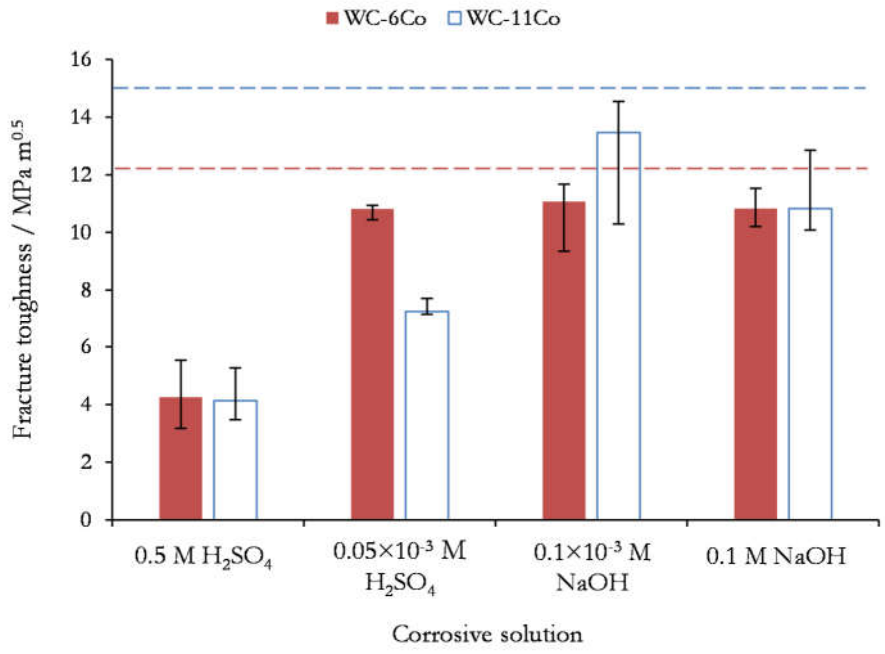

Figure 10-19: Comparison of fracture toughness post immersion for WC-6Co. Lines indicating uncorroded fracture toughness for WC-6Co (red) and WC-11Co (blue).

10.3.3 Fracture Characterisation

The fracture roughnesses are calculated from the profiles of the Palmqvist fractures, see Figure 10-20.

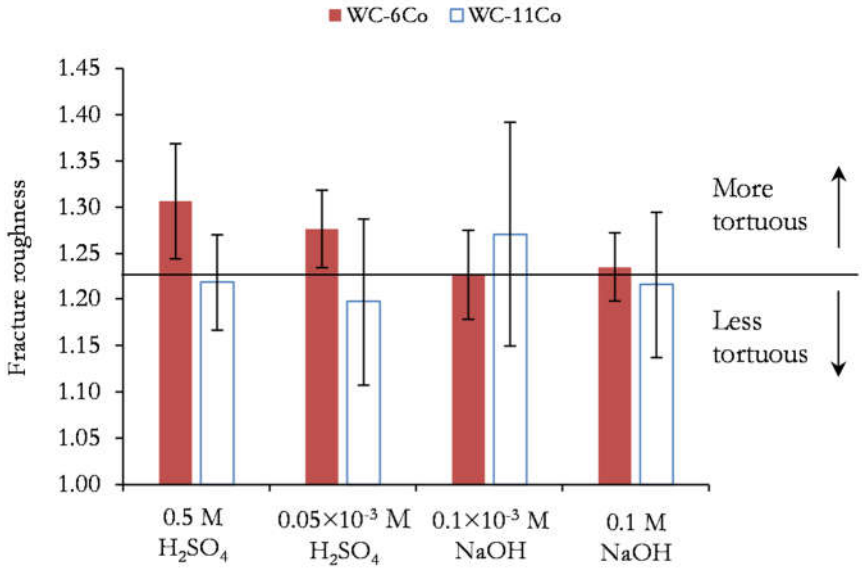

Figure 10-20: Profile roughness for WC-6Co and WC-11Co post corrosion.

The fracture roughness of the WC-6Co samples increase in acidic solutions, up to 1.3, and remain unchanged in alkaline environments. WC-11Co, on the other hand,

has mixed results and has a higher standard deviation. Fracture roughness reduced to 1.2 in acidic solution, increases in 0.1×10^{-3} NaOH and is unchanged in 0.1 M NaOH. The increase in fracture roughness is reflected with a meaningful change in the fracture profile, see Figure 10-21 and Figure 10-22. Much fewer fractures propagate parallel to the fracture direction (between -15° and 15°) as highlighted by A. In the WC-11Co the fracture profile becomes wider and flatter with fractures propagating between -25° and 25° equally. Furthermore, there is an increased tendency to propagate between 35° and 65° in the WC-6Co samples, B in Figure 10-21. By comparison, when fractures roughness was reduced propagation increases between -25° and 25° (A) and reduces outside this path (B), see Figure 10-23. The double peak that was seen in the uncorroded sample remains.

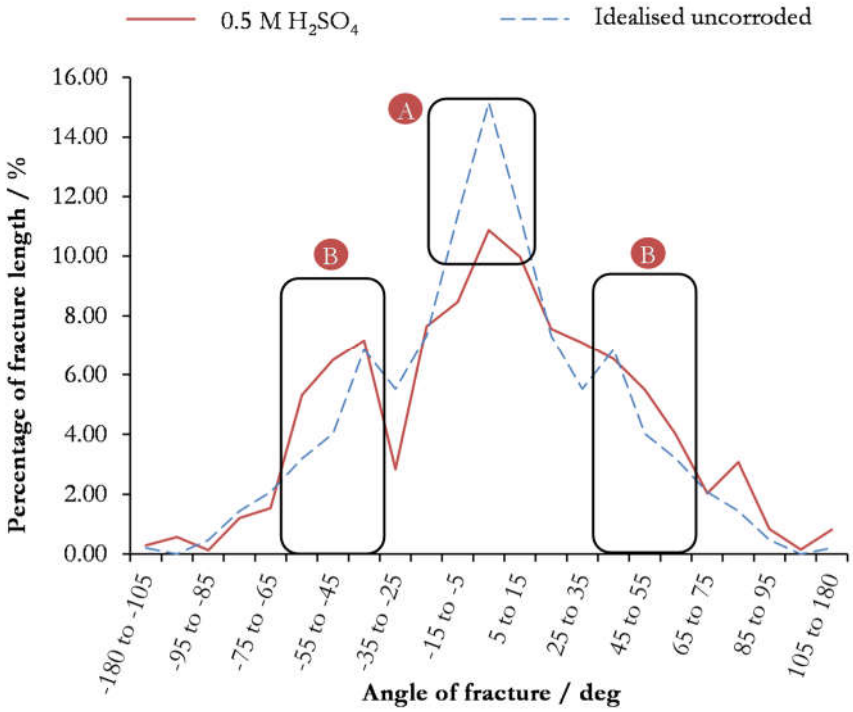

Figure 10-21: Fracture characterisation WC-6Co immersed in 0.5 M H_2SO_4 for 7 d (increased fracture roughness). A: reduced propagation direction. B: increased propagation direction.

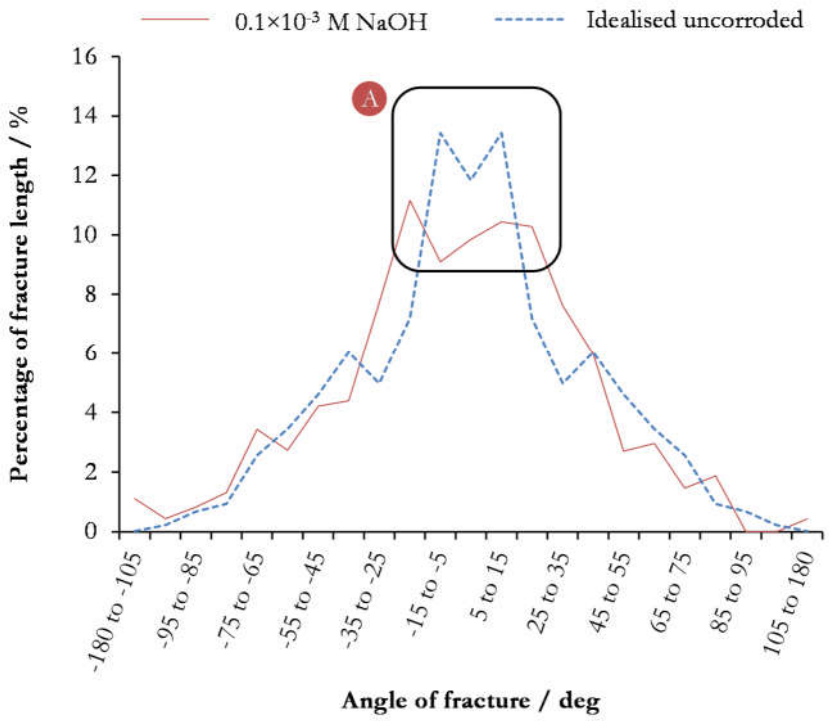

Figure 10-22: Fracture characterisation WC-11Co immersed in 0.1 M NaOH for 7 d (increased fracture roughness). A: increased propagation direction.

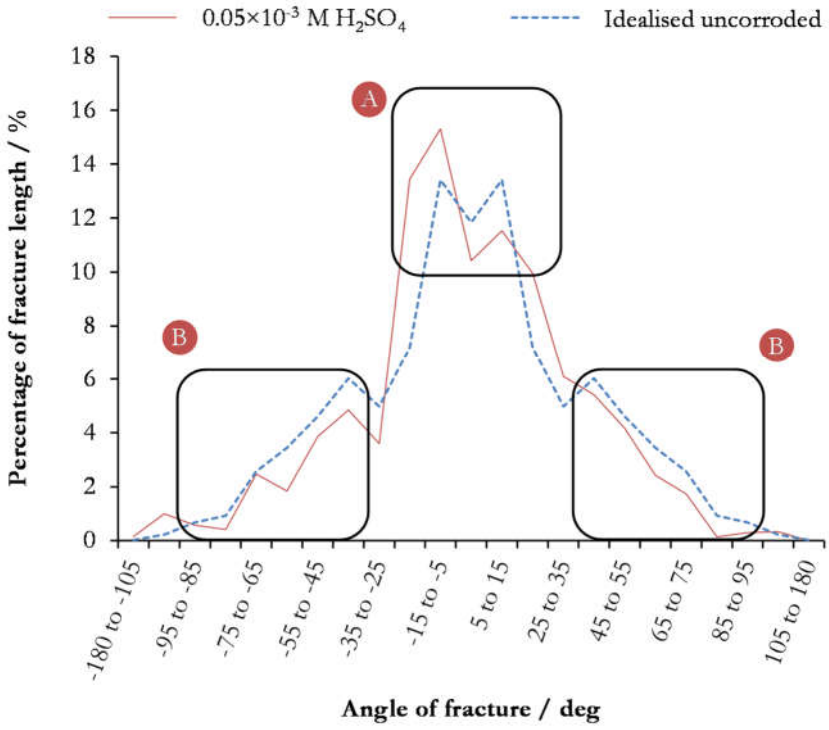

Figure 10-23: Fracture characterisation WC-11Co immersed in 0.05×10^{-3} M H_2SO_4 for 7 d (reduced fracture roughness). A: increased propagation direction. B: reduced propagation direction.

Other notable features seen in the corroded fracture are a tendency for microfracture to propagate further ahead of the fracture tip, see Figure 10-24a and Figure 10-24b. Whereas microfractures would be within 1-2 μm in uncorroded samples, in corroded samples this increased to over 5 μm. Furthermore, they were also found outside the main fracture path, see Figure 10-24c.

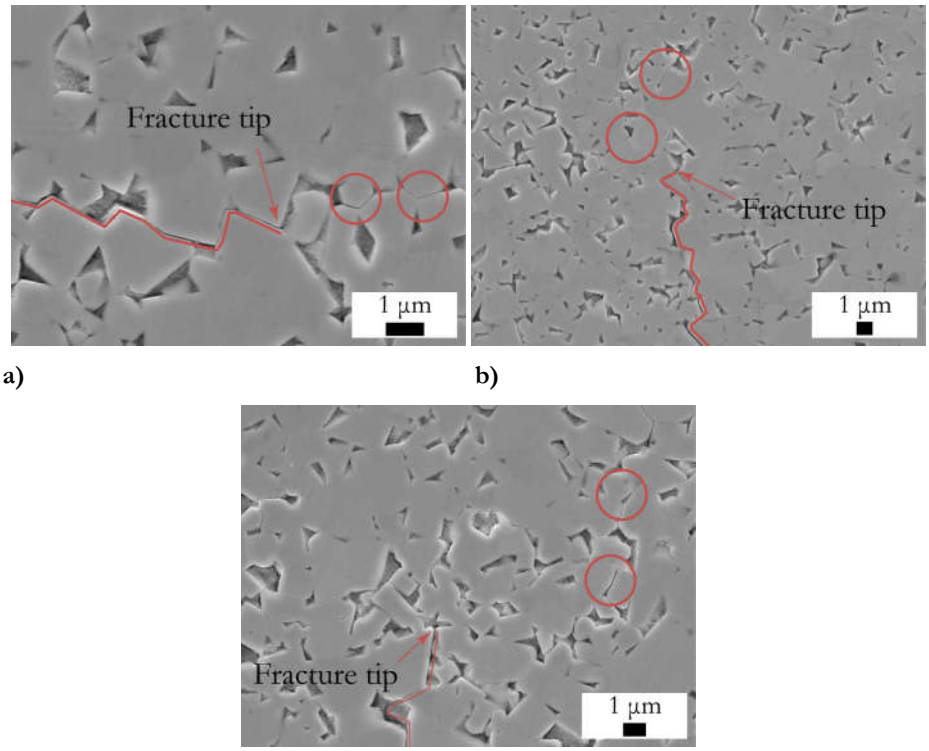

Figure 10-24: Examples of microfracture ahead of fracture tip WC-6Co sample exposed to 0.5 M H_2SO_4 for 7 d. a) and b) examples of microfractures ahead of fracture tip and c) example of microfractures outside main fracture path.

There was also more frequently observed slip bands in corroded samples in the vicinity of indentations, see Figure 10-25.

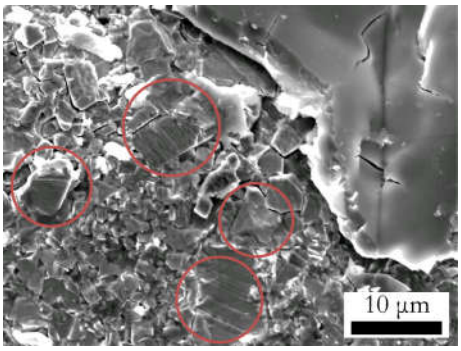

Figure 10-25: Evidence of slip planes in WC grains in WC-6Co immersed in 0.5 M H_2SO_4 for 7 d.

10.3.4 Discussion

Nanoindentation of WC-6Co samples shows a reduction in both hardness (25%) and Young's modulus (15%) in the most acidic environment (0.5 M H_2SO_4). This is likely due to the inability for stresses to be distributed through the microstructure as the binder is removed. So despite reduction in the softer material, hardness appears to reduce due to an increase stress concentrations and will result in the creation of slip bands which were more prevalent around Vickers indentations on the 0.5 M H_2SO_4 samples. This would also explain why the properties change little in the other solutions as sufficient binder remains to distribute stresses, with average value within experimental error can therefore be assumed unchanged. This result is repeated in the Vickers indentations across all loads.

While hardness may not have changed, the fracture toughness of the samples shows a significant reduction post corrosion for all samples. This shows that radial cracks are shallow enough to capture the effects of corrosion of the surface. This is also the region of most interest as it will be the surface in contact in a tribocorrosive environment. The reduction of fracture opening, which made it more difficult to identify fractures using the Alicona, is also indicative of reduced fracture toughness as energy is released quickly and along the surface.

The fracture toughness was reduced in all samples and for every solution tested. This effect was highest in the 0.5 M H_2SO_4 solution which reduced fracture toughness by around 70% and least impact on in 0.1×10^{-3} NaOH, reducing fracture toughness by less than 10%. This relationship also roughly follows the extent of degradation of the binder seen from immersion tests, indicating that this process is the driving factor behind reduction in fracture toughness. As discussed in Section 9.3, when exposed to acid there is preferential removal of the binder phase. Given that the binder is added to provide the bulk material with increased fracture toughness it would be expected that fracture toughness of the bulk material reduces after its removal. In the 0.5 M H_2SO_4 solution fracture toughness approaches that of WC (~3 MPa $m^{0.5}$).

The increase in tortuosity in the WC-6Co samples exposed to acidic solution results from an increase in intergranular fracture as the binder is no longer able to distribute stresses in the microstructure. This is reflected in the fracture profile which shows increased fracture at between 35° and 65° which is indicative of increased intergranular fracture. Furthermore, stress concentrations are increased in the WC

skeleton. This reduces the remote load required to induce fracture at WC/WC interfaces. As such, microfractures are able to initiate much further ahead of the fracture tip. As was discussed in Chapter 7, the initiation of microfractures ahead of the crack tip heavily influences the direction of fracture propagation as a new stress concentration is introduced into the domain. This process will therefore increase the tortuosity of the fracture path.

Tortuosity in the WC-11Co sample however reduced slightly. This is likely to be a result of the increased binder content and lower contiguity. The preferential depletion of the binder will therefore create larger voids in the material compared to the WC-6Co sample and thus tortuosity will reduce as the binder will not inhibit fracture propagation. Furthermore, in lower contiguity microstructures fracture will not be deflected as often by WC/WC grain boundaries. The large scatter in fracture roughness values shows that there is high variability in the fracture path which would depend on features in the local microstructure such as an area of dispersed WC grains (which would reduce fracture roughness) or a larger grain which is not orientated parallel to the fracture direction (which would increase fracture roughness).

One of the main challenges in measuring the fracture profile was identifying the fracture. Whereas the surface of uncorroded samples was smooth and defect free, corroded samples, especially those in the 0.5 M H_2SO_4 solution, binder depletion led to significant degradation of the surface with voids where the binder had been depleted. This lead to many Palmqvist fractures not able to be measured as energy has been dissipated through spalling of multiple carbides rather than through Palmqvist fractures, see Figure 10-26.

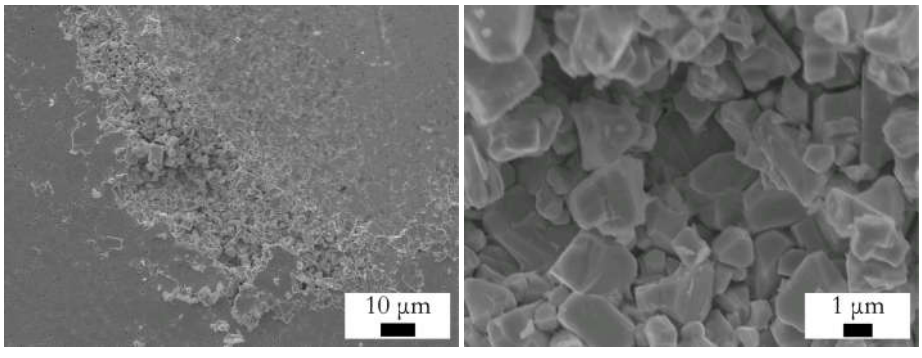

a) **b)**

Figure 10-26: Effect of binder depleted region for WC-6Co immersed in 0.5 M H_2SO_4 for 7 d.

Additionally, Palmqvist fractures are typically measured from the crack root to the crack tip. This works well for fractures which are continuous and do not bifurcate. However, as microfractures were beyond the crack tip and outside the main fracture path, energy released in these events would not be considered. If these fractures had been considered, measured fracture toughness would be reduced further.

For a given load energy dissipation will be the same for both samples. This energy is either distributed as stress through the domain or released in the fracture process of WC/WC interfaces, WC/Co interfaces, or WC and Co phases. In WC-11Co crack lengths are shorter as more energy is released in the fracture of the binder phase compared to WC/WC or WC fracture. However, this also means that the true length of the fracture is a more accurate measure of the fracture toughness compared to projected length. Even if binder content were the same, differences in the microstructure could result in differing fracture toughness being measured, even although energy dissipation through fracture would be the same. This would result from differences in tortuosity of the fracture path, which is measured by the fracture roughness. In the 0.5 M H_2SO_4 solution, fracture toughness measured using the total fracture length would be calculated to be 3.7 MPa $m^{0.5}$, 12% less than calculation using the projected length. In order to integrate this concept into the Palmqvist toughness, true fracture length can be integrated into Equation (3.15):

$$W^* = \frac{P - P_0}{\sum l_d} \tag{10.2}$$

Total fracture length be approximated by multiplying the projected length by the profile roughness:

$$\sum l_d = L_{\text{pr}} R_{\text{L}} \tag{10.3}$$

This adaption of the equation would alter Equation (10.1), which relates Palmqvist toughness to fracture toughness:

$$K_{IC} = 0.0889\left(H\left(W^* R_{\text{L}}\right)\right)^{0.5} \tag{10.4}$$

Further development of this model may also consider the depth of the fracture as deeper fractures will release more energy compared to shallower fractures.

10.4 Conclusions

Hardness measurements of WC-6Co and WC11Co samples were made using Vickers and nanoindentation techniques. Measurements from the Vickers test were close to that approximated by Lee and Gurland [67], while nanoindentation measurements were around 30% higher as a result of size effects. This poses a significant issue when comparing various studies as results are not directly comparable. Post corrosion nanoindentation found little change in the properties indicating that individual phases are not altered during corrosion thus changes to the bulk material properties arise from changes to the microstructure and interaction between WC and Co phases.

Analysis of Vickers indentations and Palmqvist fractures were able to show clear differences between the WC-6Co and WC-11Co samples. The higher fraction of binder results in reduction of hardness and increase in the fracture toughness. After exposure to corrosive solutions both sample experienced a significant reduction in fracture toughness, with highest change in the 0.5 M H_2SO_4 solution. Analysis of the Palmqvist fractures also indicate changes to how fractures propagate, for example changing from transgranular to intergranular. The two samples also diverged in behaviour after corrosion. In the WC-6Co, where there is a higher percentage of WC phase and higher contiguity fracture roughness increased as the binder was depleted. In contrast, the WC-11Co sample where binder percentage is higher and has lower contiguity fracture roughness tended to be more scattered which suggested local microstructure was heavily affecting the fracture path.

The results highlighted one of the main weaknesses in the Palmqvist approach as energy released through fracture may not always be accounted for. Effects such as tortuosity and microcracks can be significantly altered and thus have the potential to affect measured fracture toughness. A modification to Shetty's relationship between Palmqvist toughness and fracture toughness was suggested, although further research is required.

Reviewing the approach to tribocorrosion described in Section 4.1, results indicate that research on the mechanical effects of corrosion should the focus on how the microstructure is affected by corrosion (C1 in Figure 4-1) as well as the interface properties between WC/WC and WC/Co. Furthermore, these results are important to being able to validate future simulation of fracture behaviour. In a similar way to the discrete fracture steps that were described and subsequently simulated in Chapter

7, enabled validation for the model, this understanding of fracture behaviour also needs to be developed for corroded samples.

The change in the microstructure which results in the substantial reduction of fracture toughness is likely to be the primary cause of synergistic wear described in the synergy model of tribocorrosion. It can therefore be reasoned that through understanding and modelling of this effect, 'synergy' could be modelled explicitly without the need for empirical fitting parameters.

Chapter 11 – Conclusions and Future Work

Chapter Highlights

Experimental and computational modelling of WC-Co material has been conducted with a view to better understanding of the degradation mechanism in a tribocorrosion environment. Through understanding and combination of multiple disciplines (tribology and electrochemistry; experimental and modelling) new insight was achieved into what is already a well researched material. This chapter summaries the findings from this thesis as well as drawing the pieces of work from each chapter together. This section concludes with a discussion on potential areas of future work.

- FDEM was able to capture material physics without the need for empirical relationships, demonstrating its suitability for modelling WC-Co degradation.
- The effects on microstructure could be distinguished between acidic and alkaline environments. Furthermore, combination with electrochemical techniques enabled understanding of why physical effects occurred.
- Mechanical testing of corroded samples allowed material properties to be measured and is useful as a means of validating simulated fracture behaviour.

11.1 Conclusions

This thesis presents a significant departure from current approaches to the study of tribocorrosion which were found to be inadequate in predicting wear for cemented tungsten carbides. Rather than measuring mechanical and corrosive mass loss in isolation and calculating the difference with overall mass loss when combined, the approach seeks to explicitly simulate the microstructure and mechanisms that lead to mass loss. This was performed by validating a numerical model (FDEM), which could simulate the primary physics of WC-Co including fracture behaviour (see Chapter 4 till Chapter 7). Conclusions from these simulations are covered in Section 11.2. This was followed by demonstrating experimental corrosion and mechanical techniques that can be used to inform and validate this approach. Firstly the effects on the microstructure were studied, which included electrochemical techniques to help understand the processes (see Chapter 9). Following on from this the mechanical properties changes to the material were studied using nanoindentation and a novel extension of the Palmqvist method which could be used to validate fracture behaviour of simulations (see Chapter 10). Conclusions from these experimental results are covered in Section 11.3. Although this approach was designed to address the challenges of tribocorrosion of WC-Co, the principles could be applied to other tribocorrosion problems although other mechanical and corrosive behaviours, such as ploughing and passivation, may have to be considered.

11.2 Modelling Fracture of WC-Co

The modelling approach presented focused on numerical methods that used intrinsic material properties rather than empirical relationships which were identified as a weakness in the current approaches used in literature. Moving towards this kind of understanding could help in prediction of material performance and material loss mechanisms. Furthermore, one of the main challenges in modelling brittle materials, such as WC-Co, is being able to capture failure through fracture. This meant that standard numerical methods which use continuum methods are not adequate. Y-Geo, a FDEM code, was selected as a suitable platform due to its ability to capture both elastic and fracture behaviour. As Y-Geo is a research code, additional post processing was required in order to analyse results from the simulation. Matlab script was written for performing actions such as downsampling, adding node forces to calculate total element force and visualisation of fracture in relation to element

properties. Modelling work focused on the simplest and most common cemented tungsten carbide WC-Co. Simulations looked to validate the ability of FDEM to accurately simulate fracture behaviour of WC-Co, both a critical part of the degradation process and an area which is currently a weakness in numerical modelling. The work demonstrated that brittle failure can be simulated explicitly.

- In Chapter 6, Kirsch's analytical solution for stress distribution around was simulated accurately and fracture initiated within 5% of the theoretical remote applied stress.
- Through using intrinsic properties of brittle and ductile materials and varying the proportion of each, modelling in Chapter 7 was able to show that simulations could replicate the rule of mixtures relationship for bulk material fracture strength.
- This was extended in Chapter 8 by modelling at the mesoscale, which enabled microstructural parameters to be modeled explicitly. The model was able to simulate the final fracture path and capture the discrete fracture steps as described from experimental results.

Through using this approach, tribocorrosion is broken down into microstructural effects and material properties only. This removes the need for synergy values to be calculated. It is hypothesised that synergy is a result of changes to the material which affect how stresses are distributed in the microstructure and consequently alters the propensity for fracture to occur. This behaviour can be captured explicitly in simulations, provided material properties are accurate and physical behaviours can be captured.

This project lays the foundations for a new way of studying tribocorrosion and opens up a new avenue in research for WC-Co and further our understanding of the wear mechanisms. Development of a comprehensive model would allow us to systematically study the effects of individual material and microstructural influences which are difficult to isolate in experimental studies. Fundamental understanding of this nature could lead to the manufacture of optimised of WC-Co structures for a given application.

Finally, the FDEM approach would also be appropriate to study compressive failure as well as other composite material design in which there is a well-defined

heterogeneous structure. It is particularly useful to understand microstructure influences on the material strength.

11.3 Effects of Corrosion on WC-Co

Experimental methods were chosen which could complement the numerical approach presented. The two primary modelling inputs required are microstructure and intrinsic material properties and so experiments which are at the mesoscale offered the most benefit.

In Chapter 9 the effects of corrosion on the microstructure of two commercial WC-Co grades were investigated. Through a combination of electrochemical testing (open-circuit, potentiodynamic polarisation and potentiostatic polarisation) and surface analysis understanding of both the microstructural effects and underlying chemical reaction could be established. Visual inspection of the microstructure and oxide was an important aspect of this work which is not ubiquitous in the corrosion field and therefore restricts their impact in tribocorrosion modelling.

- Acidic environments are dominated by preferential binder depletion as Co is not stable in the solution. This binder depletion was found to be the cause of pseudo-passive behaviour. In a tribocorrosion scenario the corrosive weakening of the surface microstructure would result in increased mechanical wear before pseudo-passive effects are likely to become significant. Modelling of this effect would therefore only be required for studying long term effects of corrosion.

- By contrast alkaline environments are dominated by pitting behaviour. Alloying of W in the binder contributes to increased corrosion at the WC/Co interface in alkaline conditions which creates the conditions for pitting to initiate. Pits can cause significant stress raisers in the microstructure which increase the chance of fracture propagation.

From this understanding it is possible to distinguish between the corrosion effects of acidic and alkaline conditions. This knowledge enabled existing literature to be reviewed and hypothesis made on the corrosive media was which present.

In Chapter 10 the focus was on material properties and fracture behaviour of the WC-Co sample used in Chapter 9, and study the effect of corrosion on these two aspects. This was investigated using nanoindentation and analysis of Palmqvist

fractures. Initial tests were performed on uncorroded samples in order to create a baseline and also establish testing parameters. These were subsequently used to study the corroded samples from immersion tests in acidic and alkaline environments used in Chapter 9.

- There is little change in the intrinsic material properties of the WC grain post corrosion. This suggests that changes in the bulk material properties result from changes to the microstructure and interface properties.
- Analysis of Palmqvist fracture showed a reduction in measured fracture toughness in all corrosive environments. This was correlated to the extent of degradation to the binder phase.
- Change in fracture behaviour could be characterised through measuring the fracture roughness and analysing the fracture profile. In the WC-6Co samples fracture roughness tended to increase as higher contiguity meant intergranular fracture became more prevalent over transgranular fracture. In WC-11Co samples fracture roughness tended to decrease as large voids and a lower contiguity resulted in less deflection of the fracture path.

The reduction to the fracture toughness of the surface layer due to corrosion will significantly reduce the mechanical wear performance of the material. In a tribocorrosive environment the mechanical removal of this layer is likely to occur much faster than the corrosion process of the bulk material below this corroded layer. Temporal effects of corrosion are therefore unlikely to have a significant impact on wear rates unless mechanical wear is stopped and corrosion processes are allowed to continue.

A summary of the contributions to the field to WC-Co tribocorrosion are shown in Table 11-1.

Table 11-1: Summary of main contributions to the field of WC-Co tribocorrosion

Method contributions to the field	Modelling	• Proposed numerical approach to modelling tribocorrosion through explicit modelling. • The use of FDEM to model fracture behaviour of WC-Co.
	Experimental	• Palmqvist fracture tests conducted on corroded surfaces. • Fracture characterisation of Palmqvist cracks.
Knowledge contributions to the field	Modelling	• By assigning different proportions of brittle and ductile properties to individual elements, simulated tensile strength of the bulk material could replicate the rule of mixtures. • Stress is distributed in the domain primarily through the WC structure. Due to the geometry stress concentrations are created and become initiation points for microfractures ahead of the crack tip.
	Experimental	• Pseudo-passivation is caused by the binder depleted region. In WC-Co the extent of this effect is dictated by the microstructure. • Oxide contributes little to the corrosion kinetics in either acidic or alkaline conditions. • Alloying in W contributes to increased corrosion at the WC/Co interface in alkaline conditions, causing pitting. • Hardness is not changed after exposure to corrosive solutions, but fracture toughness is reduced in line with the extent of degradation to the binder phase.

11.4 Future Work

The novel approaches presented in this study opens a number of new avenues to explore the degradation of cemented tungsten carbide. By understanding numerical modelling, corrosion science and fracture experiments it has been possible to more closely align all three disciplines so that they are able to aid one another in developing our understanding of WC-Co. It is possible to advance each of these areas individually while still retaining their ability to inform one another.

11.4.1 Computational

There are many opportunities to develop and improve the accuracy of this model. These suggestions can be broken down into three areas:

i. Further simulations using existing software with information from other experimental data,

ii. Development of numerical code and

iii. Validation steps needed to achieve full tribocorrosion model.

The current platform has the ability for further studies on WC-Co to be performed. Differences between transgranular WC fracture and intergranular WC/WC fracture can be implemented through different fracture properties. This would be particularly important where there is very low binder fraction leading to more WC/WC than WC/Co interfaces. Fracture is therefore likely to progress primarily through WC areas rather than alternating through WC and Co phases as with the domain studied which had 10 wt.% binder content. There is also evidence that grain orientation affects the fracture process [86]. Provided that accurate material properties can be measured for the individual facets, it is possible to implement the structure through specifying different material properties and bias meshing to mimic preferential slip directions.

Numerically, the software can be developed through improving modelling the material behaviour. Currently, plasticity models which do exist in the literature are not present in the Y-Geo environment. This would be especially beneficial to more accurate modelling of the ductile binder phase. Adaptive mesh refinement for fracture models is also of particular interest as unlike standard FEM, the dynamic simulation leads to redistribution of stress as the fracture propagates. This means that the region of interest, usually requiring greater mesh density, moves around the

domain. Other more complex phenomena such as thermally induced in-situ stresses and phase transformation in the cobalt which affects the material properties could also be introduced. Development of three-dimensional models would add additional computational complexity and would be more difficult to validation, but is ultimately essential to fully capturing the geometry of the microstructure and any corrosion effects. These areas of development are shown visually in Figure 11-1. Notably hardness, which is often use in experimental studies, cannot be incorporated into this framework. Classically, hardness is defined as resistance to deformation or a measure of a material's plasticity. However, hardness tests are essentially empirical with no fundamental mathematical theory [199]. As such, this data could only be used in the context of validation of a simulation rather than a modelling input.

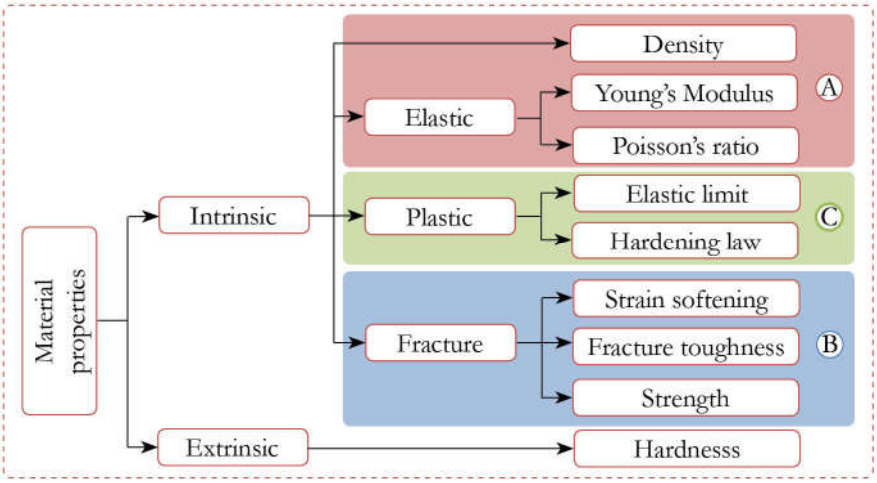

Figure 11-1: Improvement areas for modelling. Development of insert from Figure 4-1. A: Well developed B: Could be improved C: needs to be incorporated.

In order to progress to a full tribocorrosion model further validation of simulations is required for other material behaviours. This was discussed briefly in Section 4.1 when introducing the modelling approach and the milestones which were set out in Figure 4-2 can now be expanded further. In this project validation of simulations was performed through comparison with analytical solutions and experimental results for tensile tests only. Compression simulations would be the next obvious step in validating fracture behaviour. Further development, could lead to simulation and validation of a single point contact, such as an indentation, before a full scratch test simulation is performed. These steps are detailed in Figure 11-2.

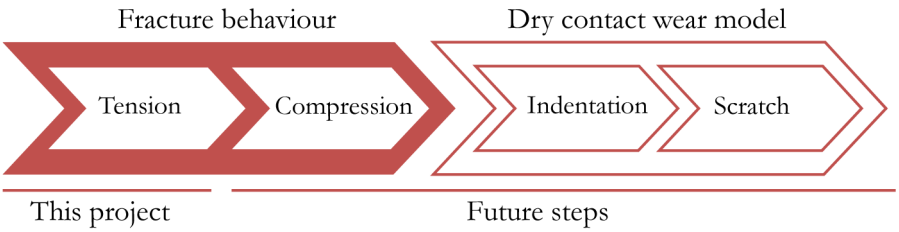

Figure 11-2: Expanding milestone which were set out in Figure 4-2.

11.4.2 Experimental

The study highlights some areas of weakness in our current understanding of the material and which requires further study. While numerical modelling has many advantages over experimental studies, the accuracy of them is dependent on a fundamental understanding of material properties and behaviours which are established through experimental work. To improve tribocorrosion models key areas of information are required. They can be broken down into the following areas:

i. Understanding of corrosion effects on the microstructure in different other corrosive solutions,

ii. Develop experimental techniques to measure fracture properties of phases and interfaces properties and

iii. Extend experiments to cover other compositions of cemented tungsten carbide, such as higher binder content or WC-Ni and WC-Co-Cr.

Corrosive solutions used in this project were limited to H_2SO_4 and NaOH. Understanding the effects of other solutions is important as they could be different to those observed in this project or have different kinetics. The most beneficial would be selection of compounds that are likely to be found downhole either from drilling fluids or naturally occurring.

One of the primary challenges for modelling is that intrinsic fracture properties are still not well understood, especially for individual in-situ phases of the composite. Shear strength is of particular interest, and although the von Mises yield criterion is likely suitable for the Co phase as it applies to ductile materials, its applicability to the WC phase is questionable. Use of the Mohr-Coulomb criterion would probably be more appropriate for the WC. This is used to define the yield strength of brittle materials and is often employed in geomechanical applications and has therefore

already been implemented in Y-Geo. Measurement of these intrinsic properties would need to be carried out experimentally. Previously, experimental studies tend either measure bulk material properties or restrict material property measurements to only a few variables making modelling even more challenging to validate. Nanoindentation has been shown to be able to measure the properties of individual phases, although this has been restricted to hardness and Young's modulus. Another experimental option would be the use of micro-pillar experiments. This approach has been used mainly applied to single-crystals or metallic materials, although has been used recently to study WC-Co [200-202]. Challenges remain in understanding material properties of the binder material however as pillars are not sufficiently small to isolate this region of the microstructure. An alternative method for obtaining these would be to use atomistic modelling which derives these values from an understanding of bonding strengths of atoms.

One of the primary difficulties faced in the experiments was working with low binder content (6% or 11%) and small grain size (around 1 μm) WC-Co. While these compositions are typically used in the industries of interest, hence why they were chosen, they are challenging to characterise and thus understand the interaction between the two phases and how corrosion affects individual phases. These influences would be more easily studied at larger scales, with binder contents up to 25% and grain sizes up to 20 μm. While these are not typically used, better understanding of the material properties can be obtained and which can be scaled down in the model. Larger differences in microstructural influences would also be apparent.

The project focused on the simplest and most common composition of cemented tungsten carbide, WC-Co. Experiments conducted on material properties of other compositions, for example those which include Ni and Cr, could allow these compositions to be modelled using FDEM and fracture behaviour validated. These compositions will affect the corrosion behaviour of the bulk material and have different microstructural effects. Furthermore, while oxides were found not to contribute to corrosion behaviour in WC-Co, they are likely to have a more significant effect in Ni compositions.

Ultimately the accuracy of models is dependent on fundamental the understanding of material properties and behaviours which are established through experimental

work. It is only through the close collaboration of both fields that a full tribocorrosion model can be developed.

References

1. BP plc, *BP Statistical Review of World Energy 2013*. June 2013.
2. US Energy Information Administration, *International Energy Outlook 2013*. July 2013.
3. D. Tabor, *Mohs's Hardness Scale - A Physical Interpretation.* Proceedings of the Physical Society. Section B, 1954. **67**(3): p. 249.
4. U. Beste and S. Jacobson, *Micro scale hardness distribution of rock types related to rock drill wear.* Wear, 2003. **254**(11): p. 1147-1154.
5. U. Beste, A. Lundvall, and S. Jacobson, *Micro-scratch evaluation of rock types—a means to comprehend rock drill wear.* Tribology International, 2004. **37**(2): p. 203-210.
6. Total S.A., *Unconventional Gas: Resources for the Future*. 2012.
7. U.S. Energy Information Administration. *The geology of natural gas resources*. 2011 [Accessed 28 Feb 2014]; Available from: http://www.eia.gov/todayinenergy/detail.cfm?id=110#.
8. G. Aitken, H. Burley, D. Urbaniak, A. Simon, S. Wykes, and L. van Vliet, *Shale gas Unconventional and unwanted: the case against shale gas*, S. Fleet, P. de Clerck, and L. Fuhr, Editors. 2012, Friends of the Earth Europe.
9. H. Cooley and K. Donnelly, *Hydraulic Fracturing and Water Resources: Separating the Frack from the Fiction*, N. Ross and P. Luu, Editors. 2012, Pacific Institute.
10. D. Aitkenhead, *Caroline Lucas: 'I didn't do this because I thought it was fun'*, in *The Guardian*. 4 April 2014.
11. Department of Energy & Climate Change, *Energy Trends - December 2013*. 2013.
12. C. Taylor, D. Lewis, and D. Byles, *Infrastructure for Business: Getting shale gas working*. 2013, Institute of Directors.
13. M. Thorning, *Liquified Natural Gas: Why Rapid Approval of the Backlog of Export Applications is Important for U.S. Prosperity*. 2013, American Council for Capital Formation (ACCF).
14. A. Kibble, T. Cabianca, Z. Daraktchieva, T. Gooding, J. Smithard, G. Kowalczyk, N.P. McColl, M. Singh, S. Vardoulakis, and R. Kamanyire, *Review of the Potential Pulic Health Impacts of Exposures to Chemical and Radioactive Pollutants as a Result of Shale Gas Extraction*. 2013, Public Health England.
15. M. Bickle, D. Goodman, R. Mair, R. Roberts, R.C. Selley, Z. Shipston, H. Thomas, and P. Younger, *Shale gas extraction in the UK: a review of hydraulic fracturing*. 2012, The Royal Society and The Royal Academy of Engineering.

16. *Shale Gas and Water: An independent review of shale gas exploration and exploitation in the UK with a particular focus on the implications for the water environment*. 2014, The Chartered Institution of Water and Environmental Management (CIWEM).

17. J.W. Tester, B.J. Anderson, A.S. Batchelor, D.D. Blackwell, R. DiPippo, E.M. Drake, J. Garnish, B. Livesay, M.C. Moore, K. Nichols, S. Petty, M.N. Toksoz, R.W. Veatch, Jr., R. Baria, C. Augustine, E. Murphy, P. Negraru, and M. Richards, *The Furture of Geothermal Energy: Impact of Enhanced Geothermal Systems (EGS) on the United States in the 21st Century*. 2006.

18. D.B. Fox, D. Sutter, K.F. Beckers, M.Z. Lukawski, D.L. Koch, B.J. Anderson, and J.W. Tester, *Sustainable heat farming: Modeling extraction and recovery in discretely fractured geothermal reservoirs.* Geothermics, 2013. **46**(0): p. 42-54.

19. Apache Corporation. *Photo Gallery*. [Accessed 11 Jul 2014]; Available from: http://www.apachecorp.com/Resources/Photo_gallery.aspx.

20. J.A. Sue, H. Sreshta, and R. Pillai, *High thermal conductivity hardfacing*. 2013, Google Patents.

21. Baker Hughes Incorporated. *Hughes Christensen Vanguard Premium Tricone Drill Bits*. 2009 [Accessed 11 Jul 2014]; Available from: http://assets.cmp.bh.mxmcloud.com/system/c44c0cb9fd21359b0158eea64d947592_tricone_vanguard_bro.pdf.

22. J. Liou. *New bits look beyond design at overall wellbore*. 2012 [Accessed 11 Jul 2014]; Available from: http://www.drillingcontractor.org/new-bits-look-beyond-design-at-overall-wellbore-16693.

23. O. Ardekani and S. Shadizadeh, *Development of drilling trip time model for southern Iranian oil fields: using artificial neural networks and multiple linear regression approaches.* Journal of Petroleum Exploration and Production Technology, 2013. **3**(4): p. 287-295.

24. A.T. Bourgoyne, *Applied drilling engineering*. SPE textbook series. 1986, Richardson, TX: Society of Petroleum Engineers. 502 p.

25. J.J. Azar and G.R. Samuel, *Drilling engineering*. 2007, Tulsa, Okla.: PennWell Corp. x, 486 p.

26. H.M. Ortner, P. Ettmayer, and H. Kolaska, *The history of the technological progress of hardmetals.* International Journal of Refractory Metals and Hard Materials, 2014. **44**(0): p. 148-159.

27. J.R. Davis and ASM International. Handbook Committee., *Tool materials*. ASM specialty handbook. 1995, Materials Park, OH: ASM International. v, 501 p.

28. A.A. Rempel, *Tungsten Carbides Structure, Properties and Application in Hardmetals Introduction.* Tungsten Carbides: Structure, Properties and Application in Hardmetals, 2013. **184**: p. 1-3.

29. K. Schröter, *Hard-metal alloy and the process of making same*, United States Patent Office, Editor. 1925, General Electric Company: USA.

30. R.L. Sessions, *Method of Preparation of Carbides*, United States Patent Office, Editor. 1932, Molybdenum Corporation of America: USA.

31. P. Ettmayer, *Hardmetals and Cermets.* Annual Review of Materials Science, 1989. **19**(1): p. 145-164.

32. *CES EduPack 2010*. Granta Design Limited, Cambridge, UK.

33. J. Larsen-Basse, *Wear of hard-metals in rock drilling: a survey of the literature.* Powder Metallurgy, 1973. **16**: p. 1-32.

34. C.M. Fernandes and A.M.R. Senos, *Cemented carbide phase diagrams: A review.* International Journal of Refractory Metals and Hard Materials, 2011. **29**(4): p. 405-418.

35. D. Mari, *Cermets and Hardmetals*, in *Encyclopedia of Materials: Science and Technology (Second Edition)*, K.H.J. Buschow, et al., Editors. 2001, Elsevier: Oxford. p. 1118-1122.

36. *Through the looking glass - the rather odd world of hardmetals.* Metal Powder Report, 2002. **57**(5): p. 28-29.

37. A.S. Kurlov and A.I. Gusev, *Tungsten carbides : structure, properties and application in hardmetals*, in *Springer Series in Materials Science,*. 2013, Springer,: Cham. p. 1 online resource (xiv, 242 pages).

38. V.K.e. Sarin, D.e. Mari, L.e. Llanes, and C.E.e. Nebel, *Comprehensive hard materials*.

39. G.S. Upadhyaya, *Cemented tungsten carbides : production, properties, and testing*. Materials science and process technology series. 1998, Westwood, N.J.: Noyes Publications. xvii, 403 p.

40. P.C. Angelo and R. Subramanian, *Powder Metallurgy: Science, Technology and Applications*. 2008, New Delhi: PHI learning Private Limited.

41. H.E. Exner, *Physical and chemical nature of cemented carbides.* International Metals Reviews, 1979. **24**(1): p. 149-173.

42. M. Christensen, G. Wahnström, S. Lay, and C.H. Allibert, *Morphology of WC grains in WC–Co alloys: Theoretical determination of grain shape.* Acta Materialia, 2007. **55**(5): p. 1515-1521.

43. S. Kim, S.-H. Han, J.-K. Park, and H.-E. Kim, *Variation of WC grain shape with carbon content in the WC–Co alloys during liquid-phase sintering.* Scripta Materialia, 2003. **48**(5): p. 635-639.

44. S. Lay, C.H. Allibert, M. Christensen, and G. Wahnström, *Morphology of WC grains in WC–Co alloys.* Materials Science and Engineering: A, 2008. **486**(1–2): p. 253-261.

45. V. Bonache, E. Rayón, M.D. Salvador, and D. Busquets, *Nanoindentation study of WC–12Co hardmetals obtained from nanocrystalline powders: Evaluation of hardness and modulus on individual phases.* Materials Science and Engineering: A, 2010. **527**(12): p. 2935-2941.

46. J.J. Roa, E. Jimenez-Pique, C. Verge, J.M. Tarragó, A. Mateo, J. Fair, and L. Llanes, *Intrinsic hardness of constitutive phases in WC–Co composites:*

Nanoindentation testing, statistical analysis, WC crystal orientation effects and flow stress for the constrained metallic binder. Journal of the European Ceramic Society, 2015. **35**(13): p. 3419-3425.

47. A. Duszová, R. Halgaš, M. Bľanda, P. Hvizdoš, F. Lofaj, J. Dusza, and J. Morgiel, *Nanoindentation of WC–Co hardmetals.* Journal of the European Ceramic Society, 2013. **33**(12): p. 2227-2232.

48. T. Csanádi, M. Bľanda, N.Q. Chinh, P. Hvizdoš, and J. Dusza, *Orientation-dependent hardness and nanoindentation-induced deformation mechanisms of WC crystals.* Acta Materialia, 2015. **83**: p. 397-407.

49. S. Sutthiruangwong, G. Mori, and R. Kösters, *Passivity and pseudopassivity of cemented carbides.* International Journal of Refractory Metals and Hard Materials, 2005. **23**(2): p. 129-136.

50. M. Hellsing, *High resolution microanalysis of binder phase in as sintered WC-Co cemented carbides.* Materials Science and Technology, 1988. **4**(9): p. 824-829.

51. S. Hochstrasser, Y. Mueller, C. Latkoczy, S. Virtanen, and P. Schmutz, *Analytical characterization of the corrosion mechanisms of WC–Co by electrochemical methods and inductively coupled plasma mass spectroscopy.* Corrosion Science, 2007. **49**(4): p. 2002-2020.

52. G.S. Upadhyaya, *Materials science of cemented carbides — an overview.* Materials & Design, 2001. **22**(6): p. 483-489.

53. K. Jia, T.E. Fischer, and B. Gallois, *Microstructure, hardness and toughness of nanostructured and conventional WC-Co composites.* Nanostructured Materials, 1998. **10**(5): p. 875-891.

54. K.P. Mingard, B. Roebuck, J. Marshall, and G. Sweetman, *Some aspects of the structure of cobalt and nickel binder phases in hardmetals.* Acta Materialia, 2011. **59**(6): p. 2277-2290.

55. F.J.J. Kellner, H. Hildebrand, and S. Virtanen, *Effect of WC grain size on the corrosion behavior of WC–Co based hardmetals in alkaline solutions.* International Journal of Refractory Metals and Hard Materials, 2009. **27**(4): p. 806-812.

56. B. Roebuck, E.A. Almond, and A.M. Cottenden, *The influence of composition, phase transformation and varying the relative F.C.C. and H.C.P. phase contents on the properties of dilute Co-W-C alloys.* Materials Science and Engineering, 1984. **66**(2): p. 179-194.

57. H. Engqvist and U. Wiklund, *Mapping of mechanical properties of WC–Co using nanoindentation.* Tribology Letters, 2000. **8**(2-3): p. 147-152.

58. W. Dawihl and W. Rix, *Über die Gitterkonstanten der Carbide und Nitride des Titans und Vanadins.* Zeitschrift für anorganische und allgemeine Chemie, 1940. **244**(2): p. 191-197.

59. A. Henjered, M. Hellsing, H.O. Andren, and H. Norden, *The presence of cobalt at WC/WC interfaces.* Science of hard materials 1984 : proceedings of the second International Conference on the Science of Hard Materials held in Rhodes, Greece on 23-28 September, 1986. **75**: p. 303-309.

60. B. Paul, *PREDICTION OF ELASTIC CONSTANTS OF MULTIPHASE MATERIALS. Technical Report No. 3*, in *Other Information: Orig. Receipt Date: 31-DEC-59*. 1959. p. Medium: X; Size: Pages: 22.

61. Z. Hashin and S. Shtrikman, *A variational approach to the theory of the elastic behaviour of multiphase materials.* Journal of the Mechanics and Physics of Solids, 1963. **11**(2): p. 127-140.

62. K.S. Ravichandran, *Fracture toughness of two phase WC-Co cermets.* Acta Metallurgica et Materialia, 1994. **42**(1): p. 143-150.

63. A.J. Gant, M.G. Gee, and A.T. May, *The evaluation of tribo-corrosion synergy for WC–Co hardmetals in low stress abrasion.* Wear, 2004. **256**(5): p. 500-516.

64. A. Krawitz and E. Drake, *Residual stresses in cemented carbides — An overview.* International Journal of Refractory Metals and Hard Materials, 2015. **49**: p. 27-35.

65. J.L. Chermant, A. Deschanvres, G. Hautier, A. Iost, and G. Manier, *Etude de la variation de la dureté sous charge réduite de composites "carbure-métal" en fonction de la composition.* physica status solidi (a), 1973. **15**(2): p. K149-K152.

66. M.G. Gee, *Low load multiple scratch tests of ceramics and hard metals.* Wear, 2001. **250**(1–12): p. 264-281.

67. H.C. Lee and J. Gurland, *Hardness and deformation of cemented tungsten carbide.* Materials Science and Engineering, 1978. **33**(1): p. 125-133.

68. J.L. Chermant and F. Osterstock, *Fracture toughness and fracture of WC-Co composites.* Journal of Materials Science, 1976. **11**(10): p. 1939-1951.

69. C.H. Allibert, *Sintering features of cemented carbides WC–Co processed from fine powders.* International Journal of Refractory Metals and Hard Materials, 2001. **19**(1): p. 53-61.

70. B. Roebuck, *Extrapolating hardness-structure property maps in WC/Co hardmetals.* International Journal of Refractory Metals and Hard Materials, 2006. **24**(1–2): p. 101-108.

71. S. Okamoto, Y. Nakazono, K. Otsuka, Y. Shimoitani, and J. Takada, *Mechanical properties of WC/Co cemented carbide with larger WC grain size.* Materials Characterization, 2005. **55**(4–5): p. 281-287.

72. H. Saito, A. Iwabuchi, and T. Shimizu, *Effects of Co content and WC grain size on wear of WC cemented carbide.* Wear, 2006. **261**(2): p. 126-132.

73. U. Beste, T. Hartzell, H. Engqvist, and N. Axén, *Surface damage on cemented carbide rock-drill buttons.* Wear, 2001. **249**(3–4): p. 324-329.

74. T.L. Anderson, *Fracture mechanics : fundamentals and applications*. 3rd ed. 2005, Boca Raton, Fla., London: Taylor & Francis. 621 p.

75. G. Kirsch, *Die Theorie der Elastizität und die Bedürfnisse der Festigkeitslehre.* Zeitschrift des Vereines Deutscher Ingenieure, 1898. **42**: p. 797-807.

76. S. Sheikh, R. M'Saoubi, P. Flasar, M. Schwind, T. Persson, J. Yang, and L. Llanes, *Fracture toughness of cemented carbides: Testing method and microstructural effects.* International Journal of Refractory Metals and Hard Materials, 2015. **49**: p. 153-160.

77. J.R. Pickens and J. Gurland, *The fracture toughness of WC · Co alloys measured on single-edge notched beam specimens precracked by electron discharge machining.* Materials Science and Engineering, 1978. **33**(1): p. 135-142.

78. S. Palmqvist, *A method to determine the toughness of brittle materials, especially hard metals.* Jernkontorets Annaler, 1957. **141**: p. 303-307.

79. L. Dobrzański and B. Dołżańska, *Hardness to toughness relationship on WC-Co tool gradient materials evaluated by Palmqvist method.* Archives of Materials Science and Engineering, 2010. **43**(2): p. 87-93.

80. H.E. Exner, *The influence of sample preparation on Palmqvist's method for toughness testing of cemented carbides.* Transactions of the Metallurgical Society of AIME, 1969. **245**: p. 677-683.

81. I.M. Ogilvy, C.M. Perrott, and J.W. Suiter, *On the indentation fracture of cemented carbide part 1 — Survey of operative fracture modes.* Wear, 1977. **43**(2): p. 239-252.

82. C.M. Perrott, *On the indentation fracture of cemented carbide II — the nature of surface fracture toughness.* Wear, 1978. **47**(1): p. 81-91.

83. D.K. Shetty, I.G. Wright, P.N. Mincer, and A.H. Clauer, *Indentation fracture of WC-Co cermets.* Journal of Materials Science, 1985. **20**(5): p. 1873-1882.

84. R. Spiegler, S. Schmauder, and L.S. Sigl, *Fracture toughness evalulation of WC-Co alloys by indentation testing.* Journal of Hard Materials, 1990. **1**(3): p. 147-158.

85. L.S. Sigl and H.E. Exner, *Experimental study of the mechanics of fracture in WC-Co alloys.* Metallurgical Transactions A, 1987. **18**(7): p. 1299-1308.

86. K.P. Mingard, H.G. Jones, M.G. Gee, B. Roebuck, and J.W. Nunn, *In situ observation of crack growth in a WC-Co hardmetal and characterisation of crack growth morphologies by EBSD.* International Journal of Refractory Metals and Hard Materials, 2013. **36**: p. 136-142.

87. J.M. Tarragó, E. Jiménez-Piqué, L. Schneider, D. Casellas, Y. Torres, and L. Llanes, *FIB/FESEM experimental and analytical assessment of R-curve behavior of WC-Co cemented carbides.* Materials Science and Engineering: A.

88. B. Roebuck and E.A. Almond, *Deformation and fracture processes and the physical metallurgy of WC–Co hardmetals.* International Materials Reviews, 1988. **33**(1): p. 90-112.

89. J.B.J.W. Hegeman, J.T.M. De Hosson, and G. de With, *Grinding of WC–Co hardmetals.* Wear, 2001. **248**(1–2): p. 187-196.

90. C.H. Vasel, A.D. Krawitz, E.F. Drake, and E.A. Kenik, *Binder deformation in WC-(Co, Ni) cemented carbide composites.* Metallurgical Transactions A, 1985. **16**(12): p. 2309-2317.

91. V.K. Sarin and T. Johannesson, *On the Deformation of WC–Co Cemented Carbides.* Metal Science, 1975. **9**(1): p. 472-476.

92. J.F. Archard, *Contact and Rubbing of Flat Surfaces.* Journal of Applied Physics, 1953. **24**(8): p. 981-988.

93. J.F. Archard and W. Hirst, *The Wear of Metals under Unlubricated Conditions.* Proceedings of the Royal Society of London. Series A. Mathematical and Physical Sciences, 1956. **236**(1206): p. 397-410.

94. K. Jia and T.E. Fischer, *Abrasion resistance of nanostructured and conventional cemented carbides.* Wear, 1996. **200**(1–2): p. 206-214.

95. N. Axén and S. Jacobson, *A model for the abrasive wear resistance of multiphase materials.* Wear, 1994. **174**(1–2): p. 187-199.

96. A.J. Gant and M.G. Gee, *Abrasion of tungsten carbide hardmetals using hard counterfaces.* International Journal of Refractory Metals and Hard Materials, 2006. **24**(1–2): p. 189-198.

97. Y. Ahn, N.-G. Cho, S.-H. Lee, and D. Lee, *Lateral Crack in Abrasive Wear of Brittle Materials.* JSME International Journal Series A Solid Mechanics and Material Engineering, 2003. **46**(2): p. 140-144.

98. K.H.Z. Gahr, *Wear by hard particles.* Tribology International, 1998. **31**(10): p. 587-596.

99. U. Beste and S. Jacobson, *A new view of the deterioration and wear of WC/Co cemented carbide rock drill buttons.* Wear, 2008. **264**(11–12): p. 1129-1141.

100. A.J. Gant and M.G. Gee, *Wear of tungsten carbide–cobalt hardmetals and hot isostatically pressed high speed steels under dry abrasive conditions.* Wear, 2001. **251**(1–12): p. 908-915.

101. J. Larsen-Basse, C.M. Perrott, and P.M. Robinson, *Abrasive wear of tungsten carbide—cobalt composites. I. Rotary drilling tests.* Materials Science and Engineering, 1974. **13**(2): p. 83-91.

102. R.I. Blombery, C.M. Perrot, and P.M. Robinson, *Abrasive wear of tungsten carbide-cobalt composites. I. Wear mechanisms.* Materials Science and Engineering, 1974. **13**(2): p. 93-100.

103. M.V. Swain, *Microscopic observations of abrasive wear of polycrystalline alumina.* Wear, 1975. **35**(1): p. 185-189.

104. J. Larsen-Basse, *Binder extrusion in sliding wear of WC-Co alloys.* Wear, 1985. **105**(3): p. 247-256.

105. P.H. Shipway and L. Howell, *Microscale abrasion–corrosion behaviour of WC–Co hardmetals and HVOF sprayed coatings.* Wear, 2005. **258**(1–4): p. 303-312.

106. D.K. Shetty, I.G. Wright, and J.T. Stropki, *Slurry Erosion of WC-Co Cermets and Ceramics.* A S L E Transactions, 1985. **28**(1): p. 123-133.

107. M.G. Gee and A.D. Gee, *A cost effective test system for micro-tribology experiments.* Wear, 2007. **263**(7–12): p. 1484-1491.

108. M.G. Gee, *Model scratch corrosion studies for WC/Co hardmetals.* Wear, 2010. **268**(9–10): p. 1170-1177.

109. K.P. Mingard and M.G. Gee, *EBSD examination of worn WC/Co hardmetal surfaces.* Wear, 2007. **263**(1–6): p. 643-652.

110. M.G. Gee, A. Gant, and B. Roebuck, *Wear mechanisms in abrasion and erosion of WC/Co and related hardmetals.* Wear, 2007. **263**(1–6): p. 137-148.

111. J.C.P. Zuñega, M.G. Gee, R.J.K. Wood, and J. Walker, *Scratch testing of WC/Co hardmetals.* Tribology International, 2012. **54**(0): p. 77-86.

112. U. Beste, S. Jacobson, and S. Hogmark, *Rock penetration into cemented carbide drill buttons during rock drilling.* Wear, 2008. **264**(11–12): p. 1142-1151.

113. S. Olovsjö, R. Johanson, F. Falsafi, U. Bexell, and M. Olsson, *Surface failure and wear of cemented carbide rock drill buttons—The importance of sample preparation and optimized microscopy settings.* Wear, 2013. **302**(1–2): p. 1546-1554.

114. S. Ndlovu, K. Durst, and M. Göken, *Investigation of the sliding contact properties of WC-Co hard metals using nanoscratch testing.* Wear, 2007. **263**(7–12): p. 1602-1609.

115. D. Landolt, S. Mischler, and M. Stemp, *Electrochemical methods in tribocorrosion: a critical appraisal.* Electrochimica Acta, 2001. **46**(24–25): p. 3913-3929.

116. E.J. Wentzel and C. Allen, *The erosion-corrosion resistance of tungsten-carbide hard metals.* International Journal of Refractory Metals and Hard Materials, 1997. **15**(1–3): p. 81-87.

117. H. Engqvist, U. Beste, and N. Axén, *The influence of pH on sliding wear of WC-based materials.* International Journal of Refractory Metals and Hard Materials, 2000. **18**(2–3): p. 103-109.

118. A.J. Gant, M.G. Gee, D.D. Gohil, H.G. Jones, and L.P. Orkney, *Use of FIB/SEM to assess the tribo-corrosion of WC/Co hardmetals in model single point abrasion experiments.* Tribology International, 2013. **68**(0): p. 56-66.

119. P.H. Shipway and S. Wirojanupatump, *The role of lubrication and corrosion in abrasion of materials in aqueous environments.* Tribology International, 2002. **35**(10): p. 661-667.

120. A.J. Gant, M.G. Gee, and A.T. May, *Microabrasion of WC–Co hardmetals in corrosive media.* Wear, 2004. **256**(9–10): p. 954-962.

121. M.R. Thakare, J.A. Wharton, R.J.K. Wood, and C. Menger, *Investigation of micro-scale abrasion–corrosion of WC-based sintered hardmetal and sprayed coating using in situ electrochemical current-noise measurements.* Wear, 2009. **267**(11): p. 1967-1977.

122. C.O.A. Olsson and M. Stemp, *Modelling the transient current from two rubbing electrode configurations: insulating pin on metal substrate and metal pin on insulating substrate.* Electrochimica Acta, 2004. **49**(13): p. 2145-2154.

123. P. Jemmely, S. Mischler, and D. Landolt, *Electrochemical modeling of passivation phenomena in tribocorrosion.* Wear, 2000. **237**(1): p. 63-76.

124. P. Ponthiaux, F. Wenger, D. Drees, and J.P. Celis, *Electrochemical techniques for studying tribocorrosion processes.* Wear, 2004. **256**(5): p. 459-468.

125. S.L. Chawla and R.K. Gupta, *Materials selection for corrosion control*. 1993, Materials Park, OH: ASM International. xiii, 508 p.

126. R.W. Revie and H.H. Uhlig, *Corrosion and corrosion control : an introduction to corrosion science and engineering*. 4th ed. 2008, Hoboken, N.J.: Wiley-Interscience. xx, 490 p.

127. A.M. Human, B. Roebuck, and H.E. Exner, *Electrochemical polarisation and corrosion behaviour of cobalt and Co(W,C) alloys in 1 N sulphuric acid.* Materials Science and Engineering: A, 1998. **241**(1–2): p. 202-210.

128. M. Pourbaix, *Atlas of electrochemical equilibria in aqueous solutions*. 1966, Oxford: pergamon.

129. A.M. Human and H.E. Exner, *Electrochemical behaviour of tungsten-carbide hardmetals.* Materials Science and Engineering: A, 1996. **209**(1–2): p. 180-191.

130. S. Sutthiruangwong and G. Mori, *Corrosion properties of Co-based cemented carbides in acidic solutions.* International Journal of Refractory Metals and Hard Materials, 2003. **21**(3–4): p. 135-145.

131. M.H. Ghandehari, *Anodic Behavior of Cemented WC - 6% Co Alloy in Phosphoric Acid Solutions.* Journal of The Electrochemical Society, 1980. **127**(10): p. 2144-2147.

132. W.J. Tomlinson and C.R. Linzell, *Anodic polarization and corrosion of cemented carbides with cobalt and nickel binders.* Journal of Materials Science, 1988. **23**(3): p. 914-918.

133. B. Bozzini, G.P. De Gaudenzi, M. Serra, A. Fanigliulo, and F. Bogani, *Corrosion behaviour of WC-Co based hardmetal in neutral chloride and acid sulphate media.* Materials and Corrosion, 2002. **53**(5): p. 328-334.

134. H.S. Kalish, *Corrosion of Cemented Carbides*, in *Metals handbook: Volume 13 Corrosion*. 1992, American Society for Metals: Metals Park, Ohio.

135. A. Foelske and H.-H. Strehblow, *Passivity of cobalt in borate buffer at pH 9.3 studied by x-ray photoelectron spectroscopy.* Surface and Interface Analysis, 2000. **29**(8): p. 548-555.

136. M. Metikoš-Huković and R. Babić, *Passivation and corrosion behaviours of cobalt and cobalt–chromium–molybdenum alloy.* Corrosion Science, 2007. **49**(9): p. 3570-3579.

137. V.A. Pugsley, G. Korn, S. Luyckx, H.G. Sockel, W. Heinrich, M. Wolf, H. Feld, and R. Schulte, *The influence of a corrosive wood-cutting environment on the*

mechanical properties of hardmetal tools. International Journal of Refractory Metals and Hard Materials, 2001. **19**(4–6): p. 311-318.

138. J.M. Tarragó, G. Fargas, E. Jimenez-Piqué, A. Felip, L. Isern, D. Coureaux, J.J. Roa, I. Al-Dawery, J. Fair, and L. Llanes, *Corrosion damage in WC–Co cemented carbides: residual strength assessment and 3D FIB-FESEM tomography characterisation.* Powder Metallurgy, 2014. **57**(5): p. 324-330.

139. ASTM Standard G119, *Standard guide for determining synergism between wear and corrosion*. 1993 (1998), ASTM International: West Conshohocken, PA.

140. C.H. Pitt and Y.M. Chang, *Jet Slurry Corrosive Wear of High-Chromium Cast Iron and High-Carbon Steel Grinding Ball Alloys.* Corrosion, 1986. **42**(6): p. 312-317.

141. D. Kotlyar, C.H. Pitt, and M.E. Wadsworth, *Simultaneous Corrosion and Abrasion Measurements under Grinding Conditions.* Corrosion, 1988. **44**(4): p. 221-228.

142. B.W. Madsen, *Measurement of wear and corrosion rates using a novel slurry wear test*. Vol. 26. 1987.

143. B.W. Madsen, *Measurement of erosion-corrosion synergism with a slurry wear test apparatus.* Wear, 1988. **123**(2): p. 127-142.

144. B.W. Madsen, *Corrosion and erosion corrosion of Fe-Al alloys in aqueous solutions and slurries*, in *Wear-Corrosion Interactions in Liquid Media*, A.A. Sagues and E.I. Meletis, Editors. 1991: Warrendale, PA. p. 49-78.

145. M.M. Stack and T.M. Abd El Badia, *On the construction of erosion–corrosion maps for WC/Co–Cr-based coatings in aqueous conditions.* Wear, 2006. **261**(11): p. 1181-1190.

146. M.M. Stack, *Mapping tribo-corrosion processes in dry and in aqueous conditions: some new directions for the new millennium.* Tribology International, 2002. **35**(10): p. 681-689.

147. M.M. Stack, N. Corlett, and S. Zhou, *A methodology for the construction of the erosion-corrosion map in aqueous environments.* Wear, 1997. **203**: p. 474-488.

148. P.E. Sinnett-Jones, J.A. Wharton, and R.J.K. Wood, *Micro-abrasion–corrosion of a CoCrMo alloy in simulated artificial hip joint environments.* Wear, 2005. **259**(7–12): p. 898-909.

149. C. Hodge and M.M. Stack, *Tribo-corrosion mechanisms of stainless steel in soft drinks.* Wear, 2010. **270**(1–2): p. 104-114.

150. J.O. Bello, R.J.K. Wood, and J.A. Wharton, *Synergistic effects of micro-abrasion–corrosion of UNS S30403, S31603 and S32760 stainless steels.* Wear, 2007. **263**(1–6): p. 149-159.

151. S. Akonko, D.Y. Li, and M. Ziomek-Moroz, *Effects of cathodic protection on corrosive wear of 304 stainless steel.* Tribology Letters, 2005. **18**(3): p. 405-410.

152. N. Espallargas and S. Mischler, *Tribocorrosion behaviour of overlay welded Ni–Cr 625 alloy in sulphuric and nitric acids: Electrochemical and chemical effects.* Tribology International, 2010. **43**(7): p. 1209-1217.

153. S. Mischler, S. Debaud, and D. Landolt, *Wear‐Accelerated Corrosion of Passive Metals in Tribocorrosion Systems.* Journal of The Electrochemical Society, 1998. **145**(3): p. 750-758.

154. S. Mischler, A. Spiegel, and D. Landolt, *The role of passive oxide films on the degradation of steel in tribocorrosion systems.* Wear, 1999. **225–229, Part 2**(0): p. 1078-1087.

155. H. Uhlig, *Mechanism of fretting corrosion.* Journal of Applied Mechanics, 1954. **21**(4): p. 401-407.

156. S. Mischler, *Triboelectrochemical techniques and interpretation methods in tribocorrosion: A comparative evaluation.* Tribology International, 2008. **41**(7): p. 573-583.

157. Q. Luo, S. Ramarajan, and S.V. Babu, *Modification of the Preston equation for the chemical–mechanical polishing of copper.* Thin Solid Films, 1998. **335**(1–2): p. 160-167.

158. P.J. Blau, *How common is the steady-state? The implications of wear transitions for materials selection and design.* Wear, 2015. **332–333**: p. 1120-1128.

159. J. Jiang, M.M. Stack, and A. Neville, *Modelling the tribo-corrosion interaction in aqueous sliding conditions.* Tribology International, 2002. **35**(10): p. 669-679.

160. J. Jiang and M.M. Stack, *Modelling sliding wear: From dry to wet environments.* Wear, 2006. **261**(9): p. 954-965.

161. C.B. von der Ohe, R. Johnsen, and N. Espallargas, *Modeling the multi-degradation mechanisms of combined tribocorrosion interacting with static and cyclic loaded surfaces of passive metals exposed to seawater.* Wear, 2010. **269**(7–8): p. 607-616.

162. V. Livescu, B. Clausen, J.W. Paggett, A.D. Krawitz, E.F. Drake, and M.A.M. Bourke, *Measurement and modeling of room temperature co-deformation in WC–10 wt.% Co.* Materials Science and Engineering: A, 2005. **399**(1–2): p. 134-140.

163. M.H. Poech, H.F. Fischmeister, D. Kaute, and R. Spiegler, *FE-modelling of the deformation behaviour of WC-Co alloys.* Computational Materials Science, 1993. **1**(3): p. 213-224.

164. B.O. Jaensson and B.O. Sundström, *Determination of Young's modulus and poisson's ratio for WC-Co alloys by the finite element method.* Materials Science and Engineering, 1972. **9**: p. 217-222.

165. T. Sadowski and T. Nowicki, *Numerical investigation of local mechanical properties of WC/Co composite.* Computational Materials Science, 2008. **43**(1): p. 235-241.

166. L.S. Sigl and S. Schmauder, *A finite element study of crack growth in WC-Co.* International Journal of Fracture, 1988. **36**(4): p. 305-317.

167. P.E. McHugh and P.J. Connolly, *Micromechanical modelling of ductile crack growth in the binder phase of WC–Co.* Computational Materials Science, 2003. **27**(4): p. 423-436.

168. J.R. Rice and D.M. Tracey, *On the ductile enlargement of voids in triaxial stress fields.* Journal of the Mechanics and Physics of Solids, 1969. **17**(3): p. 201-217.

169. H. Dębski and T. Sadowski, *Modelling of microcracks initiation and evolution along interfaces of the WC/Co composite by the finite element method.* Computational Materials Science, 2014. **83**: p. 403-411.

170. U.A. Özden, A. Bezold, and C. Broeckmann, *Numerical Simulation of Fatigue Crack Propagation in WC/Co based on a Continuum Damage Mechanics Approach.* Procedia Materials Science, 2014. **3**: p. 1518-1523.

171. U.A. Özden, K.P. Mingard, M. Zivcec, A. Bezold, and C. Broeckmann, *Mesoscopical finite element simulation of fatigue crack propagation in WC/Co-hardmetal.* International Journal of Refractory Metals and Hard Materials, 2015. **49**: p. 261-267.

172. H.F. Fischmeister, S. Schmauder, and L.S. Sigl, *Finite element modelling of crack propagation in WC-Co hard metals.* Materials Science and Engineering, 1988. **A105/106**: p. 305-311.

173. P.A. Cundall and O.D.L. Strack, *A discrete numerical model for granular assemblies.* Géotechnique, 1979. **29**(1): p. 47-65.

174. Kemutec USA. *Mucon Promo-Flow for discharging difficult flowing powders from silos*. 2015 [Accessed 16-Apr 2015]; Available from: http://kemutecusa.com/products/valves/mucon-promo-flow.html.

175. A. Munjiza, *The combined finite-discrete element method*. 2004, Hoboken, NJ: Wiley. x, 333 p.

176. A. Munjiza, J. Xiang, X. Garcia, J.P. Latham, G.G.S. D'Albano, and N.W.M. John, *The Virtual Geoscience Workbench, VGW: Open Source tools for discontinuous systems.* Particuology, 2010. **8**(2): p. 100-105.

177. O. Mahabadi, A. Lisjak, A. Munjiza, and G. Grasselli, *Y-Geo: new combined finite-discrete element numerical code for geomechanical applications.* International Journal of Geomechanics, 2012. **12**(6): p. 676-688.

178. O. Mahabadi, G. Grasselli, and A. Munjiza, *Y-GUI: A graphical user interface and pre-processor for the combined finite-discrete element code, Y2D, incorporating material heterogeneity.* Computers & Geosciences, 2010. **36**(2): p. 241-252.

179. O.K. Mahabadi, G. Grasselli, and A. Munjiza, *Numerical modelling of a Brazilian Disc test of layered rocks using the combined finite-discrete element method.* In Proceedings of 3rd Canada-US (CANUS) Rock Mechanics Symposium (RockEng09). Toronto, Canada. 9-14 May, 2009.

180. R.H. Kraft and J.F. Molinari, *A statistical investigation of the effects of grain boundary properties on transgranular fracture.* Acta Materialia, 2008. **56**(17): p. 4739-4749.

181. R.H. Kraft, J.F. Molinari, K.T. Ramesh, and D.H. Warner, *Computational micromechanics of dynamic compressive loading of a brittle polycrystalline material using a distribution of grain boundary properties.* Journal of the Mechanics and Physics of Solids, 2008. **56**(8): p. 2618-2641.

182. B.S.A. Tatone and G. Grasselli, *A calibration procedure for two-dimensional laboratory-scale hybrid finite–discrete element simulations.* International Journal of Rock Mechanics and Mining Sciences, 2015. **75**: p. 56-72.

183. G. Hondros, *The evalulation of Poisson's ratio and the modulus of materials of a low tensile resistance by the Brazilian (indirect tensile) test with particular reference to conrete.* Austrilian Journal of Applied Science, 1959. **10**: p. 243-268.

184. B. Roebuck, *Terminology, testing, properties, imaging and models for fine grained hardmetals.* International Journal of Refractory Metals and Hard Materials, 1995. **13**(5): p. 265-279.

185. M.G. Gee, B. Roebuck, P. Lindahl, and H.O. Andren, *Constituent phase nanoindentation of WC/Co and Ti(C,N) hard metals.* Materials Science and Engineering: A, 1996. **209**(1–2): p. 128-136.

186. I.M. Hutchings, *The contributions of David Tabor to the science of indentation hardness.* Journal of Materials Research, 2009. **24**(3): p. 581-589.

187. A.C. Fischer-Cripps, *Nanoindentation*, in *Mechanical engineering series*. 2002, Springer: New York. p. xx, 197 p.

188. W.C. Oliver and G.M. Pharr, *An improved technique for determining hardness and elastic modulus using load and displacement sensing indentation experiments.* Journal of Materials Research, 1992. **7**(06): p. 1564-1583.

189. W.C. Oliver and G.M. Pharr, *Measurement of hardness and elastic modulus by instrumented indentation: Advances in understanding and refinements to methodology.* Journal of Materials Research, 2004. **19**(01): p. 3-20.

190. K. Kanaya and S. Okayama, *Penetration and energy-loss theory of electrons in solid targets.* Journal of Physics D: Applied Physics, 1972. **5**(1): p. 43.

191. A.M. Human and H.E. Exner, *The relationship between electrochemical behaviour and in-service corrosion of WC based cemented carbides.* International Journal of Refractory Metals and Hard Materials, 1997. **15**(1–3): p. 65-71.

192. R.D. Armstrong and A.F. Douglas, *The anodic oxidation of the binary compounds of the transition elements in sulphuric acid.* Journal of Applied Electrochemistry, 1972. **2**(2): p. 143-149.

193. Z.-H. Xu and J. Ågren, *A modified hardness model for WC–Co cemented carbides.* Materials Science and Engineering: A, 2004. **386**(1–2): p. 262-268.

194. N. Cuadrado, D. Casellas Padró, L.M. Llanes Pitarch, I. Gonzalez, and J. Caro, *Effect of crystal anisotropy on the mechanical properties of WC embedded in WC-Co cemented carbides.* Proceedings of the Euro PM2011 Powder Metallurgy Congress & Exhibition, 2011: p. p. 215-220.

195. B. Roebuck, P. Klose, and K.P. Mingard, *Hardness of hexagonal tungsten carbide crystals as a function of orientation.* Acta Materialia, 2012. **60**(17): p. 6131-6143.

196. R.W. Armstrong, *The Hardness and Strength Properties of WC-Co Composites.* Materials, 2011. **4**(7): p. 1287-1308.

197. R.K. Abu Al-Rub and G.Z. Voyiadjis, *A physically based gradient plasticity theory.* International Journal of Plasticity, 2006. **22**(4): p. 654-684.

198. R.K. Abu Al-Rub and G.Z. Voyiadjis, *Analytical and experimental determination of the material intrinsic length scale of strain gradient plasticity theory from micro- and nano-indentation experiments.* International Journal of Plasticity, 2004. **20**(6): p. 1139-1182.

199. K. Herrmann, *Hardness testing principles and applications*. 2011, ASM International: Materials Park, Ohio. p. vi, 255 p.

200. J.M. Tarragó, J.J. Roa, E. Jiménez-Piqué, E. Keown, J. Fair, and L. Llanes, *Mechanical deformation of WC–Co composite micropillars under uniaxial compression.* International Journal of Refractory Metals and Hard Materials, 2016. **54**: p. 70-74.

201. M. Trueba, A. Aramburu, N. Rodríguez, I. Iparraguirre, M.R. Elizalde, I. Ocaña, J.M. Sánchez, and J.M. Martínez-Esnaola, *"In-situ" mechanical characterisation of WC–Co hardmetals using microbeam testing.* International Journal of Refractory Metals and Hard Materials, 2014. **43**: p. 236-240.

202. T. Csanádi, M. Bľanda, A. Duszová, N.Q. Chinh, P. Szommer, and J. Dusza, *Deformation characteristics of WC micropillars.* Journal of the European Ceramic Society, 2014. **34**(15): p. 4099-4103.